# A study of the nucleation and growth mechanism of graphene on copper

*Author:*

**HoKwon Kim**

*Supervisors:*

**Prof. Eduardo Saiz**

**Prof. Manish Chhowalla**

**Dr. Cecilia Mattevi**

Dissertation submitted by HoKwon Kim in partial fulfilment of the requirements for the Degree of Doctor of Philosophy in Materials

*Date of Submission:*

**07/11/2012**

# Declaration of Originality

I, HoKwon Kim, herewith declare that the materials presented in this dissertation are of original work, otherwise properly cited or acknowledged.

_____ _____

Signature Date

# Copyright Declaration

# Abstract

Two approaches for the large scale synthesis of graphene were investigated with the objective of achieving high-quality graphene for practical applications: (1) non-covalent solution based exfoliation of graphite, and (2) chemical vapour deposition of graphene on copper. As the processing conditions, structure, and properties of graphene are inherently connected, the aim of the study was to gain fundamental insights on the critical mechanisms that govern the properties and device performance of graphene. The first part of this thesis describes the efficient non-covalent exfoliation of graphite to produce few-layer-graphene dispersion in N-methylpyrrolidone and large-scale thin film deposition using the Langmuir-Blodgett assembly. In the second part, the chemical vapour deposition of polycrystalline graphene films on copper was investigated as it has emerged as the most promising route toward large scale synthesis of monolayer graphene for optoelectronics applications due to its properties approaching that of ideal graphene and the relatively low cost of copper. An extensive range of growth parameters was employed to develop a model of two-dimensional nucleation and self-limited growth of graphene on the surface of copper. The analysis of the nucleation and growth kinetics has revealed the relationship between atomic processes that impart two distinct temperature regimes of nucleation, whereas the growth of the individual nuclei was shown to be rate-limited by the carbon attachment at the nuclei edges. Moreover, the growth on high index copper surfaces has shown that graphene nanostructures of controlled shapes, density, and dimensions can be produced, depending on the Cu crystal orientation. Interestingly, few-layer-graphene grown on Cu frequently exhibits AA stacking with interlayer spacing of ~3.6 Å, with a preserved linear dispersion relationship. This work thus provides practical guidelines for achieving wafer scale single crystal graphene as well as the control over the mesoscale structure by the careful selection of the growth parameters.

# Acknowledgements

I would like to thank Prof. Eduardo Saiz, Prof. Manish Chhowalla, and Dr. Cecilia Mattevi for their supervision, support, and advices. Moreover, I would like thank the examiners, Prof. John Robertson, Prof. Norbert Klein, and Prof. David McPhail for their thorough and insightful review and suggestions for the final version of the thesis.

The work presented here would not have been accomplished without generous help of my colleagues and collaborators who spent time with me to have insightful discussions, aided sample characterizations and trained me with many necessary skills. Specifically, I would like to acknowledge Dr. Goki Eda for probe station training, Ye Xiao and Dr. Rob Maher for his help in the Raman measurements, Onur Menteş and Andrea Locatelli for the beam time collaboration at Trieste, Elettra, Dr. H. Kim and Prof. Richard Riman for providing the centrifuge, and Langmuir-Blodgett deposition system, Dr. Mahmoud Arakani and Dr. Cati Ware for the training on SEM and EBSD, Richard Chater for AFM training, Richard Sweeney for XRD training, Dr. Suelen Barg for surface energy measurements, Dr. Na Ni for cross sectional TEM image, Florian Colleaux for his electrical measurements, Dr. Salvador Eslava for the optical interferometry measurements, Dr. M. Reyes Calvo for the STM measurements, and Dr. Stefano Agnoli for the XPS measurements.

I also would like to thank undergraduate students, Kyung Tae Park, David Lee, Toby Davis, Jing Ge, Raj Rajanarayanan, and Sarah Synder who have helped me with various aspects in the course of the project.

I also would like to express my gratitude to Prof. Zhenghong Lu of University of Toronto for his single crystal copper samples.

This acknowledge will not be complete without saying thanks to my grandparents, parents, aunt, uncle, and other family members who have been always supportive of me as they always have been.

Last but not least, I am grateful to all of my friends, office mates, lab mates, and neighbours who constantly gave me the courage to face all the challenges of my work and personal life that I have encountered throughout the course of the PhD program. Lastly, I would like to thank anyone whom I accidently forgot to include when this acknowledgement was written.

Funding for my project was mainly provided by the Department of Materials, Leverhulme Grant, EPSRC, and NSERC of Canada (Postgraduate Scholarship).

# Table of Contents

# List of Tables



# List of Figures

# List of Equations

$$\delta = 4.65\sqrt{\frac{xd}{\mathrm{Re}}} \quad (6) \quad 66$$

$$k_m = \frac{D_{gas}}{\delta} = \frac{2}{3}\sqrt{\frac{k^3}{\pi^3 m_{gas}}}\frac{T^{3/2}}{Pd_{gas}{}^2} \times \frac{1}{4.65}\sqrt{\frac{\mathrm{Re}}{xd}} = 3.1\sqrt{\frac{k^3\,\mathrm{Re}}{\pi^3 m_{gas} xd}}\frac{T^{3/2}}{Pd_{gas}{}^2} = 3.1\sqrt{\frac{v_g}{P\eta(T)}}\frac{k^2}{\pi^3 x}\frac{T}{d_{gas}{}^2} \quad (7)$$

66

$$k_s \propto \exp\left(-\frac{\Delta G}{kT}\right) \quad (8) \quad 67$$

$$\Delta p = \frac{64}{\mathrm{Re}}\frac{l}{d}\frac{\rho v_g^2}{2} \quad (9) \quad 67$$

$$A = \ln\frac{I_I}{I_T} = \alpha c l \quad (10) \quad 85$$

$$A = \alpha' t \quad (11) \quad 85$$

$$\alpha \approx \frac{Z_0 \sigma_{op}}{2} \quad (12) \quad 85$$

$$\sigma_{DC} = \frac{LG_{DC}}{tW} = \frac{L\Delta I_{DS}}{tW\Delta V_{DS}} \quad (13) \quad 86$$

$$\mu_{FET} = \frac{\Delta I_{ds}}{C_{ox}\frac{W}{L}V_{DS}\Delta V_{GS}} \quad (14) \quad 86$$

$$\exp\left(\frac{-\pi R_a}{R_S}\right) + \exp\left(\frac{-\pi R_b}{R_S}\right) = 1 \quad (15) \quad 87$$

$$\sigma_{dc}(t) = \sigma_{bulk}^{DC}\left(\frac{t-t_c}{t+t_c}\right)^p \quad (16) \quad 96$$

$$T = \left(1 + \frac{Z_0}{2R_s}\frac{\sigma_{Op}}{\sigma_{DC}(t)}\right)^{-2} \quad (17) \quad 97$$

$$\mu_{FET} = \frac{\Delta I_{ds}}{C_{ox}\frac{W}{L}V_{DS}\Delta V_{GS}} \quad (18) \quad 98$$

$$n_h(T) = \frac{16\pi}{h^2 c_o} kT \ln\left[1 + \exp\left(\frac{\Delta}{kT}\right)\right] \quad (19) \quad 100$$

$$\frac{1}{\mu(T)} = \frac{1}{\mu_b} + \frac{1}{\mu_{th}(T)} = \frac{1}{\mu_b} + BT^{\alpha} \quad (20) \quad 100$$

$$\Delta G = -N_{tot}\Delta\mu_C + \sqrt{\frac{N_{tot}}{2}}\gamma_{edge} + N_{tot}(E_{strain} + E_b) \quad (21) \quad 112$$

$$N_s^3 \sim P_{CH_4} \times \exp\left(\frac{2E_{att} - E_d - E_{ad}}{kT}\right) \quad (22)$$ ..... 114

$$N_s^2 \sim P_{CH_4} \times \exp\left(\frac{E_{des} + E_{att} - E_d - E_{ad}}{kT}\right) \quad (23)$$ ..... 115

$$N_s^{i+2} \sim P_{CH_4}{}^i \times \exp\left(\frac{(i+1)E_{att} + E_i - E_d - iE_{ad}}{kT}\right) \quad (24)$$ ..... 115

$$N_s^2 \sim P_{CH_4}{}^i \times \exp\left(\frac{E_{att} + E_i - E_d + i\left(E_{des} - E_{ad}\right)}{kT}\right) \quad (25)$$ ..... 116

$$\frac{dA_G}{dt} = k_{att} c_{cu} \sqrt{A_G} - k_{det} \sqrt{A_G} \quad (26)$$ ..... 124

$$c_{cu} = c_{nuc} - c_G \quad (27)$$ ..... 124

$$c_G = A_G \rho_G \quad (28)$$ ..... 124

$$A_G = A_{sat}\left(\frac{e^{F(t-t_0)}+1}{e^{F(t-t_0)}-1}\right)^2 \quad (29)$$ ..... 124

$$A_{sat} = \frac{c_{nuc} - c_{eq}}{\rho_G} \quad (30)$$ ..... 124

$$A_G = A_{sat}\left(1 - e^{k(t-t_0)^n}\right) \quad (31)$$ ..... 125

$$n = b + pm \quad (32)$$ ..... 125

$$CH_{4(g)} + 5S_{(Cu)} \underset{k_{-1}}{\overset{k_{+1}}{\rightleftarrows}} C_{(a)} + 4H_{(a)} \quad (33)$$ ..... 126

$$4H_{(a)} \underset{k_{-2}}{\overset{k_{+2}}{\rightleftarrows}} 2H_{2(g)} + 4S_{(Cu)} \quad (34)$$ ..... 127

$$C_{(a)} \underset{k_{-3}}{\overset{k_{+3}}{\rightleftarrows}} Graphene_{(a)} \quad (35)$$ ..... 127

$$r_{ad} = \frac{P}{\sqrt{2\pi mkT}} s_0 \exp\left(\frac{-E_{ad}}{kT}\right) f\left(\theta_s\right) \quad (36)$$ ..... 128

$$r_{des} = v_n \exp\left(\frac{-E_{des}}{kT}\right)[A]^n \quad (37)$$ ..... 128

$$r_{+1} = k_{+1} P_{CH_4} \left[S_{Cu}\right]^5 \quad (38)$$ ..... 129

$$r_{-1} = k_{-1}[C][H]^4 \quad (39)$$ ..... 129

$$K_1 = \frac{1}{\rho_s v_1 \sqrt{2\pi m_{CH_4} kT}} \exp\left(\frac{-\Delta H_{ad\_CH_4}}{kT}\right) = \frac{(\theta_C)(\theta_H)^4}{P_{CH_4}(\theta_S)^5(1-\theta_G)^5} \quad (40) \ldots 129$$

$$s_0 f(\theta_s) = \theta_s = 1-\theta_H-\theta_C-\theta_G \quad (41) \ldots 129$$

$$K_2 = \rho_s^2 v_2^2 \left(2\pi m_{H_2} kT\right) \exp\left(\frac{2\Delta H_{ad\_H_2}}{kT}\right) = \frac{\left(P_{H_2}\right)^2 (\theta_S)^4 (1-\theta_G)^4}{(\theta_H)^4} \quad (42) \ldots 129$$

$$r_{+3} = k_{+3}[C] = a_{cu} v_{+3\_Cu} \exp\left(\frac{-E_{att}}{kT}\right)[C] \quad (43) \ldots 129$$

$$r_{-3} = k_{-3} = \frac{v_{-3\_G}}{a_G} \exp\left(\frac{-E_{\det}}{kT}\right) \quad (44) \ldots 130$$

$$K_3 = \frac{a_{cu} a_G v_{+3\_Cu}}{v_{-3\_G}} \exp\left(\frac{-\Delta H_{form\_G}}{kT}\right) = \frac{1-\theta_G}{\theta_C \rho_s} \quad (45) \ldots 130$$

$$\theta_G = 1 - \frac{K_2^{\frac{1}{4}} \left(P_{H_2}\right)^2}{K_1 K_2^{\frac{5}{4}} K_3 P_{CH_4} \rho_s - K_1 K_2^{\frac{5}{4}} P_{CH_4} - \left(P_{H_2}\right)^{\frac{5}{2}}} \quad (46) \ldots 130$$

$$\theta_G \approx 1 - \frac{[C]_{eq}}{[C]_{\sup}} \quad (47) \ldots 132$$

$$c_{cu}(t \to \infty) = c_{eq} = [C]_{eq} \quad (48) \ldots 134$$

$$A_G(t \to \infty) = A_{sat} = \theta_G \approx 1 - \frac{[C]_{eq}}{[C]_{\sup}} \quad (49) \ldots 134$$

$$\frac{dA_G(t \to \infty)}{dt} = 0 \Rightarrow k_{att} c_{nuc} (1-\theta_G) = k_{det} \quad (50) \ldots 134$$

$$A_G = \theta_G \left(\frac{e^{F(t-t_0)}+1}{e^{F(t-t_0)}-1}\right)^2 \quad (51) \ldots 135$$

$$F = k_{att}\sqrt{\theta_G} = \frac{k_{+3} c_{nuc} \sqrt{N_s \theta_G}}{\rho_G} = \frac{a_{cu} v_{+3\_Cu}}{\rho_G} \exp\left(\frac{-E_{att}}{kT}\right) c_{nuc} \sqrt{N_s \theta_G} \quad (52) \ldots 135$$

$$k_{att} = \frac{k_{+3}\sqrt{N_s}}{\rho_G} \quad (53) \ldots 135$$

$$F = \frac{k_{+3} c_{nuc} \sqrt{N_s \theta_G}}{\rho_G} = \frac{a_{cu} v_{+3\_Cu}}{\rho_G} \exp\left(\frac{-E_{att}}{kT}\right) c_{nuc} \sqrt{N_s \theta_G} \quad (54) \ldots 135$$

# List of Abbreviations

**AFM**. atomic force microscopy
**ARPES**. angle resolved photoemission spectroscopy
**BSE**. backscattered electron
**CCD**. charge-coupled device
**CMOS**. complementary metal oxide-semiconductor
**CNT**. carbon nanotubes
**CVD**. chemical vapour deposition
**DC**. direct current
**DFT**. density functional theory
**DMEU**. 1,3-Dimethyl-2-imidazolidinone
**DMF**. Dimethylformamide
**DSPE-mPEG**. 1,2–distearoly-sn-glycero-3-phosphoethanolamine -N-[methoxy(polyethylene glycol)-5000]
**EBSD**. Electron backscattered diffraction
**FESEM**. field emission gun SEM
**FET**. field effect transistor
**FIT**. fluctuation induced tunnelling
**FLG**. few-layered graphene
**FWHM**. full width at half maximum
**GBL**. γ-Butyrolactone
**GEM**. generalized effective medium
**GIC**. graphite intercalation compounds
**GO**. graphene oxide
**HEMT**. high electron mobility transistors
**HOPG**. highly oriented pryolytic graphite
**HRTEM**. high resolution transmission electron microscopy
**ITO**. indium tin oxide
**JMAK**. Johnson-Mehl-Avrami-Kolmogorov
**LB**. Langmuir-Blodgett
**LEED**. low energy electron diffraction
**LEEM**. low energy electron microscopy
**LO**. longitudinal optical

**MFC**. mass flow controller
**NMP**. N-methyl-pyrrolidone
**OLEC**. organic light-emitting electrochemical cell
**OLED**. organic light emitting diode
**PAH**. polyacyclic aromatic hydrocarbon
**PAN**. polyacrylonitrile
**PCA**. 1-pyrenecarboxylic acid
**PEEM**. photoemission electron microscopy
**PES**. photoemission spectra
**PID**. proportional integral differential
**rGO**. reduced graphene oxide
**RMS**. root mean square
**SE**. secondary electron
**SEM**. scanning electron microscopy
**STB**. simple two band
**STM**. scanning tunneling microscopy
**TEM**. transmission electron microscopy
**UHV**. ultrahigh vacuum
**UPS**. ultraviolet photoemission spectroscopy
**VRH**. variable range hopping
**XPEEM**. X-ray photoemission electron microscopy
**XRD**. X-ray diffraction

# 1 Introduction

The emergence of novel materials with exceptional properties has always been at the forefront of technological evolution. For instance, each of the major eras in history is often associated with the advancement of a staple material that led to creation of the new tools with a profound impact in civilization. The last of such materials is probably silicon, which brought forth the Digital Revolution enabled by Si based semiconductor devices in the late 20th century. Similarly, graphene, atomically thin, two-dimensional $sp^2$ carbon, which has not been easily accessible until 2004, holds an enormous potential to drive the next technological revolution in a wide range of applications due to its unique optoelectronic properties.[1] Curiosity driven research led by Prof. Andre Geim and his assistant, Dr. Konstantin Novoselov to develop a simple procedure, using a scotch tape to peel thin layers off from a single crystal of pryolytic graphite, resulted in the isolation of graphene on an insulating substrate in 2004. The material has revealed the existence of massless charge carriers with record carrier mobilities and demonstrated other unusual phenomena such as room temperature half-integer quantum Hall effect[2,3] which have been recognized by the award of the Nobel Prize in Physics in 2010 to Andre Geim and Konstantin Novoselov "for groundbreaking experiments regarding the two-dimensional material graphene".[4] While being fascinating for fundamental physics, graphene also has a multitude of promising properties that are of technological importance. For example, its superior carrier mobilities, greater than 200,000 $cm^2/Vs$, exceeding that of any other electronic material at room temperature[5,6] are especially suitable for high frequency electronics; its excellent conductivity and transparency serve as a promising transparent electrode in photovoltaics and display devices[7,8]; the extremely high mechanical strength (~200 times greater than steel) and stiffness (~1 TPa) are attractive for its use in reinforced structures and composites.[9]

To implement the graphene for practical applications, beyond the scope of laboratory experiments, the challenge still remains to develop approaches for the efficient synthesis and processing of graphene films compatible with current manufacturing process. The scotch tape

method that was used to produce the first isolated graphene layers on insulating substrates is labour intensive and can only yield a few small graphene crystallites of lateral size less than 100 μm on a centimetre scale substrate. High-throughput methods for scalable synthesis of high quality graphene over large areas are required for the realization of graphene-based applications in the real world.

To this end, several large scale fabrication approaches have been recently explored. The most commonly studied methods are: (1) solution phase exfoliation,[10-13] (2) epitaxial growth on SiC,[14-16] and (3) chemical vapour deposition on transition metals.[17-21] There are mainly two categories of solution phase exfoliated graphene: non-covalent exfoliation and covalent exfoliation. Non-covalent exfoliation leads to nano-flakes of pristine graphene of few layers with a small portion of single layers, while covalent exfoliation leads chemically functionalized graphene in monolayer form with altered electrical properties. The graphene is grown on SiC via sublimation of Si at high temperature from 1200 to 1800 ℃ in ultrahigh vacuum or inert atmosphere. Although this method can directly produce high quality, wafer-scale graphene on an insulating substrate with a relatively good control of the number of layers, the high manufacturing costs due to the use of relatively expensive single crystal SiC and high processing temperatures, and the limitations on the subsequent transfer of graphene onto different substrates have hindered its usability for various applications. Chemical vapour deposition on transition metals is enabled by catalytic decomposition of carbon sources such as hydrocarbons or organic polymers at the surface of the transition metals such as copper and nickel at temperatures typically ranging from 700 – 1100 ℃ in low vacuum or atmospheric pressure. The transfer of graphene onto many ranges of arbitrary substrates and high electronic quality of CVD graphene, close to micromechanically exfoliated graphene, has made it most suitable for a wide range of optoelectronic applications.

In this work, solution based exfoliation in an organic solvent and CVD of graphene on Cu were chosen as experimental approaches for the fabrication of high-quality graphene thin films with good reproducibility and properties adequate for optoelectronic applications. The main challenge here is to understand how the processing conditions affect the properties of the graphene film and in turn engineer graphene structures with desired properties. Currently, there is a lack of clear understanding on the critical experimental parameters that affect the quality of graphene by both approaches, although the exceptional properties reported for

graphene strongly rely on achieving defect-free high crystalline structures. For instance, the electronic properties of CVD graphene have not yet reached those of ideal single crystal graphene. This has been attributed to formation of polycrystalline graphene films through the nucleation and growth of individual domains of graphene in the initial stages of the film formation. Therefore, understanding of the nucleation and growth mechanism by performing a systematic study of the effect of growth parameters is critical to provide a rational way to determine the thickness, morphology and crystal sizes of CVD graphene. This dissertation will address such issues that are of fundamental importance in the synthesis of high quality graphene.

The dissertation has been organized into following parts: (1) the literature review of the structure, basic properties, major synthesis methods of graphene, and its applications (chapter 2), (2) description of the experimental design of the solution phase exfoliation and CVD methods (chapter 3 and 4), (3) description of main experimental characterization techniques (chapter 5), (4) results and discussion on the structural and optoelectronic characterization of the non-covalently exfoliated graphene (chapter 6), (5) development of the nucleation and growth mechanisms of CVD graphene on copper based on the parametric study (chapter 7), (6) effect of Cu crystal orientations on graphene nucleus density, shape, and alignment (chapter 8), (7) characterization and growth mechanism of few-layer graphene produced by CVD (chapter 9), and lastly, (8) summary and future outlook (chapter 10).

# 2 Literature Review

## 2.1 Introduction

This chapter will critically review the relevant literature data on the properties of graphene, major synthesis routes and their advantages and disadvantages pertaining to large-scale production, and potential applications emanating from such synthesis methods. This literature review contains five parts: (1) historical perspective on the discovery of graphene; (2) technologically relevant properties of graphene, (3) synthesis; (4) potential applications of graphene; and (5) challenges in the synthesis of graphene for optoelectronic applications.

## 2.2 Discovery of Graphene: Historical Perspective

Long before the isolation of graphene on insulating substrates by A. Geim's group in 2004[1] sparked widespread research interest, graphene was cited in the theoretical work by P.R. Wallace entitled "The Band Theory of Graphite" in 1947[22] which has been used as a basis for the study of graphite intercalation compounds (GICs), fullerenes, and carbon nanotubes (CNTs). Wallace showed that graphene was a semimetal with unusual linear dispersion relationship, but at that time the possibility of a purely 2D material was thought to be impossible to realize. Indeed, the existence of a free standing atomically thin 2D crystal was predicted to be impossible by Peierls and Landau since such layer would be unstable against folding or aggregation into curved structures based on thermodynamic arguments.[23,24]

However, graphene in supported form has been known to exist on surfaces of transition metals for about 50 years as a by-product from catalysis reactions for conversion of hydrocarbons.[25] The formation of a single layer of graphite was first observed on surfaces of single crystal Pt[26] and Cu.[27] The annealing of these metals led to the segregation of carbon impurities from the bulk to the surface. In the case of Ni and Co metals, used as industrial heterogeneous catalysts, it has been shown in the early 1960s that reactions involving hydrocarbons cause the formation of graphitic carbon on the catalyst surface, which deactivate the catalytic activity.[25,28-30]

The attempts to peel off and manipulate single sheets of graphite using mechanical means were reported by Ruoff, who demonstrated the isolation of thin graphitic layers (less than ~10 nm).[31] The isolation of graphene on insulating substrates was finally achieved by utilizing the "scotch-tape method" by Geim[1]. Moreover, he was able to easily distinguish monolayer graphene from thicker layers under an optical microscope due to the fortuitous interference effects obtained by placing it on 300 nm thick $SiO_2$ on Si. This ability not only to exfoliate but also to easily identify and locate high-quality graphene has allowed easy access to the material so that a wide variety of experiments to investigate the fundamental phenomena could be quickly carried out. This invention of the scotch tape method has led to a rapid growth in the field of graphene especially within the physics community.

### *2.3 Graphene: Definition and Structure*

Graphene is an atomically thin sheet of $sp^2$ hybridized carbon atoms that are arranged in a two-dimensional honeycomb lattice. It is the latest nanomaterial in the family of carbon allotropes to generate intense scientific interest. Carbon is well known to form different types of bonding through orbital hybridization. In Figure 1a, the two-dimensional hexagonal lattice structure of graphene is depicted with the unit cell vectors. The four valence electrons in a carbon atom hybridize to form three $\sigma$ bonds and one $\pi$ bond. The $\pi$ conjugation with the neighbouring atoms results in delocalized electrons (Figure 1b). These $\pi$ electrons constitute the valence band (bonding, $\pi$ band) of graphene that is completely filled and meets the empty conduction band (anti-bonding, $\pi^*$ band) with zero band gap imparting the semi-metallic characteristics.

Graphene can be considered conceptually as the building block for other $sp^2$ allotropes[2] as illustrated in Figure 2. Starting from the planar, hexagonal geometry (which arises from the planar trigonal coordination of $sp^2$ hybridization), graphene can be folded to form fullerenes by replacing some of the hexagons with pentagons that induce curvatures, nanotubes by rolling, or stacking many sheets to form bulk graphite. Graphene exhibits significantly different electrical properties from bulk graphite.[32] A stack of 2-10 layers of graphene also exhibits intermediate properties that are different from a single sheet of graphene or graphite.[33] The latter is generally defined as few-layered graphene (FLG).

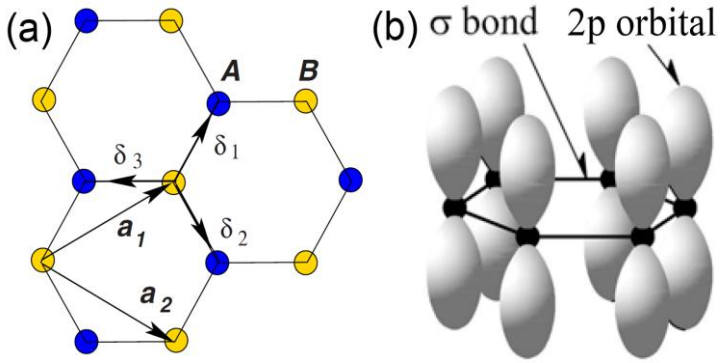


**Figure 1** a) Lattice structure of graphene. $\mathbf{a_1}$ and $\mathbf{a_2}$ are the lattice unit vectors. The nearest carbon – carbon distance is 1.42 Å. There are two atoms (A and B) per unit cell.[32] b) the hexagonal arrangement of carbon atoms in graphene depicting the σ bonding and the p orbitals that form π bonds.[14]

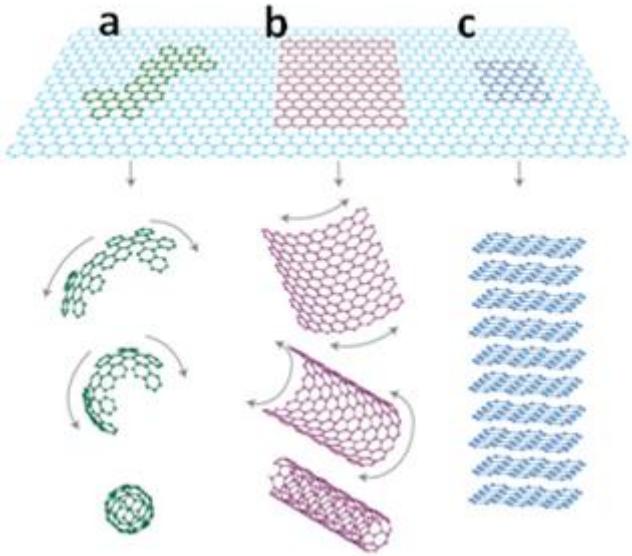


**Figure 2** Graphene as building block for other sp2 carbon allotropes. Conceptual diagram illustrates how sheets of graphene can be folded to form a) fullerenes ($C_{60}$), b) rolled into a carbon nanotube, and c) stacked to form graphite.[2]

In Figure 3, the most common stacking orientations for FLG obtained from exfoliation of natural graphite are shown.[14,34,35] The most stable stacking order that can be seen in crystalline graphite such as highly oriented pryolytic graphite (HOPG) and natural graphite is Bernal stacking (also called AB stacking) which has a periodic arrangement of two graphene sheets stacked on top of each other with one sheet rotated by 60˚ relative to the other about the c axis. This stacking contains non-equivalent sublattice atoms: an A atom directly above an A atom in the sheet below and a B atom with no atom below or above in the adjacent sheets. Other possible stacking orders are rhombohedral stacking, (ABCABC…) where the

first two sheets are stacked in the same way as for Bernal stacking but the third sheet having the same orientation with the second sheet is translated by ($2a_G/3$, $b_G/2$), simple hexagonal (AAAA…) stacking where the sheets are stacked unrotated with respect to each other without any translation, and AA' stacking where the second sheet is translated by half of a unit vector. Often in the case of few-layered graphene or graphite produced at low temperature, no stacking order can be observed. This type of random stacking is called turbostratic where no preferential orientation angles between crystalline lattices of two adjacent graphene sheets are present.

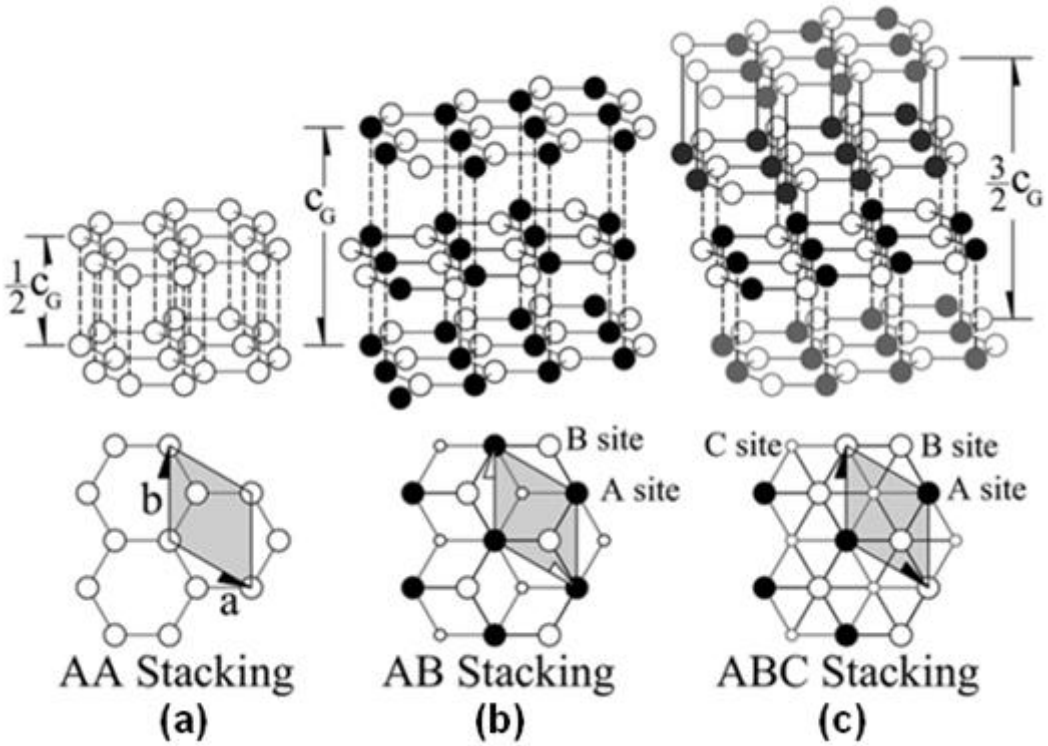


**Figure 3** Common stacking orders found in multilayer graphene exfoliated from natural graphite. a) hexagonal AA stacking, b) Bernal AB Stacking, and c) ABC stacking. Shaded areas are unit cells. $C_G$ = 0.6708 nm at 297 K.[14]

The edges of a graphene sheet of finite size can be categorized into two main types: zigzag and arm-chair. The zigzag edge is produced when graphene is cut along the unit vector directions depicted in Figure 1a, whereas the armchair edge follows the direction perpendicular to the zigzag edge. The type and functionalization at the edge by impurities can have significant influence in the properties of graphene of size smaller than few tens of nanometres.[36-38] Other than the edges, crystalline defects such as vacancies, Stone-Wales like defects[39-41] (5 – 8 membered rings instead ideal 6), $sp^3$ hybridized carbon, and grain

boundaries can be present within the interior of the graphene. The vacancies are the least stable form of defects in pristine graphene as enough annealing can reconstruct the pin-hole containing lattice to a completely vacancy-free hexagonal or polygonal (5- 8 membered rings) one.[42]

## *2.4 Materials Properties of Graphene*

Graphene is a semimetal with unusual linearly dispersing electronic states giving rise to Dirac fermions. The charge concentration in graphene can be controlled by application of external electric and magnetic fields, or by altering sample geometry and/or topology.[1,3] As a consequence of the Dirac fermions in graphene, charge carrier mobilities up to 500,000 $cm^2/Vs$ with ballistic transport characteristics over distances approaching a micron at room temperature, along with unusual phenomena such as the half-integer Hall effect[2] have been observed. In addition, as a consequence of the strong in-plane σ bonds, it has robust mechanical properties, exceptional thermal conductivities, and high chemical resistance.[43]

### 2.4.1 Optoelectronic Properties of Graphene

Many of the unique properties of graphene arise from its unusual electronic structure, the Brillouin zone of which is shown in Figure 4a. The linear dispersion relationship between the energy and crystal momentum for valence and conduction bands as predicted by tight binding approximation is shown in Figure 4b. The Fermi level of the intrinsic graphene lies on the point where the valence and conduction bands meet. This point is also known as the charge neutrality or the Dirac point. The absence of a band gap separating the valence and conduction bands and zero density of states at the Fermi level gives graphene its semi-metallic character. As the effective mass of charge carrier is the inverse of second derivative of the dispersion relationship, the low energy electrons have zero mass, which makes charge carriers, electrons and holes, to behave as massless Dirac fermions that are governed by the Dirac equation in relativistic quantum mechanics. This is quite unusual because, in the case of 3D bulk metals and semiconductors, the effective mass is finite and charge carrier dynamics is described by the non-relativistic Schrödinger equation. The Dirac particles are usually associated with quantum electrodynamics involving high-energy particles. Being able to observe them in graphene allows them to be readily accessible so that fundamental features predicted by theory such as ballistic transport and quantum Hall effects[2] at room temperature can be observed.

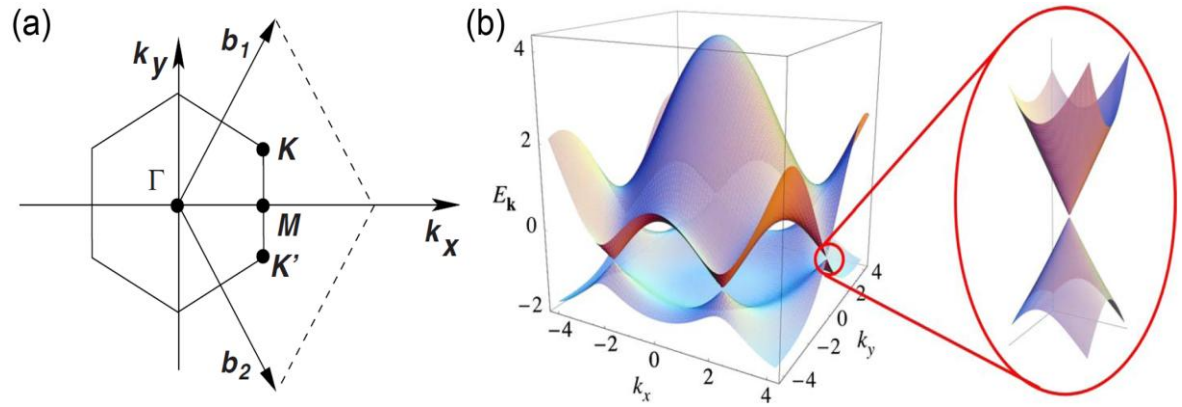


**Figure 4** a) The 1st Brillouin zone of graphene. $b_1$ and $b_2$ are reciprocal lattice unit vectors in the momentum space. Dirac cone is found at K and K` points; b) The dispersion relationship of graphene near Fermi level with magnified view of the linear dispersion relationship (Dirac cone).[32]

In graphene, the massless charge carriers travel with an effective speed that is about 300 times less than the speed of light, $v_F \sim 10^6$ m/s and have very large mean free path,[32] allowing ballistic transport. Charge carrier mobility of up to 1,000,000 $cm^2/Vs$ at low temperature (~5 K)[44] has been observed in pristine, suspended graphene. At room temperature, the mobility has been measured to typically range from 10,000 to 120,000 $cm^2/Vs$.[45,46] This value is at least 100 times faster than what is observed in silicon. The scattering mechanisms that limit the mobility values in graphene are not yet fully understood. Scattering in graphene does not depend strongly on temperature for $T < 400$ K[6] but it is influenced by the charged impurities of the supporting substrate and other extrinsic impurities that may be present.[6,32,45-47] For instance, the carrier mobility is typically on the order of 10,000 $cm^2/Vs$ for polar $SiO_2$ substrate limited by the graphene-$SiO_2$ interaction.[32] On the other hand, graphene placed on more inert, hexagonal boron nitride (BN) substrate exhibited the mobility of 500,000 $cm^2/Vs$.[48,49] Substitutional defects are unlikely in graphene as the carbon atoms form strong in-plane bonds and graphene seems to form perfect crystal without vacancies in the range of microns at room temperature.[41] Furthermore, graphene forms corrugations or puddles of charges which can act also as scattering centres.[50]

Conductivity of graphene can be tuned by doping through fabrication of a field effect device structure where the application of gate voltage modulates the Fermi level (Figure 5). Figure 5a depicts the density of states and ambipolar transport in graphene where it can be seen that both the hole and electron densities can be easily controlled with the gate voltage. Because the density of state increases linearly away from the charge neutrality point, the

conductivity also varies linearly with gate voltage. The mobility, however, remains constant over a wide range of gate induced doping. At low temperatures, graphene approaches a universal conductivity of $4e^2/h$ and does not undergo metal to insulator transition as theoretically expected for a material even with very low concentration of charge carriers near the Dirac point.[2] This minimum quantized conductivity has been predicted by the theory describing the 2D Dirac fermions.

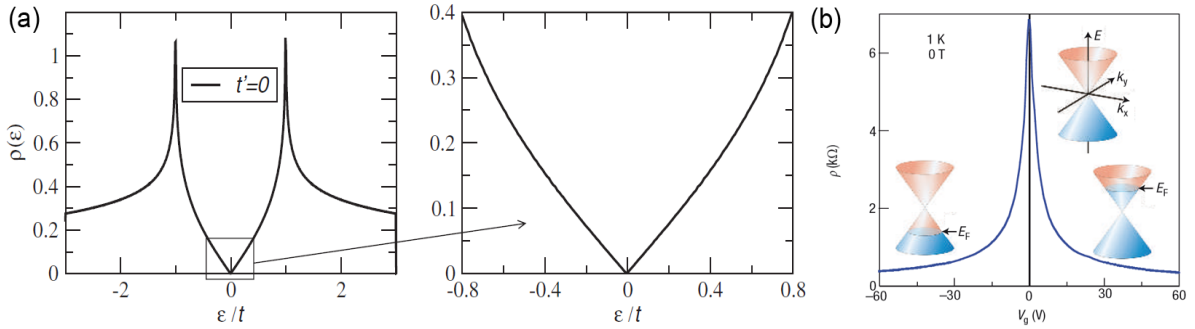


**Figure 5** a) Calculated density of states of graphene. Close to the Fermi level, the density of states ρ(ε), is linear with respect to the energy. t = ~2.8 eV (nearest neighbour hopping energy).[32] b) ambipolar transport characteristic of graphene. Field induced by gate voltage, *V*g can control concentration and polarity of charge carriers. Positive (negative) gate voltage increases Fermi level, increasing carrier concentration of holes (electrons).[2]

Thermal conduction in graphene can also occur through ballistic phonon transport with theoretical values of the thermal conductivity predicted to be ~8000 W/mK while indirect measurements have yielded values ranging from 600 to 5000 W/mK that are comparable to that of bulk graphite (≤2000 W/mK).[51-55] The wide range in values stems from the substrate effect and assumptions made during measurements and calculations. More direct thermal conductivity measurements are needed and being investigated to clarify the values.[52] The high thermal conductivity makes graphene promising for heat dissipation and transport applications.[56,57]

The optical properties of graphene also exhibit intriguing features as a consequence of the Dirac fermions. Its transmittance in visible and infrared wavelengths up to ~ 6000 nm remains constant at 97.7 %, a constant that can be derived from quantum optical conductance (e/2h) of ideal, undoped graphene (Figure 6).[58,59] The decrease in transmittance toward the UV region arises from the π-π* optical transition at the M point of the Brillouin zone with transition energy of ~ 4.4 eV.[60,61] It has been demonstrated that the optical properties of graphene can be significantly modulated by the doping which can lead to novel

optoelectronic effects and devices.[62] This is especially evident for far-infrared to THz region where the interaction between the free charge carriers and incident photons becomes significant in accordance to the Drude model.[63-65] In addition, the sub-wavelength scale surface plasmons in graphene has long excitation lifetime and strong coupling with light and can be modulated easily by turning the Fermi level.[66,67] Furthermore, the very fast carrier relaxation of excited charge carriers of grpahene can allow a broad population inversion by optical pumping and stimulated emssision in the infrared range making it very promising for room temperature THz laser applications.[68]

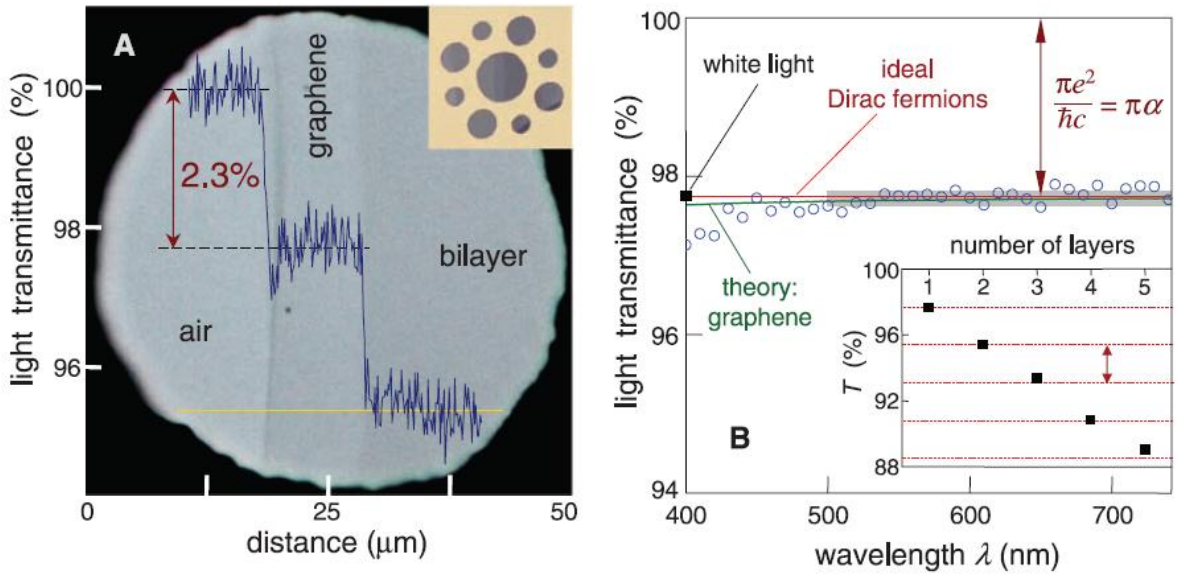


**Figure 6** a) Optical transmittance of mechanically exfoliated monolayer and bilayer graphene. b) The transmittance of graphene remains constant demonstrating that the minimum conductance of graphene is defined by the fine structure constant ($\alpha=e^2/\hbar c$).[58]

For applications such as electrical interconnects and transparent electrodes, few-layered graphene is required to provide higher conductivity and current density.[69,70] The properties of multi-layer graphene depend on both the number and stacking orientation of the layers. The π electrons in different layers of graphene can interact with each other significantly to impart the unique electronic structure of FLG. The thickness dependence continues up to 10 layers after which the properties approach that of bulk graphite. For example, bilayer graphene with Bernal stacking no longer exhibits massless Dirac fermions and has a more complex band structures (Figure 7).[32] An exception is turbostratic graphene where individual sheets have the properties of monolayer graphene.[16] The screening length of graphene is only ~ 5 Å (less than thickness of a bilayer) which means bulk and surface

properties must be considered separately for the few-layered graphene with thickness of greater than four layers.[2]

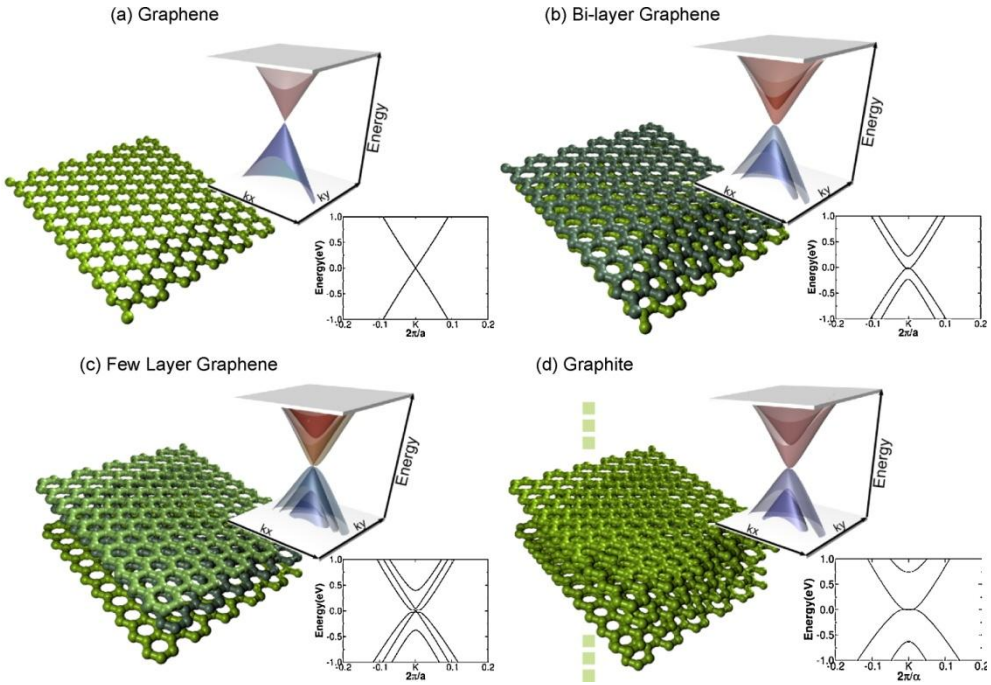


**Figure 7** Thickness dependent band structures for (a) monolayer graphene, (b) AB stacked bilayer graphene, (c) AB stacked trilayer graphene, and (d) AB stacked graphite calculated by DFT. [71] Note that because of interlayer interactions, the valence and conduction bands from each layer splits into two and the parabolic dispersion relationship develops at the Fermi level in AB stacked bilayer (b), whereas the Dirac point again appears in trilayer. AB stacked 3D graphite structure exhibits broad, parabolic dispersion relationship.

### 2.4.2 Mechanical Properties

Along with its extraordinarily high electrical and thermal properties, graphene also exhibits outstanding mechanical strength. It has been observed that graphene has mechanical strength of ~125 GPa (~200 times greater than strength of typical high strength alloy steel[72]) and Young's modulus of ~1.0 TPa.[9,73] It can be elastically stretched to a 20% strain.[74] These excellent mechanical properties of graphene have important implications in structural materials such as graphene reinforced composites[75] and resonator elements in micro/nanoelectromechanical systems.[76]

### 2.4.3 Chemical and Surface Properties

Another outstanding quality that makes graphene suitable for a wide range of applications is its chemical nature. Like graphite, graphene is generally a chemically stable

material and it is thermally stable in air up to temperatures of ~500 ˚C.[77] Graphene has a very large surface area, ~2600 $m^2/g$[78,79] which is useful for catalyst and energy storage applications. Graphene can also serve as a template for sensing adsorbed gas molecules[80] and forming nanoparticle assemblies.[81]

Graphene can be functionalized through chemical modifications such as oxidation, hydrogenation, and fluorination. Oxidation renders graphene hydrophilic and allows further alteration of the functional groups by organic molecules (e.g. acylation followed by $SOCl_2$ activation for polymer linkage and treatment by diazonium salts for improved solubility in polar organic solvents).[82,83] Hydrogenation can render graphene insulating[20] and may have implications in hydrogen storage.[84] Fluorination of graphene makes it strongly hydrophobic, induces p-type doping, and can also open up a band gap.[85,86] Through functionalization, the optoelectronic, chemical, and surface properties of graphene can be engineered for multitude of applications.

## *2.5 Synthesis Methods for Graphene Thin Films*

### 2.5.1 Micromechanical Exfoliation of Graphite

Graphene sheets in graphite interact via van der Waals forces. This weak bonding allows layers of graphene to easily peel or slide off by rubbing against a surface or tip.[31,87] The exfoliation or micromechanical cleavage of graphite essentially exploits this weak bonding to obtain graphene. In one of the earlier attempts to mechanically exfoliate graphite, AFM tips were used to peel off thin layers of graphite from pre-patterned HOPG islands that were laid down onto Si(100).[31] Later, trials with tipless AFM cantilever to stamp nanoscale flakes of HOPG onto $SiO_2$/Si substrates (Figure 8) were attempted.[88] However, these approaches usually yielded graphitic layers with thickness values of > 10 nm.

The “scotch tape” method[1] utilizes the common cellophane adhesive to peel off graphene layers from HOPG. After the removal, the tape is pressed onto the desired substrate (typically 300 nm thick $SiO_2$ on Si). In addition to large amounts of graphitic particles, sheets of single to few monolayers are also deposited. The monolayers can be observed by optical microscopy (Figure 9) and the thickness can be verified by Raman spectroscopy (The details regarding Raman spectroscopy of graphene are given in Chapter 5).

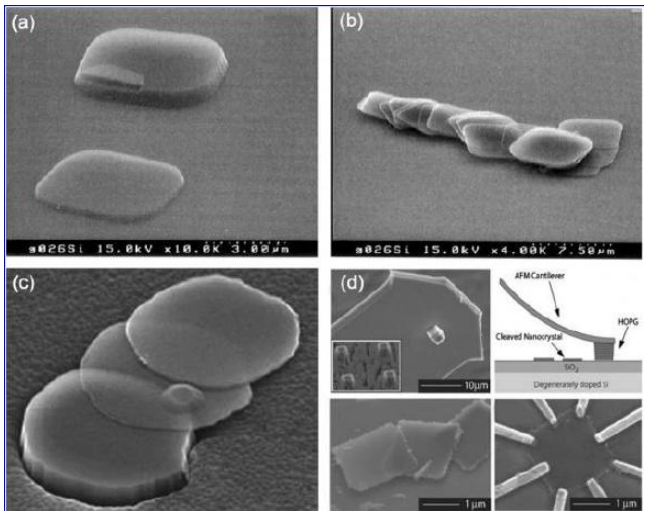


**Figure 8** One of the earliest attempts to mechanically exfoliate graphene from HOPG: (a) and (b) are SEM images of graphite layers peeled away by a AFM tip.[31] (c) and (d) are images of transferred graphite to $SiO_2$ substrates from a tipless AFM cantilever with which slabs of HOPG were deposited on and image of a typical device fabricated for electrical measurements.[88]

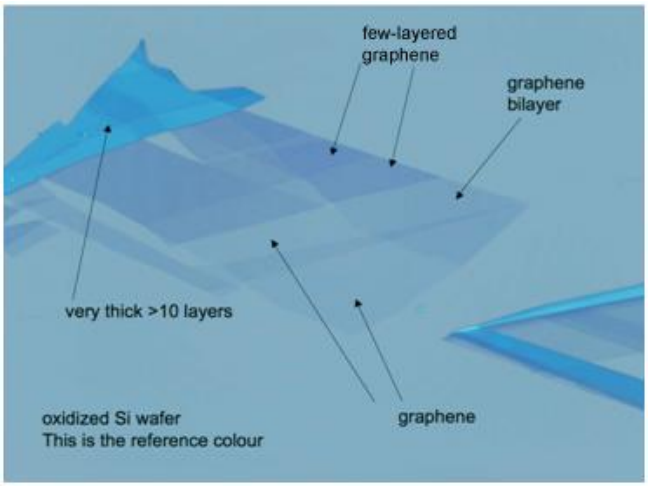


**Figure 9** Optical microscope image of micromechanically exfoliated sheets of graphene and graphite on $SiO_2$/Si deposited by the scotch tape method. Regions of different thicknesses are indicated.[89]

Recent efforts building on mechanical exfoliation include transfer-stamping of FLG from graphite by using pre-patterned stamp templates to precisely position and control the thickness of graphene with a well-defined area.[90-92] However, realizing large area deposition of graphene thin films through mechanical exfoliation may be challenging due to the development of alternative methods for graphene production.

### 2.5.2 Solution Phase Exfoliation of Graphite

One of the promising routes to synthesize large quantities of graphene for large area applications is to exfoliate graphite in solution to produce a dispersion of graphene flakes.

Such exfoliation methods rely on covalent and non-covalent interactions introduced by external molecules to disrupt the van der Waals interactions between the graphene sheets. This has been performed by introducing intercalants in graphite through covalent functionalization, non-covalent exfoliation in compatible organic solvents, and/or in presence of surfactants.

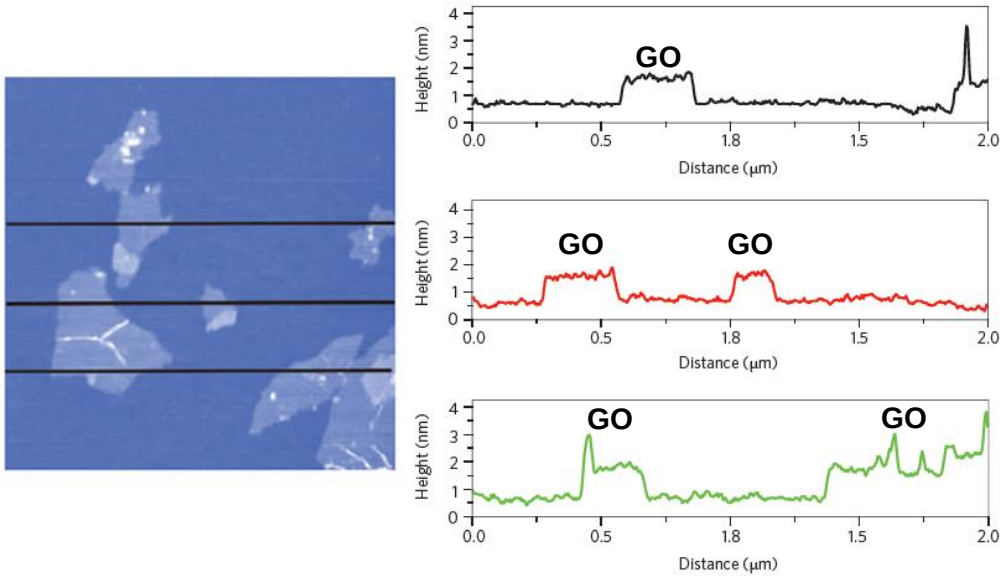


**Figure 10** AFM image of graphene oxide flakes deposited on a substrate and its height profiles through the three horizontal lines. The height profiles show the thickness of GO to be ~1 nm.[93]

### *2.5.2.1 Graphene Oxide*

Graphene oxide (GO) is the most widely investigated solution based precursor to graphene and was first proposed by Ruoff in 2006 (Figure 10).[75] GO is graphene functionalized with hydroxyl, epoxy, and carbonyl groups (Figure 11).[94] The preparation of GO involves conversion of graphite to graphite oxide using strong acids and oxidizing agents.[75,95,96] The functionalization breaks the van der Waals interaction between the sheets and renders them hydrophilic leading to efficient exfoliation of graphite oxide into monolayers of GO when stirred or sonicated in water. Because the functionalization by oxygen disrupts the $sp^2$ conjugation and introduces $sp^3$ bonds, GO is insulating. To restore conductivity, the oxygen groups have to be removed to recover the $sp^2$ conjugation. This can be done mainly through reduction by reducing agents (usually hydrazine, $N_2H_4$), followed by thermal annealing in inert gas at 200 – 1000 °C.[11,97] Other reducing agents include $NaBH_4$ and KOH.[82] Other approaches of reduction in the literature are: (1) electrochemical

reduction[98]; (2) light activated reduction by a strong pulse of light[99]; and (3) catalytic reduction by $TiO_2$ and NaOH under UV radiation.[100]

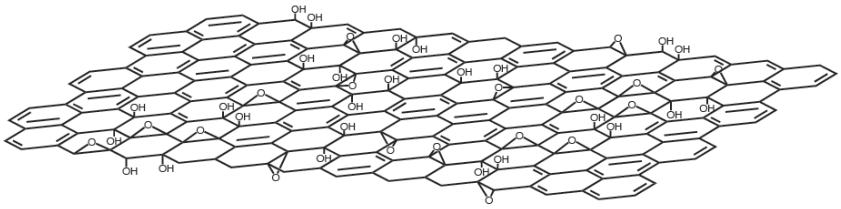

**Figure 11** Chemical Structure of GO.[101]

The reduction step is able to make the reduced form of graphene oxide (rGO) fairly conductive with ambipolar transport properties,[102,103] but with best conductivity and mobility values that are two or three orders of magnitude lower than that of mechanically exfoliated graphene. The reason for the poor electrical properties of rGO is that the oxidation and reduction processes produce defects. Raman spectroscopy on graphene oxide and reduced graphene oxide indicates that both rGO and GO contain large amount of defects as evidenced by the large D to G peak intensity ratio and broad G peak. Some oxygen groups remain strongly bonded and defects such as vacancies and non-hexagonal structures can be seen in rGO as can be observed by XPS, high resolution TEM, and annular dark field imaging.[104,105]

#### *2.5.2.2 Non-covalent Exfoliation of Graphite*

Recent development in solution phase production of graphene is non-covalent exfoliation of graphite in the presence of amphiphilic surfactants[10,106,107] or organic solvents[13,108-111] that have compatible surface energies to graphite. This leads to separation and dissolution of dispersed graphene sheets without any covalent funtionalization. These methods can result in graphene with high crystallinity and minimal lattice defects that are associated with the covalent functionalization. The choices of the solvents or surfactants employed in these works are often the ones previously used to debundle single walled carbon nanotubes as they exhibit similar surface properties.[112]

In the first report of non-covalent exfoliation of graphite, mono-to-few-layered graphene was obtained by sonication in N-methyl-pyrrolidone (NMP), Dimethylformamide (DMF), γ-Butyrolactone (GBL), and 1,3-Dimethyl-2-imidazolidinone (DMEU).[13] The surface energies of these solvents are close to that of graphite so that exfoliation is facilitated. It was found that NMP was the best in terms of yield of monolayer graphene and stability of dispersion

(Figure 12).[110] Other works have shown that DMF,[108] chloroform,[108,111] 1-pyrenecarboxylic acid (PCA),[113] and chlorosulphonic acid[114] can also produce exfoliated graphene of high-quality. The dispersibility of graphene in solvents is predicted to depend on the compatibility of surface energy, solubility parameter, π-π interactions, charge transfer between the two.[115,116] Surfactants such as 1,2–distearoly-sn-glycero-3-phosphoethanolamine-N-[methoxy(polyethylene glycol)-5000] (DSPE-mPEG) and sodium chlorate have been used to produce aqueous dispersions of surfactant coated graphene with the yield comparable to exfoliation in NMP.[10,117] Although non-covalent exfoliation reduces process steps and is shown to produce graphene sheets of high crystal quality (as evidenced by Raman spectroscopy; Figure 13), the transport properties are comparable to graphene oxide and not as good as those of mechanically exfoliated graphene.[13,108,111] This is attributed to the small flake sizes where the charge carrier transport is mediated by defective edges rather than the bulk basal plane.

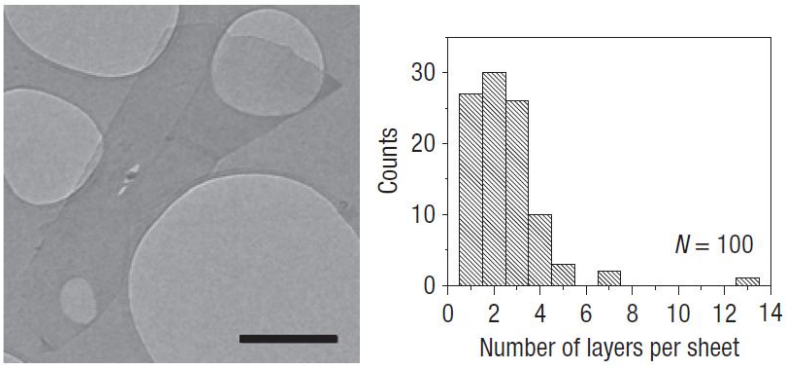


**Figure 12** a) TEM image of graphene sheet exfoliated in NMP. Scale bar, 500 nm. b) Histogram describing distribution of number of layers per flake in NMP exfoliated graphene.[13]

### *2.5.2.3 Thin Film Deposition Methods of Solution-processed Graphene*

Depositing thin films of graphene on a planar substrate is a crucial step toward device integration. Uniform deposition over large area and precise thickness control are needed. Spin-coating (or spin-casting) is one of the most frequently used methods to deposit solution-processed graphene films (Figure 14a and b).[118-121] It has enabled large area uniform deposition of chemically derived graphene films and polymer-graphene composite films to fabricate GO based sensors and field emission devices. Another frequently used method is vacuum filtration where the diluted solution of dispersion is filtered through a nano-porous membrane.[13,97,122] Vacuum filtered GO films have been used as transparent electrodes for solar cells and to produce GO paper (Figure 14c).

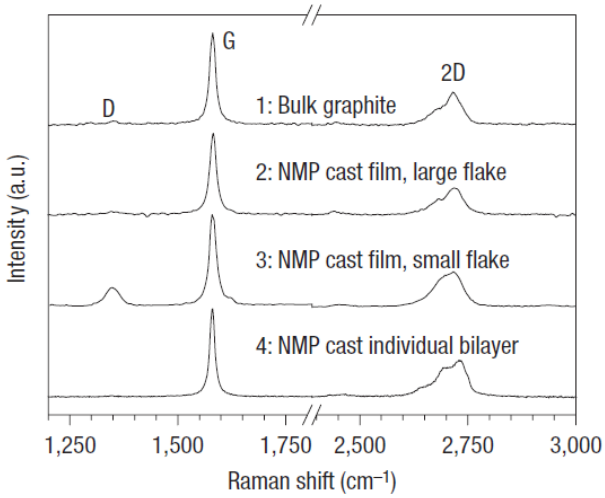


**Figure 13** Raman spectra of few-layered graphene exfoliated in NMP compared to a bulk graphite spectrum.[13]

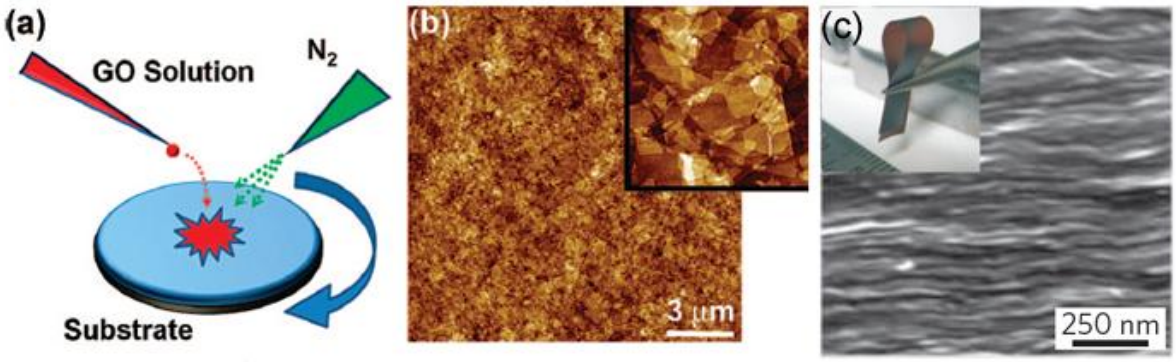


**Figure 14** a) Schematic illustrating spin-coating procedure and b) spin-coated multi layered GO film.[123] c) GO paper produced by vacuum filtration (inset) and SEM image of cross section of the graphene oxide paper.[93]

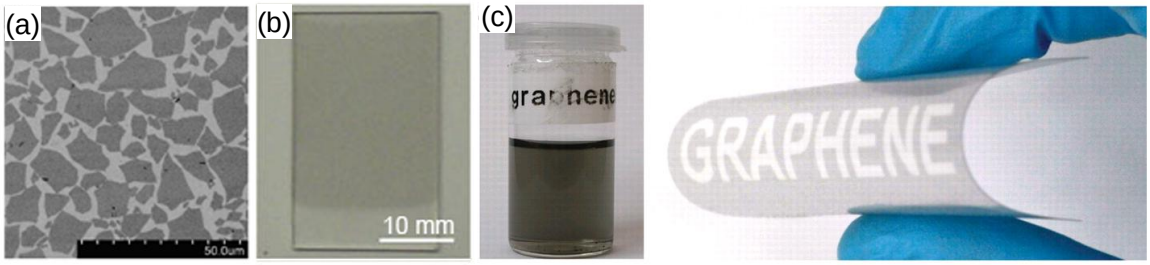


**Figure 15** a) SEM image of single layer of GO film deposited by Langmuir-Blodgett Assembly.[124] b) Photography of multi-layer Langmuir-Blodgett film on a quartz slide.[117] c) Graphene dispersion in chloroform and spray coated graphene thin film on a flexible transparent substrate.[73]

Self-assembly of chemically derived graphene at the water/air interface, known as Langmuir-Blodgett assembly allows layer-by-layer deposition of graphene films on variety of substrates. In Langmuir-Blodgett assembly of GO, electrostatic repulsion leads to formation

of close-packed GO film lying smoothly on the surface of water that is then transferred onto a substrate of choice (Figure 15a and b).[117,124] Self-assembly at liquid-liquid interface is also possible between two immiscible liquids.[111]

Other deposition techniques worth mentioning are spray-coating (Figure 15c)[73] and ink-jet printing.[125,126]

### 2.5.3 Growth on Silicon Carbide

Graphite formation by thermal decomposition of SiC was first discovered more than a century ago by Acheson,[127,128] and epitaxial growth of FLG on SiC was shown for the first time in the 1970s.[129] SiC exists in many energetically similar bulk polytypes (250 crystalline forms). The two polytypes that are of the most interest for electronics (and consequently the most available) are the hexagonal 4H and 6H polytypes (energy gaps of 3.3 eV and 3.0 eV, respectively).[130] Both are formed by stacking basal plane "bilayers" of Si and C, with 0.25 nm *c*-axis spacing and an in-plane lattice constant of 0.307 nm. For the 4H polytype, the unit cell *c* dimension is 1.00 nm (4 bilayers) and 1.51 nm (6 bilayers) for the 6H material. Heating of SiC(0001) in vacuum or inert atmosphere to 1200 to 1800 ˚C, leads to the selective sublimation of silicon atoms while the remaining carbon atoms rearrange forming an hexagonal lattice parallel to the a-b plane.[14,131-133] As a result, several atomically thin carbon layers can appear and generally speaking, depending on the annealing time, it is possible to tune the number of graphene layers. This growth is defined as epitaxial and the lattice mismatch between the honeycomb lattices of graphene and SiC(0001) is ~22 %.[134]

Graphene films on silicon and carbon terminated surfaces are substantially different. For example, growth on (0001) Si-face is usually self-limiting to 4 – 5 layers, while on the (000**1**) C-surface, graphitic layers thicker than 10 layers are usually obtained. The very first graphene layer grown on the SiC is insulating due to charge transfer to the substrate and serves as a buffer layer that electronically decouples the upper graphene layers from the substrate. Angle resolved photoemission spectroscopy (ARPES) on graphene form the (0001) Si-face has confirmed that the energy versus momentum relation, *E(k)* is linear for monolayer graphene and quadratic for a bilayer as expected from the Bernal type stacking.[135,136]

Graphene growth on the C-terminated SiC(000**1**), as for the Si face, progresses by thermal decomposition in vacuum and or inert gas environment. However, on the Si-face graphene grows epitaxially [e.g., showing sharp spots in low-energy electron diffraction

(LEED)] while UHV-grown C-face graphene shows many rotational domains, or even sprouts of nanotubes. Control of the C-face graphitization is improved by enclosing the SiC substrate by carefully controlling the Si sublimation rate in an inert atmosphere[132]; however this method preferably produces few-layered epitaxial graphene albeit of high-quality (Figure 16). Monolayer graphene over a large portion of the surface with good reproducibility has not been demonstrated. Furthermore, C-face graphitization results in step edge formation with width of tens of nanometres that affects the homogeneity of graphene films. Islands of size on the order of 300 – 700 nm with varying number of layers are also often reported.

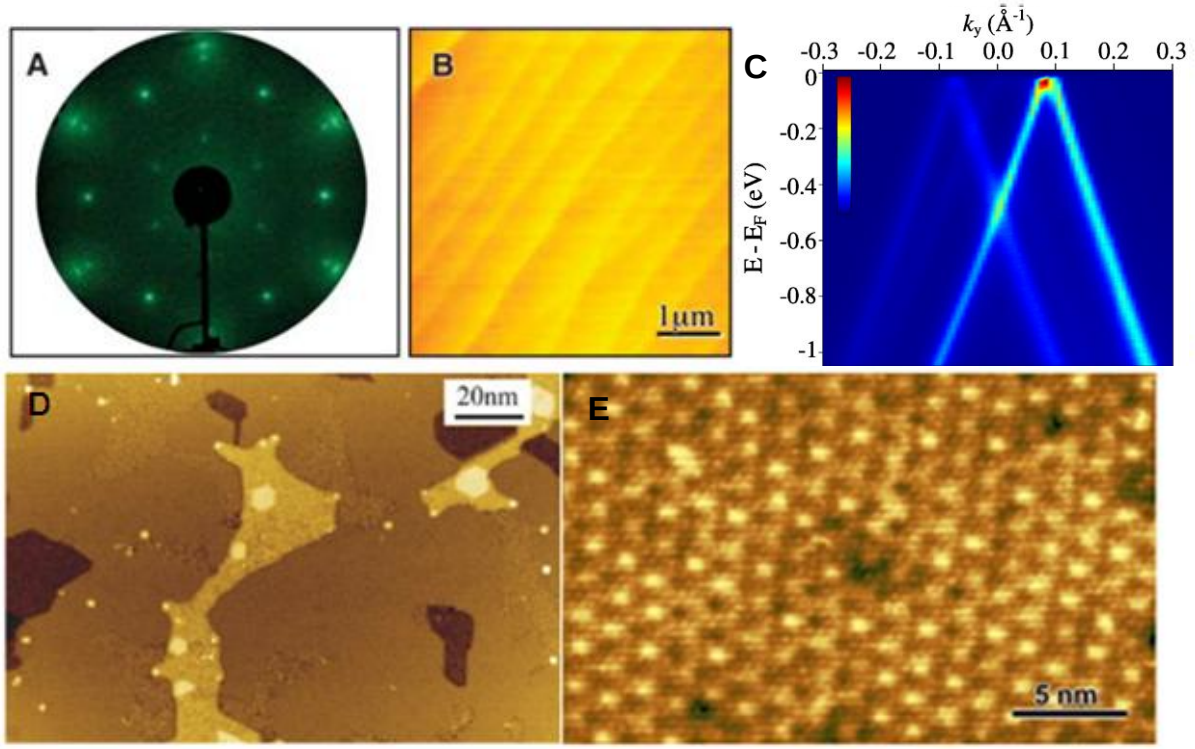


**Figure 16** a) LEED image of graphene grown on SiC.[137] b) AFM topograph of SiC surface.[137] c) Linear dispersion and Dirac cone of multilayer epitaxial graphene grown on SiC(000**1**) observed by ARPES.[136] d) Scanning tunneling microscopy (STM) image with incomplete coverage of graphene monolayer on SiC.[138] The darkest regions are bilayer graphene. e) Atomic resolution STM image demonstrating the crystalline nature of graphene grown on SiC.[138]

The electronic properties of graphene on C-face appear to be better than that of graphene grown on Si-face. Hall effect mobility of few-layered epitaxial graphene on C-face at room temperature can be up to 20,000 cm$^2$/Vs and up to 15,000 cm$^2$/Vs for a single layer.[139] The electronic properties of graphene on Si-face are significantly different as there is significant interaction with the substrate which leads to doping (-0.5 eV electron doping), band gap of

0.25 eV, and strong electron-phonon interactions. As a result, the mobility (~1,500 $cm^2/Vs$) of graphene grown on Si-face is more than an order of magnitude lower than that of graphene grown on C-face. However, high frequency devices (e.g. HEMT - high electron mobility transistors) have been fabricated on graphene grown on Si terminated SiC(0001) wafer and have been demonstrated to operate at frequencies on the order of up to 300 GHz.[140]

Despite the high-quality of the epitaxial graphene obtained on SiC(0001), there are no reliable methods to transfer graphene onto other substrates.

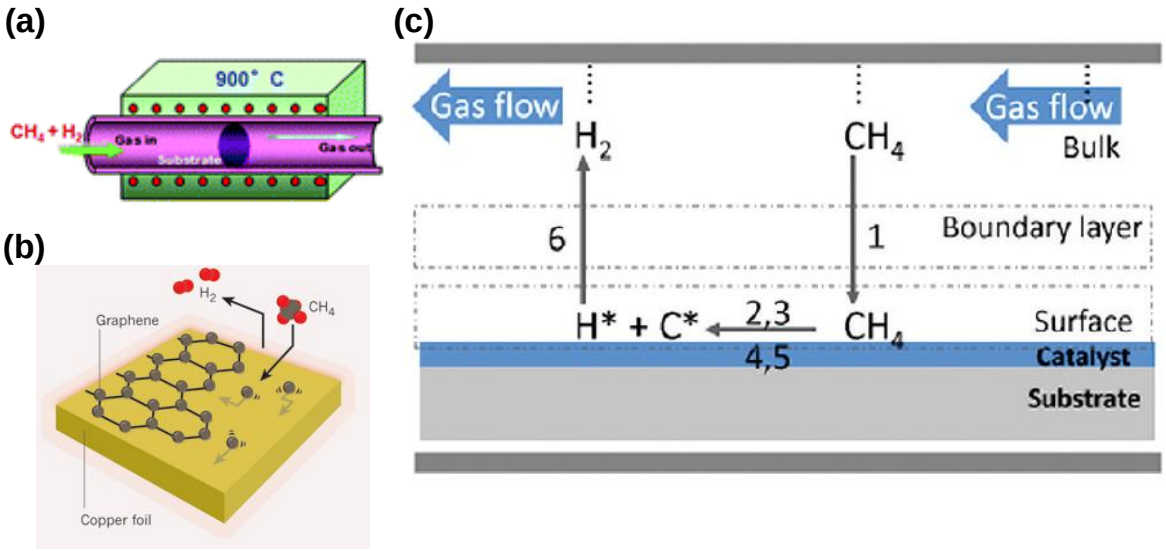


**Figure 17** a) Schematic of CVD system for graphene deposition in a hot-wall tube furnace with a metal catalyst as substrate and $CH_4$ as gaseous carbon source.[141] b) Schematic of possible surface processes for CVD on Cu.[142] c) Illustration of vapour phase mass transport highlighting the role of the mass flow and boundary layer that forms on the substrate surface inside the CVD furnace.[143]

### 2.5.4 Catalytic Chemical Vapour Deposition

Graphene has been successfully synthesized by CVD via decomposition of hydrocarbon gases catalysed by a transition metal that is also the support substrate for the growth (Figure 17). The synthesis can be enabled by a wide range of growth parameters. Various metals including Ni,[17] Fe,[144] Cu,[20,145] Au,[146,147] Ag,[148] Co,[149] Ru,[150] Pt,[151,152] Ir,[153] Pd,[154] and Rh[155], and alloys such as stainless steel,[156,157] Ni-Cu,[158-160] Au-Ni,[161] and Ni-Mo[162] have been successfully used to form graphene in presence of carbon containing molecules (e.g. $CH_4$, $C_2H_4$, $C_2H_6$, and CO) at temperatures ranging from 300 °C[163] to 1120 °C.[17,164] Recent effort has focused on the development of graphene deposition at either low vacuum or atmospheric pressure, which would enable cost-effective, high-throughput fabrication.[17,19,117]

In this type of growth, a simple system such as a hot-wall tube furnace (Figure 17a) is adequate for the growth of graphene films of relatively high quality.

In order to make the CVD graphene useful for transparent electrodes, flexible electronics, and field effect device applications, transfer techniques similar to the one shown in Figure 18 have been developed to transfer graphene grown on metallic layers onto insulating substrates. The wet transfer techniques involve coating a polymer support onto the graphene layer and etching away the metallic layer to place the polymer support/graphene film on a different substrate. Because of the presence of water and etchant, the transferred graphene can contain contaminants and exhibit unintentional doping. Alternatively, etchant-free electrochemical delamination,[165] and completely dry transfer techniques involving strongly adhering layers of polymer coatings[166,167] have been recently developed. In addition, low temperature growth of graphene at the interface between a dielectric and metal catalysts[168] and electrical isolation of graphene on metal by oxide intercalation[169] have been demonstrated to bypass the need for transfer process altogether.

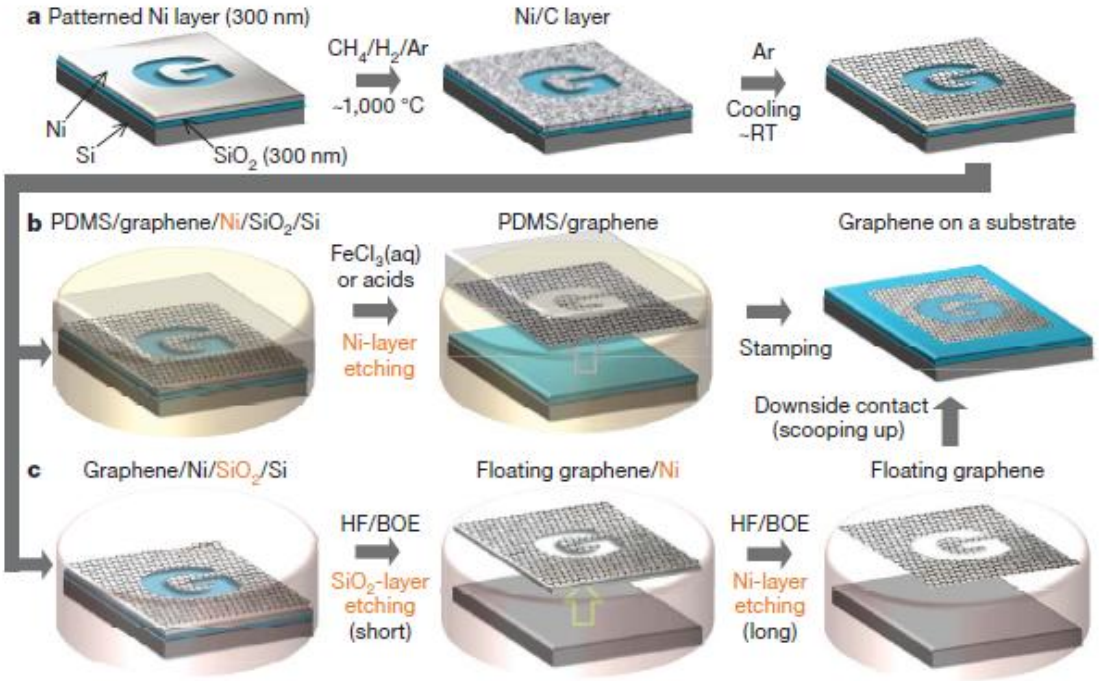


**Figure 18** Possible transfer processes for patterned graphene grown on Ni[19]. After graphene is grown on Ni (a), the graphene can be transferred onto another substrate by coating a polymer support followed by etching (b), or direct etching of the Ni to obtain free standing graphene (c).

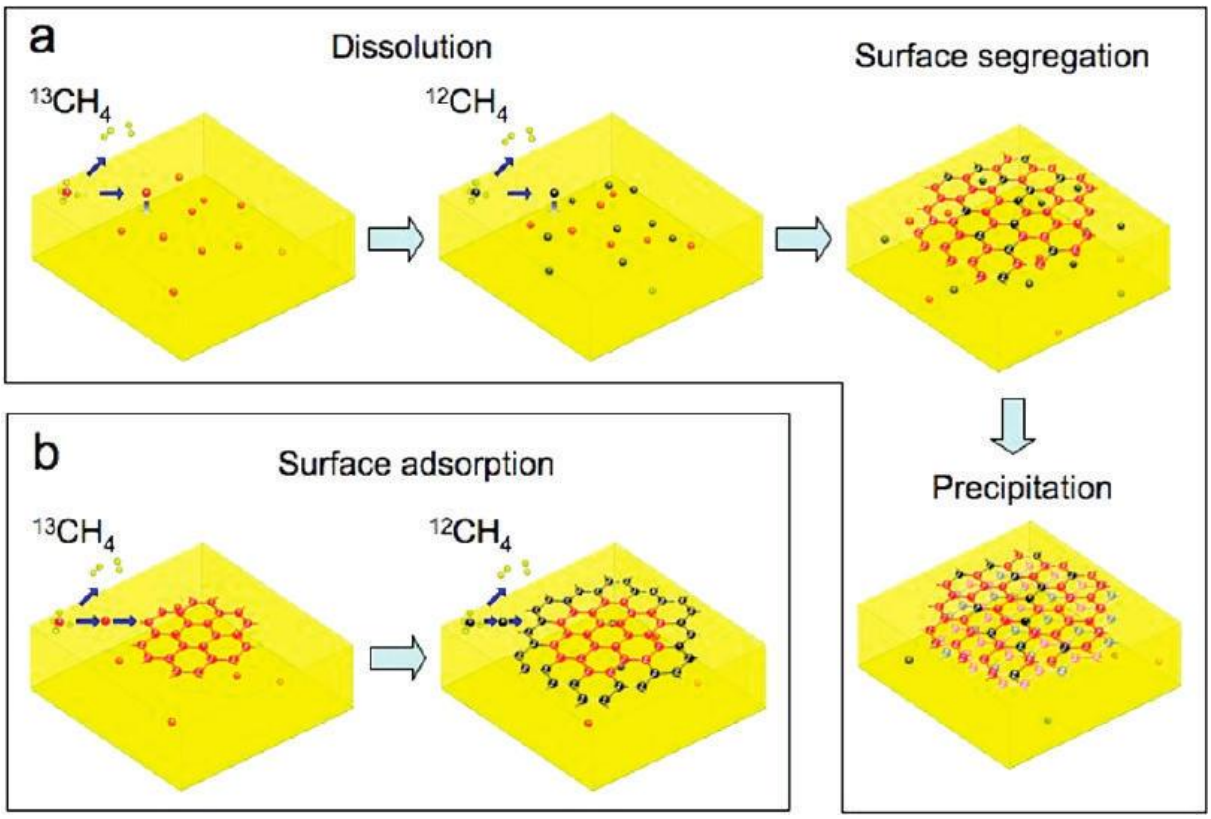


**Figure 19** Growth mechanism of graphene on Ni (a) and Cu (b) investigated by successive introduction of the precursor gases ($CH_4$) containing different isotopes of carbon. On Ni, graphene growth occurs by surface segregation and precipitation (crystallization) while on Cu it occurs by surface adsorption.[170]

### *2.5.4.1 Effect of catalyst substrates*

In CVD, the thickness, stacking, and crystalline orientations of graphene layers obtained primarily depends on the metal catalyst used. In fact, metal-carbon interactions determine the mechanisms of growth and lead to different growth morphologies. Metal that dissolves carbon at or near the growth temperature is favourable for FLG deposition. Thus, solubility of carbon is a critical parameter for choosing a catalyst for graphene. Generally, metals with partially filled d-orbital have more interaction toward carbon than metals with completely filled d-orbitals.[171]

Of the numerous types of suitable metals, Ni and Cu are the most promising for cost-effective, large area deposition. The mechanism of graphene growth is, however, different for these two metals (Figure 19a). In the case of Ni, which has partially filled d-orbitals, 1.3 wt% of carbon dissolves into the Ni substrate at 1000 ˚C as shown in the phase diagram in Figure 20a.[172] Upon cooling, the carbon and metastable $Ni_3C$ phase diffuse out and precipitate into

graphene. Typically, multi-layered graphene is formed at the surface. As the carbon segregation-precipitation continues, a new graphene layer is formed underneath the first layer and so on until there is no supersaturation of carbon in the bulk Ni or out-diffusion becomes kinetically hindered at lower temperatures. In this growth mechanism, the thickness of resulting graphene layer mainly depends on the initial amount of carbon supplied into the bulk, the thickness of the catalyst, and the cooling rate.[17,170]

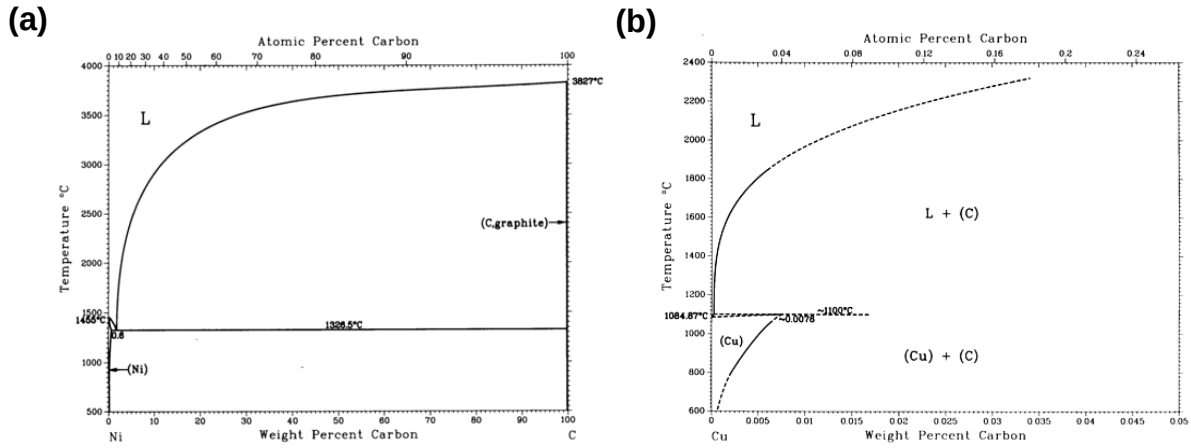


**Figure 20 a)** Ni-C binary phase diagram.[173] b) Phase diagram of Cu-C system.[174] The solubility of carbon in Cu is more than an order of magnitude lower than that of Ni in comparable temperatures.

The mechanism on Cu which has no partially filled d-orbital to interact with carbon is different from Ni in that carbon cannot diffuse into the substrate at typical growth temperatures due to the negligible solubility of carbon in Cu (<1.4 ppm at 1000 ˚C; Figure 20b).[174] Therefore, graphene on Cu is formed by direct, catalytic decomposition of the hydrocarbon ($CH_4$) gas and 2D crystallization effects on the substrate surface (Figure 19b). After nucleation of graphene, progressive covering of the surface continues until the catalytic decomposition of hydrocarbon stops. The process is therefore self-limited to mostly a single monolayer. Indeed, after growth, ~ 95 % of the surface can be covered by a monolayer with the rest being patches of multi-layered graphene.[20] The mechanism has been verified by using $^{12}CH_4$ and $^{13}CH_4$ carbon precursors and Raman mapping.[170] Recently, the use of alloy catalysts such as Ni-Cu, Ni-Mo with varying degrees of carbon solubility has been demonstrated to control the number of layers and achieve lower growth temperature than Cu-only growth.[158-161]

The most common substrates for the CVD growth are polycrystalline foils as they are cheaply available. However, polycrystalline foils exhibit grain boundaries which can nucleate

extra layers and random surface facets of different crystal orientations resulting in non-uniformity.[175-177] The different crystal facets are known to affect the growth behaviour and quality of the graphene overlayer.[178] In addition, step edges produced by surface roughness or vicinal surfaces can also result in different nucleation and growth behaviour from perfectly flat surfaces (Figure 21).[153,179] Thin metal films grown on single crystal substrates such as sapphire or MgO have been used to overcome this problem resulting in uniform single crystal substrate.[178,180] Using liquid Cu at growth temperature above its melting point (> 1080 °C) has been recently shown to be another way to eliminate the Cu grain boundaries and obtain uniform, high-quality graphene.[164,181]

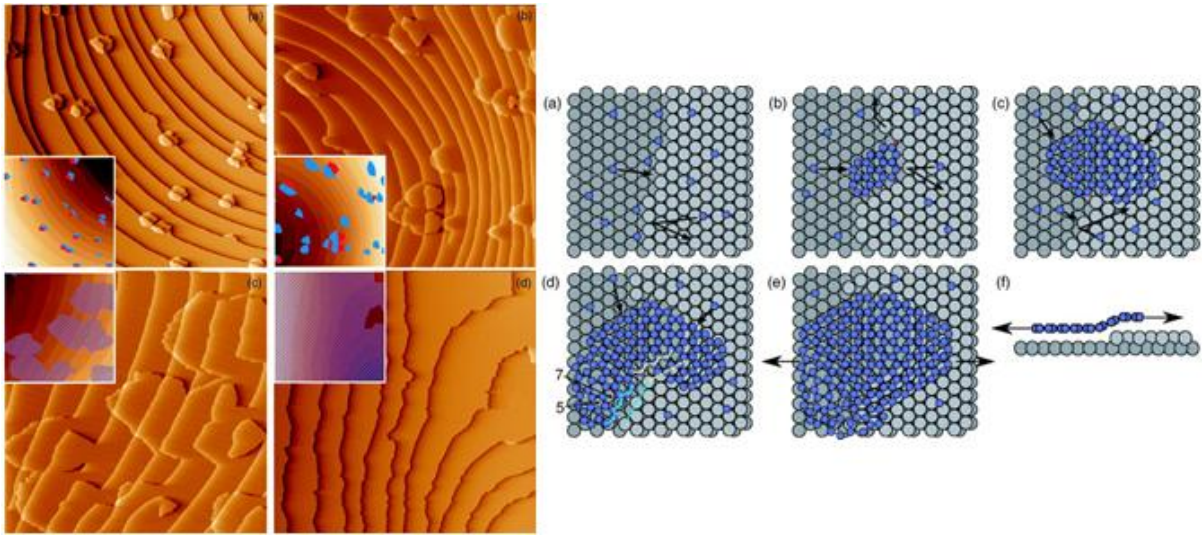


**Figure 21** STM topography of graphene islands formed on Ir (111) step edges with different growth times and atomistic model of graphene island growth.[153]

### *2.5.4.2 Effect of carbon precursor sources*

The type of carbon source is an important parameter as it can influence kinetics and yield. The decomposition temperature and rate of growth depend on the sources of carbon due to different activation energies. The most common source is $CH_4$ which is known to be less reactive than acetylene, ethylene, and alcohols, but it makes the growth more controllable. Alternative sources of carbon such as camphor,[182] liquids (e.g. benzene,[183] toluene,[184] ethanol[185]), polymers [e.g. polymethylmethacrylate (PMMA),[186,187] polystyrene (PS),[188] and polyacrylonitrile (PAN),[188]] and other organic materials[189] have been also investigated to produce graphene films of various thicknesses. The efficiency of these sources for graphene production has not yet been fully investigated. Generally, low feed rate of the

carbon source is preferred for uniform monolayer graphene growth with high crystal quality.[190,191]

#### 2.5.4.3 Effect of carrier gases

Other than the carbon source, inert (e.g. Ar and $N_2$) and hydrogen gases are introduced into the system during the growth as carrier gasses. Ar and $N_2$ are unlikely to be involved in the reactions, whereas $H_2$ plays an important role in cleaning the catalyst substrate by etching away oxides during the pre-growth annealing step, and also partially etching away the amorphous carbon that usually forms in excess of the carbon precursor.[192] In addition, it has been suggested that $H_2$ stabilizes the zigzag edges of graphene, thus affecting the growth rate.[193,194] In addition, etching of graphene on Cu by $H_2$ due to hydrogenation of graphene has been reported.[195-197] Furthermore, $H_2$ has also been revealed to be detrimental to the morphology of catalysts surfaces via diffusion into grain boundaries or any voids within the catalyst resulting in hydrogen blisters.[198,199] It must be also noted that at high temperature and very low pressure conditions in the absence or low flow rate of the carrier gas (e.g. UHV conditions), significant sublimation of the substrate metal can occur due to its finite vapour pressure during graphene growth affecting the growth morphology.[200] Thus, further investigation of overall pressure and the role of carrier gases are also required.

#### 2.5.4.4 Current status of growth mechanism studies on Cu

Some of the basic variables for understanding the surface nucleation and growth mechanism on Cu, such as the growth rate of graphene islands, have been analysed so far for a limited range of growth conditions (Figure 22) by scanning electron microscopy,[201] Raman mapping,[170] scanning probe microscopes[202], and in-situ LEEM imaging.[200,203] However, a detailed understanding of the growth mechanisms such as the reaction kinetics and the critical experimental parameters (temperature, gas composition, etc.) that govern the quality of the material has not yet been extensively investigated.

On Ru and Ir, in-situ LEEM observation of graphene surface nucleation has shown that the graphene growth rate is limited by attachment of multi-atom clusters at the growing edges of nuclei[150,204] (Figure 23a). No such analysis has been done for graphene growth on Cu although that similar atomic processes such as adsorption, surface diffusion, and edge attachment take place. Many empirical works using trial-and-error approaches have demonstrated that an ideally flat surface, low flow rates, low partial pressure of gaseous

carbon source relative to the partial pressure of hydrogen, and high temperature generally result in low density of nuclei and large graphene single crystal domains[176,177,190,191] (Figure 23b, c). However, these works lack insights on the exact underlying mechanisms of surface nucleation and growth and on the control of the various mesoscale features (e.g. nucleus density, lateral size, shape, and edge structure) of graphene nucleation.

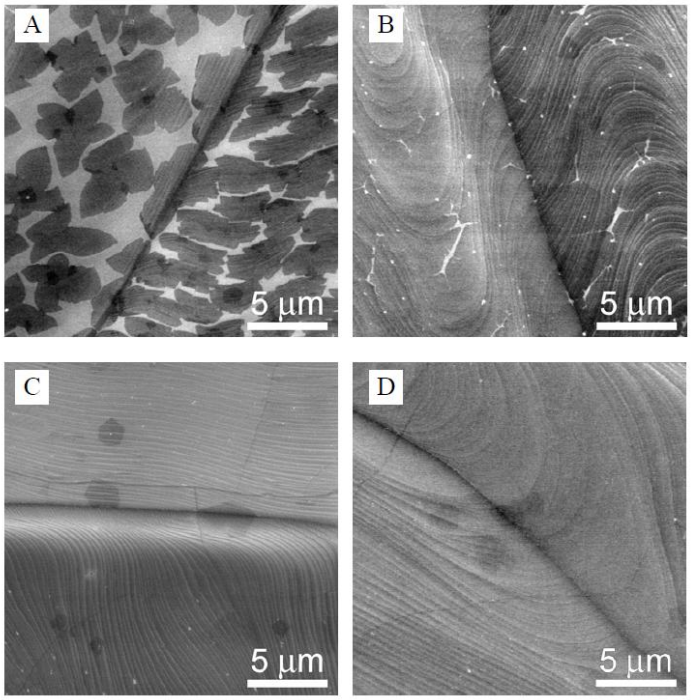


**Figure 22** SEM image of graphene on grown on polycrystalline Cu for different times. a) 1 min, b) 2 min, c) 10 min, and d) 60 min.[20] The graphene nuclei form at random sites on Cu (a), enlarge and emerge to form a continuous film of graphene (b-c). The growth self-terminates as Cu surface is entirely covered by the monolayer graphene (d).

Moreover, various works from literature report nucleation of a concentric stack of multi-layer graphene at a single nucleation centre in addition to a monolayer. This behaviour deviates from the self-limited picture of monolayer growth on Cu and warrants closer examination. Various mechanisms such as release of carbon during cooling from defects sites,[205] differences in gas flow conditions on surface defects sites that leads to greater flux of carbon precursors toward surface protrusions,[143] and vapour phase decomposition of hydrocarbons by Cu vapour[206] have been proposed to give explanation for the multilayer formation.

It is worth noting that most of the proposed mechanisms of graphene growth on Cu in the literature so far are either too phenomenological without much quantitative, predictive

power[143] or too narrow in terms of applicability and heavily relying on computational modelling and simulations under idealized conditions[194,207-209]. For example, many modelling and simulation papers consider calculating energies of adsorbed carbon and carbon clusters only on flat, ideal Cu(111) surfaces, although many of practical applications involve the use of rough, polycrystalline Cu foils for graphene synthesis. In addition, the growth process is a complex non-equilibrium problem whose understanding requires taking account the competition of various atomic processes such as mass transport from the vapour phase, heterogeneous decomposition of carbon source, surface diffusion, carbon cluster/nuclei formation, edge enlargement by carbon attachment, nucleus coalescence, and their respective reverse reactions. Thus, independent modelling work relying on a single method such as DFT calculations or molecular dynamics cannot entirely represent a global view of the process. Lastly, many of the predictions made by such studies, for examples, the actual nature carbon species on Cu surfaces and their interactions with the growing edges[209,210] are yet to be verified by experiments.

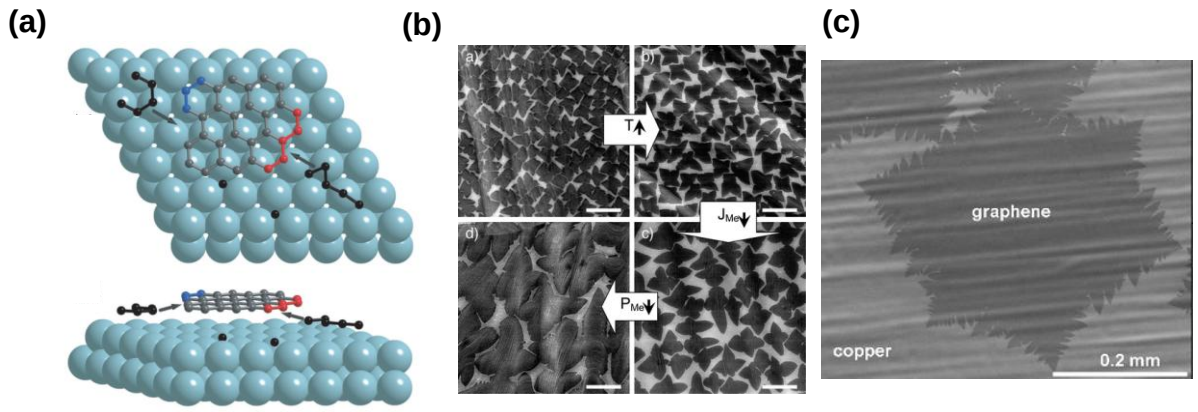


**Figure 23** a) Illustration of graphene nucleus growth limited by attachment of 5-carbon atom chain on Ir(111).[204] b) Influence of growth parameters on the lateral sizes of graphene nuclei during CVD on Cu.[191] Scale bar, 10 μm. $J_{Me}$ and $P_{Me}$ represent methane flow rates, and methane partial pressure, respectively. c) Growth of graphene inside a copper foil enclosure. As the flow of carbon containing gas is limited inside the enclosure, the nucleation and growth rates become much slower leading to significantly less density of nuclei with much larger lateral dimensions.[190]

### *2.5.4.5 Characteristics of CVD grown graphene films on Cu*

The structural and electronic qualities of CVD grown graphene are much better than that of graphene produced by solution based methods and comparable to SiC grown graphene, but

usually lower than that of mechanically exfoliated graphene. Recently, ARPES measurements on graphene grown on Cu(111) and Cu(100) have shown that the linear dispersion relationship is preserved attesting the weak graphene-metal interactions.[211] Moiré structure of graphene on Cu was observed by STM due to the rotational domains and lattice mismatch.[202]

The growth of FLG, which deviates from the self-limited model of monolayer graphene, has been investigated by Raman spectroscopy[172] and TEM.[212] Small patches of 1-5 L FLG covering less than 10% of the total area are often reported in the literature (e.g. Figure 24).[20,172,213] The stacking order of the FLG grown by CVD has been shown to be a mixture of AB, ABC, and random stacking.[206,212,214] Thus, the FLGs produced by CVD methods are expected to have varying degree of electronic properties different from mechanically exfoliated graphene which exhibit the AB stacking order.[215-217]

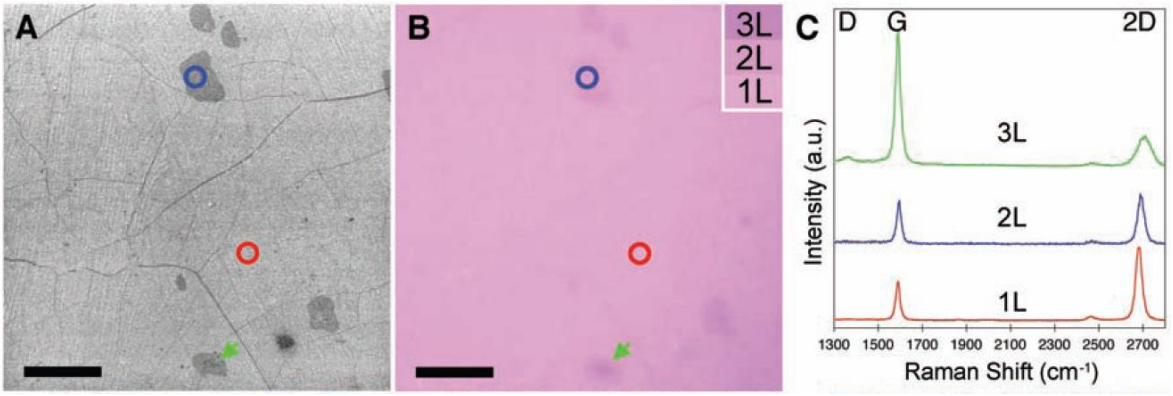


**Figure 24** a) SEM and b) optical images of graphene transferred onto $SiO_2$/Si substrate. c) Raman spectra of 1-3 layer graphene corresponding to red circled area (1L), blue circled area (2L), and green arrow (3L) of (a) and (b).[20]

As mentioned earlier, the nucleation and growth mechanism of CVD results in polycrystalline graphene. The grains of various rotational orientations can be imaged over large area by diffraction filtered, DF-imaging within electron microscopy techniques such as TEM and LEEM[178,218,219]. Figure 25a shows crystal domains of different orientations colour mapped by the composite dark field TEM images of all possible orientations. The typical size of the rotational domains or grains can range from ~ 10 nm to more than 100 μm depending on conditions. The large angle grain boundary between the rotated grains typically contains alternating arrangements of heptagon-pentagon pairs as illustrated by HRTEM imaging in Figure 25b.

The polycrystallinity of CVD graphene results in a variation of the electronic properties of graphene from device-to-device.[219,220] Within a single crystal CVD graphene, the carrier mobility can exceed mobility of 10,000 $cm^2/Vs$ on $SiO_2$[191,215,221] similar to that of micromechanically exfoliated graphene. Nevertheless, Tsen et al.[219] has recently shown that well interconnected grains can actually exhibit carrier mobility values close to that of single crystals possibly confirming the theoretical prediction that many of ideal line defects act as weak scatterers.[222-224] However, most of the reported values in literature still have a large variation in the mobility values from 500 to 10,000 $cm^2/Vs$,[20,191,218,225-227] potentially arising from the discontinuity between the graphene nuclei and the charged impurities originating from the wet transfer process.[227]

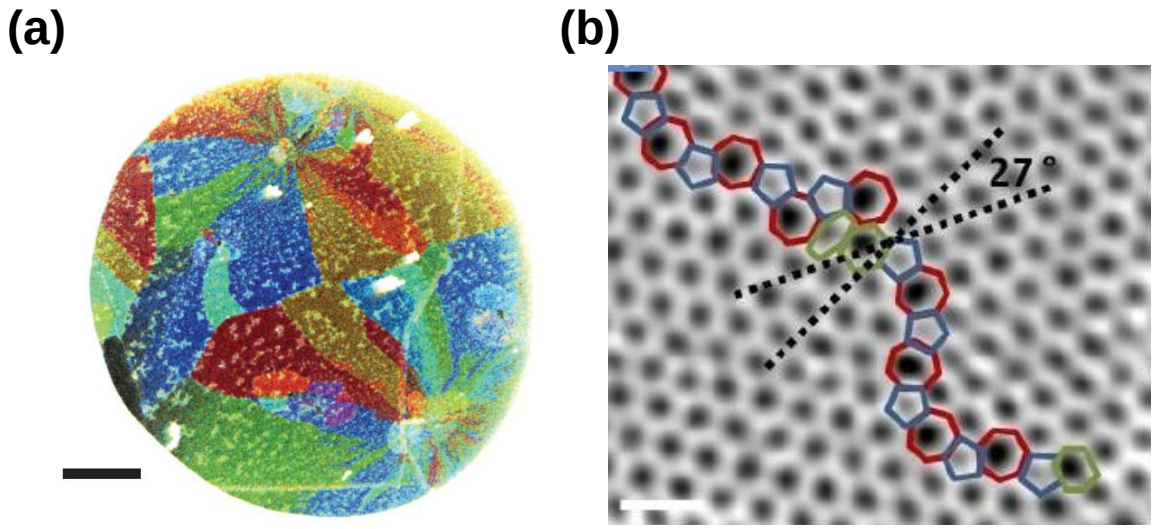


**Figure 25** a) a combined TEM dark filed image orientation dependent colour mapping of rotational domains in polycrystalline CVD graphene grown on Cu of random grain orientations.[218] Scale bar, 500 nm. b) HRTEM filtered image of a grain boundary between two graphene grains. The heptagons, hexagons, and pentagons that constitute a grain boundary is marked blue, green, and red, respectively.[218] Scale bar, 0.5 nm.

### 2.5.5 Other Synthesis Methods

As an alternative to top-down, solution based exfoliation of graphite to produce dispersion of graphene flakes, a bottom-up approach where graphene flakes are built by cyclodehydrogenation and planarization of small benzene based planar molecules called polyacyclic aromatic hydrocarbons (PAHs), is actively investigated using the versatile tools of organic chemistry.[228,229] Graphene nano-discs of PAHs up to 222 carbon atoms (diameter

of 3.2 nm) have been synthesized.[230] Their limited size remains as a challenge as increasing size of the molecule generally decreases solubility, and increases side reactions.[231,232]

Solvothermal method of directly converting alcohol to graphene through pyrolysis of ethanol in the presence of sodium has been developed.[233] A few other substrate free production routes involving pyrolysis of alcohol in gaseous phase have been investigated.[234-236] However, these methods of production have not been clearly demonstrated to be competitive in terms of quality and yields when compared to the most popular large-scale synthesis methods described in the previous sections.

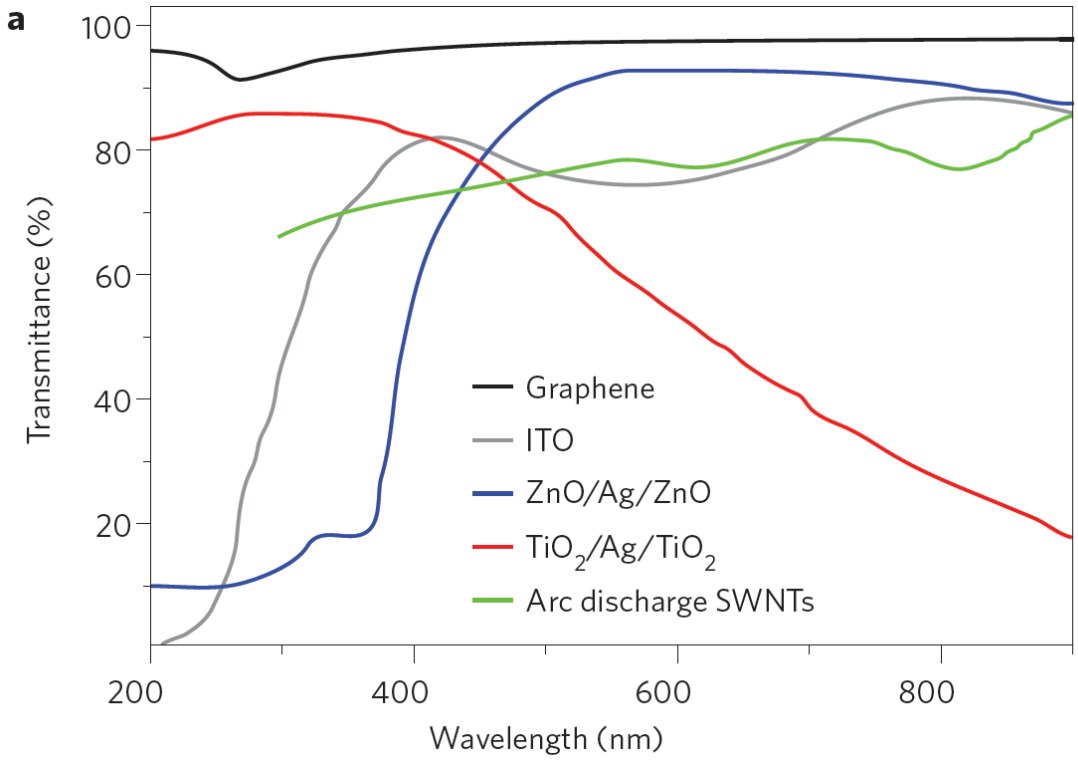


**Figure 26** Transmission of a monolayer graphene film (red), in comparison with ITO (black) , and other commonly used transparent conductive films (SWNTs, ZnO/Ag, and TiO2/Ag).[7]

## *2.6 Applications of Graphene*

### 2.6.1 Graphene Based Electrodes

Graphene retains very good conductivity and transparency in the mid-infrared to UV range of the electromagnetic spectrum (Figure 26). This makes graphene a good candidate for transparent and conducting electrodes for optoelectronic applications such as solar cells,[141,237-240] organic light emitting diodes (OLEDs),[241-244] organic light-emitting

electrochemical cells (OLECs),[245] and touch screens.[18,19,246] For more than four decades, indium tin oxide (ITO) has been used as the transparent and conducting electrode.[247,248] ITO has an excellent transmittance and sheet resistance. However, it faces several technological challenges.[249] First, it tends to crack during bending which makes it unsuitable for flexible electronics. Second, choices of the substrates are limited by its high temperature deposition. High-quality ITO is usually deposited on glass by sputtering at temperature around 400 ˚C. Although deposition at lower temperature has been demonstrated, this results in higher sheet resistance. Third, ITO is chemically unstable in acidic environments limiting device lifetime. Lastly, the limited global supply of indium is causing the rise in the price of ITO. Hence, a transparent and conducting material with good chemical stability, flexibility, and scalability to replace ITO is urgently needed.

To this end, graphene based transparent electrodes with promising performance characteristics have been demonstrated. The essential performance characteristics for a transparent conductor are its sheet resistance versus transmittance relationship. Generally for thin metallic films, transmittance, T, is related to the sheet resistance, $R_s$ by eq. 1:[250]

$$T = \frac{1}{\left(1 + \frac{Z_0}{2R_s}\frac{\sigma_{Op}}{\sigma_{DC}}\right)^2} \qquad (1)$$

where $Z_0 = 337\ \Omega$ is the impedance of free space, and $\sigma_{Op}$ and $\sigma_{DC}$ and are the optical and DC conductivities respectively. The ratio ($\sigma_{DC}/\sigma_{Op}$) can be considered as a figure of merit to evaluate the performance of transparent electrode. For example, the minimum industrial requirement for LCD application is T ~ 80% at Rs ~ 10 Ω/□, which leads to $\sigma_{DC}/\sigma_{Op}$ value of 35.[251] For electroluminescent displays and touch screen panels which require lower performance, $\sigma_{DC}/\sigma_{Op} = 11$ (T ~ 80 % at $R_s$= 300 Ω/□).[252]

Intrinsically, graphene and FLG in undoped state is expected to have $\sigma_{DC}/\sigma_{Op}$ of 2.6 – 11,[253] much lower than that of ITO which has $\sigma_{DC}/\sigma_{Op}$ of 170 (transmittance of 85% and Rs = 13 Ω/□).[248] However, doping high-quality graphene while preserving its high carrier mobility can lead to the have sheet resistance as low as ~30 Ω/□[6] at transmittance of 97.7 % giving much higher $\sigma_{DC}/\sigma_{Op}$ of ~560.

Experimentally, best $\sigma_{DC}/\sigma_{Op}$ values of graphene films obtained through solution based methods are 2.6 for rGO[254] and 27 for non-covalently functionalized graphene.[111] Doped CVD graphene exhibits better quality with values of $\sigma_{DC}/\sigma_{Op}$ ranging from 50[255] to 198,[18] already comparable to or exceeding that of ITO. This makes the CVD synthesis a very promising route for production of high performance transparent graphene electrodes.

Current developments in large-area graphene have led to demonstration of optoelectronic devices where graphene as transparent anodes has yielded promising results that is approaching the performance of ITO based control devices.

In addition to optoelectronic applications, graphene and FLG sheets have been studied as electrode materials for electrochemical/electrocatalytic applications such as lithium-ion batteries,[157,256-262] electrochemical fuel cells,[263-268] and ultracapacitors[259,269-277] which can benefit from graphene's chemical stability and large surface area-to-volume ratio along with high conductivity. Furthermore, graphene interconnects (conductive wires embedded in integrated circuits) are expected to outperform conventional copper interconnects in many aspects[278] such as higher current density limit (~100 times larger than Cu)[279] and thermal conductivity (~ 10 times higher than Cu).[51]

### 2.6.2 Graphene Based Transistors

The high mobility of graphene makes it useful for field effect transistors (FET).[280-283] The 2D planar configuration of graphene has the advantage that the current complementary metal oxide-semiconductor (CMOS) technology can be utilized for fabrication. However, the limitations of graphene are that it cannot currently be deposited onto wafer scale substrates and more fundamentally it does not turn off due to its zero band gap nature. The low on/off ratios (~10) in graphene mean that it cannot be utilized for logic devices.[284] The on/off ratio can be improved by inducing a band gap by utilizing graphene nano-ribbons (GNR)[285-290] or quantum dots.[280] However, these solutions introduce other fabrication issues as well as undermining the planar processing advantages of graphene. Furthermore, the mobilities of GNRs are much lower.[222,291]

Thus, the most promising device application of graphene may be high radio frequency analogue devices (also known as HEMTs), which require on/off ratios of only 10-100.[73] Recently, IBM has reported a device operating at cut off frequency of 300 GHz fabricated

from CVD graphene grown on Cu and SiC converted graphene (Figure 27).[292] The estimated cut of frequency of ideal graphene device can reach up to 1420 GHz outperforming the state-of-art silicon and III-V semiconductor devices which have operating frequencies of 400 – 600 GHz.[293] However, in order for graphene to ultimately replace them, many technical issues remain such as obtaining well-defined current saturation at high drain-source voltage, and finding suitable substrate, top-gate dielectric, and metallic contacts to minimize interface-induced carrier scattering and contact resistance.[293]

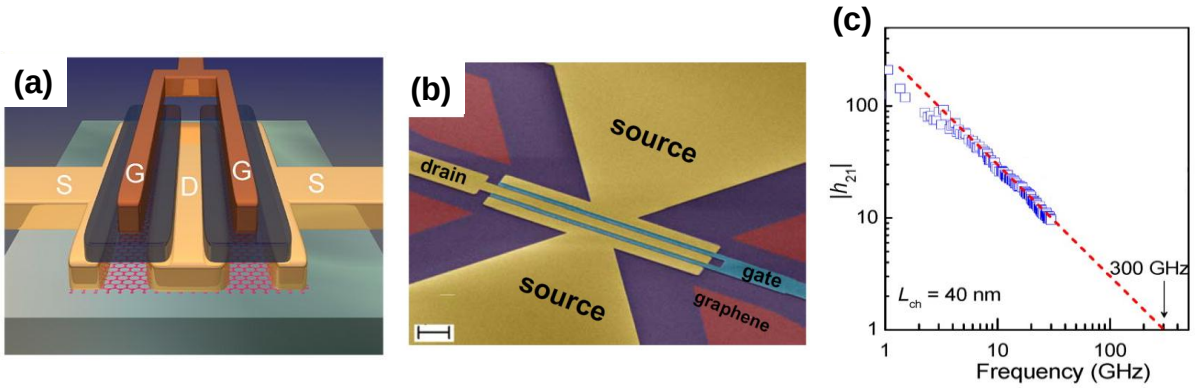


**Figure 27** a) Schematic cross-sectional view of a graphene based HEMT. b) Top-view of a HEMT device imaged through SEM (scale bar, 2µm). c) Current gain($|h_{21}|$) of a HEMT fabricated by CVD graphene transferred onto diamond like carbon wafer as a function of operating frequency.[294]

### 2.6.3 Other Applications

Graphene embedded in materials such as polymer and ceramics can significantly improve the mechanical properties of the composites such as strength, stiffness, and hardness potentially resulting in a mechanically robust, low-weight graphene based composite with thermal shock resistance.[75,295-297] It was shown that even less than 1 wt% of graphene can significantly increase Young's modulus and hardness of the polymers such as PMMA, polyvinyl acetate (PVA), and PAN.[296,298,299] In addition, only 0.05 wt% of graphene in PMMA can increase glass transition temperature by 40 ˚C. High-quality graphene containing thermoresponsive polymer hydrogels of poly(N-isopropylacrylamide)[300] and poly(N-vinylcaprolactam)[296,301] were recently realized by non-covalent exfoliation of graphite in monomer based solvents followed by direct frontal polymerization of the unfunctionalized graphene-monomer solution. Improvement of composites through functionalization and cross-linking of graphene to enhance the filler – matrix interaction are currently being sought.[295]

Graphene has an excellent potential to become an active element for molecular sensors due to the exceptionally low noise characteristics and extremely high surface area to volume ratio.[73] Physisorbed molecules can influence the electrical and mechanical properties of graphene which can be detected through measuring the changes in chemical potential[80,302-306] or the quality factor, Q of mechanical resonator made of a graphene membrane.[118,307] This makes graphene promising material as chemical sensors because it has the potential to detect toxic gases of concentration as small as 1 ppb which fulfil the sensitivity requirement for industrial and military monitors.[80,304] However, the limited selectivity of pristine graphene is considered as a major problem for graphene based sensors.

Graphene's strong interaction with light over a wide wavelength range can lead to variety of applications for optical communications.[293,308] Some of the promising applications include energy-efficient, ultrawide-bandwidth, CMOS compatible graphene based optical modulators with ultrafast responses,[309] high throughput metal-graphene-metal photo-detectors,[310] and ultrahigh gain graphene-quantum dot hybrid phototransistors.[311]

Other numerous proof-of-concept demonstrations of many types of graphene based applications are present in literature. They include field emission device,[120,312,313] diffusion barrier membranes,[314,315] support membrane for TEM grids,[316] saturable absorber for laser mode-locking,[317,318] and hydrogen storage.[319,320]

### *2.7 Conclusions*

The extraordinary properties of graphene make it promising for many commercial applications especially in thin film electronics. To implement graphene in such applications, highly reproducible methods for large-scale synthesis of defect-free material of uniform properties must be developed. For example, mobility values greater than 10,000 $cm^2/Vs$ are required for operation of transistors at THz frequencies.[294] For transparent electrode applications, sheet resistance of less than 100 Ω/□ at transmittance of 90 % is required.[321] Precise control of the properties of graphene must be achieved via doping to achieve better performance. Lastly, the synthesis method must be compatible and scalable with existing technologies for facile integration of graphene into current electronics. The advantages and disadvantages of different methods for obtaining graphene are summarized in Table 1. Of these, non-covalent solution phase exfoliation and CVD on Cu offer the most promising routes for high throughput production of graphene for large area graphene of reasonable

quality. SiC wafers are expensive but the ability to make wafer-scale graphene using this method is also appealing.

The non-covalent solution phase exfoliation method is at an early stage of development and hence improvements in critical aspects such as the materials properties and thin film deposition methods as well as much better fundamental understanding of the relationship between processing conditions and quality-limiting mechanisms are the main challenge to be addressed in this dissertation.

Similarly, while we have seen a rapid advance in the qualitative understanding of the CVD growth of graphene resulting in materials with improved properties, we still lack the predictive ability to precisely control the graphene structure and thus its properties. Inhomogeneity within the CVD graphene structure should be minimized by elimination of grain boundaries and precise control over number of layers and their coverage. To this end, guidelines for growing single crystal graphene will be sought. This is to be achieved by acquiring a detailed understanding of the growth parameters and underlying physicochemical mechanisms.

| | Advantages | Disadvantages | Single crystal grain size | Room temperature mobility ($cm^2/Vs$) |
|---|---|---|---|---|
| Solution phase exfoliation | ▪ Inexpensive/high-throughput<br>▪ Large scale deposition on variety of substrates via printing<br>▪ Less expensive (processed in close to ambient, room temperature conditions) | ▪ Poor electrical properties due to defects and small flake sizes<br>▪ Polydispersity in lateral sizes and number of layers | ~1 μm[110] (for non-covalent exfoliation) 100μm[322] (for GO) | 100[125,323] (for overlapped layers with non-covalent exfoliation) 10-1,000[254,324] (for rGO) |
| SiC decomposition | ▪ Direct growth on insulating substrate<br>▪ Wafer scale growth<br>▪ Good electrical properties already demonstrated | ▪ High temperature<br>▪ Expensive SiC wafer<br>▪ Large variability in quality<br>▪ Morphology issues<br>▪ No reliable transfer method | ~10 μm[325] | 10,000 – 30,000[138,139,326] |
| CVD Graphene | ▪ Growth at temperatures <1000 ˚C<br>▪ Inexpensive catalysts substrates (Cu, Ni…)<br>▪ Wafer scale growth<br>▪ Good electrical properties already demonstrated<br>▪ Transfer onto many kinds of substrates | ▪ Wrinkles<br>▪ Polycrstallinity<br>▪ Contamination and damage during the transfer process | ~1 mm[327,328] | 10,000 – 45,000[219,221] |

**Table 1** Summary of advantages and disadvantages of the three large area synthesis methods. Best single crystal grain size (in terms of order of magnitude) and room temperature charge carrier mobility values (given in terms of range due to a large spread of values in the literature) for each method are also included for quantitative comparison.

# 3 Experimental Setup of Langmuir-Blodgett Deposition of Graphene Exfoliated in NMP

## *3.1 Introduction*

In the first part of the thesis work, I have carried out the investigation on non-covalent exfoliation of graphene in NMP, which was newly demonstrated in 2008. This study presented in this dissertation has been completed and presented at the MRS Fall 2009 Meeting, Boston, U.S.A (a manuscript is also under preparation). The motivation for the non-covalent exfoliation arose from the fact that properties of graphene oxide after reduction were not satisfactory for high-end applications of graphene. Thus, the aim was to explore another solution-processed method and obtain thin films with optoelectronic properties superior to graphene oxide.

In this chapter, the experimental setup of the non-covalent exfoliation work will be described in three parts: (1) background theory of graphene exfoliation in organic solvents without covalent functionalization and thin film formation via Langmuir-Blodgett assembly, (2) experimental procedures for obtaining high quality graphene in NMP, and (3) large area thin-film deposition methodology via Langmuir-Blodgett assembly.

## *3.2 Background Theory*

### 3.2.1 Exfoliating Graphite in a Solvent

The exfoliation of graphite can only occur if the net energetic cost is very small, that is, if the enthalpy of mixing (per unit volume) where in our case the solvent and the graphitic flakes, is very small. This has been calculated to be[110]:

$$\frac{\Delta H_{mix}}{V_{mix}} = \frac{2}{t_{flake}} \left( \delta_G - \delta_{sol} \right)^2 \phi \qquad (2)$$

where $\delta_i = \sqrt{E_{sur}{}^i}$ is the square root of the surface energy ($E_{sur}$) of phase i, $t_{\text{flake}}$ is the thickness of a graphene flake and $\phi$ is the graphene volume fraction. This equation, reminiscent to the Hildebrand–Scratchard equation of regular binary solutions[329] states that the enthalpy of mixing is dependent on the balance of graphite and solvent surface energies. For graphite, the surface energy is defined as the energy per unit area required to overcome the van der Waals forces when peeling two sheets apart. From eq. 2, we expect the minimum energy cost of exfoliation for solvents whose surface energy matches that of graphite, 40 mJ/m$^2$. Although this approach assumes only dispersive force contributions in the surface energy,[330] solvents whose surface energies are close to 40 mJ/m$^2$ have been experimentally demonstrated to yield high concentration of graphene dispersions.[110]

### 3.2.2 Langmuir-Blodgett Film Formation

Conventionally, Langmuir-Blodgett assembly refers to the monolayer formation of amphiphilic organic molecules at the air-water interface.[331-333] Due to the attractive force between polar "head" of the amphiphilic molecule and water, and the hydrophobicity of the non-polar "tail" of the molecule, the molecule preferentially align vertically with the polar heads in contact with water and the non-polar tails pointing away from the surface. Initially, the molecules on water tend to spread evenly on the water surface in a random fashion at low surface concentration. As the concentration reaches a critical micelle concentration, the molecules can form a closed packed monolayer by adding a sufficient amount of the molecules onto the water surface or by compressing the molecules together through a movable trough wall which effectively increases the surface pressure (difference between surface tension of water and surface tension due to the molecules). The monolayer then can be transferred easily onto a wide range of solid substrates by immersing the substrate before the assembly and carefully pulling out the substrate onto which the monolayers are adhered.

In the last two decades, Langmuir-Blodgett assembly technique has been extended to monolayer formation of hydrophobic nanoparticles,[334] nanorods,[335] nanotubes,[336] and graphene oxide[117,124,337] that reduce the overall interface energy by spreading out and forming a monolayer on the water surface.

### 3.3 Preparation of graphene in NMP

The initial conditions of exfoliation of graphite in NMP used in this study were based on the method developed by Y. Hernandez et al.[13] as displayed in Figure 28. The effect of the exfoliation conditions such as the initial concentration of graphite powder, sonication time ($t_s$), centrifugation speed/time, and additional stirring process was investigated further in order to optimize the method to yield high quality, well-exfoliated graphene dispersions of high concentrations.

Graphite and NMP were purchased from Sigma-Aldrich (product number: 332461). Before exfoliation, large particles were removed by a 125 µm mesh sieve. The mixture was then sonicated in ultrasonic bath while being stirred by a custom made stirrer. For each experiment, great care was taken to maintain the same level of water and position of the beaker containing the mixture in the ultrasonic bath every time in order to ensure reproducibility. The mixture was then purified by centrifugation (Beckman Coulter Avanti J-26 with JA-20 rotor), with centrifugal force of 10,000 g for 30 – 90 minutes. Note that the centrifugation step must be followed right after the sonication/stirring step with minimal delay between the steps to prevent reaggregation. The top 80% of the supernatant was taken out from the centrifuge tube and stored in vial for further experiments. Refer to Figure 28 for the overall illustration of the procedure.

### 3.4 Longmuir-Blodgett Thin-film Deposition

As highlighted in the literature review, one of the crucial aspects of solution-processed graphene for optoelectronic application is its compatibility with solution based thin-film deposition techniques. The challenge for thin-film deposition from graphene in NMP is that high boiling point of solvent makes spin-coating or spray-coating difficult due to the flake aggregation due to slow drying speed and poor wetting. Moreover, the high solubility of many kinds of polymers in NMP also introduces difficulties in vacuum filtration approach as many existing filters are made of polymer materials.

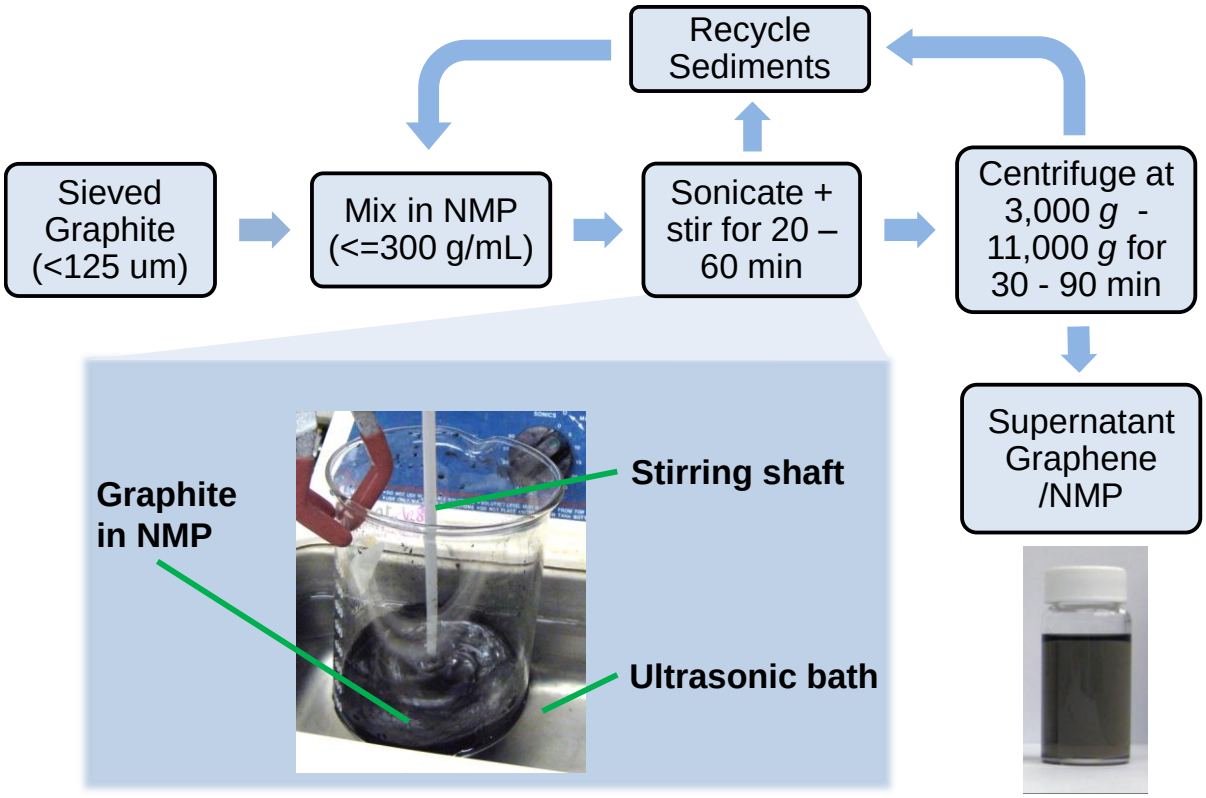


**Figure 28** Graphene exfoliation in NMP and Langmuir-Blodgett deposition process. The processing step is largely adapted from the work by Y. Hernandez et al.[13] In order to significantly improve the efficiency and yield, we have introduced the simultaneous stirring of the solution during the sonication step.

In this work, we employ the Langmuir-Blodgett scheme[331,338,339] to produce thin film of graphene on various substrates. Here, the graphene/NMP suspension is carefully deposited on a trough of DI water through the Langmuir-Blodgett assembly, which exploits the hydrophobicity of the solute (in this case graphene) and high surface energy of water to self-assemble a layer on the water surface. As the dispersion is gently dropped onto the surface of water, the NMP dissolves into the water but graphene, which is hydrophobic, remains floating on the surface of water. Because of the high surface energy of water the flakes would tend to spread out as much as possible which effectively decreases the total surface energy. Continuous film forms at the appropriate concentration of graphene on the surface of water. The film can then be deposited onto variety of substrates by first immersing the substrate in the water bath, then injecting the graphene suspension to allow the graphene layer formation, and finally pulling out the substrate from the water.

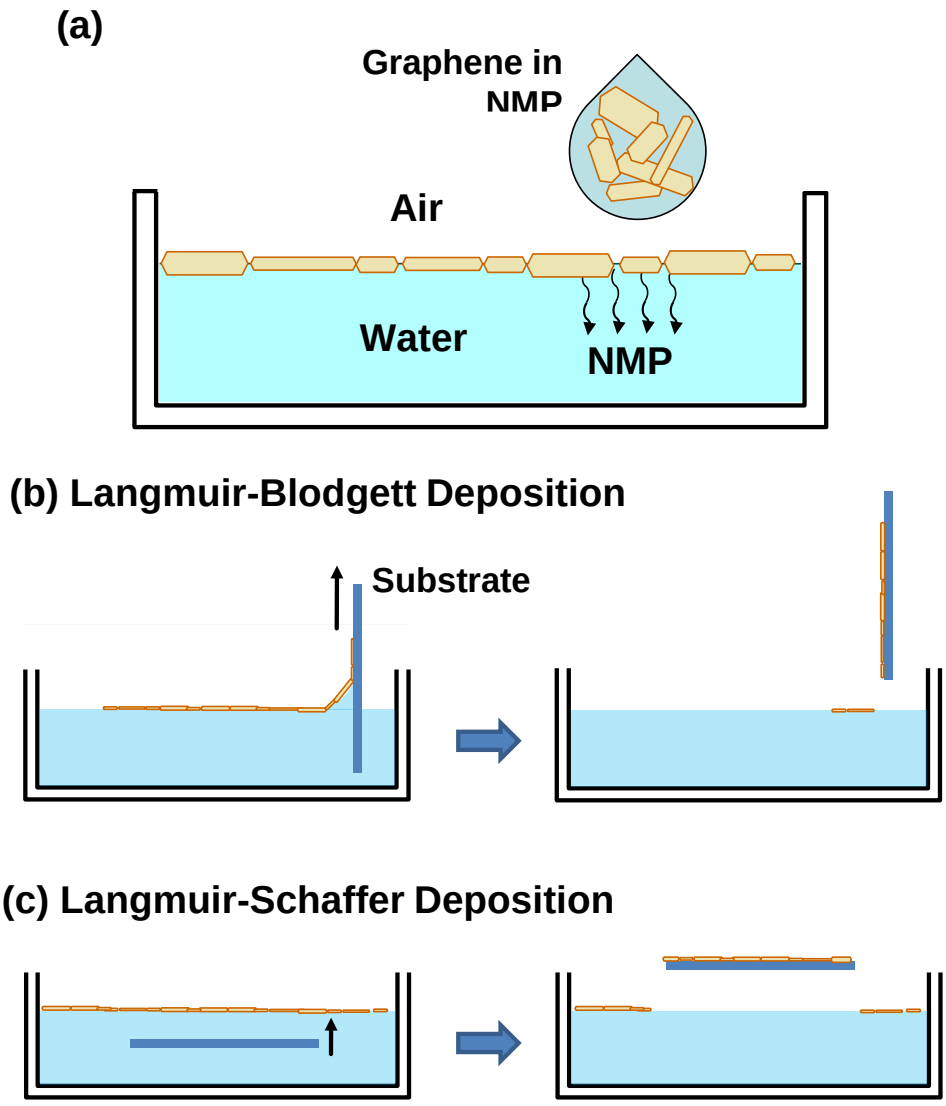


**Figure 29** Schematic of film deposition processes using Langmuir-Blodgett assembly at the air-water interface. a) When dispersion of graphene/NMP is dropped onto a bath of water, Langmuir-Blodgett film forms on the surface of water as graphene is immiscible with water while NMP readily dissolves in water. After the formation of a Langmuir-Blodgett film, the film can be deposited on a pre-immersed substrate by Langmuir-Blodgett Deposition (b) or Langmuir-Schaffer Deposition (c).

Depending on the orientation of the substrate with respect to the graphene/water surface during the pull-out process, the deposition technique is called Langmuir-Blodgett when the substrate is orthogonal to the surface (Figure 29b) and Langmuir-Schaefer[340] when it is horizontal (Figure 29c). For the large scale deposition (for areas larger than 2 cm × 2 cm), we utilized an automated dip-coater to control the speed of the substrate's vertical movement in Langmuir-Blodgett deposition, and an automatic syringe pump (Baxter, Model AS40A) to simultaneously control the input rate of graphene dispersion dropped onto the surface of

water (Figure 30). For deposition on small-scale $SiO_2$/Si substrates (1 cm × 1 cm) for FET device measurements, we have employed the simpler Langmuir-Shaffer deposition method where the substrate was pulled from the water bath horizontally.

The above deposition procedure can be repeated for multiple times on a same sample after drying the film in air for 30 min followed by heating the sample on a hot plate (~120 ℃) for 10 min, in order to obtain thicker films of FLG.

### *3.5 Conclusion*

In this chapter, we have described the novel approaches to graphite exfoliation for high throughput production of non-covalently functionalized graphene dispersed in NMP and large area thin film deposition techniques from the graphene/NMP dispersion for optoelectronic characterizations and fabrication of graphene based devices.

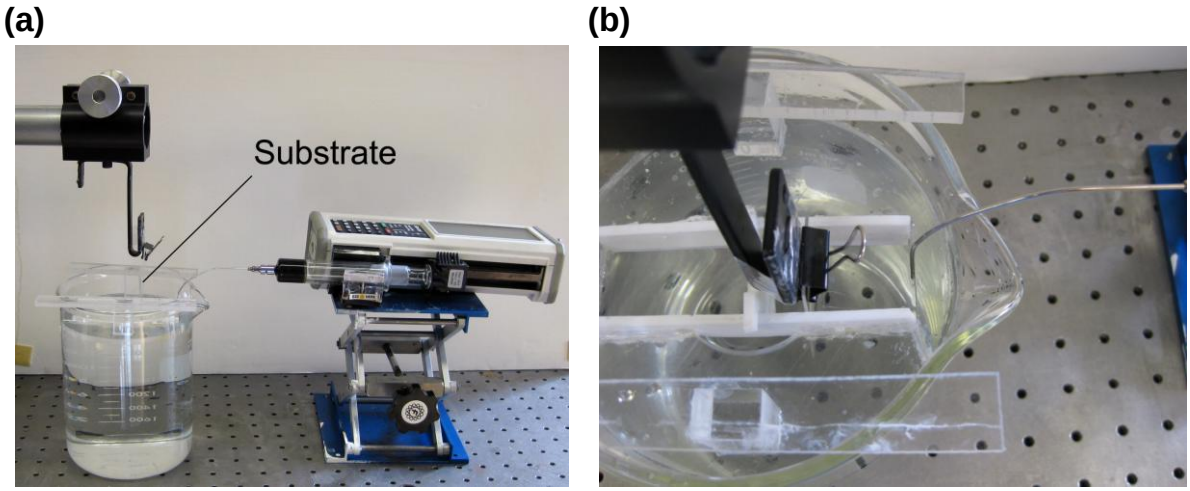


**Figure 30** Photographs of the automated Langmuir-Blodgett deposition/dip-coater assembly. a) Side view of the dip-coater setup. b) Close-up, top view of the dip-coater setup. The substrate (glass slide) immersed in the custom-made trough is clamped to the automatically actuated arm that slowly pulls the substrate vertically up, while the injection of graphene/NMP dispersion onto the surface of water within the trough was controlled by the automated syringe pump. The trough is constructed by the walls made of Teflon and Plexiglas.

# 4 Experimental Design of Chemical Vapour Deposition of Graphene on Copper

## *4.1 Introduction*

The limitations of solution-processed graphene led us to pursue chemical vapour deposition for scalable synthesis of high quality graphene. As discussed in the literature review, copper has some distinct advantages over other catalysts for graphene growth such as low cost, ability to generate self-limited growth of single layer graphene over the entire surface and compatibility with facile solution based transfer methodologies for transferring graphene onto any other substrates. The primary challenge is to achieve reproducible and uniform deposition of high quality graphene with a precise control over the crystalline grains, number of layers and continuity. The aim is therefore to elucidate the growth mechanisms and provide guidelines for achieving high quality graphene with a desired structure. This understanding can be reached by studying the effect of the growth conditions over extensive ranges and developing a general model to accurately predict the growth behaviour and tailor the properties of graphene as outlined in Table 2.

In this chapter, the design of the experimental system for the CVD growth of graphene, a parametric study of the growth conditions, as well as experimental methodology for substrate preparation and transferring CVD grown graphene that was employed throughout the study will be discussed.

## *4.2 Chemical Vapour Deposition System*

Our CVD work was based on the initial report by the Ruoff group[20] where the growth of graphene on Cu was reported for the first time. Follow-up studies have confirmed the result and also the preferential growth of a single graphene layer over multilayers.[18,70,143,170,191,341] These studies have shown that the material has to be improved due to the polycrystalline nature of the CVD graphene. Up until now, only a few reports have

investigated systematically the effect of various growth conditions with limited insights on the physicochemical growth mechanisms.

| Growth process parameters | Structural characteristics of CVD graphene | Optoelectronic performances of CVD graphene |
|---|---|---|
| • Pressure<br>• Gas composition<br>• Growth time<br>• Surface roughness<br>• Cu crystal orientations<br>• Temperature | • Coverage and continuity<br>• Grain size and orientations<br>• Morphology:<br>  • wrinkles<br>  • grain boundaries<br>• Thickness<br>• Stacking order | • Sheet Resistance vs. Transmittance<br>• Field-effect Mobility<br>• Temperature-Dependent characteristics |

**Table 2** Summary of the main parameters involved in growth process – materials characteristics – optoelectronic performances relationship in CVD graphene. Many of the critical structural and optoelectronic properties are expected to be inherently dependent on the growth conditions.

We have set up a hot wall tube furnace for low pressure CVD growth and begun by reproducing the results of the previous studies using the $CH_4/H_2$ mixture and Cu foil at 1000 ˚C as the standard conditions. Indeed, our initial results have indicated that high quality graphene can be obtained in our furnace.

The schematic of the CVD system is shown in Figure 31. The system is a hot wall, tube furnace system that contains an electrically powered furnace, quartz tube chamber, power supply, gas cylinders, mass flow controllers, vacuum pump, and vacuum gauge. The quartz tube (3.5 cm in diameter and 100 cm in length, 99.995% purity, Robson Scientific) is placed at the centre of the cylindrical furnace at which the copper substrates are to be inserted. The temperature of the furnace is monitored and maintained by a proportional-integral-differential (PID) controller (Eurotherm 2204) with a thermocouple (TC) installed near the centre of the furnace. The temperature reading has been calibrated at the beginning of the project by an independent measurement using an external thermocouple. The furnace contains a single heating zone (45 cm in length) that operates on the principle of Joule heating by the resistive

coils embedded in the furnace. Figure 32 displays the temperature profile across the furnace measured by inserting a thermocouple from one end of the furnace when the set temperature is 1000 ℃. The temperature stays relatively constant near the centre with temperature difference of < ~2 ℃ for a length of ~ 5 cm. At the end of a growth experiment, power supply is turned off and the furnace is left to cool naturally to room temperature, although the cooling rate of the sample itself can be much faster by quickly pulling the quartz tube out of the furnace at the end of the growth (rapid cooling). The typical heating and cooling rates of the furnace are shown in Figure 33.

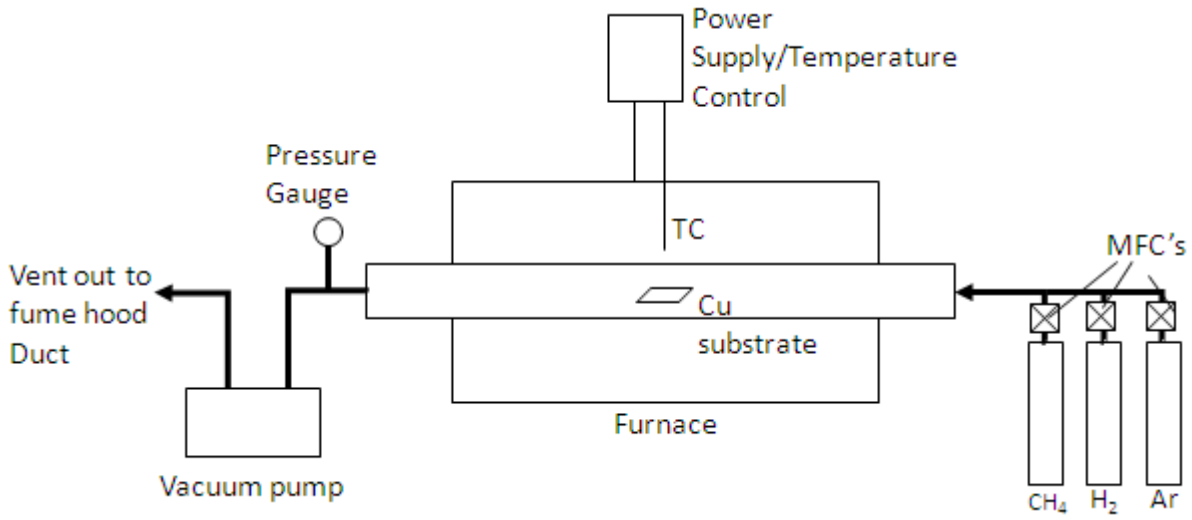


**Figure 31** Schematic of the CVD system.

The gases are supplied by compressed gas cylinders from BOC (CP grade Ar, CP grade hydrogen, and zero grade $CH_4$). Initially, all of the gas flow rates to the system were controlled by mass flow controllers calibrated for each gas (Aalborg MFC GFC series). Later, a manual leak valve (Kurt J. Lesker VZMD95) was used to control the flow rate of $CH_4$ below 0.5 sccm instead of the mass flow controller for the low $P_{CH4}$ study.

A base pressure of ~ $1 \times 10^{-3}$ mbar was achieved by a two-stage rotary pump (Leybold D8B). The pressure of the system during growth was monitored by a capacitive pressure gauge (Agilent CDG-500, full pressure range of 10 torr) installed near the downstream end of the tube and were controlled through the needle valve attached at the inlet of pump. Above 10 mbar, a Bourdon gauge (Kurt J. Lesker, KJLD GMBAR) was used to monitor the vacuum condition when the chamber is being evacuated and purged.

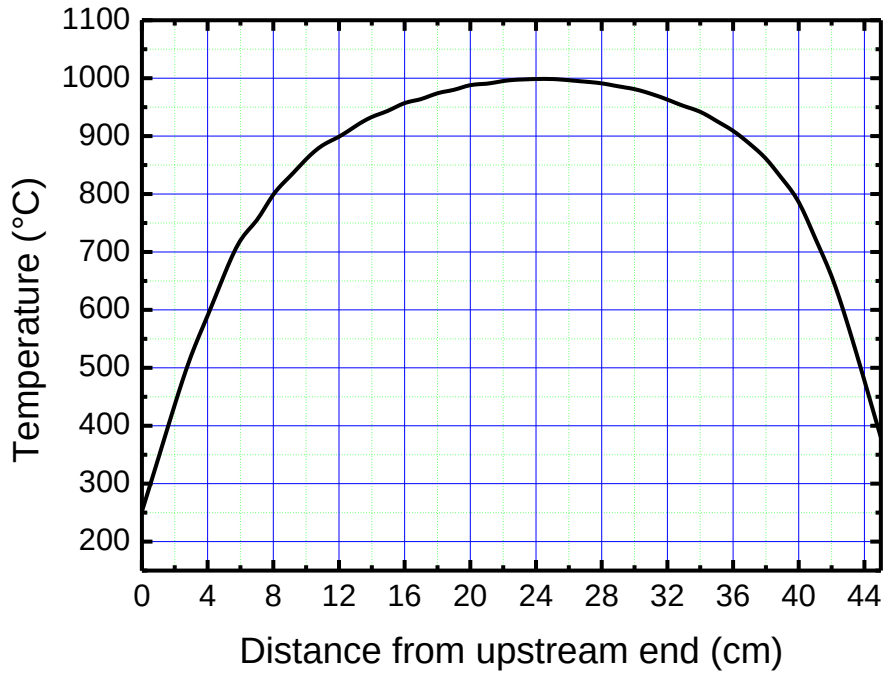


**Figure 32** Temperature profile of the CVD furnace measured from the upstream end of the tube furnace by an external thermocouple.

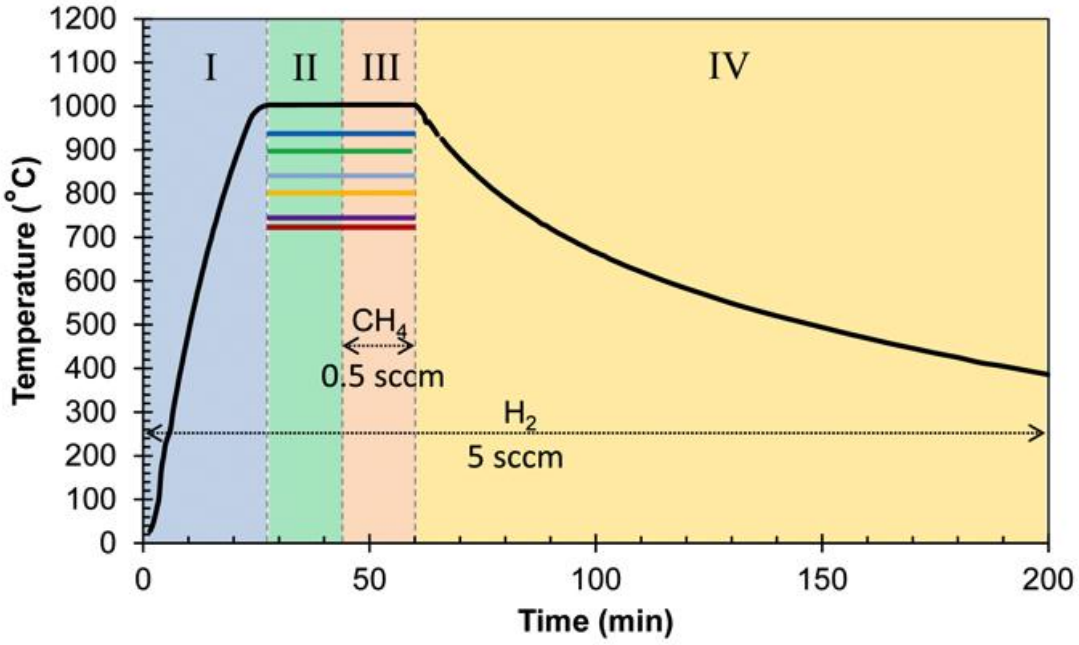


**Figure 33** Temperature, gas flow rates at different stages of the CVD process: I-heating, II-annealing, III-growth, IV-cooling. The coloured lines indicate lower ranges of annealing and growth temperatures investigated.

### 4.2.1 Fluid Mechanical Considerations

As the CVD depends on the composition and partial pressure of the gases that flow across the substrate, critical flow parameters (temperature, mass flow rate, partial pressures, diameter of the tube furnace, dimensions of substrate and support, etc.) of the system that determine the pressure drop and flow uniformity must be addressed. The importance of such flow conditions in CVD graphene growth was highlighted for the first time by Bhaviripudi et al.[143]

At the pressure range employed for the study (~ 1 mbar), the mean free path of the atoms and molecules in the reactor is much smaller than the dimensions of the reactor (Knudsen number <<1).[342] Hence, one can employ the continuum fluid mechanics for viscous gases. One of the important dimensionless parameters that determine the flow regime across the tubular furnace is the Reynolds number, Re:

$$\mathrm{Re} = \frac{\rho v_g d}{\eta} \qquad (3)$$

where ρ is the density of the fluid, $v_g$ is the average gas velocity (in m/s), $d$ is the inner diameter of the quartz tube (3.4 cm), and η is the dynamic (or absolute) viscosity of the fluid (in Pa·s). $R_e$ can be considered as ratio of magnitude of inertial force to the viscous-drag force on the fluid.[342] It is empirically determined that if $R_e$ is much less than 1200, the flow inside the tube would be laminar in which the behaviour of the fluid (streamline, pressure etc.) can be easily predicted. If $R_e$ is 1200-2000 or greater, turbulence can occur that would produce irregular variations (eddies and vortices) in flow velocity and pressure which can be difficult to predict.[342] The density of a gas can be calculated by using the ideal gas law relationship:

$$\rho = \frac{MP}{RT} \qquad (4)$$

where M is a molar mass, P, pressure, T, temperature, and R, gas constant (8.314 $J \cdot K^{-1} \cdot mol^{-1}$). The molar mass values of Ar and $H_2$ are 39.95 g/mol, and 2.016 g/mol respectively.

The gas velocity in terms of volumetric flow rate, Q ($m^3/s$) through the tubular furnace is:

$$Q = Av = \frac{\pi v d^2}{4} \Rightarrow v = \frac{4Q}{\pi d^2} \qquad (5)$$

where A is the cross sectional area of the tube, *d*, is the diameter of the tube. Then, viscosity values of the gases are primarily a function of temperature and generally higher for the gases of larger molecular weight. For instance, $\eta_{Ar}$ = 6.56 Pa·s,[343] $\eta_{H2}$ = 2.17 Pa·s,[344] and $\eta_{CH4}$ = ~3 Pa·s[345] at 1300 K. Therefore, for a fixed geometry of system, Re generally increases as temperature, pressure, and flow rates increase. In typical conditions of the experimental setup (P~ 4 mbar, T ~ 1300 K, and Q = 10 sccm = (101325 pa / 400 pa ) × 1.7 × $10^{-7}$ $m^3$/s = 4.31 × $10^{-5}$ $m^3$/s), Re ~ 0.04 (when considering Ar atmosphere to calculate the upper limit of Re). Thus, it was very likely that the flow inside the furnace was laminar.

Another critical fluid dynamic parameter for the CVD is the thickness of the boundary layer (or stagnant layer), δ, across the sample surface. Due to the surface shear drag, $v_g$ is zero at the surface of the sample (y = 0) and asymptotically reaches the main flow rate away from the surface (y = δ) in the direction perpendicular to the direction of the flow. The thickness of boundary layer from the leading edge of the substrate placed parallel to the flow direction (x = 0) is:[346]

$$\delta = 4.65\sqrt{\frac{xd}{\mathrm{Re}}} \qquad (6)$$

As the Re is quite small for the system of the current work, we expect significant effect of the viscous flow. However, as the extent of the boundary layer cannot increase indefinitely, and is limited by the diameter of the tube, the velocity profile above the surface is expected to be homogenous for $\delta > d$. (For instance, $\delta$ = 13.6 cm already, when *x* is 1 mm, which is unphysical as $\delta > d$.) As Re is much lower than 1, this gives effectively uniform boundary layer for most of the sample surface except for the region near the leading edge.

The inhomogeneous boundary layer is expected to be detrimental for thin film morphology especially in the mass-flow regime where the overall reaction is limited by the mass transport (or gas diffusion) from the vapour phase to the substrate surface across the boundary layer. The rate in this regime is determined by the concentration gradient across the boundary layer and reaction constant, $k_m$:[347,348]

$$k_m = \frac{D_{gas}}{\delta} = \frac{2}{3}\sqrt{\frac{k^3}{\pi^3 m_{gas}}}\frac{T^{3/2}}{P{d_{gas}}^2} \times \frac{1}{4.65}\sqrt{\frac{\mathrm{Re}}{xd}} = 3.1\sqrt{\frac{k^3\,\mathrm{Re}}{\pi^3 m_{gas} xd}}\frac{T^{3/2}}{P{d_{gas}}^2} = 3.1\sqrt{\frac{v_g}{P\eta(T)}}\sqrt{\frac{k^2}{\pi^3 x}}\frac{T}{{d_{gas}}^2} \quad (7)$$

where $D_{gas,}$ is the diffusion coefficient of a gas, $d_{gas}$, gas molecular diameter, $m_{gas}$, gas molecular mass, $k$, Boltzmann's constant. For surface reaction limited regime, $k_m$ is much higher than the overall surface reaction constant, $k_s$, which essentially follows the Arrhenius relationship:

$$k_s \propto \exp\left(-\frac{\Delta G}{kT}\right) \qquad (8)$$

where $\Delta G$ is the change in the free energy of the surface reaction. Bhaviripudi et al.[143] have shown that low pressure graphene growth is likely surface reaction limited and the growth rate is uniform of over the entire area of the substrate. However, it must be noted that limited $v_g$ of $CH_4$ or high temperature which increases $k_s$ much more steeply than $k_m$ can result in the transition from the surface reaction regime to mass transport regime.

Lastly, the pressure drop, $\Delta p$, across the sample due to the viscous flow must be addressed. This can be calculated by the Darcy–Weisbach equation in the laminar flow regime:[346]

$$\Delta p = \frac{64}{\mathrm{Re}} \frac{l}{d} \frac{\rho v_g^2}{2} \qquad (9)$$

where $l$ is the sample length. For the typical set of conditions, this results in negligible pressure drop ( < 1 Pa) across the entire region heated by the furnace.

Throughout the study, most of the pressure and mass flow rates of the gases were kept in the regime of laminar flow, surface reaction limited deposition, and low pressure drop, in order to ensure the reproducibility of the CVD experiment.

### *4.3 The Parametric Study*

In table 2, the growth parameters and their ranges are summarized. These ranges were determined based on literature studies, fluid mechanical analysis of the system in the previous section, and the limitations of our experimental setup. For example, the temperature range was limited by the minimum temperature required for cracking of hydrocarbons precursors (> ~ 650 °C), and the melting point of the catalyst (for copper, ~1080 ˚C). Additionally, the total pressure was kept at least two orders of magnitude above the vapour pressure of Cu (Figure A1 in Appendix) by mainly controlling the pumping rate and introducing Ar for most of growth experiments in order to minimize sublimation of Cu.[349] Other than these restrictions,

ranges of growth conditions were set to be as wide as possible in order to maximize the applicability of the interpretation of the results. The conditions of all of the experiments performed throughout the study are summarized in Table A1 in Appendix.

| Growth Parameters | Range of Parameters |
|---|---|
| Annealing temperature | 650 - 1070 ˚C |
| Annealing pressure | 0.08 mbar - 1000 mbar (atmospheric pressure) |
| Annealing time | 10 seconds to <10 hours |
| Growth temperature | 650 - 1070 ˚C |
| Growth pressure | 0.08 mbar - 1000 mbar (atmospheric pressure) |
| Growth time | Flash exposure (< 3 sec) to <10 hours |
| $P_{CH4}$ | 0.0001 mbar to 30 mbar |
| $P_{H2}$ | 0.1 mbar to 10 mbar |
| $P_{Ar}$ | 0 mbar to 10 mbar |
| Cu surface roughness | As-received vs. electropolished |
| Cu crystal orientations | Single crystal (100), (111), and high index orientations |
| Cu purity | 99.8% (low purity) to 99.999 % (high purity) |
| Heating rate | Normal (~ 30 ˚C / min) or rapid |
| Cooling rate | Normal (by natural cooling of furnace) or rapid |

**Table 3** Range of main experimental growth parameters that were investigated.

The effect of each parameter on the growth process can be systematically distinguished by varying one parameter at a time while the rest of the parameters remain fixed. The main results of this parametric study will be presented in the next chapters and they will form basis for developing the model of graphene growth on Cu.

### *4.4 Preparation of Cu Substrates*

We have employed four different kinds of Cu foils: 1) 0.127 mm thick copper foil of 99.9 at. % purity (Alfa Aesar #13380); 2) 0.025 mm thick copper foil of 99.8 at. % purity (Alfa Aesar #13302 lot H18W024); 3) another 0.025 mm thick low purity copper foil of 99.8 at. % purity using a different manufacturing process (Alfa Aesar #46986); 4) 0.025 mm thick high purity copper foil of 99.999 at. % purity (Alfa Aesar Puratronic® #10950) (Note: #13302 0.025 mm thick Cu foils other than lot H18W024 are electrochemically coated with a thin film of chromic oxide[184] which is difficult to remove without electrochemical polishing and Alfa Aesar has recently created a new catalogue number, 46365 for the same Cu foil without the chromic oxide plating to be used for graphene growth). Additionally, single crystal Cu(100) and Cu(111) discs were used (Surface Preparation Laboratory, Netherlands 99.9999 at. % purity). In order to prepare them for the graphene growth, the substrates were

always cleaned by a sonication bath in acetone for 15 min followed by sonication bath in ethanol for 15 min, and dried quickly by blowing compressed argon gas or dry air.

Acid treatments mainly by acetic acid were used to minimize surface contaminations, in particular CuO and $Cu_2O$ that may hinder the nucleation of graphene. In this treatment, Cu samples were immersed in 100 % acetic acid (VWR) at room temperature for ~ 15 min and they were immediately loaded into the tube furnace for the growth. This has been shown to improve graphene morphology by removal of oxide particles.[350]

Surface defects on Cu surfaces such as scratches and rolling features have been shown to create additional nucleation sites for graphene growth.[176] In order to obtain smooth surfaces and remove the extrinsic surface defects such as rolling features and scratches of Cu foils, the copper foils were electropolished. One side of Cu foil was coated with a polymer and immersed in a stainless steel beaker of poly(ethylene glycol) (molecular weight, 400 from Sigma Aldrich) and phosphoric acid solution (1:3 volume ratio).[176] Stainless steel tweezers were used to make electrical contact to the Cu foil that was used as the anode, and the stainless steel beaker was used as cathode. Voltage of ~1.9 V was applied on the foil for 30 min by a DC power supply. After the electropolishing, the foil was immediately rinsed in water and cleaned in ultrasonic bath of acetone and ethanol.

In order to make the surface of the foils even smoother and as flat as possible, annealing and mechanical polishing were sometimes employed before electropolishing. The Cu substrates were annealed in a tube furnace for an hour at a temperature above 1030° C in the 10 vol% $H_2$ and 90 vol% Ar mixture in the atmospheric pressure. For mechanical polishing, the Cu foils were mounted in a Cu cylinder and mechanically polished by polishing discs (with Agar B8223 selvyt cloth, dia. 250 mm) for several cycles using alumina suspensions of successively finer particle sizes (1 μm, 0.3 μm, and 0.05 μm). After the mechanical polishing, the sample must be electropolished to remove residual alumina particles which are difficult to remove using an ultrasonic bath.

In order to re-use the single crystal Cu discs, after characterizing the obtained graphene film, it was removed by $O_2$ plasma etching (Solarus Model 950), and the substrate was electropolished as described above.

### 4.5 Typical growth procedure

To give an example of the step-by-step growth procedure, typical CVD conditions employed in the study (especially in Chapter 7) are used here. The Cu substrate was placed inside a quartz tube that was loaded into the horizontal cylindrical furnace. The quartz tube was then evacuated by a rotary pump to a base pressure of ~$1 \times 10^{-3}$ mbar, and 100 sccm of Ar was introduced into the chamber for 30 min to replace air before heating the furnace to annealing/growth temperature of 720 ℃ - 1000 ℃ (Figure 31). Next, Ar was shut off, and 5 sccm of $H_2$ ($P_{H2}$ ~ 4 mbar) was introduced. The furnace was heated according to Figure 33 to an annealing temperature of 1030 ℃ (or some other set temperature; refer to Table A1). After annealing with the same $H_2$ flow rate for 30 min, the temperature of furnace was changed to the growth temperature of 1000 ℃, and $CH_4$ was introduced to the furnace at the flow rate of 0.5 sccm ($P_{CH4}$ ~ 0.4 mbar; total growth pressure = 4.1 mbar) to start the growth once the temperature became stabilized. After the growth time between 1 sec (flash exposure) and 30 min, the methane flow and power to the furnace were shut off, and the sample was allowed to cool down naturally inside the furnace with the hydrogen flow rate of 5 sccm.

In order to reduce the density of nuclei and increase the size of a graphene nucleus further, an enclosure method modified from the one employed by Li et al.[190] was used to obtain grain of ~ 100 μm in lateral size at the growth temperature of 1070 ℃. Instead of making the enclosure entirely of the copper foil, the substrates were placed inside an alumina crucible (Almath), and its opening was covered by a copper foil. This modification prevents the copper substrates from bonding to the Cu enclosure at elevated temperatures.

### 4.6 Transfer of Graphene

Graphene samples grown on Cu were transferred onto different substrates for further characterization such as Raman spectroscopy or XPEEM. We have followed the procedure that were outlined by X. Li et al.[255] to transfer graphene. The polymer support, Poly(methyl methacrylate) (PMMA) dissolved in anisole (MicroChem) was spin-coated at a spin speed of 3500 rpm for 1 min on the as-grown graphene film on Cu foil. Afterward, the Cu foil was etched in a solution of $FeCl_3$ (Sigma Aldrich) (3.5 g) dissolved in DI water (100 mL) + HCl (10 mL) solution. Alternatively, 5.7g of ammonium persulfate [$(NH_4)_2S_2O_8$] mixed in 250 mL of DI water was used as an etchant. A free standing PMMA/graphene film floating on the water bath was obtained after a few hours of Cu etching. Several washing cycles in DI water

were necessary to eliminate the residual of $FeCl_3$. The freestanding graphene/PMMA membrane was transferred onto glass slides, $SiO_2$/Si, quartz, or Au/mica substrates for further characterizations. Following the transfer, the PMMA was dissolved in an acetone bath at ~40 ℃ for 30 min. Here, applying a PMMA film with the right thickness (~ 300 nm; by controlling the spinning speed) and using several washing cycles in DI water were crucial in obtaining clean and uniform transferred films as inspected by optical and scanning electron microscopies. Additionally, some of the transferred graphene samples were cleaned further in a tube furnace by annealing in an inert atmosphere (Ar) for > 1 hour at a temperature greater than 300 ℃.

## *4.7 Conclusion*

The complex methodologies for the CVD study of graphene and our choice of growth conditions to understand the graphene growth process have been outlined in this chapter. The careful selection of growth conditions, finding appropriate preparation techniques for the Cu surface prior to the growth, and employing clean transfer procedures were among the most critical aspects in the experimental methods of the study.

# 5 Characterization Techniques

## 5.1 Introduction

Understanding the growth mechanism and performing quality control of atomically thin films of graphene require a set of sensitive, state-of-art characterization techniques to obtain critical information regarding its morphology, structure, and chemistry of the sample. In this chapter, various microscopic, crystallographic, spectroscopic techniques as well as optoelectronic property measurement techniques that have been used together to analyse the solution-processed and CVD graphene (as-grown and transferred) samples are described.

## 5.2 Field Emission Scanning Electron Microscopy

Scanning electron microscopy (SEM) was one of the most frequently employed characterization techniques in this work to probe the morphology of the CVD graphene samples (Figure 34a). It enables easy imaging of the surface topology over a large area with high resolution to determine the presence, coverage, uniformity, and thickness of graphene. This is especially true for a field emission gun SEM (FESEM) where the field emission gun is used for electron source that produces electron beam with the incident beam spot size (< 5 nm[351] on a flat surface) generally much narrower than SEMs equipped with conventional filament based guns.

SEM imaging is performed by raster scanning the sample surface by a high energy (1-30 keV), focused electron beam in high vacuum (< $2 \times 10^{-5}$ mbar) to low vacuum in environmental SEM (~ 10 mbar).[352] The beam becomes scattered at the surface to be picked up by the electron detectors close to the sample. The scattering of electrons can be categorized largely into either elastic (backscattered) or inelastic (secondary) depending on the nature of the interaction of the incident beam with the sample. In backscattered electron (BSE) imaging mode, electrons that are elastically scattered are used to form an image. However, due to the large interaction volume (Figure 34b), the resolution using this mode is limited to 10 - 100 nm. Whereas, in secondary electron (SE) imaging mode, the interaction

volume is much less due to its low energy, making resolution of the imaging in the order of 1- 10 nm.

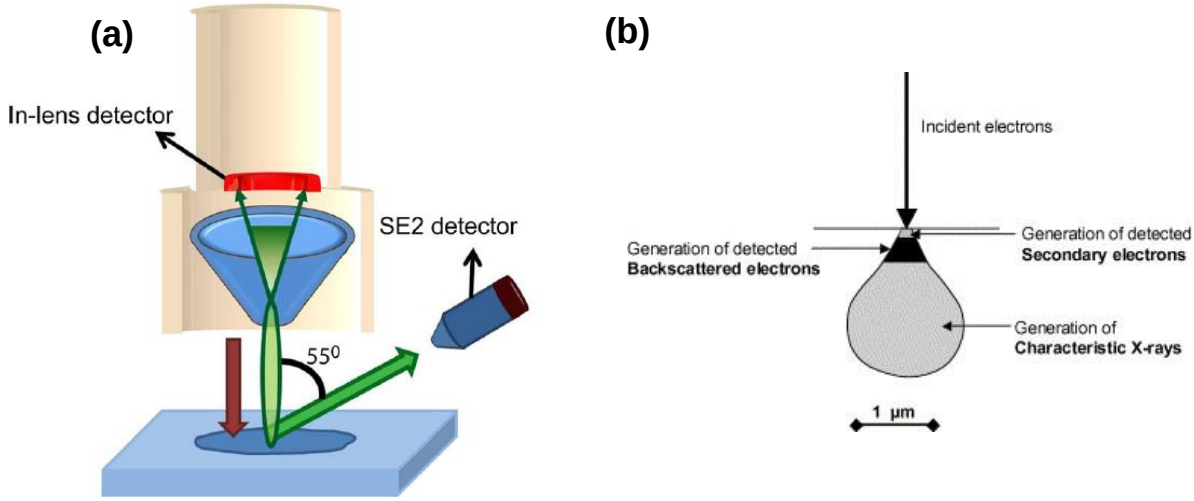


**Figure 34** (a) Schematic illustrating the SEM setup used to image graphene samples (indicated by the brown arrow).[353] (b) Cross section of interaction volume of incident electron underneath sample surface.[354]

As the graphene growth occurs only at the surface level, the samples were typically imaged using SE mode. It must be noted that the FESEM (Gemini 1525 FEGSEM) was equipped with two electron detectors: (1) one standard SE detector that was located away from the lens facing the sample surface at an angle, and (2) in-lens detector that was embedded in the electron lens that directly faces the sample surface. Due to the proximity of the in-lens detector and the sample surface and high sensitivity to low energy electrons (< few tens of eV), the in-lens image produces very sharp thickness contrast for the thin graphene layers (< 10 layers) on the sample surface.[353] As a result of the larger attenuation of the reflected electrons in thicker graphene film, the thinner layers of graphene appear much lighter than thicker layer, and it can give an enough contrast to distinguish the thickness, layer by layer. The acceleration voltage of the incident electron, $V_{HT}$ was chosen to be 5 – 10 kV. Although even lower $V_{HT}$ (1 kV) is preferred for the highest contrast,[353] the stability and the resolution of the image was optimized at higher voltages (5 – 10 kV) due to the instrumental limitations of the system that result in blurry and highly noisy images at $V_{HT}$ < 5 kV. The low voltage is also beneficial toward reducing the electron beam damage and charging of the sample surface which become significant at high magnification (more than 20,000 X).[355]

### *5.3 Electron Backscattered Diffraction*

Electron backscattered diffraction (EBSD) technique is one of the complementary characterization tools of SEM that can be used within the same experimental setup of the SEM. The technique has been used extensively to study the Cu substrate texture, and epitaxial relationship between the individual crystal orientation of the Cu substrate and thin film of CVD graphene grown on the substrate.

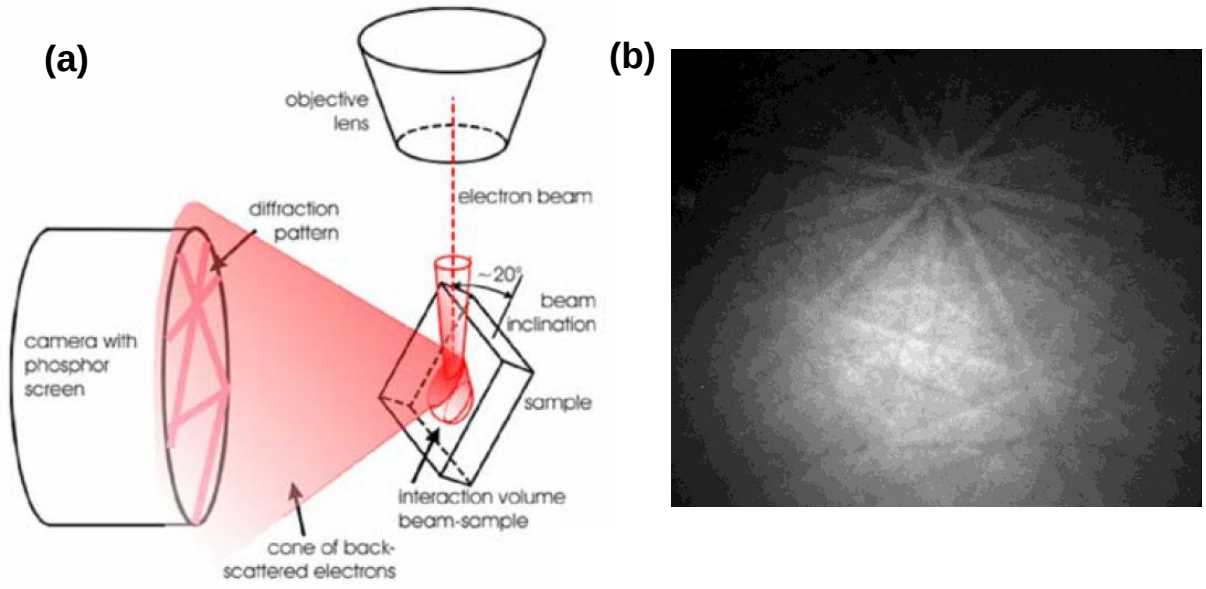


**Figure 35** a) Schematic of EBSD setup within the SEM chamber.[356] b) An example of Kikuchi pattern projected on the phosphor screen acquired by the CCD detector.[357]

In EBSD, the BSEs that are reflected from the crystalline surface form a diffraction pattern known as Kikuchi bands which are detected by a phosphor screen equipped with CCD camera (Figure 35). If the crystal structure and dimensions are already known and specimen surface is fixed respect to the electron beam and the camera, the Kikuchi band patterns can be deconstructed to give the relative crystalline orientations of the surface. Since the BSEs have interaction volume of 10 - 100 nm depending on the material and beam energy, EBSD is applicable for the crystal orientation determination of thick layers (10 - 100 nm) only and cannot be used to determine the crystallinity of atomically thin layers deposited on much thicker substrates. The most advantageous feature of EBSD over other crystallographic techniques such as X-ray crystallography and TEM selected area diffraction is that it can perform spatial mapping of crystallographic orientations of sample over large areas with

spatial resolution of approximately 10 – 50 nm[358] which then can be correlated with the morphological information obtained by the SEM imaging.

Throughout the study, Oxford EBSD detector and hkl Analysis Software package were used for the technique to probe crystal orientation of the substrate. For the measurement, $V_{HT}$ = 20 kV was used and the sample was mounted with 70° tilt to allow the BSEs to be projected onto the phosphor screen (Oxford Instruments). One of the limitations of EBSD is that the surface must be relatively flat for accurate orientation measurement. Performing EBSD on Cu foil sample can be difficult as it exhibits the rolling features and considerable surface roughness due to the manufacturing process. The rolling features must be the aligned with the direction of the tilt in order to minimize roughness induced scattering and distortion. The error in the angle of experimental crystalline orientation of the surface plane analysed by the EBSD technique was estimated to be less than ±5 °.

The crystalline orientations are commonly illustrated in terms of pole figures and the collection of the pole figures from a large area of the sample gives the texture of the sample. Mainly the low Miller index pole figures, (100), (110), and (111) in the case of FCC material such as Cu and Ni are often reported in literature to illustrate the angle of misorientation from the surface to the main low index planes.

### *5.4 Micro-Raman Spectroscopy*

Micro-Raman spectroscopy is one of the most versatile, non-destructive, and high-throughput methods to identify and characterize graphene thin films. In this work, the main uses of the technique involved the identification of graphene structure, thickness, defects, and stacking order of multilayers. The ambient condition of the measurement without much need for sample preparation allows the facile acquisition of the Raman spectra with the lateral scale and resolution of optical microscopy (~ 1 μm).

The Raman process is an inelastic scattering of light where the incident light interacts with lattice vibrations (phonons). It can involve either emission (Stokes scattering) or absorption (anti-Stokes scattering) of phonons.[359] The loss of incident light energy, $E_L$ (usually fixed in the visible – UV light range) leads to shift in the wavelength of the scattered light (measured in $cm^{-1}$) which depends on the electronic structure and phonon dispersion of the specimen. The detailed theory of Raman spectroscopy of graphene and its related

structure is far too complicated and beyond the scope of current work. In this section, we give description of the apparatus and briefly discuss the main features of Raman spectra of mono to few-layer graphene that are relevant to the structural characterization of the solution-processed and CVD graphene films.

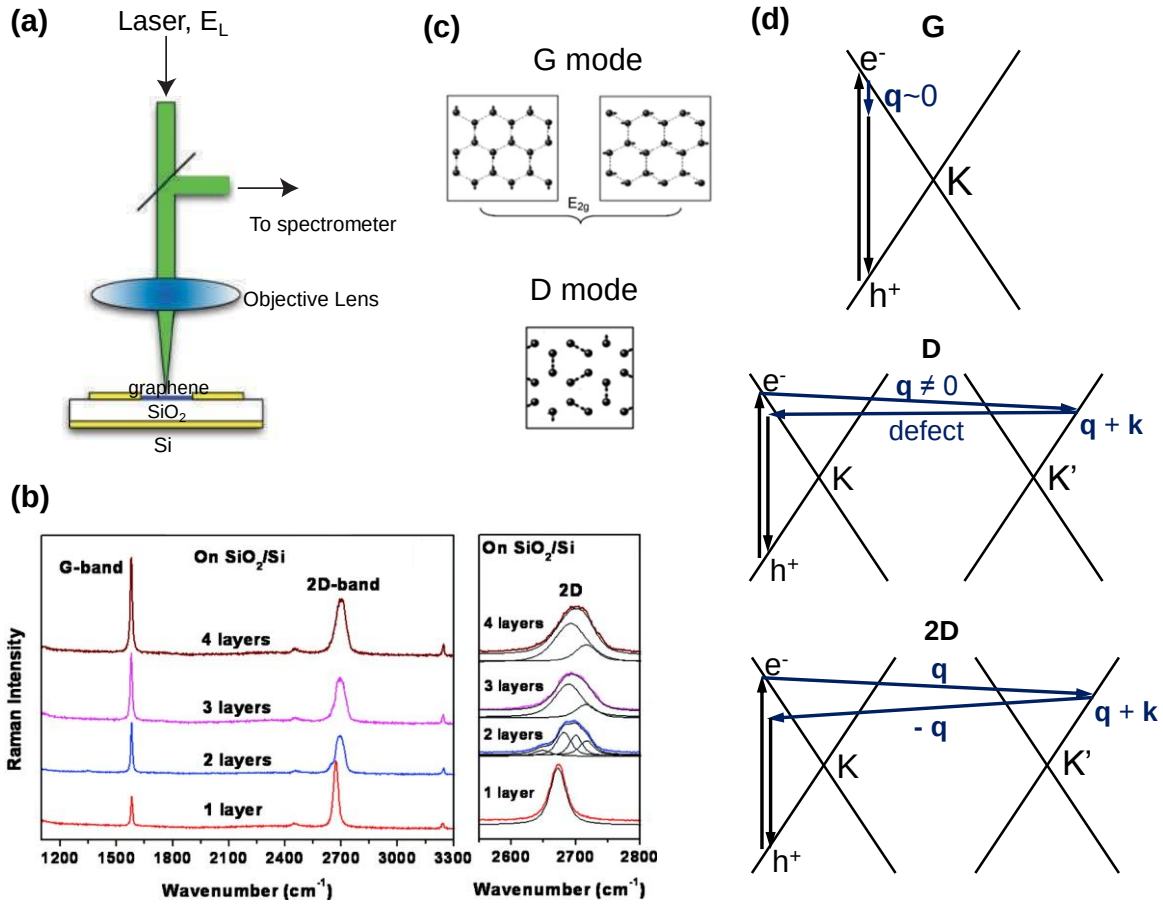


**Figure 36** (a) Basic schematic of Raman spectroscopy setup on a graphene based structure.[360] (b) Raman spectra of graphene with different number of layers.[361] (c) Illustration of the main vibrational modes of graphene lattice (G and D).[361] (d) Phonon scattering mechanism for G, D and 2D bands in the graphene dispersion relationship near K and K' points.

Figure 36a illustrates the basic experimental setup of micro-Raman spectroscopy system for the measurement on a graphene structure placed on a substrate. The model of the system used in this work was Reinshaw inVia Raman spectrometer system. Typically, a single energy of either $E_L$ = 1.96 eV ($\lambda_L$ = 633 nm) or 2.41 eV ($\lambda_L$ = 514 nm) was used as the excitation energy of the laser beam because these wavelengths have been commonly used for $sp^2$ carbon materials due to the large scattering cross-section, giving high signal-to-noise ratio. Other than the common laser energies, $E_L$'s from 1.9 eV to 3.5 eV have been used especially

for the phonon dispersion study of graphene.[362,363] The Raman spectra were acquired by filtering the scattered light through a monochromator over the range of 1000 to 3000 $cm^{-1}$ with a resolution of ~ 1 $cm^{-1}$. The counts and intensity of the excitation laser light (10 - 50 mW) were adjusted so that the balance of signal-to-noise ratio, laser irradiation induced damage of the sample, and acquisition time were optimized. In a micro-Raman system, the system is coupled with an optical microscope to image and perform Raman measurement on the same area. The spatial resolution is about 1 μm, which is limited by the size of the focused laser beam on the sample due to the diffraction of light. Our system also contained a motorized stage that can automatically capture a map of Raman spectra in the x and y directions.

The most prominent features that are commonly found in the Raman spectra of graphene are G, D, and 2D bands[364] as displayed in Figure 36b. The G band peak is found at ~ 1582 $cm^{-1}$ with $E_L$ = 2.41 eV and is related to the doubly degenerate $E_{2g}$ mode (Figure 36c) which is a first order Raman scattering process (only one phonon is involved). It is a non-dispersive mode (Figure 36d) where the peak position is mostly independent of $E_L$ (except for highly defective graphene).[363] The disorder-induced D band is at ~1350 $cm^{-1}$ when $E_L$ = 2.41 eV, and it is related to the radial breathing mode of the $sp^2$ rings and this process is symmetrically forbidden in ideal graphene lattice unless the electron/hole is scattered by a defect through a doubly resonant, fourth order process.[365] For the activation of the D band, an incident photon from the laser generates an electron-hole pair (i); the electron with lattice momentum, k, is scattered by a phonon with a momentum q ~ K (ii); then elastically scattered by a defect near K' point (iii); and finally, recombines with a hole (iv). Because of the linear phonon dispersion relationship for the Raman active, longitudinal optical (LO) phonon with a Khon anomaly at the K point, the position of D peak is strongly dispersive with $E_L$ (~50 $cm^{-1}$ /eV).[365-367]

The D band intensity to the G band intensity ratio [I(D)/I(G)] serves as an indicator for degree of disorder.[365,368] Traditionally, the relationship between I(D)/I(G) has been described by the Tuinstra and Koenig relation in nanocrystalline graphite where I(D)/I(G) is inversely proportional to the mean grain size, $L_a$.[369] This relation is expected to be held until $L_a$ ~ 2 nm where the significant proportion of ideal $sp^2$ rings within the sample starts to decrease to reduce I(D)/I(G). Recently, vacancy-like defects with the mean inter-defect

distance, $L_D$, has been shown to give rise to D peak with relationship, $I(D)/I(G) \propto 1/L_D^2$ for $L_D > 10$ nm.[363] Below $L_D \sim 10$ nm, I(D)/I(G) still increases till about $I(D)/I(G) \sim 14$ at $E_L$ = 2.41 eV and decreases as $I(D)/I(G) \propto L_D^2$ for $L_D < 3$ nm.

In low defect regime, where I(D)/I(G) increases with the degree of disorder, it has been recently shown that by comparing I(D) with the intensity of another small defect related, D' peak I(D') at ~1620 $cm^{-1}$, which is generated by the intravalley process, the nature of defect can be identified as vacancies [where $I(D)/I(D') \sim 7$], $sp^3$ functionalization induced defects [$I(D)/I(D') \sim 13$], and grain boundaries [$I(D)/I(D') \sim 3.5$].[370] Since a typical graphene sample in a real condition cannot contain purely one type of defects, the precise identification and quantification of the defects, however, still remain as a challenge. It must also be noted that the D peak cannot identify other kinds of disorder that are not Raman active, but still may degrade the electronic properties of graphene. They include zigzag edges, physically adsorbed dopants, and uniaxial and biaxial strains.[363]

The 2D band (also known as G' peak) which occurs at twice the frequency of D peak (~ 2700 $cm^{-1}$ at $E_L$ = 2.41 eV) corresponds to the overtone of D band.[365] This process involves two electron scattering events by phonons of opposite momentum (**q**, **-q**) so that the total momentum is conserved. This makes the 2D band Raman active even for a defect free graphene lattice with $E_L$ dependent dispersive relationship (~ 100 $cm^{-1}$/eV).[371] The shape of the 2D peak is a very useful indicator to identify stacking order and thickness of the graphene layers. The monolayer has a single Lorentzian 2D peak with a narrow FWHM (~25 $cm^{-1}$).[372] For turbostratic multilayers the peak tends to get broader (FWHM > 40 $cm^{-1}$) and shifted toward higher wavelength (> 10 $cm^{-1}$).

In AB stacked FLG where the interlayer interaction is more significant, the 2D peak can be de-convoluted into four Lorentzian peaks with FWHM of ~ 24 $cm^{-1}$ due to the splitting of the electronic band structure in valence and conduction bands.[372] The evolution of the 2D bands can be a useful indicator for the thickness identification of AB stacked multilayer as shown in Figure 36b. For higher thicknesses (> 10 layers), 2D band approaches that of natural graphite which is described by a convolution of two Lorentzian peaks.

In the case of G band, the $E_{2g}$ modes are no longer degenerate in FLG and split into the symmetric ($E_g$) and anti-symmetric ($E_u$) modes leading to the G peak broadening or splitting especially for supported or doped FLG.[372]

Raman spectroscopy also can determine the degree of mechanical strain and doping in monolayer graphene. In the case of CVD graphene, which is produced at a high temperature, a large biaxial compressive stress is induced during cooling due to the mismatch between the thermal expansion coefficients of the graphene overlayer and substrate. The 2D and G peak will blue-shift by up to ~30 $cm^{-1}$ and ~20 $cm^{-1}$, respectively with biaxial strain of -0.5 % as determined by the CVD graphene grown on Cu at high temperature (> 1000 °C).[373]

Doping can always be present in graphene due to the wet processing, substrate, unintentional contamination, air, moisture, and substrate that lead to changes in the Raman spectra.[367,374] Das et al.[360] has observed the shifts in the G and 2D peaks by electrochemically doping graphene in a top-gated structure where the 2D peak is blue-shifted by up to 15 $cm^{-1}$ by p doping ($n_h$ ~ 3 x $10^{13}$ $cm^{-2}$), and red-shifted by up to 10 $cm^{-1}$ with n-doping ($n_e$ ~ 3 x $10^{13}$ $cm^{-2}$). On the other hand, G peak always blue-shifts upon both types of doping (~20 $cm^{-1}$ when $n_e$ = 3 x $10^{13}$ $cm^{-2}$). The ratio I(G)/I(2D) and the FWHM are to also increase due to doping.

Recently, for twisted multilayers, misorientation angle dependent symmetry conditions have been shown to generate additional double resonance Raman scattering process resulting in additional Raman peaks near the D peak. They are called either R band[375] or I band.[376-378] These peaks have an important implication in the study of multilayers produced by CVD or solution-processed films where stacking orders different from Bernal stacking are present. In addition to the R band, also recently, C band has been found at a very low wavenumber (30 – 50 $cm^{-1}$) which arise from in-plane $E_{2g}$ shear mode and it tends to red-shift with increase in number of graphene layers due to the interlayer interactions.[379]

### *5.5 Atomic Force Microscopy*

The atomic force microscopy (AFM) is one of most commonly used probe-tip based nanoscale imaging techniques with extremely high resolution down to the atomic scale. This technique has been used to obtain three-dimensional topology of as-grown graphene on Cu and graphene transferred onto thermally oxidized Si wafers ($SiO_2$/Si) and measure the surface roughness of the samples.

Basic operating principle of AFM is illustrated in Figure 37. The microfabricated cantilever tip's movement is controlled by piezoelectric actuators that are regulated through a

feedback mechanism. The feedback mechanism is governed by the proportional-integral differential (PID) controller which uses the signal from a photodiode that detects the laser light reflected off from the head of the cantilever tip. In contact mode, one of most frequently used operational modes in AFM, the tip touches the surface with a constant contact force (in the order of nN) while the deflection of the tip is monitored by the feedback mechanism. This gives three-dimensional surface profiles that can be used to monitor the thickness and morphology of the surface. Another frequently used AFM mode is tapping or intermittent contact mode. Here, the tip oscillates with frequency in order of 100's of KHz in and out of contact momentarily with the surface to map the surface topology. This mode is particularly useful toward studying the surface of fragile and soft samples including graphene where damage and distortion of the sample surface are minimized. The shift in the phase of oscillation of the tip due to the damping of the oscillation by the surface of different mechanical properties also provides complementary information as a phase image of the spatial distribution of materials with different mechanical properties alongside the 3D height image. The disadvantage of the tapping mode is that longer acquisition time is often required compared to the contact mode AFM and the oscillation of the tip can induce additional surface deformations and artefacts.[380]

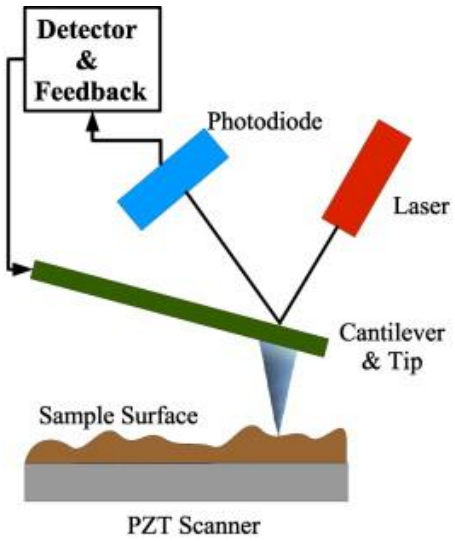


**Figure 37** Illustration of atomic force microscopy setup.[381]

The lateral resolution of AFM is typically limited by the tip radius and the condition of the tip. The typical materials used in the tips are silicon and silicon nitride, which have high hardness and stiffness. The radius of curvature of typical $Si/Si_3N_4$ based tip is not usually sharper than 2-3 nm. In ambient conditions, the maximum lateral resolution of 5 nm can be

achieved.[381] However, tips can easily worn out and attract small loose particles reducing the lateral resolution. Artefacts and ghost images can be seen in an AFM image produced by a damaged tip which needs replacement. The height resolution in the vertical direction is expected to be as small as Angstroms, however, due to the effect of surface adsorbates in ambient condition, the measured thickness can be much thicker than the actual thickness.[364] Therefore, a caution must be exercised when determining number of layers of multilayer stack of graphene as it can overestimate the thickness. Other practical limitations of AFM are the low scan speed, smaller scan area (typically < 100 μm × 100 μm) compared to SEM and optical microscope, and difficulty in imaging large features with height differences greater than 1 μm.

The AFM instrument used in the study was manufactured commercially by Veeco (Model name: NanoScope Multimode AFM) and all the measurements were performed in ambient conditions. The model names of the tips used were AFM Si tip NSC15 (tip radius, 10 nm) for tapping mode and CSC (tip radius, 10 nm) for contact mode.

### *5.6 X-ray Synchrotron Techniques: Low Energy Electron Microscopy and Photoemission Electron Microscopy UV-Vis Optical Transmittance/absorbance Spectrophotometry*

Low energy electron microscopy (LEEM) is a powerful UHV surface imaging technique that is aided by a versatile range of complementary tools that can be used within the same system for simultaneous imaging and analysis. This setup was used to analyze the thickness dependent morphology, crystalline orientations of graphene domains (using low energy electron diffraction), and stacking order of graphene thin films as grown on Cu, and transferred onto Au and $SiO_2$/Si substrates. The LEEM and the complementary techniques discussed were performed by A. Locatelli and T. O. Menteş in the Nanospectroscopy beamline at Elettra Synchrotron light source, Trieste, Italy.[382]

In LEEM (Figure 38a), the high energy electrons (15 – 20 keV) produced by electron gun ($LaB_6$) is passed through series of condenser lenses, deflected by the magnetic separator, and decelerated to much low kinetic energy (1 – 100 eV) as it moves toward the sample that is held at a negative potential. Due to the short inelastic mean free path of low energy electrons in most of materials, the incident electrons are backscattered from only a few top atomic layers at the surface of the samples. The elastically backscattered electrons reflected

from the surface are deflected by the magnetic beam separator and projected onto the imaging plane through the electron-optics and energy filter. If the specularly reflected electron beam is used form the real space image, the operation mode is called bright field imaging (Figure 38b). For crystalline sample, the diffracted beam can be used to give the low energy electron diffraction (LEED) patterns (Figure 38c), the 2D reciprocal space of the surface. Specifically selecting the primary or secondary LEED beam that has undergone a finite parallel momentum transfer provides dark field images, which enable a selective view of crystalline domains of particular interest.

In the bright field imaging mode of LEEM, the lateral resolution is < 10 nm and the field of view (FOV) can be as large as a few tens of μm. For μLEED measurement, the aperture size can be reduced to area less than 1 μm in diameter. Since the intensity of the reflected beam is usually high the imaging by LEEM does not require a long acquisition time allowing *in-situ* analysis of surface processes in real time, for example, in-situ growth of graphene[204] and etching/doping of graphene on metal substrates.[383]

Moreover, for very thin films such as graphene layers thinner than 10 ML, the low energy electrons (<10 eV) can exhibit quantum well resonance with oscillations in the reflected electron intensity with the incident electron energy that leads to N dips (and N-1 peaks) in the oscillation for N number of atomic layers.[384,385] This observation has been used in many occasions to determine the thickness and illustrate thickness distribution of thin films in energy dependent LEEM imaging.

Photoemission electron microscopy (PEEM) is a complementary technique to LEEM where the electron gun is replaced by a light source of high energy. The purpose of the technique in this study was to identify any surface contaminants before and after the growth and after the wet transfer process. This technique was also used to locally probe the electronic structure of the samples (through angle resolved photoemission spectroscopy) on as-grown graphene on Cu and transferred graphene on Au and $SiO_2$/Si substrates.

The light source of PEEM was a highly collimated, high energy radiation (soft X-rays; from 40 eV up to 1000 eV) generated by a synchrotron light source. As the beam hits the sample surface electrons are emitted from the surface by the photoelectric effect.[386] The emitted electrons are collected by the same set of electron optics used by the LEEM to form a PEEM image to provide photoemission spectra (PES) commonly obtained in ultraviolet

photoemission spectroscopy (UPS) and X-ray photoemission spectroscopy (XPS) with spatial resolution smaller than 30 nm (Figure 38d). This provides a rich set of information regarding the surface composition, chemical states, and density of states as a function of binding energy below the Fermi level with energy resolution of ~300 meV.

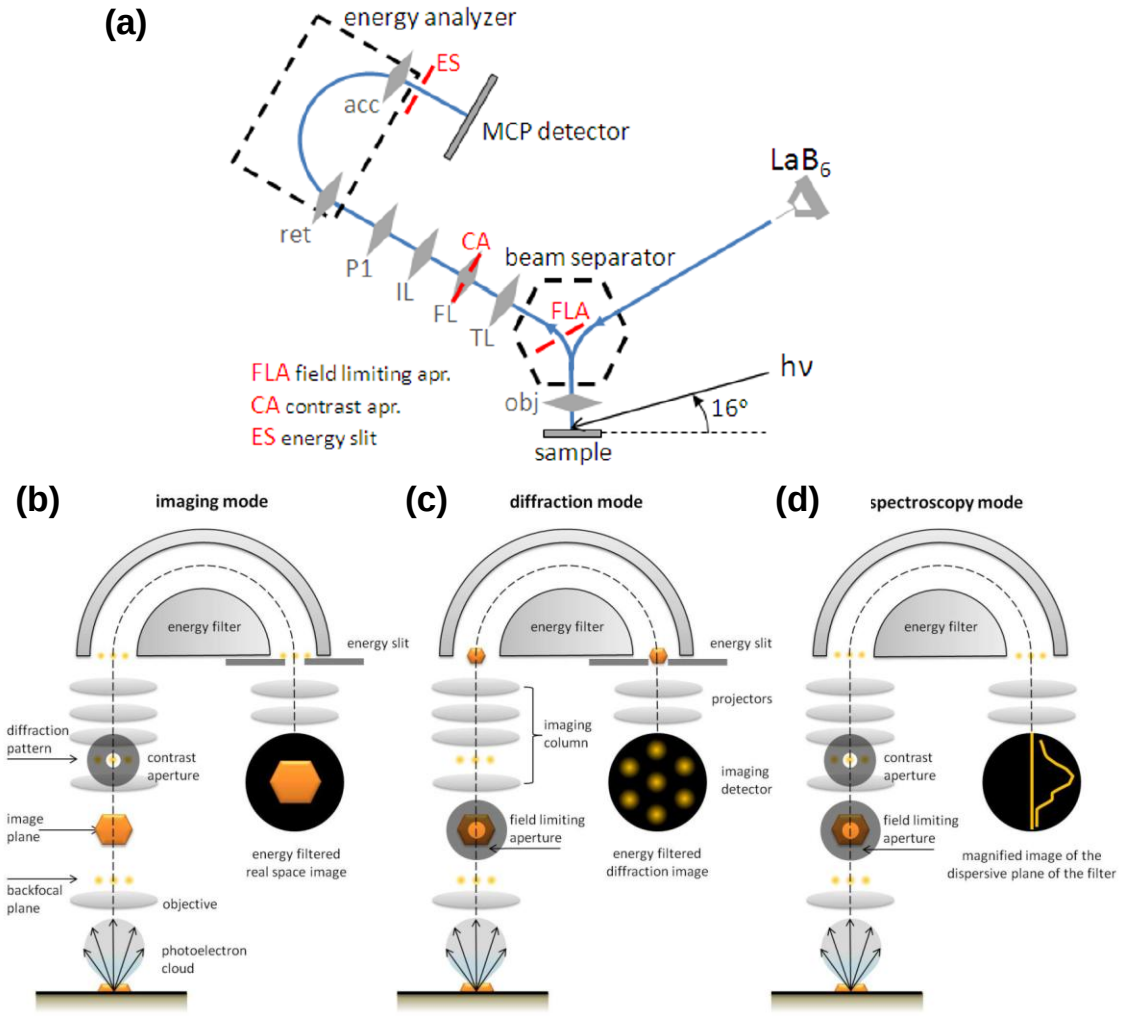


**Figure 38** a) Schematic of the LEEM/PEEM setup. The energy slit, the contrast and field-limiting apertures, are marked in red. The lenses depicted are the objective (obj), transfer (TL), field (FL), inner (IL), projector-1 (P1), accelerating (acc) and retarding (ret) lenses.[387] b-d) Various operation modes of LEEM/PEEM: b) bright field imaging. c) dark field/ diffraction imaging. d) micro probe XPS).[388]

In a similar manner as LEED, the emitted electrons with finite momenta parallel to the surface can be selectively detected and analyzed to give a map of the electronic band structure along the high symmetry crystal planes in angle resolved photoemission

spectroscopy (ARPES). In the case of non-uniform samples, selected area or μARPES can be performed by introducing field limiting aperture to the image plane to reduce the probed area down to ~1 μm in diameter.

ARPES is an excellent tool to directly probe the two-dimensional electronic structure of graphene below the Fermi level. The main point of interest is a direct observation of the Dirac cone in the valence band near K point of graphene's reciprocal space along the M-K-Γ direction. As the shape of the cone changes with the number of layers, stacking orientation, substrate-graphene interaction, and crystal quality, ARPES provides a rich set of complementary information for determining the electronic and structural property of graphene thin films.[389]

### *5.7 UV-Vis Optical Transmittance/Absorbance Spectrophotometry*

The optical transmittance/absorbance properties are characteristic of light's interaction with the electronic structures and scattering centres within the material. It holds a practical importance when transparency in the visible range of electromagnetic spectrum is concerned. Moreover, the thickness and concentration of light absorbing solvents can be determined by the transmittance measurement. In the present study, the transmittance/absorbance measurement was performed on the graphene thin films on transparent substrates (glass slides) to assess the optical transparency in the UV-visible range and on graphene dispersion in NMP placed in Quartz cuvette to determine the concentration of graphene dispersed in the solvent.

The model of the instrument was Ocean Optics S2000-UV-Vis. In this experimental set-up, a white light produced by a halogen lamp was transmitted through the thin film sample, and after substrate background subtraction, the intensity of transmitted light was measured in terms of wavelength (from 300 nm to 800 nm) by a diffraction grating equipped with a CCD camera which has a spectral resolution of ~ 1.5 nm.

For the determination of concentration of light absorbing solute in a solution, the absorbance of solution placed in a quartz cuvette was first measured. Then, the concentration is related to the absorbance according to the Beer-Lambert's Law,

$$A = \ln \frac{I_I}{I_T} = \alpha c l \qquad (10)$$

where $A$ is the absorbance of solution, $I_I$, intensity of incident light, $I_T$, intensity of transmitted light, $c$, concentration of solute, $l$, path length of light (width of the quartz cuvette, 1cm), and $\alpha$, the absorptivity of the dispersion at a given wavelength. For instance, the absorptivity of graphene dispersion in NMP at the wavelength of 660 nm is $<\alpha_{660}>$ = 2,460 L/gm.[13]

Similarly, for the thin metallic film of thickness smaller than the wavelength of incident light, the absorbance can be described by the equation:

$$A = \alpha' t \qquad (11)$$

where $\alpha'$ is the thin film absorption coefficient and $t$ is the thickness of the film. In this limit, absorption coefficient can also be related to the optical conductivity, $\sigma_{op}$ by[390]:

$$\alpha \approx \frac{Z_0 \sigma_{op}}{2} \qquad (12)$$

where $Z_0$ is the impedance of free space (376.7 Ω).

For ideal graphene films, $\alpha'$ is equal to 0.0297 $nm^{-1}$[58,391] in the most of the visible range determined by the fine structure constant which is related to a fundamental unit of conductance.

### *5.8 Two-Probe Electrical Conductivity and Mobility Measurement*

One of most commonly used techniques to assess the electrical properties of graphene is to probe field effect properties of a back gated field effect transistor (FET) structure of a graphene thin film deposited on a $SiO_2$/Si wafer substrate (Figure 39a). Here, highly p-doped Si(100) substrate acts as the back gate, below a thermally grown $SiO_2$ with thickness of 300 nm, which acts as a gate dielectric. On top of the graphene layer, two Au electrodes (source and drain) were deposited with thickness of > 30 nm by thermal evaporation of Au wire through patterned shadow masks. The distance between the electrodes or the channel length, L, was 20 μm, and the length of the electrode or the channel width, W, was 500 μm.

The conductivity ($\sigma_{DC}$) of graphene thin films within the channel disregarding the edge effects can be calculated by:

$$\sigma_{DC} = \frac{LG_{DC}}{tW} = \frac{L\Delta I_{DS}}{tW\Delta V_{DS}} \qquad (13)$$

where $G_{DC}$ is the DC conductance of the channel, $I_{DS}$, current between the source and drain electrodes, $V_{DS}$, voltage applied between the source and drain electrodes, and *t*, the thickness of the thin film.

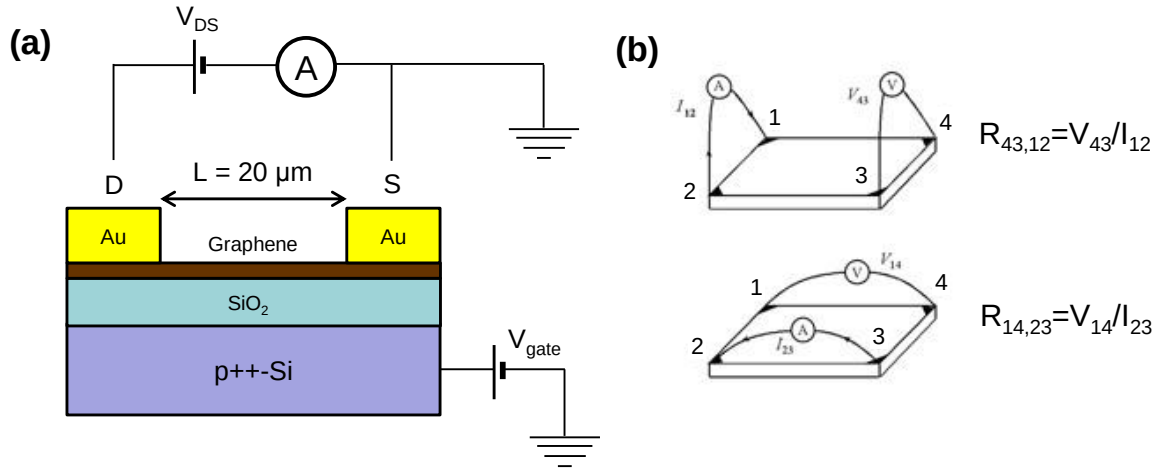


**Figure 39** a) Back gated field effect transistor (FET) schematic. b) Illustration of 4 probe measurement method to measure the sheet resistance of the rectangular thin film sample.[392]

In order to calculate the field effect mobility ($\mu_{FET}$), the transfer characteristic ($I_{DS}$ versus gate voltage, $V_{GS}$ for a fixed $V_{DS}$) must be first obtained. From the slope of the linear part of the curve ($\Delta I_{DS}/ \Delta V_{GS}$), the $\mu_{FET}$ values can be calculated by eq. 14[90]:

$$\mu_{FET} = \frac{\Delta I_{ds}}{C_{ox}\frac{W}{L}V_{DS}\Delta V_{GS}} \qquad (14)$$

where $C_{ox}$ is the oxide capacitance ($C_{ox} = \varepsilon_{ox}\varepsilon_0/t_{ox}$ ; $\varepsilon_{ox} = 3.89$ and $\varepsilon_0 = 8.854 \times 10^{-12}$ F/m).

The measurement system was equipped with tungsten probes to make contacts with the gate and electrodes, and pre-programmed parametric analyser (HP4140B). For the temperature dependent conductivity measurements, the sample was placed inside a cryostat (ST-500, Janis) in temperatures ranging from 178 K (liquid nitrogen was used as coolant) to 300 K in a high vacuum of $10^{-5}$ torr maintained by a turbomolecular pump.

### *5.9 Four- Probe Sheet Resistance Measurement*

The Van der Pauw 4-probe technique enables measurement of electrical conductivity over a centimetre scale without the need to deposit patterned electrodes of well-defined

geometry and the obtained value is not affected by the contact resistance unlike the two-probe configuration in which the contact resistance can increase the measured values of the thin film resistance.

In order to obtain the sheet resistance, $R_s = (\sigma_{dc}t)^{-1}$ of the film, contacts were made at the four corners (labelled 1, 2, 3, and 4) of the rectangular sample (typically, ~ 1 cm × 1cm) on insulating substrates (glass and $SiO_2$/Si) using a probe station equipped with four tungsten probes connected to Keithly 2400 Sourcemeter. An electric current, $I_{12}$ was flown from the contact no. 1 to contact no. 2 while measuring the voltage difference between contact no. 4 and no. 3, $V_{43}$. The ratio $V_{43}/I_{12}$ gives $R_{12,43}$ (Figure 39b). This process was repeated for all other 3 edges. Then, $R_s$ can be calculated by the solving the following equation[392]:

$$\exp\left(\frac{-\pi R_a}{R_S}\right)+\exp\left(\frac{-\pi R_b}{R_S}\right)=1 \qquad (15)$$

where $R_a$ and $R_b$ are average of $R_{12,43}$ , $R_{21,34}$ , $R_{34,12}$ , and $R_{43,12}$, and average of $R_{23,14}$, $R_{32,41}$, $R_{41,32}$, and $R_{14,23}$, respectively. The solution for $R_s$ can be obtained by solving the equation graphically or through numerical methods.

### *5.10 Conclusion*

In this chapter, the main characterization techniques performed on graphene dispersions and solution-processed and CVD graphene thin films on various substrates were discussed. The combination of the above techniques performed on the same type of the sample was employed to provide useful complementary information allowing a clear correlation among the morphology, structure, and optoelectronic quality of the samples.

# 6 Langmuir-Blodgett Deposition of Graphene Exfoliated in NMP and Optoelectronic Characterizations

## *6.1 Introduction*

This chapter follows the previous chapter on the Experimental Setup of Langmuir-Blodgett deposition of graphene in NMP to present the main results and discussion of the experiments towards the aim of obtaining high quality solution-processed graphene. Specifically, the chapter will focus on: (1) evaluation of graphene/NMP dispersion obtained in various conditions; (2) characterization of thickness and quality of graphene by Raman spectroscopy and TEM; (3) surface and optoelectronic properties of Langmuir-Blodgett films of graphene; and (4) temperature dependent charge carrier transport properties.

## *6.2 Graphene Dispersion in NMP*

Figure 40 contains the photographs of the graphene dispersions prepared using various exfoliation conditions. The three main types of graphene dispersions that were used in this study are outlined in Table 4.

High rotational speed of centrifugation generally reduces the amount of thick and large unexfoliated graphite in NMP, however it also significantly decrease the concentration of the final supernatant as can be seen in Figure 40. Applying stirring to the mixture during the sonication step has been found to markedly improve the concentration of the exfoliated graphene by more than an order of magnitude (Figure 40). The absorbance measurement of the dispersion has shown that graphene concentrations greater than 1 mg/ml can be obtained by simultaneously stirring and sonicating the mixture for 30 min followed by centrifugation at 12,000 rpm (r.c.f. = 1,700 g). The significant improvement in the concentration can be explained by shear thinning.[393-395] When the initial concentration of graphite is more than 500 mg/ml, the suspension may become so viscous in a gel-like state that it would

dramatically damp out the ultrasonic excitations. Rotation of the stirring shaft induces shear in the mixture to momentarily increase the fluidity and allow the sonication to remain effective so that final concentration of > 1 mg/ml can be obtained within tens of minutes of sonication time. This increased efficiency is a significant improvement over the previous report by Umar et al.[12] where sonication time of more than two weeks would be required to achieve the similar concentration of graphene without the application of stirring.

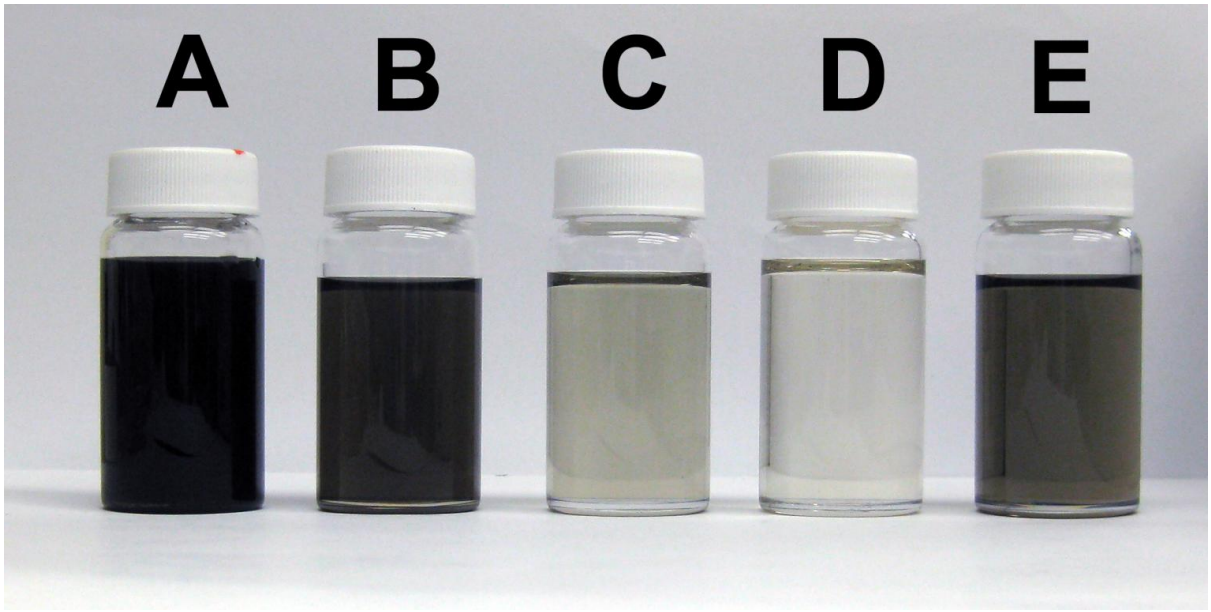


**Figure 40** Effect of centrifugation speed and stirring on the solute concentration. Photographs of A: supernatant solution before the final centrifugation step, B: supernatant after centrifugation at 3000 rpm for 30 min without stirring, C: supernatant centrifuged at 6000 rpm for 30 min without stirring, D: supernatant centrifuged at 12000 rpm for 30 min without stirring, and E: supernatant centrifuged at 12000 rpm for 30 min with stirring applied.

| Label | Initial Concentration of Graphite Powder | Sonication Time | Initial Centrifugation Speed | Final Centrifugation Speed |
|---|---|---|---|---|
| GNMP1 | ~200 mg/mL | 20 min | 2000 rpm for 90 min | 12000 rpm for 30 min |
| GNMP2 | ~200 mg/mL | 30 min | 2000 rpm for 90 min | 12000 rpm for 30 min |
| GNMP3 | ~200 mg/mL | 60 min | 2000 rpm for 90 min | 12000 rpm for 30 min |

**Table 4** Processing conditions for three different types of suspensions produced for the study.

### *6.3 Characterization of Exfoliated Graphene*

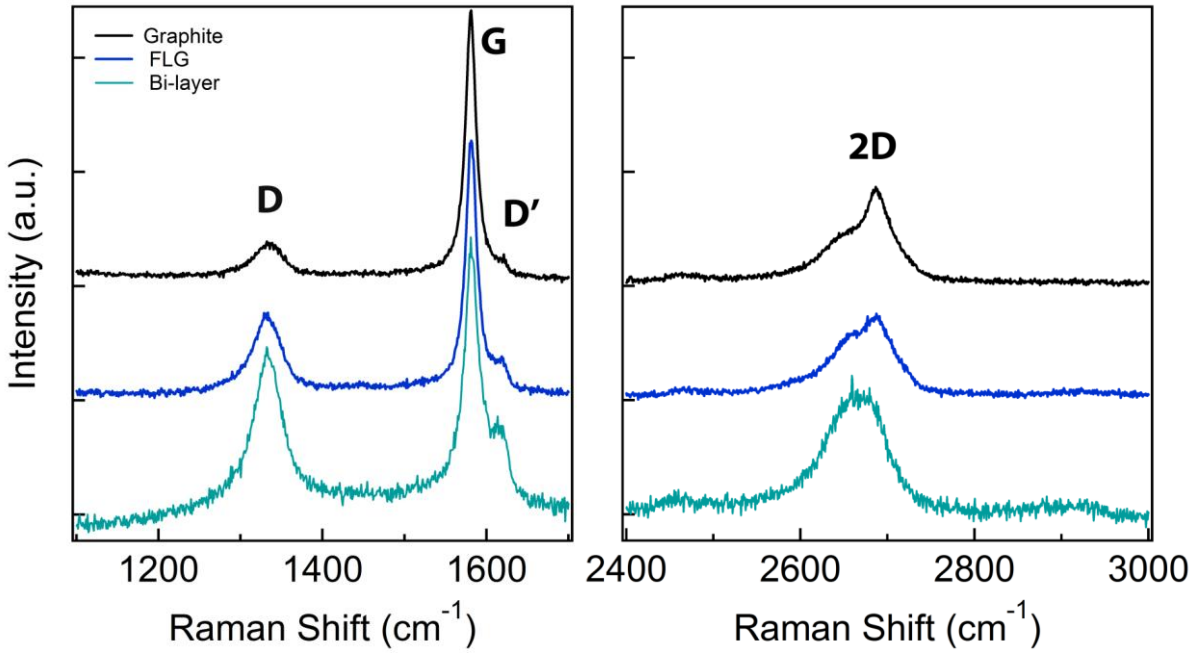


**Figure 41** Raman spectra of graphite, exfoliated few-layer graphene (FLG), and exfoliated bilayer graphene deposited on $SiO_2$/Si substrate from the graphene/NMP suspension. Laser excitation wavelength, 633 nm.

The purified supernatant obtained after the centrifugation of dispersion has been characterized for its thickness, crystal quality, and lateral flake sizes. The Raman spectroscopy on the drop-cast and Langmuir-Blodgett films was used to determine the thickness of individual graphene flakes by analysing the shape and position of the 2D peak of the spectra (Figure 41). Comparison with the 2D peaks reported in the literature for mechanically exfoliated graphene indicates that most of the individual graphene flakes have thickness of 2-5 layers reflecting that the flakes have been well exfoliated.[364]

To investigate the crystal quality of graphene, the D to G peak ratios and G peak FWHM have been analysed for the same Raman spectra. As evident in Figure 41, the D to G peak ratio of NMP exfoliated graphene is much less than that of graphene oxide and closer to that of the starting graphite.[93] Furthermore, the FWHM of the G peak remains unchanged indicating good crystallinity. As expected for the non-covalent exfoliation, the degree of defect appears to be much less than that of covalently functionalized graphene. The main reason for the appearance of the D peak following the exfoliation from the starting graphite is

likely due to the edge defects of exfoliated graphene flakes of smaller lateral sizes (< 200 nm) that are produced during the vigorous exfoliation process.[116]

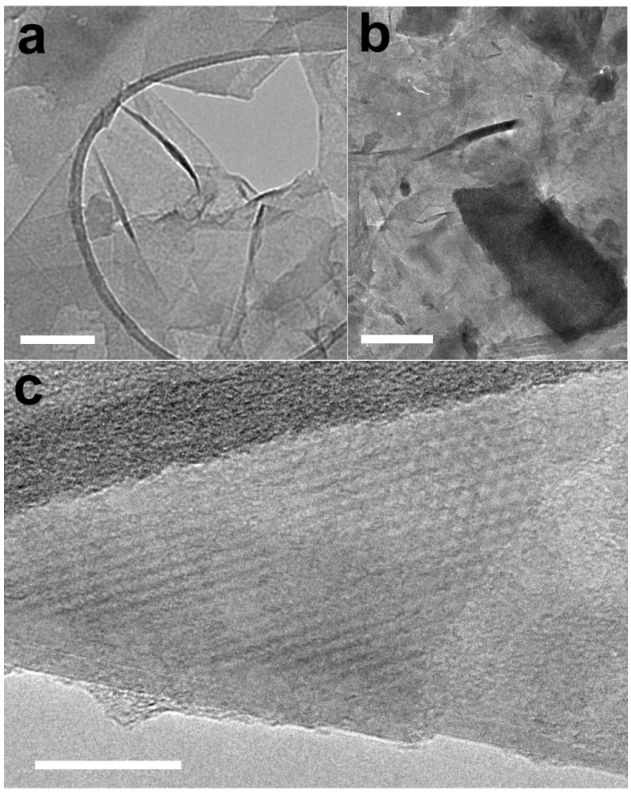


**Figure 42** Bright field TEM images of exfoliated graphene flakes from GNMP1 and its centrifugation sediments. a) Exfoliated graphene flakes of supernatant suspension, which was drop-cast on TEM grid. Scale bar, 100 nm. b) Sediment obtained after final centrifugation step for GNMP1. Scale bar, 200 nm. c) HRTEM image of a FLG. Scale bar, 20 nm.

Figure 42 shows the transmission electron microscopy (TEM) images of graphene flakes which further support the effectiveness of the method to produce exfoliated few-layer graphene (FLG) of high crystal quality. The flakes from supernatant in Figure 42a appear to be much thinner compared to the particles found in the centrifugation sediment in Figure 42b. The flakes appear to be thin enough to be highly transparent to electrons under TEM. The high resolution TEM image in Figure 42c illustrates the basal plane atomic lattice of FLG, which demonstrates high degree of crystalline order within the flakes.

### *6.4 Properties of Langmuir-Blodgett Deposited Film*

The LB deposited films on glass and Si(100) substrates with 300 nm thick thermally grown silicon oxide were dried in a mixture of Ar and $H_2$ (10:1 ratio) at 420 ˚C for 30 min in order to remove any residual solvents for analysis. The representative AFM images of LB

films from dispersions of graphene prepared using three different sonication times ($t_s$ = 20 min, GNMP1; $t_s$ = 30 min, GNMP2 ; $t_s$ = 60 min, GNMP3; Table 4) are shown in Figure 43a-e. The lateral size of the graphene flakes decreases as $t_s$ increases as shown in the flake size distribution (Figure 43f). This is consistent with general sonication phenomena of particle scission where the dimensions of particle decrease as $t_s^{-1/2}$ [116,396,397].

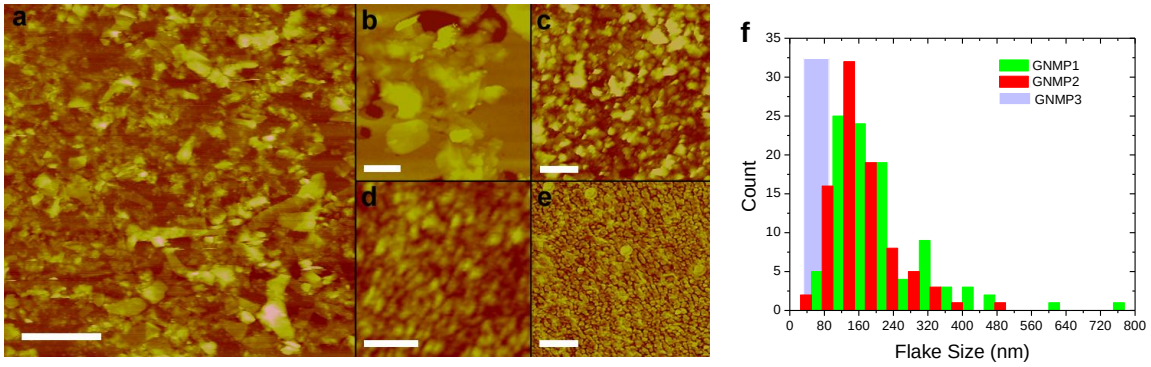


**Figure 43** Atomic force microscopy height image LB films of different types of graphene in NMP and different number of deposition, n. a) GNMP1, n = 1 (scale bar, 800 nm), b) GNMP2, n = 2 (Scale bar, 200 nm), c) GNMP2, n = 5 (scale bar, 1 μm), and d) GNMP3, n = 2 (scale bar, 200 nm). e) AFM Phase image of GNMP3 with n = 2 (Scale bar, 400 nm). f) Lateral size distribution of graphene flakes obtained from the AFM images of LB films for the three different types of suspensions.

A problem often seen in the case of drop-cast film of graphene/NMP is that poor wetting and slow drying time of the solvent induce aggregation of exfoliated graphene flakes into graphitic particles that hinder further characterization. Langmuir – Blodgett deposition on the flat water-air interface prevents the agglomeration and makes the flakes remain aligned relatively parallel to the substrate surface. The samples however have a large degree of roughness resulting in large apparent thicknesses (>10 nm) possibly due to the overlap and folding of the flakes during deposition and drying process. The average thickness for each deposition was nevertheless consistent as it appears to increase linearly with the number of depositions, n (Figure 44).

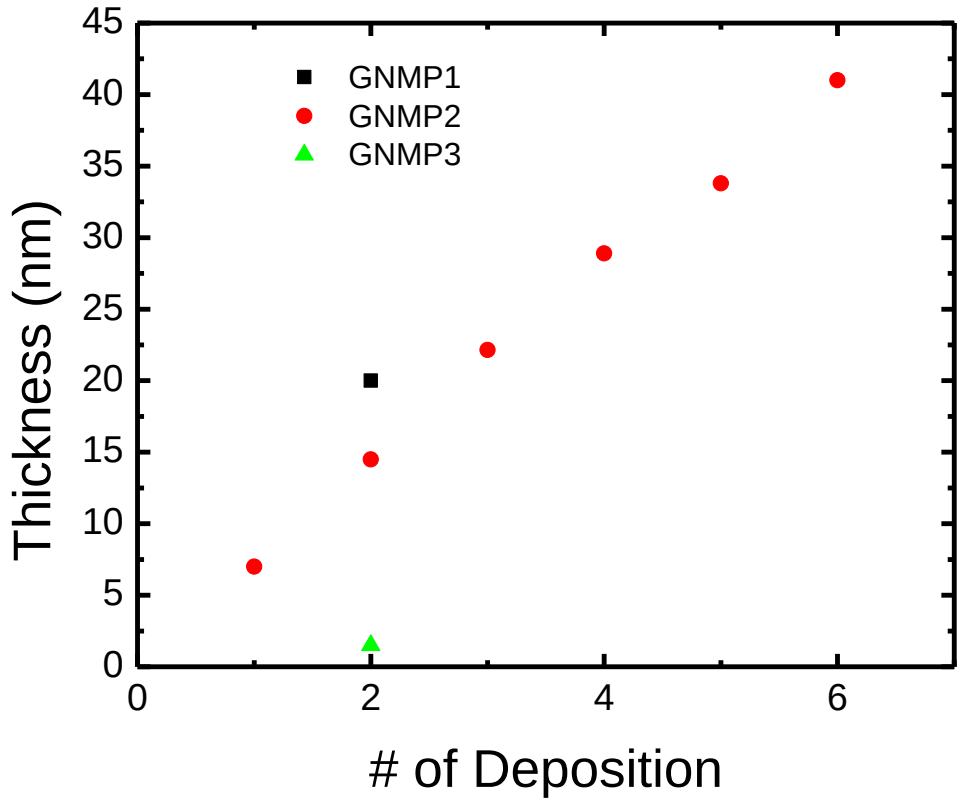


**Figure 44** Thickness versus number of deposition for three types of graphene/NMP dispersions.

Surface energy of the LB film was determined by the Fowkes method[398] using water and formamide as solvents for the contact angle measurement on a 20 nm thick LB film on quartz, and it found to be 43 mN/m. In comparison to the ideal surface energy of graphene based films reported in literature, our surface energy value is similar to the value of unfunctionalized graphene ( 46.7 mN/m) rather than that of graphene oxide (62.1 mN/m).[399] This result indicates that exfoliation in NMP does not significantly alter the surface chemistry of the graphene sheets as in the case of graphene oxide where the surface energy is changed dramatically by functionalization of surface and edges by oxygen functional groups.

### *6.5 Optoelectronic Characteristics of Langmuir-Blodgett Films*

The optical transmittance of the LB film in the visible spectrum displays consistent decrease in transparency as with film thickness (Figure 45 and Figure 46). The highest transparency (considered at $\lambda$ = 550 nm) for a single deposition (produced from GNMP3), was found to be about 98 %, corresponding to monolayer graphene. Increasing the graphene film thickness led to a consistent decrease in transparency, down to 55 % for n = 5.

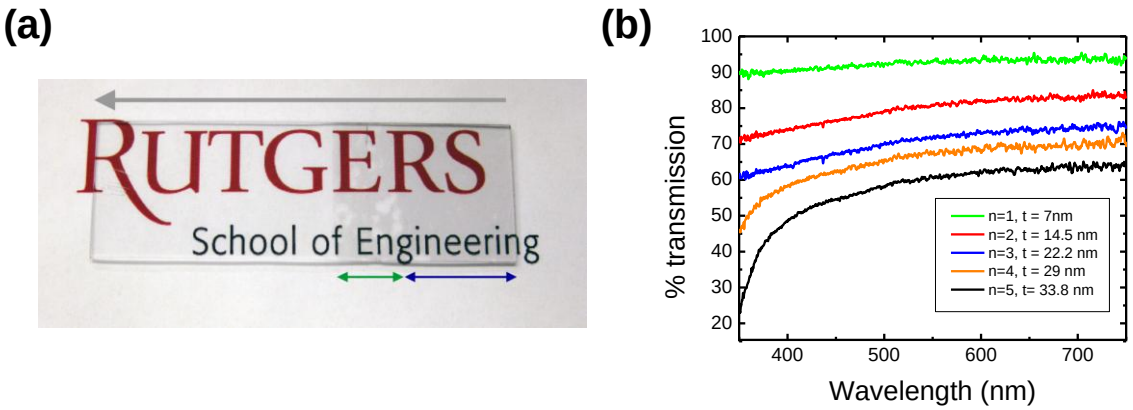


**Figure 45** a) GNMP2 deposited onto a glass slide by the Langmuir-Blodgett deposition method. Grey arrow line indicates the direction of vertical movement of substrate during the LB deposition. Green line region indicates initial stage of deposition where the film contains pin-holes and non-uniformity. Blue line region indicates homogenous film deposition after the initial stage. b) Optical transmittance for different number of LB deposition, n, on glass in the visible spectrum (from GNMP2).

From the thickness versus transmittance behaviour, the calculated absorption coefficient is 0.0058 $nm^{-1}$ which is much less than that of ideal graphene film (0.02970 $nm^{-1}$)[58,391] (Figure 46). However, the smaller value is expected due to the loose stacking of graphene sheets and presence of empty spaces between flakes that result in a large density of pinholes.

Significant improvement of the conductivity was detected after annealing in the $Ar/H_2$ (10:1 ratio) atmosphere. Therefore, remaining NMP in the as-deposited film may be a crucial limiting factor for electric properties in the as-deposited graphene films. We also found that the electrical conductivity depends on the size of the flakes as well as the thickness of the films. The film with the largest average flake sizes, 220 nm (Figure 47a), exhibited the highest conductivity of 100 S/cm (GNMP1) while the film with the lowest average flake size of 80 nm (GNMP3) exhibited much lower conductivity of $4.4 \times 10^{-3}$ S/cm. This dependence of the conductivity on the flake sizes indicates that the sheet-to-sheet junction resistance may be a dominant factor in charge transport.

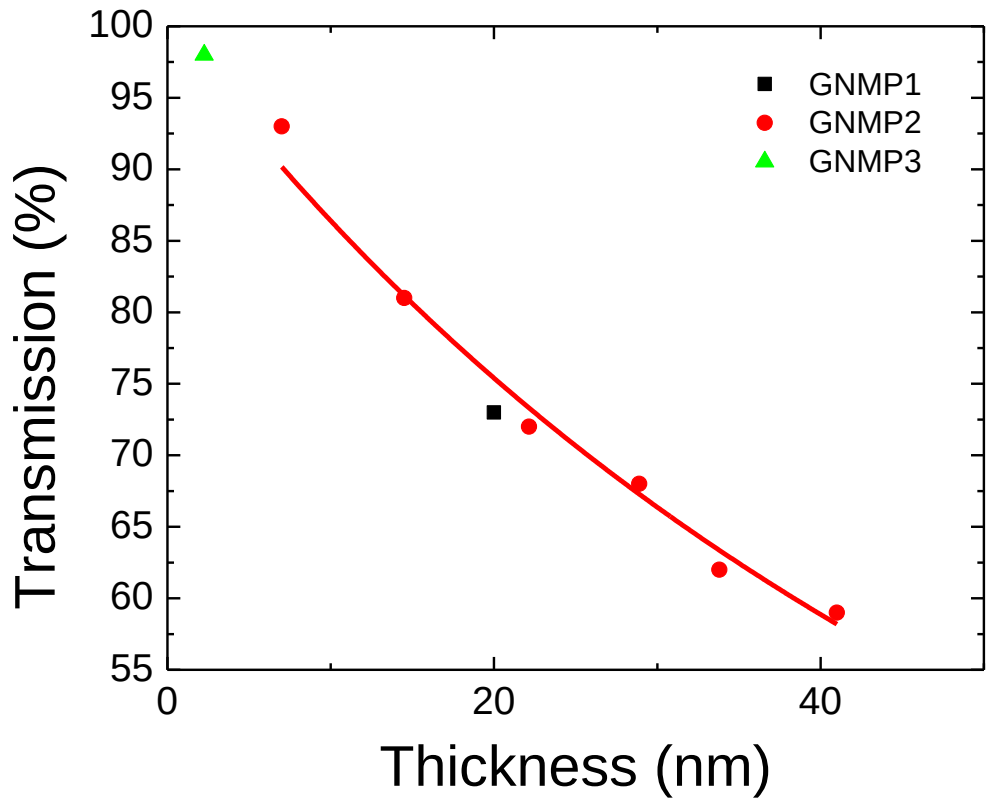


**Figure 46** Transmittance vs. thickness. The fitting was based on eq. 10 in the Characterization Techniques chapter. The absorbance coefficient for GNMP2 obtained from the fitting (eq. 10) is 0.0058 $nm^{-1}$.

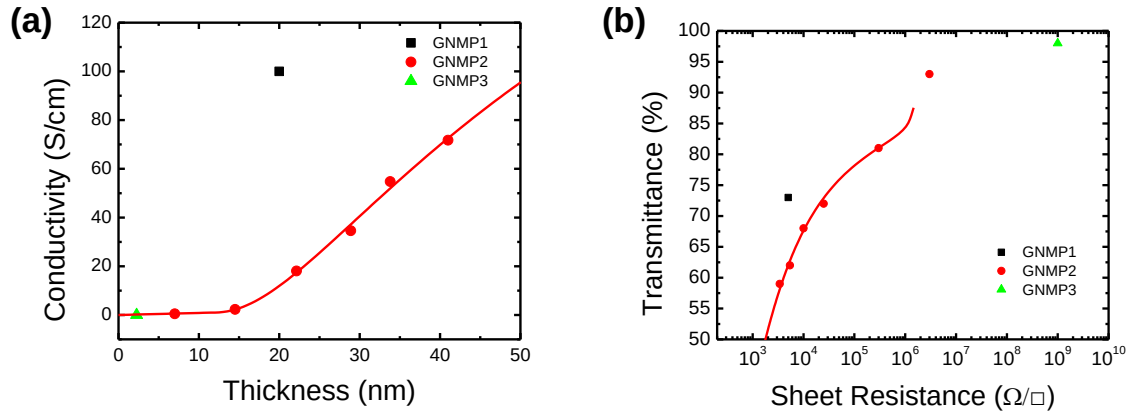


**Figure 47** a) Conductivity vs. Thickness graph for LB films. The curve fitting was performed according to eq. 16. b) Transmittance vs. the sheet Resistance graph for LB Films for different number of deposition. The curve fitting was performed according to eq. 17.

However, the conductivity also increases with thickness of the films (Figure 47a), suggesting that the relatively high roughness (which can be as high as the half of the film

thickness) and the presence of pin holes are responsible for the reduced electrical properties of the thin films[107]. This thickness dependent behaviour can be explained in the framework of percolation theory. The difference between the bulk film and thin film of exfoliated graphene can be attributed to reduced effective volume fraction due to the volume that does not participate in charge carrier conduction at the surface.[400] We assign a thickness to this non-percolative volume, $\Delta t$, and approximate the effective percolative volume fraction to be $\phi = t/(t+\Delta t)$. Using a simplified form of generalized effective medium (GEM) model of percolation, the relationship for the thickness conductivity, $\sigma_{dc}(t)$ above the critical percolation thickness, $t_c$ can be written as [401,402]:

$$\sigma_{dc}(t) = \sigma_{bulk}^{DC}\left(\frac{t-t_c}{t+t_c}\right)^p \qquad (16)$$

Here, we assume $t_c = \Delta t$ which is a threshold thickness for the formation of a percolative network of graphene flakes. $p$ is critical percolation exponent related to the geometry and interaction between the flakes, and $\sigma_{bulk}^{DC}$ is the bulk conductivity as $t$ approaches infinity. The curve fitting performed on the conductivity vs. thickness for GNMP2 shown in Figure 47a predicts the behaviour fairly well giving $t_c$ value of ~ 10 nm. This value is reasonable as we expect the first layer ($t$ = 7 nm) to be just below $t_c$ due to the characteristic conformation of graphene flakes on the surface of the water bath during the Langmuir-Blodgett assembly where most of the contacts between the graphene flakes are made only at their poorly conductive edges.[124] After the 2nd deposition ($t$ > 14 nm), we expect the overlap between the graphene flakes to be large enough for the percolation to take place. The obtained value of $p$ = ~2.5 is greater than what is predicted by scaling arguments for isotropic systems ($p$ = ~2 for 3D systems[403]; $p$ = ~1.3 for 2D[404]). However, the high values of the exponents ($p$ > 2) were experimentally found in the other similar thin film systems of exfoliated graphite[125,405,406] and can be attributed to the highly anisotropic dimensions and orientation of the graphene flakes.[401]

From the fitting, it is clear that the $\sigma_{DC}(t)$ values in the range of thickness of practical importance (T > 50 %) are well below the bulk DC conductivity and $\sigma_{DC}(t)$ is only attained when t >> 100 nm. Then the relationship between transmittance and sheet resistance, $R_s$ for thin films is determined by $\sigma_{DC}(t)$ through the following equation[400] :

$$T = \left(1 + \frac{Z_0}{2R_s}\frac{\sigma_{Op}}{\sigma_{DC}(t)}\right)^{-2} \qquad (17)$$

where $Z_0 = 376.7\ \Omega$ is the impedance of free space, and $\sigma_{Op}$ is the optical conductivity of the film which is constant in the thickness ranges investigated. As shown in Figure 47b**,** the fitted curve using the calculated value of $\sigma_{DC}(t)$ from Figure 47a well describes the percolation behaviour of the $R_s$ versus % transmission above the percolation threshold. Considering the effect of percolation, the film with the largest mean flake sizes (GNMP1) exhibited the best optoelectronic property having transmittance of 73% at $R_s$ of 5 k Ω/□ as evident in Figure 47b. The DC conductivity to optical conductivity ratio (which is considered as a figure of merit for transparent conductors) for the best film obtained from GNMP1 was 0.48 at thickness of 20 nm. This is comparable to other solution-processed graphene films reported in literature,[11,12] however, $\sigma_{DC}(t)/\sigma_{Op}$ values can be further increased by careful optimization of the deposition conditions (e.g. reduction of pinholes by applying lateral surface pressure during the LB deposition) to improve the percolation parameters so that $\sigma_{DC}^{bulk}$ can be reached at lower thickness. $\sigma_{DC}^{bulk}$ obtained for GNMP2 from the curve fitting is about 300 S/cm which is still much less than that of bulk graphite. However, this is expected as the film still contains a large amount of trapped solvents and voids in the bulk of the film. From the optical density of our film obtained by comparing the value of absorption coefficient with that of ideal multilayer graphene, we estimate that maximum possible conductivity of fully densely packed film would be ~1500 S/cm. This value is on the same order of magnitude of polycrystalline pryolytic graphite.[407]

Field effect was also observed in our thin film field effect transistor (FET) devices. The transfer characteristics of the FET devices shown in Figure 48a indicate that the on/off ratio is very small, close to one, even for a large voltage sweep (from -100 V to 100 V). In addition, the film was found to be heavily p-doped with the charge neutrality point located at a gate voltage ($V_{GS}$) greater than 40 V. This is possibly due to the residual solvents trapped between the sheets and doping from the edge states and defects which act as electron traps.[407] We also observed the hysteresis effects for different sweeping directions and saturation currents at high bias voltages. This gives further evidence for presence of defect states, in the form of oxygen functionalities which introduce $sp^3$ carbon or other extended imperfections [408] giving

rise to the trapped states.[409] From the slope of the transfer characteristics, the field effect carrier mobility ($\mu_{FET}$) values of a thin film can be calculated by eq. 18[90]:

$$\mu_{FET} = \frac{\Delta I_{ds}}{C_{ox}\frac{W}{L}V_{DS}\Delta V_{GS}} \qquad (18)$$

where $C_{ox}$ is the oxide capacitance ($C_{ox} = \varepsilon_{ox}\varepsilon_0/t_{ox}$), W, the channel width, L, the channel length, and $V_{DS}$ the source to drain voltage. The best room temperature hole mobility value we measured was 0.9 $cm^2/Vs$ which was again obtained from the films with largest average lateral flake sizes (GNMP1). The average electron mobility was about an order of magnitude smaller than the hole mobility values likely due to the presence of the defects and impurities that disproportionally affect the mobility of the charge carriers. It must be noted the measured value of $\mu_{FET}$ is an underestimate of the actual carrier mobility as percolated conductive paths comprise only a fraction of the film area. Improving the percolation path should be expected to improve the field effect mobility values in the thin film composed of two dimensional flakes. Mobility values of up to ~ 95 $cm^2/Vs$ were recently reported in inkjet-printed film of graphene exfoliated in NMP.[125] This was achieved only after careful optimization of deposition parameters such as substrate surface functionalization and packing of graphene flakes.[125]

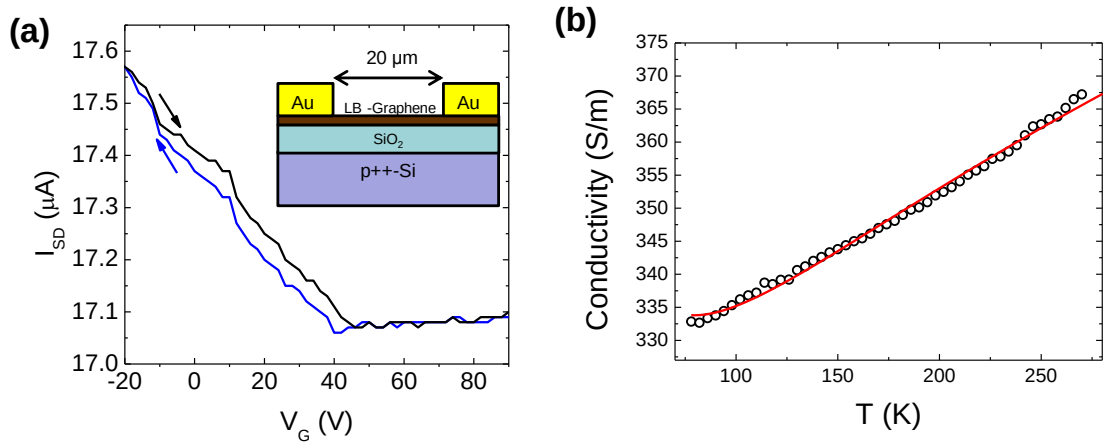


**Figure 48** a) FET transfer characteristics for GNMP2. b) Temperature dependent conductivity from a GNMP2 device. Curve fit was performed according to the STB model of polycrystalline graphite.

### 6.6 Temperature Dependent Electrical Measurements

In order to gain further insights into the main limiting factors of the electrical property, we have performed temperature dependent conductivity and mobility measurements from 78 K to 280 K. This will specifically elucidate the transport mechanism of the bulk conductivities ( $\sigma_{DC}^{bulk}$ ) as the percolation parameters ($p$ and $t_c$) can be considered to be independent of temperature. The weak temperature dependence and semimetallic/semiconducting behaviour with positive temperature coefficient of conductivity for a GNMP2 device are shown in Figure 48b. The increase in conductivity with increasing temperature has been typically ascribed to various charge localization models such as Mott type variable range hopping (VRH),[410] fluctuation induced tunnelling (FIT),[411] and simple thermal activation for the case of disordered conducting polymers,[411-414] and thin film network of carbon nanotubes,[415-419] covalently modified graphene.[102,103] stemming from the presence of energy barrier between conductive regions in the network. However, the weak and almost linear dependence of conductivity with temperature did not yield reasonable values for the models above even if the combination of the models were used for different temperature ranges. The temperature dependent mobility values also do not support the presence of mobility gap in the film at low temperature as it is a decreasing function of temperature (Appendix, Figure A2).

Unlike a network of carbon nanotubes that partly contains semiconducting nanotubes and a film of disordered conductors, there seems to be much more overlap and interaction between the conductive regions of the graphene flakes without strong localization above the percolation threshold. This is further supported by the room temperature value of the $\sigma_{DC}^{bulk}$ approaching that of polycrystalline graphite. Then, we can consider the film to be an oriented, polycrystalline mixture of turbostratic and Bernal stacked few-layer graphene flakes, and apply the band theory of charge carrier transport to the temperature dependence. In single crystal graphite, finite overlap between conduction and valence bands leads to a finite density of states at the Fermi level and results in metallic like conduction. However, in pryolytic graphite of small crystalline size and very thin layer of graphite (flake thickness ~ 10 nm), the density of the states at the Fermi level diminishes as the overlap becomes very small.[420,421] Then, the conduction behaviour can be well explained by the simple two band (STB) model[88,422,423] of graphite where two symmetric parabolic bands are used to describe the

density of electrons and holes in conduction and valence bands, respectively. This model has been successfully used to describe the electronic behaviours of polycrystalline graphite[424], mesoscopic graphite flakes[88,423], and carbon nanotubes[425,426]. In our case of a heavily p-doped film where the overlap between the two bands is negligible compared to the shift in Fermi energy, and $n = n_h >> n_e$,

$$n_h(T) = \frac{16\pi}{h^2 c_o} kT \ln\left[1 + \exp\left(\frac{\Delta}{kT}\right)\right] \quad (19)$$

where $h$ is Planck's constant, $c_0 = 6.71 \times 10^{-10}$ m, c-axis lattice parameter of graphite, k, Boltzmann's constant, $\Delta$ is magnitude of shift in $E_F$ from the charge neutrality point.

The carrier mobility, $\mu$ can be described in terms of lattice scattering due to electron-phonon interaction, and boundary scattering.

$$\frac{1}{\mu(T)} = \frac{1}{\mu_b} + \frac{1}{\mu_{th}(T)} = \frac{1}{\mu_b} + BT^{\alpha} \quad (20)$$

where B and α are temperature independent constants.

Therefore, using the Drude formula for conductivity ($\sigma = en\mu$), the conductivity can be fitted according to the STB model as illustrated in Figure 48b. The curve fitting yielded $\Delta = 2$ meV, which is quite reasonable considering the hole doping on the order of $10^{18}$ $cm^{-3}$ as estimated from the position of the charge neutrality point in Figure 48a. In addition, $\alpha = 0.82$, which is also a reasonable value as it can range from 0.5 to 1.6 in polycrystalline graphite.[424] The deviations from STB theory can possibly arise from the temperature dependence of contact resistance at the electrode-graphene junction, activation of trapped charges at higher temperatures, inhomogeneous charge carrier density, and temperature dependent α.

The gradual decrease of $\mu_{FET}$, with increasing temperature can also be explained by this approach as $\mu_{FET}$ remains fixed at low temperature as the mean free path is mainly limited by the crystalline size, and at high temperature, mobility is dominantly limited by thermal scattering of the charge carriers, although the scatter in data points is considerably large to perform reliable fitting (Appendix, Figure A2).

### *6.7 Conclusion*

Summarizing, scalable methods for efficient production of highly concentrated solution of graphene in NMP (> 1 mg/mL) and large area deposition of graphene have been developed.

The dispersion contains high quality, unfunctionalized graphene flakes that are well exfoliated with thickness between monolayer to FLG. The thin films exhibit good optoelectronic properties for solution-processed graphene without need for additional processing steps. However, the large area optoelectronic properties appear to be limited by the small flake size (< 200 nm) resulting from the vigorous sonication step and by the percolation limited conduction of charge carriers due to loose packing of graphene flakes in the LB assembly and subsequent deposition. The conduction mechanism can be explained by the simple two band model and exhibits similarity to that of polycrystalline turbostratic graphite.

# 7 Nucleation and Growth Mechanism of CVD Graphene on Cu

## *7.1 Introduction*

In the race to obtain high quality CVD graphene, most of the experimental works so far have focused on finding the optimal conditions by trial and error basis.[143,176,190,196] Although this has led to a significant improvement in the crystal grain size and electrical properties, a full understanding of the precise physicochemical mechanisms that govern film formation and that can potentially lead to the rational engineering of the growth of wafer-scale single crystal graphene is still lacking. Here, we present the most significant results of our parametric study described in the previous chapter to develop a general model that can reasonably predict the quantitative details of the experiments over a wide range of conditions. To this end, we systematically analyse the CVD process in the framework of existing theories for two-dimensional nucleation and growth of thin films, which describe the key stages that determine the nucleation density, distribution of nuclei, and final coverage. We have identified competing atomic phenomena such as adatom mobility *versus* desorption whose balance define characteristic nucleation regimes with very different activation energies depending on the temperature. The growth rates are limited by carbon attachment to the graphene edges without significant dependence on the crystal orientation of the Cu substrate. However, both nucleation and growth are affected by the microscopic substrate roughness that determines nuclei distribution and can impart distinctive morphological features to the final film. Predictions, whether a given growth condition would produce a continuous, pinhole-free graphene film, are possible by employing modified Langmuir model of adsorption and self-terminating, 2D crystallization. Our study offers new fundamental insights on the CVD graphene growth, highlighting the key distinguishing aspects and defining clear guidelines for the large-scale fabrication of high quality graphene and ultimately, single crystal graphene films.

Much of the findings in this chapter have been recently published in ACS Nano.[427] This chapter provides additional details and updates to the results of our experiments and implications of the model beyond the published work. A manuscript containing some of the additional works has also been submitted and it is currently under review.

## *7.2 Results*

### 7.2.1 Characteristics of the Cu Polycrystalline Foils

The copper catalyst used for the work presented in this chapter, is a polycrystalline Cu foil (25 μm thickness, 99.8 %, Alfa Aesar item. No. 13382) with an average grain size of about 5 μm. After annealing at 1000 °C, the foil exhibits a bimodal grain size distribution, composed by grains with average lateral size of about 100 μm as well as grains which have undergone an "abnormal growth" giving an average lateral size of 2 mm (Figure 49a, c). Therefore, taking into account that we typically grow graphene onto samples of about 5 mm x 5 mm, we should consider that the abnormal grains can occupy more than the half of the surface. Crystallographic analysis by electron backscattered diffraction (EBSD) (Figure 49e) and X-ray diffraction (XRD) (Figure 49d) demonstrates that most of the Cu grains show (100) or (310) orientations while only a small fraction of grains exhibit (111) or (211). Below the temperature of 1000 °C, we have found similar grain orientations albeit with smaller mean grain sizes. The as-received foil surface presents regular rolling features produced by the manufacturing process that run across the entire surface (Figure 49b, c). Their average height and width are 800 nm and 15 μm, respectively. The resulting average RMS surface roughness is 250 nm as measured by AFM (Figure 49b) and optical interferometer (Figure 49c).

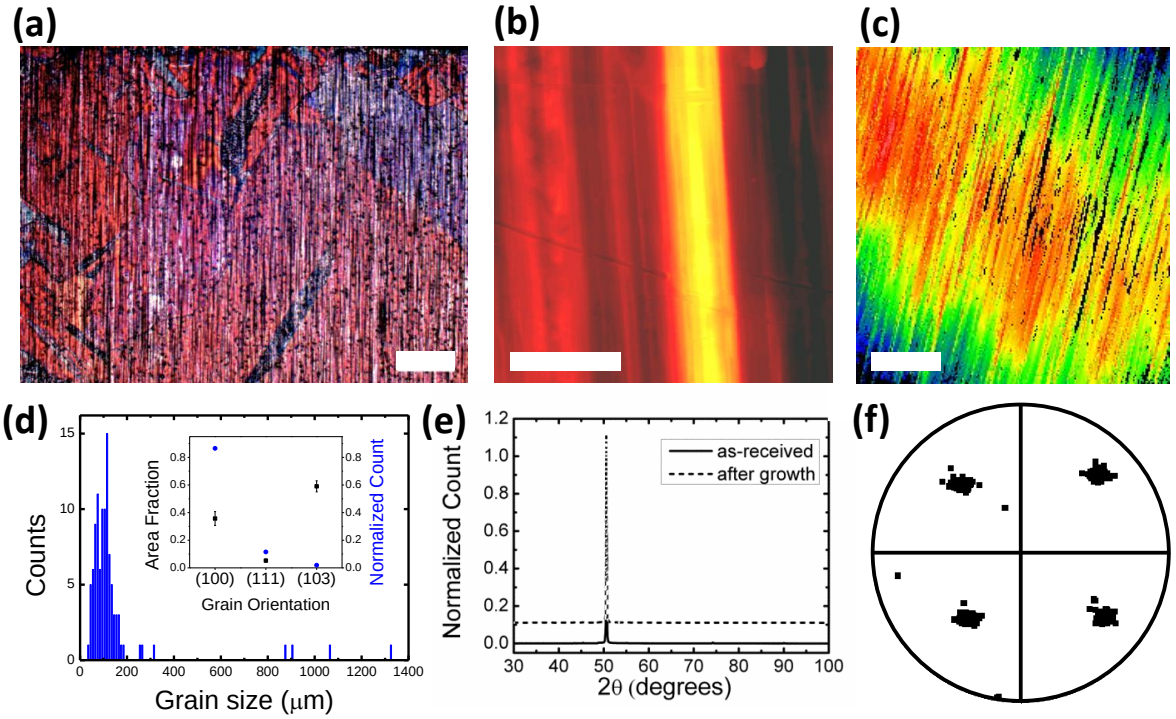


**Figure 49** Characteristics of polycrystalline Cu foil substrate. a) Optical microscope image of Cu foil after growth. Scale bar, 500 μm. b) AFM height image of as-received Cu foil. Scale bar, 10 μm. c) Optical interferometry image of surface profile of as-received Cu foil. Scale bar, 200 μm. d) Gain size distribution of Cu foil after growth. (inset) Area fraction of Cu grains of different grain orientations. e) X-ray diffraction of the Cu substrate before and after the growth. f) (111) pole figure of Cu grains characterized by EBSD.

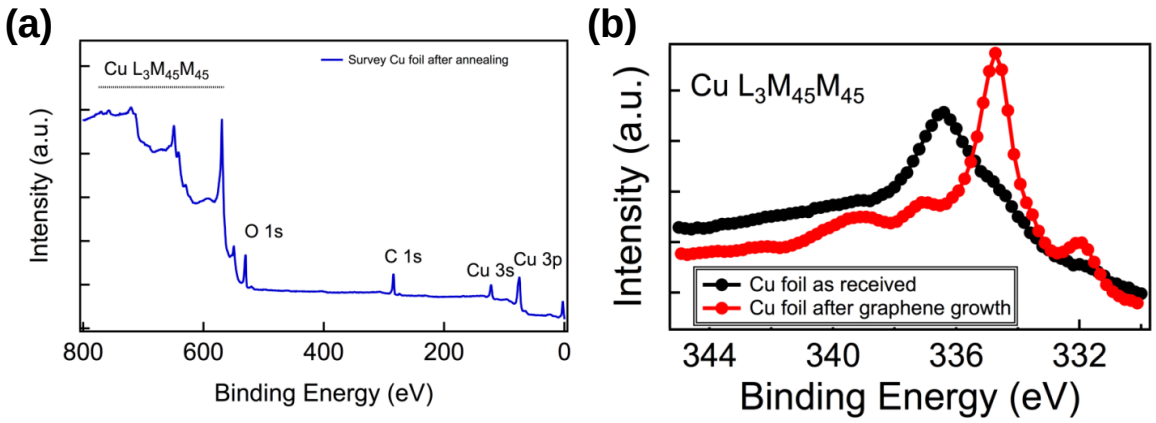


**Figure 50** XPS spectra of a Cu foil: (a) survey of Cu surface after annealing without graphene growth (collected using Al Kα source; $E_{h\nu}$ = 1486.7 eV); (b) Cu Auger peak LMM shows an entirely metallic character after graphene growth in contrast with the initial oxidized character in as received foil (Mg Kα source; $E_{h\nu}$ = 1253.6 eV).

### 7.2.2 X-ray Photoelectron Spectroscopy Analysis of Cu Substrates

Although it could be expected that impurities that are commonly present in Cu (*e.g.* S, Sn, Ag, $O_2$, *etc.*) could segregate to the surface at high temperature this appears not to be the case. Only a negligible amount of S < 1% was seldom detectable after annealing of a Cu single crystal with 5 mm of thickness. The XPS analysis (Figure 50) of the substrate before and after the growth experiments suggests that the only impurity present at the Cu surface is carbon.

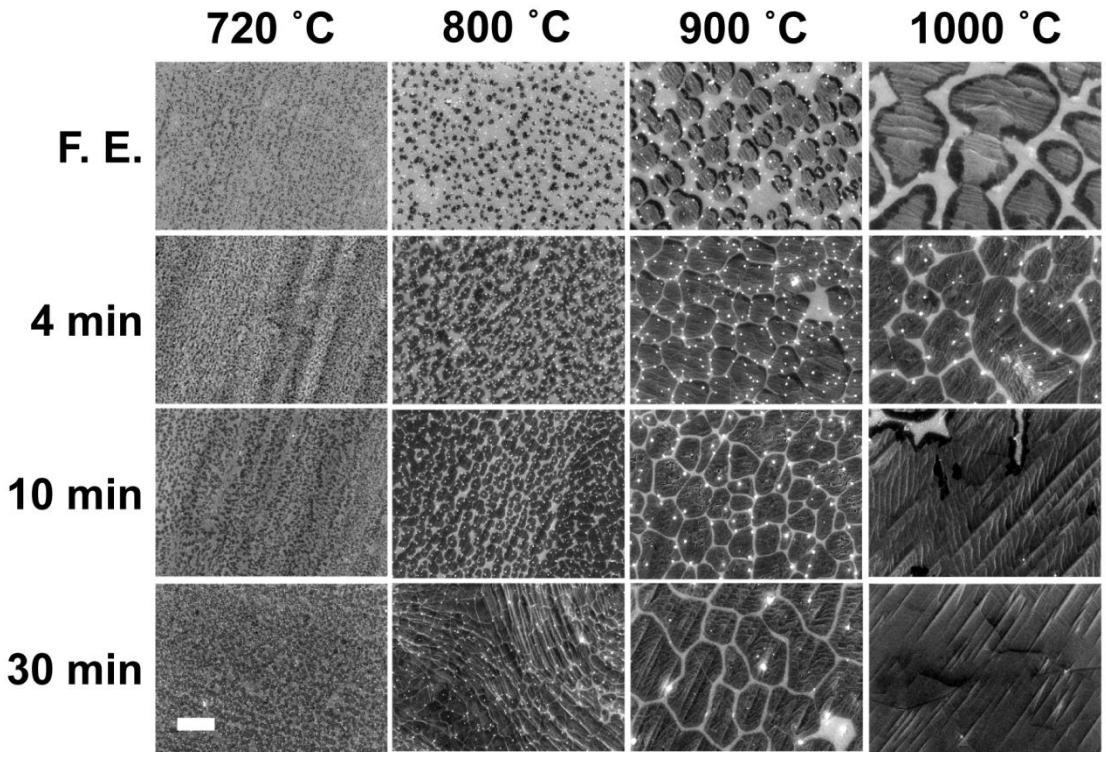


**Figure 51** High-resolution scanning electron microscope (SEM) images of graphene nuclei grown on Cu for different growth temperatures and times. These are identifiable as areas darker than the exposed Cu surface, which quickly oxidize in air after being taken out from the CVD growth system. F.E. stands for flash exposure (growth time of less than 3 sec). Scale bar, 1 μm.

### 7.2.3 Time and Temperature Dependent Evolution of Graphene Nuclei on Cu

We investigated the growth of graphene from 720 ℃ up to 1050 ℃ (Details are given in Chapter 4) for different time durations, from a flash exposure to methane up to 30 min in order to follow the evolution of the graphene and to extract the growth rates. The temperature range of growth includes the minimum temperature (720 ℃) at which graphene nucleation was observed while the maximum temperature (1050 ℃) was chosen close to the Cu melting

point (1084 ℃). Methane flow was chosen to be 0.5 sccm ($P_{CH4}$ = 0.4 mbar), and hydrogen flow rate was 10 sccm ($P_{H2}$ = 4 mbar). In order to understand the effect of substrate on graphene formation, we carefully characterized crystallinity and morphology of the Cu substrates before and after annealing at the growth temperatures. Upon exposure to $CH_4$, graphene nucleates very rapidly, grows and coalesces to form large domains (Figure 51). Using this growth approach, three key phenomena attracted our attention: (1) nucleation only occurs during the initial instants and no new nuclei are formed even after only 4 min of growth time at any temperature (Figure 51); (2) higher temperature leads to a lower nucleus density (number of nuclei per unit area) with larger lateral size (Figure 51 and Figure 52); (3) the domains do not evolve to fully cover the substrate surface, rather, the fractional coverage of graphene saturates for temperatures below 1000 ℃ under our experimental conditions. Growth times as long as up to 150 min have been attempted, but the area of graphene never could reach a complete surface coverage with pores remaining in the film.

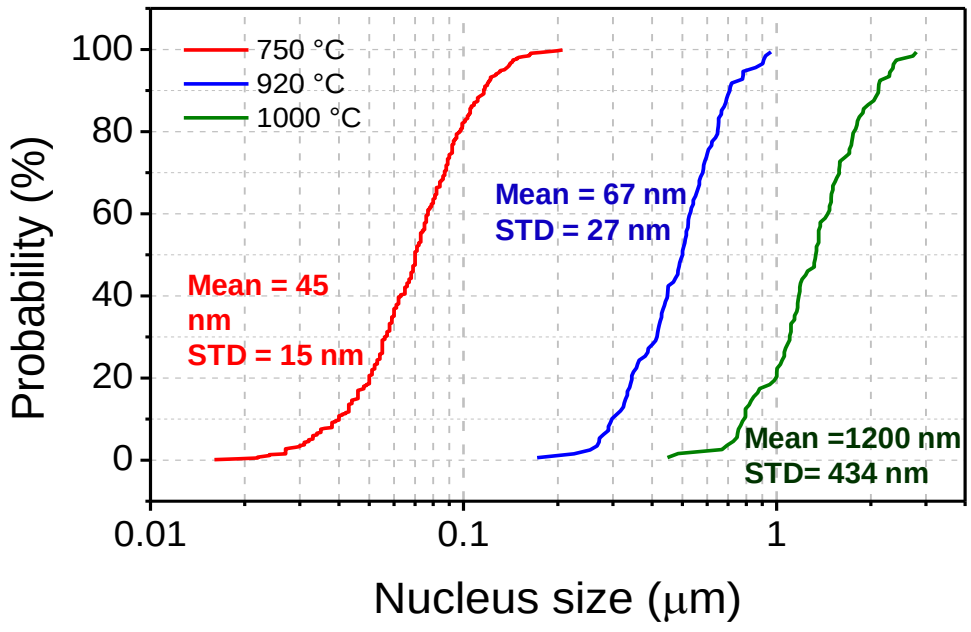


**Figure 52** Cumulative distribution plot of graphene nucleus size of graphene/Cu samples obtained at flash exposure for growth temperatures, 750 ℃, 920 ℃, and 1000 ℃. The graphene nucleus size measurements were performed by using Image J software on the large area SEM images (number of nuclei > 100) from respective conditions under the assumption of circular nuclei where the obtained nuclei diameter corresponds to the approximate lateral size.

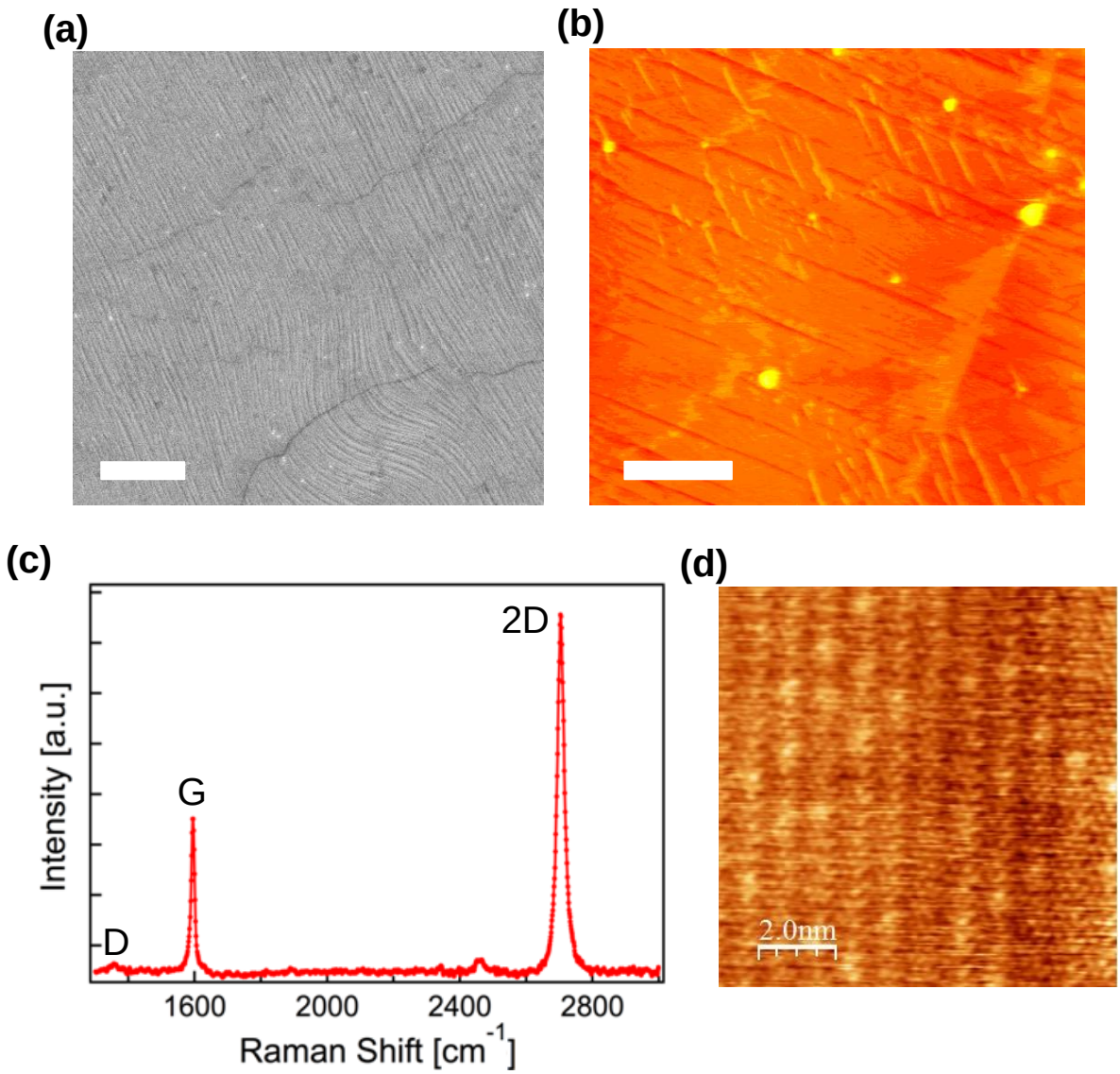


**Figure 53** Graphene thin film characteristics. a) SEM image of a continuous graphene on Cu at $T_{growth}$ = 1000 C, with $t_{growth}$ of 30 min. Scale bar, 5 μm. The wrinkles produced due to differences in thermal expansion coefficient (dark curled lines) and underlying Cu surface facets that run across the diagonal (bright and dark undulations) are visible. b) AFM topography of a continuous graphene on Cu displaying the surface facets from the substrate. Scale bar, 2 μm. c) Raman spectra of a continuous monolayer graphene film grown at 1000 ℃. d) Atomic scale STM image recorded with an Omicron LT-STM at 77 K of graphene film grown under the same condition. The relatively low D peak and the ordered lattice structure demonstrate the high crystal quality of the film.

In order to obtain a continuous graphene film we needed to reach growth temperature of ≅1000℃ and exposure time of about 30 min. Figure 53a shows the SEM image of as-grown graphene film on Cu. Other than the wrinkles produced due to thermal expansion coefficient

mismatch and underlying Cu surface facets, the film appears quite uniform without apparent thickness variations. Similar facet-like features were observed from the AFM image in Figure 53b indicating the graphene film follows the morphology of the underlying substrate. This continuous film is mostly a single graphene layer as Raman spectroscopy and STM indicate (Figure 53c, d respectively). The 2D/G peak ratio is about 2 and the 2D FWHM is about 28 $cm^{-1}$ as reported for single layer graphene grown by CVD.[20] In addition, the D peak is negligible over most of the surface scanned, suggesting reasonably good continuity of the film and low level of defects. The STM image shows the expected linear Moiré pattern generated by the presence of a Cu lattice with (100) crystallographic orientation.[428] It is worth noting that the individual flow rates of $H_2$ and $CH_4$ and the growth pressure of the CVD process were chosen so that growth occurs in the surface reaction regime[143] to obtain uniform single layer of graphene over more than 95% of the surface within growth time of 30 min at 1000 ℃. These conditions were kept constant throughout the study unless otherwise noted.

## *7.3 Discussion*

### 7.3.1 Model of 2D Nucleation and Growth

Kinetics of two-dimensional nucleation and growth on surfaces has been both theoretically and experimentally investigated extensively in other systems; *e.g.* thin film deposition and crystallization of amorphous phases at surfaces. We employ a general approach based on three well established models in order to understand the nucleation and growth of graphene on a Cu surface from an atomistic to macroscopic level: (1) the rate equation model[429-433] developed in the 1960s originally intended for study of physical vapour deposition of thin films on a planar substrate in UHV; (2) the Johnson-Mehl-Avrami-Kolmogorov (JMAK) model of phase transformation[434-436]; and (3) Langmuir theory of adsorption.[171,437]

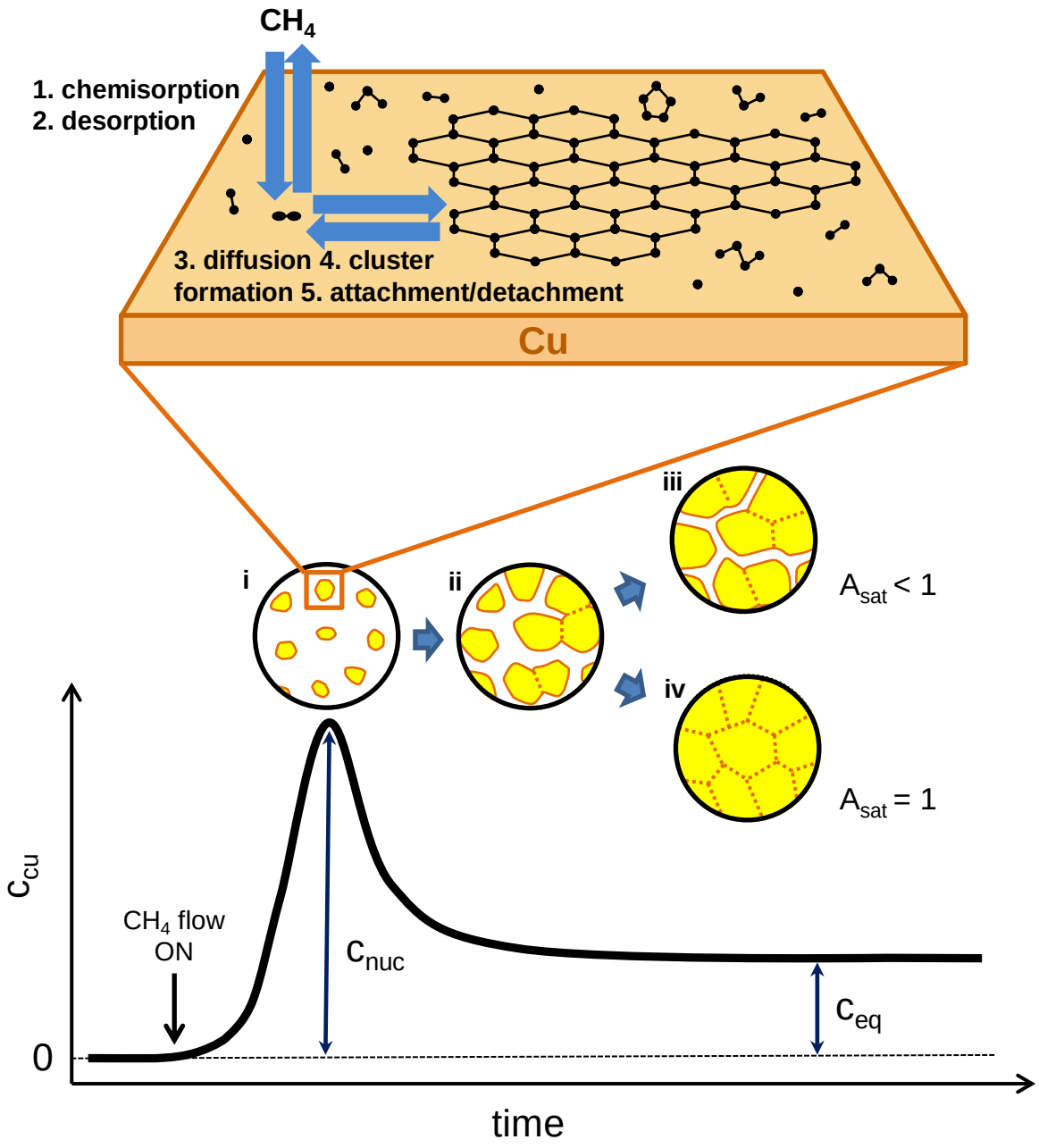


**Figure 54** Overall illustration of the nucleation and growth mechanism of graphene on Cu. The decomposition of methane leads to supersaturation of carbon adatoms at the Cu surface. When $c_{cu}$ reaches a critical supersaturation point ($c_{nuc}$) graphene domains nucleate and begin to grow possibly involving multi-atom carbon cluster formation and attachment of the clusters (i). Graphene nuclei coalesce as the growth proceeds further (ii). The growth stops either when the amount of superstaurated carbon species are consumed (iii) or when the domains merge together to completely cover the surface of Cu (iv).

Figure 54 illustrates the overall processes of graphene formation on Cu on the bases of the models developed for graphene growth on metals with higher carbon affinity (namely with higher carbon solubility).[150,204] Upon breakdown of methane through dissociative chemisorption on the Cu surface, the surface concentration of the active carbon species, $c_{cu}$, increases until it reaches a critical supersaturation level ($c_{nuc}$), where nucleation of stable graphene nuclei takes place. As the nucleation and growth of the supercritical nuclei deplete the adsorbed carbon species surrounding them, the $c_{cu}$ is quickly reduced to a level where the nucleation rate is negligible while growth of the nuclei continues until the supersaturated amount of surface carbon species above the equilibrium level $c_{eq}$ is consumed and the equilibrium between graphene, surface carbon, and $CH_4/H_2$ is reached. Depending on the available carbon, the degree of supersaturation ($c_{nuc}/c_{eq}$), graphene nuclei either coalesce to form eventually a continuous film or stop growing to reach a saturated, final incomplete coverage.[150,204]

It must be noted that the exact nature of the active carbon species adsorbed on Cu surface that leads to graphene nucleation has not been well identified yet. Several theoretical calculations[207,438,439] have predicted that dissociation of methane to a carbon monomer on Cu is highly endothermic and carbon dimers are more stable than isolated C adatoms (by over 2 eV) as the carbon-Cu interaction is weak and the diffusion barrier of carbon is low. In the surface mediated growth of graphene on Ru and Ir, 5-atom carbon clusters were found to be direct precursors of stable nucleus.[150,204] However, here, we generally refer to the active carbon species as carbon monomers because there is no conclusive experimental evidence for the presence of mobile carbon clusters based on our analysis. However, additional work is necessary to definitively rule out the absence of the clusters. We also rule out that high temperature poisoning by non-carbon impurities at the surface could be the reason for the observed growth saturation behaviour on the bases of X-ray photoelectron spectroscopy (XPS) characterizations (Figure 50).

### 7.3.2 Nucleation: Critical Nucleus Size

On the basis of the standard theory of nucleation,[440,441] we expect that the driving force for graphene nucleation is the degree of supersaturation of the adsorbed carbon and barriers to nucleation are mainly created by the excess energy of edge carbon atoms of graphene nuclei. One of the central parameters in the theory of nucleation is the critical size of nucleus

where the driving force of supersaturation is balanced by excess energy of edge atoms that make the nucleus unstable. Once the nucleus exceeds the critical size, the only way to reduce the total chemical free energy is via enlargement of the nucleus through attachment of new carbon at the edge. This in turn leads to significant nucleation and growth of supercritical nuclei. Therefore, determination of the critical nucleus size is of fundamental importance toward understanding of the nucleation kinetics.

Let us first consider the top-down, continuum approach for calculating the formation energy of graphene nucleus on Cu, i.e. the edge and interfacial properties of a nucleus are independent of size and identical to the macroscopic properties of graphene on Cu.

Then, the free energy of formation of a graphene nucleus of compact hexagonal geometry is:

$$\Delta G = -N_{tot}\Delta\mu_C + \sqrt{\frac{N_{tot}}{2}}\gamma_{edge} + N_{tot}(E_{strain} + E_b) \qquad (21)$$

where $N_{tot}$ is the total number of carbon atoms within the graphene nucleus, $\Delta\mu_C$, the supersaturation chemical potential per carbon atom which is a function of growth conditions, $\gamma_{edge}$, the edge energy per carbon atom, $E_{strain}$, the strain energy induced by the lattice mismatch between graphene and Cu, and $E_b$, interfacial binding energy of graphene on Cu. Recently, the energy of a stable graphene nucleus on Cu(111) which is made up of zigzag edges has been calculated to be $\gamma_{edge}$ = - 0.4 eV/atom.[442] Due to the relative small lattice mismatch and week interaction between graphene and Cu(111), the interface related energies have been calculated to be quite small: $E_{strain}$ = 0.11 eV/atom[179] and $E_b$ = - 0.035 eV/atom.[443] Employing a typical value for $\Delta\mu_C$ = 0.5 eV,[179,444] the critical size when $\Delta G$ = 0 is estimated to be ~ 2 atoms.

However, eq. 21 is not expected to be accurate for $N_{tot}$ < ~50 as the properties of atomic size nucleus significantly deviate from the bulk-like properties of graphene on Cu at the macroscopic level.[445] The carbon atoms on metal surface have been predicted to exhibit various stable configurations such as chains and arches of discrete number of carbon atoms before transforming into a hexagonal graphene structure.[207,438] Also, the hexagonal nucleus is predicted to bulge out of the planar substrate due to the significant curvature induced by the metal-edge interaction at the periphery.[209,438] On Ru and Ir, a collision of six 5-atom chains

is expected to give a 30 atom critical nucleus which is independent of temperature as the edge atoms are stabilized through interaction with surface metal atoms as revealed by in-*situ* LEEM.[204] For Cu, it has been theoretically predicted that minimum size of stable nuclei are at least two atoms and the critical size can be affected by the partial pressure of methane, hydrogen, and temperature.[207,446,447] However, direct observation of the critical nuclei size was not possible as the nucleation time was extremely short compared to the time scale of the experiment. The extrapolation of the data resulted in significant errors due to substantial coalescence and negligible nucleation at longer growth times and did not yield a physically realistic value. As our experimental results indicate that all nucleation occurs in the initial stages of the process, it is much easier to directly measure the saturation nuclei density at different temperatures and compare with existing models.

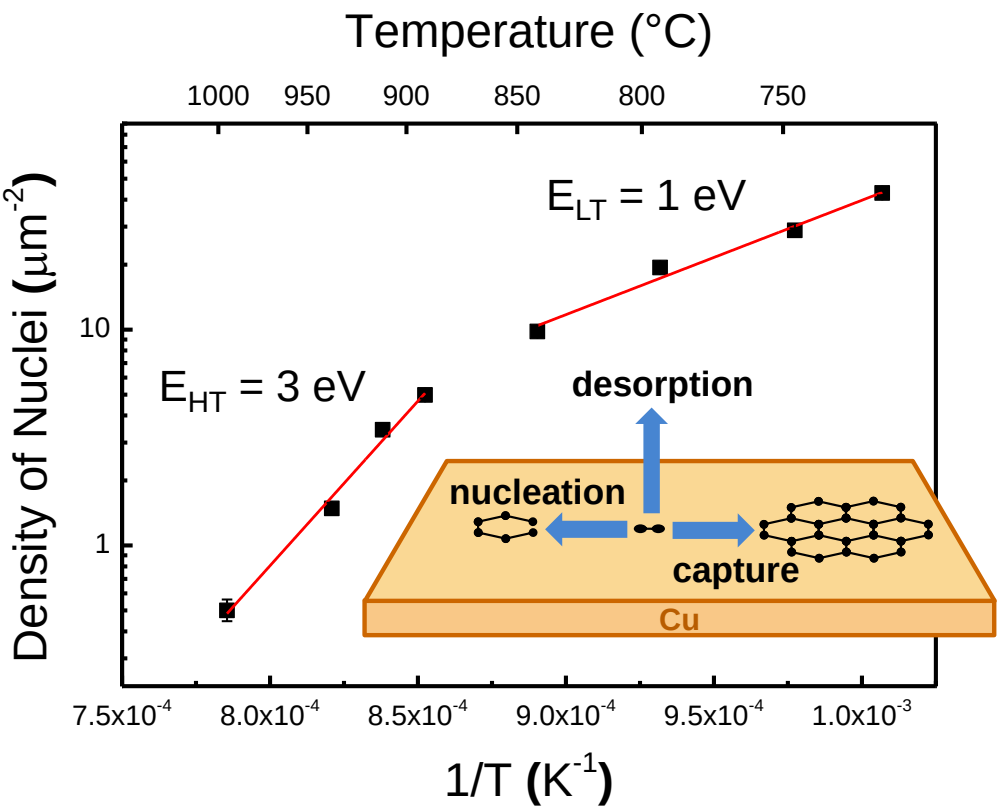


**Figure 55** Analysis of graphene nucleation behaviour. a) Natural logarithm of density of graphene nuclei *vs.* 1/T from SEM analysis at flash exposure. The linear fits are performed for the two regimes; desorption controlled (> 850 °C) and capture controlled (< 850 °C).

Here, we assume that the size of critical nucleus is temperature independent and a critical nucleus is made up of a small number of atoms since this is often the case for the quantitative

rate equation treatment of the nucleation theory that the critical nucleus size is a fixed *a priori*.[440] Moreover, the atomic scale critical nucleus seems to be a reasonable assumption supported by previous experimental and theoretical analysis of the initial steps of carbon nanotube formation using metallic catalysts.[448]

### 7.3.3 Nucleation: Saturation Density of Nuclei

In order to understand the nucleation kinetics within the framework of the existing nucleation model, we need to examine the density of nuclei as a function of temperature. Figure 55 shows the Arrhenius plot of the temperature dependent saturation density of graphene nuclei, *Ns*, estimated from density of graphene nuclei at flash exposure. We could identify two distinct slopes (below and above 870 ℃), which reflect the presence of two different nucleation mechanisms governed by different activation energies.

According to the rate equation model, under the assumption of temperature independent critical nucleus size, the occurrence of two nucleation regimes is a result of the competition between the processes of adatom capture, surface diffusion and re-evaporation.[150,429,433] In the low temperature regime (<870 ℃), the desorption of carbon adatoms is negligible due to its high activation energy (~ 6 eV[207]) so that the lifetime of an adatom at the surface before nucleation or attachment of carbon at the graphene nuclei edges is determined by carbon surface mobility. This regime then can be assigned as the capture-controlled regime where the nucleation rate is limited by capture of a carbon adatoms by supercritical nucleus. In the high temperature regime (>870 ℃), the desorption rate can be significant compared to the mobility of carbon adatoms so that the adatom lifetime and nucleation rate can be said to be desorption controlled.

The saturation density of nuclei ($N_s$) in the capture-controlled regime follows the relationship below under the assumption of atomic size critical nuclei for the methane partial pressure of $P_{CH_4}$:

$$N_s^3 \sim P_{CH_4} \times \exp\left(\frac{2E_{att} - E_d - E_{ad}}{kT}\right) \quad (22)$$

Therefore, the apparent nucleation activation energy in the low temperature regime corresponds to $E_{LT} = (2E_{att} - E_d - E_{ad})/3 = 1$ eV (Figure 55a), where $E_{att}$ is a barrier of attachment for the capture of a monomer by supercritical nucleus, $E_d$, activation energy of

surface diffusion of a monomer, and $E_{ad}$, activation energy for dissociative adsorption of $CH_4$ on Cu.

Similarly, in the desorption controlled regime,

$$N_s^2 \sim P_{CH_4} \times \exp\left(\frac{E_{des} + E_{att} - E_d - E_{ad}}{kT}\right) \quad (23)$$

the high temperature nucleation activation energy, $E_{HT} = (E_{des} + E_{att} - E_d - E_{ad})/2 = 3$ eV (Figure 55a) where $E_{des}$ is the desorption energy of a carbon monomer on Cu surface .

Considering the known values of $E_d \sim 1.8 - 0.06$ eV,[439,447,449] $E_{ad} \sim 1.7 - 1.9$ eV,[446,450,451] $E_{des} \sim 6$ eV[207] on Cu and $E_{att} \sim 2$ eV estimated from the growth on Ru,[204] the obtained values of $E_{LT}$ and $E_{HT}$ are in a reasonable agreement with the values expected from the model of capture-controlled and desorption controlled nucleation, respectively.

In both cases, the decrease in the saturation density of nuclei for increasing temperature can be explained by the increase in the capture probability of a supercritical nucleus relative to the nucleation rate due to the increase in the carbon adatom mobility (at the low temperature regime) or desorption rate (at the high temperature regime), reducing the probability of further nucleation. Furthermore, reducing the rate of hydrocarbon decomposition by lowering the methane partial pressure ( $P_{CH_4}$ ) can also decrease density of the nuclei in which the effect is expected to be more significant at high temperatures.

It must be noted that, in eq. 23, $E_{des}$ of 6 eV for desorption of carbon adatom was chosen to fit the experimental value for $E_{HT}$ instead of that of reverse reaction of $CH_4$ chemisorption as the activation energy barrier for the reverse reaction is ~ 0.8 eV[207] and too small to fit the experimental result. However, the activation energy of 6 eV may be prohibitively high for the actual carbon adatom desorption to physically occur. Alternative explanation may be that in the high temperature regime, multi-atomic carbon clusters can be significantly mobile and can decompose easily until they reach a certain critical size. The general equation for capture controlled nucleation involving the active species made of *i* carbon atoms was obtained by Venables et al.[452]

$$N_s^{i+2} \sim P_{CH_4}{}^i \times \exp\left(\frac{(i+1)E_{att} + E_i - E_d - iE_{ad}}{kT}\right) \quad (24)$$

where $E_i$ is the surface diffusion barrier for i-atom clusters. This equation reverts back to eq. 22 when $i = 1$ (monoatomic case).

Similarly, for desorption controlled regime, the general expression for $N_s$ is:

$$N_s^2 \sim P_{CH_4}{}^i \times \exp\left(\frac{E_{att} + E_i - E_d + i\left(E_{des} - E_{ad}\right)}{kT}\right) \qquad (25)$$

Therefore, the higher $E_{HT}$ value than $E_{LT}$ may arise from the activation of the carbon clusters that significantly contribute to the nucleation and growth. However, further quantitative analysis is difficult as reasonable values for what might be $i$ and the additional term, $E_i$ remain so far unknown.

More details on how eq. 22 and 23 were obtained are given in the *Saturation nucleus density solution* section of Appendix. The details for eq. 24 and 25 can be found in the articles written by J. A. Venables et al.[452,453]

### 7.3.4 Nucleation: Effect of Substrate Surface Morphology and Nucleation Exclusion Zone

So far we have modelled the graphene nucleation on an ideal, smooth homogeneous surface. However, the polycrystalline Cu foil substrate exhibits various degrees of surface roughness, grain boundary grooves, and stepped terraces that may play an important role in determining the density and shape of the nuclei, and therefore the final density of grain boundaries of the polycrystalline graphene. Different surface morphologies can be induced by several types of features that are either extrinsic or intrinsic in nature. They include (1) rolling features and other large scale irregular dents and protrusions produced during foil manufacturing (Figure 49 and Figure 56a, b, d, e,), (2) grain boundary grooves evolving at higher temperatures due to the polycrystalline nature of the substrate[454,455] (Figure 57b), (3) phantom grain boundaries grooves formed during Cu grain growth[454,455] (Figure 57b), (4) step edges and kinks formed due to the misorientation of low-index crystal facets (Figure 4c), and (5) dislocations (Figure 57b).

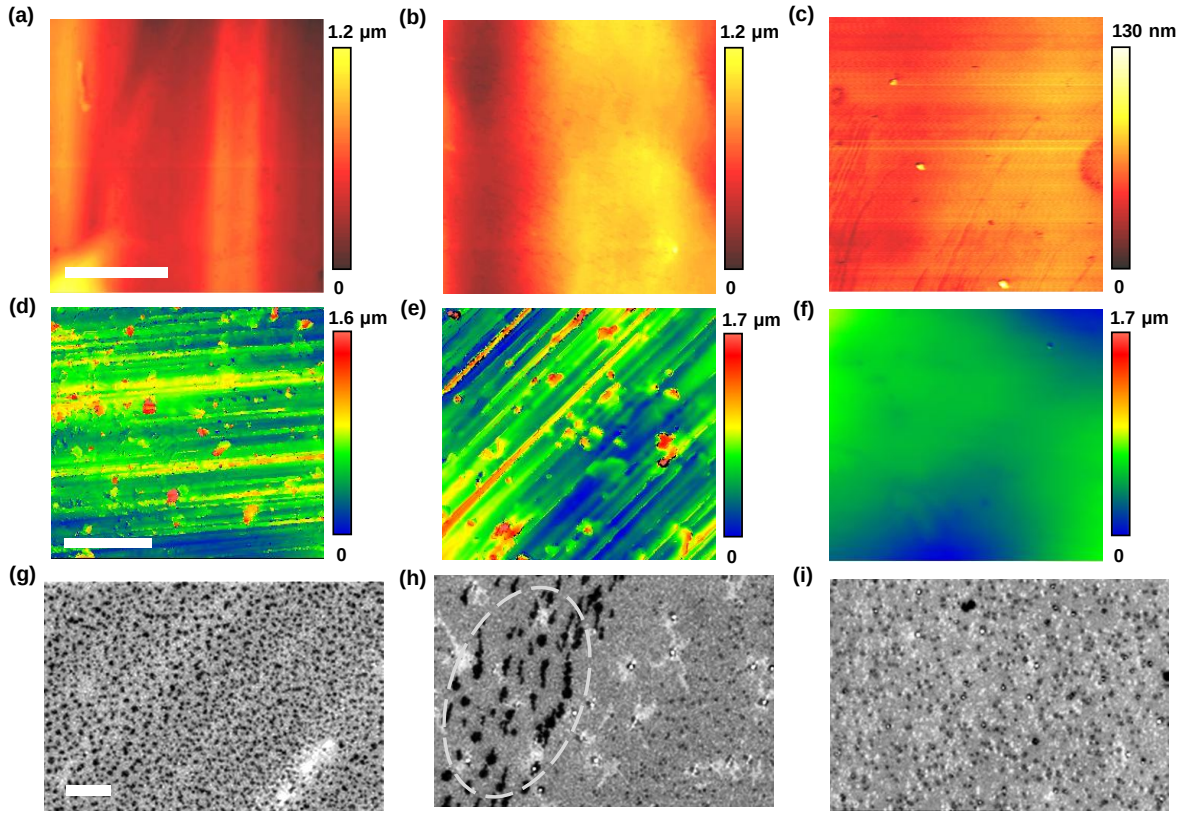


**Figure 56** Effects of different Cu morphologies are compared in order to understand the preferential nucleation sites. (a, b, c) Surface profiles imaged by AFM (scale bar, 5 µm), (d, e, f) optical interferometry (scale bar, 100 µm) and (g, h, i) SEM (scale bar, 1 µm) performed on graphene/Cu samples produced at different polishing and annealing conditions. (a, d, g) unpolished Cu substrate with annealing temperature of 750 ℃ and growth temperature of 750 ℃ (b, e, h) unpolished Cu substrate with annealing temperature of 1000 ℃ and growth temperature of 750 ℃. The dashed circle in (h) indicates a region of preferential nucleation on the rough area of Cu surface. (c, f, i) electro-polished Cu substrate with annealing temperature of 1000 ℃ and growth temperature of 750 ℃. Roughness measurement by AFM has yielded 18 nm, 8 nm, and 3 nm RMS for samples a, b, and c, respectively.

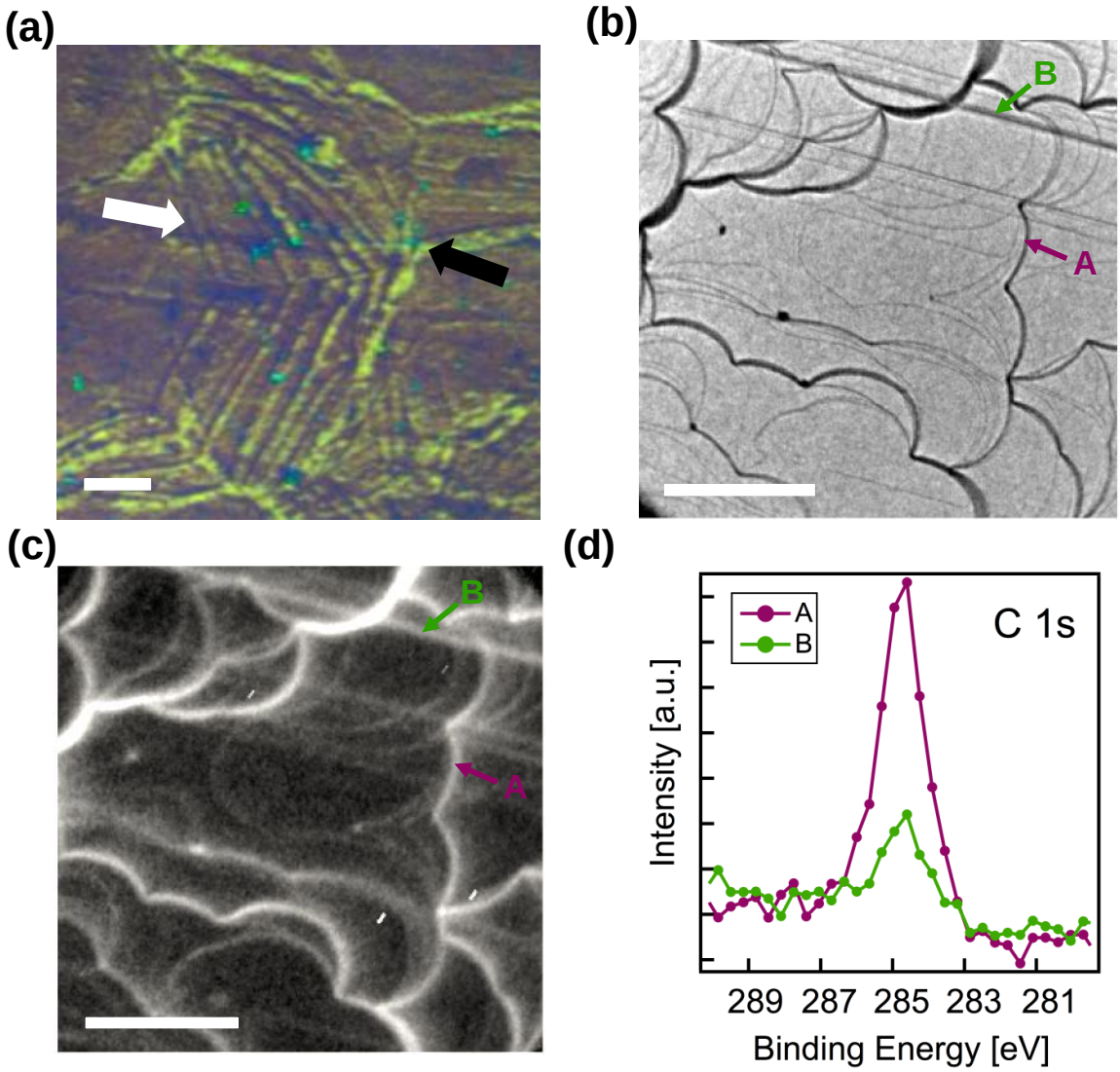


**Figure 57** a) Optical micrograph of transferred graphene onto $SiO_2$ where graphene thickness distribution reflects the Cu morphology. The darker multi-layer regions (*e.g.* white arrow) follow the graind boundaries and grooves of Cu underneath whereas brighter monolayer regions (*e.g.* black arrow) appear on a smooth Cu surface. Scale bar, 10 μm b) The LEEM image (electron energy 3.5 eV) shows Cu (100) single crystal after several cycles of sputtering and annealing at 950 ℃. Step edges (A) as well as dislocations (B) appear darker because of the different orientation with respect to the incident beam. Scale bar, 2 μm (c) C1s XPEEM map of the same region in (b) demonstrates that carbon is preferentially segregated at the step edges (A) and at the dislocations (B) (photon energy = 397.05 eV). Scale bar, 2 μm. (d) C 1s spectra at the step edge (A) and dislocation (B) in the region marked in (b, c).

On a bare Cu substrate we observed that after annealing at 1000 °C, the substrate rolling features become smooth as an expected effect of volume and surface self-diffusion of Cu,[456] but do not disappear completely (Figure 56b, e). Further, grain boundary grooves are naturally formed by Cu self-diffusion at high temperature and also phantom grain boundaries, a characteristic signature of boundary migration,[454] are visible on the transferred graphene film on $SiO_2$ (Figure 57b). We observe that these features can significantly affect graphene nucleation and growth. Preferential nucleation on top of the rolling marks in comparison with flat Cu area is observed as well as preferential growth of multilayer graphene at the grain boundaries and step edges/terraces of the grooves (Figure 57b). This is the experimental demonstration that step edges can act as energetically favourable sites for nucleation with lower size of critical nucleus and/or lower energy barrier for monomer attachment. Theoretical simulations[179] have recently predicted that lower size of critical nucleus is likely to occur at the metal step edges, although an experimental confirmation is still needed.

The lower energy barrier for carbon adsorption at step edges has been clearly demonstrated by monitoring in-*situ* the evolution of carbon impurities at the single crystal Cu surface during cleaning of the surface by $Ar^+$ sputtering and annealing at about 950 °C. Through low energy electron microscope (LEEM) (Figure 57b) and X-ray photoemission electron microscopy (XPEEM) (Figure 57c), we could observe the segregation of residual carbon species (Figure 58) and their preferential distribution along the Cu step edges and dislocations after several cycles of cleaning (Figure 57b, c). In Figure 57c, the C 1s core level intensity distribution across the surface reveals a higher concentration of carbon at the step edges in comparison to the flat areas. The C 1s binding energy (Figure 57d) is observed at 285.3 eV with FWHM of 1.4 eV. This indicates the presence of a complex mixture of $sp^2/sp^3$ carbon species with possible presence of hydrogenated bonds.[457] Step–edges (location A) with variable carbon amount can be identified as well as carbon accumulation at the crystal dislocation (location B).

From the morphological and chemical characterization of the same region, it emerges that the dangling bonds at the Cu(100) step edges preferentially anchor carbon impurities that are probably from the manufacturing and handling process even though Cu at the surface is entirely reduced to its metallic state. However, we should also consider that these carbon impurities might be present also on the Cu foils annealed at 1000 °C in $H_2$. Indeed, ex-*situ*

XPS has proven the presence of carbon impurities on the Cu foil after the surface preparation procedure while the Cu is completely reduced (Figure 50). Therefore, we should consider that this residual carbon might perturb growth and contribute to the formation of multilayer graphene at the Cu step edges.

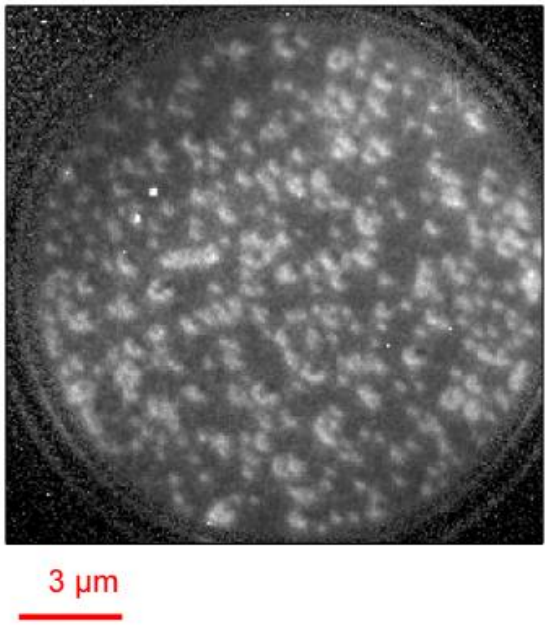


**Figure 58** C1s XPEEM image of Cu (100) surface after a few cycles of Ar ion sputtering and annealing at 600 ℃. The aggregates of amorphous carbon contaminants appear as white spots in the image. $E_{hv}$=397.05 eV.

It is difficult to decouple the roles of temperature and surface morphology in imparting the density of nuclei as the latter evolves during annealing. Thus, we also compared nucleation and growth on as received, annealed and electropolished Cu substrates where no rough rolling features are present and the surface roughness is less than 3 nm (Figure 56c, f). In Figure 56g, h, i, we can see dissimilar nucleus densities and spatial distributions on the two surfaces after growth at 750 ℃. On the unpolished sample (Figure 56g, h), graphene appears to preferentially nucleate along the rolling features evidenced by the higher density of nuclei in comparison with the lower density of nuclei away from the rolling features. While on the electro-polished Cu substrates (Figure 56i), the density of nuclei was homogenous over the whole surface. Contrary to a previous experimental finding,[176] where electro-polishing reduced the nucleation density, the overall density of nuclei was actually higher for our electro-polished sample. This is possibly due to the higher degree of supersaturation required for nucleation in the smoother surface resulting in larger $c_{nuc}/c_{eq}$. This could also explain the

shorter time needed to reach full coverage on the polished sample (Figure 59). However, electropolishing has some drawbacks as our observations suggest pitting of the Cu surface during the process could result in large defects in the graphene film (Figure 59b).

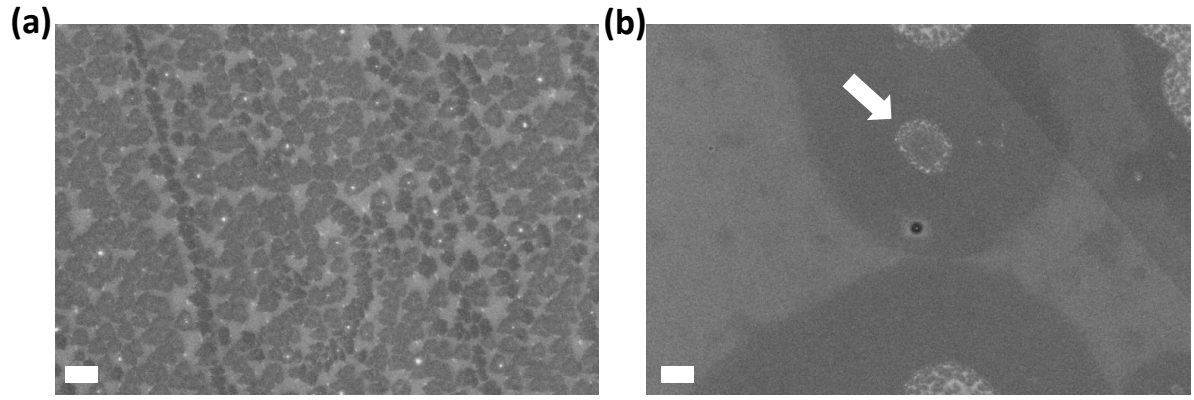


**Figure 59** SEM images of graphene grown on: (a) unpolished Cu foil (b) electropolished Cu foil at 880 ℃ for 30 sec. The arrow indicates a pit produced by electropolishing that affects uniformity of deposited graphene. Scale bar, 2 μm.

In addition, we can observe that the nucleus density on the smoother region of as-received foil (Figure 56h), which contains the corrugated regions of alternating degree of surface roughness arising from the rolling features, is significantly lower (2 $\mu m^{-2}$) than the average density in the electropolished samples (11 $\mu m^{-2}$), which is uniformly flat. This is due to the fact that lower supersaturation carbon concentration is needed to nucleate graphene in the rough regions where the carbon-adatom species are less mobile, in comparison to a flat surface. As the nucleation occurs on the rough region first, the capture of carbon adatoms by the nuclei in the rough region will further reduce the likelihood of nucleation of the smooth region within the range of the nucleation exclusion zone that depends on the surface diffusion length of carbon adatom.[458] Therefore, under the same condition of temperature and pressure, the resulting graphene nuclei density will be lower in the smoother regions of an alternating rough/smooth surface than the average density found on a uniformly flat, polished surface. In the light of this, we can conclude that the lowest nucleation density occurs not on a continuously smooth Cu surface, but on smooth regions of an alternating rough/smooth surface.

More discussions on the effect of surface morphology in the limit of low $P_{CH4}$ will be given in the next chapter when isolated graphene nuclei are studied with low *N*s on different Cu crystal orientations.

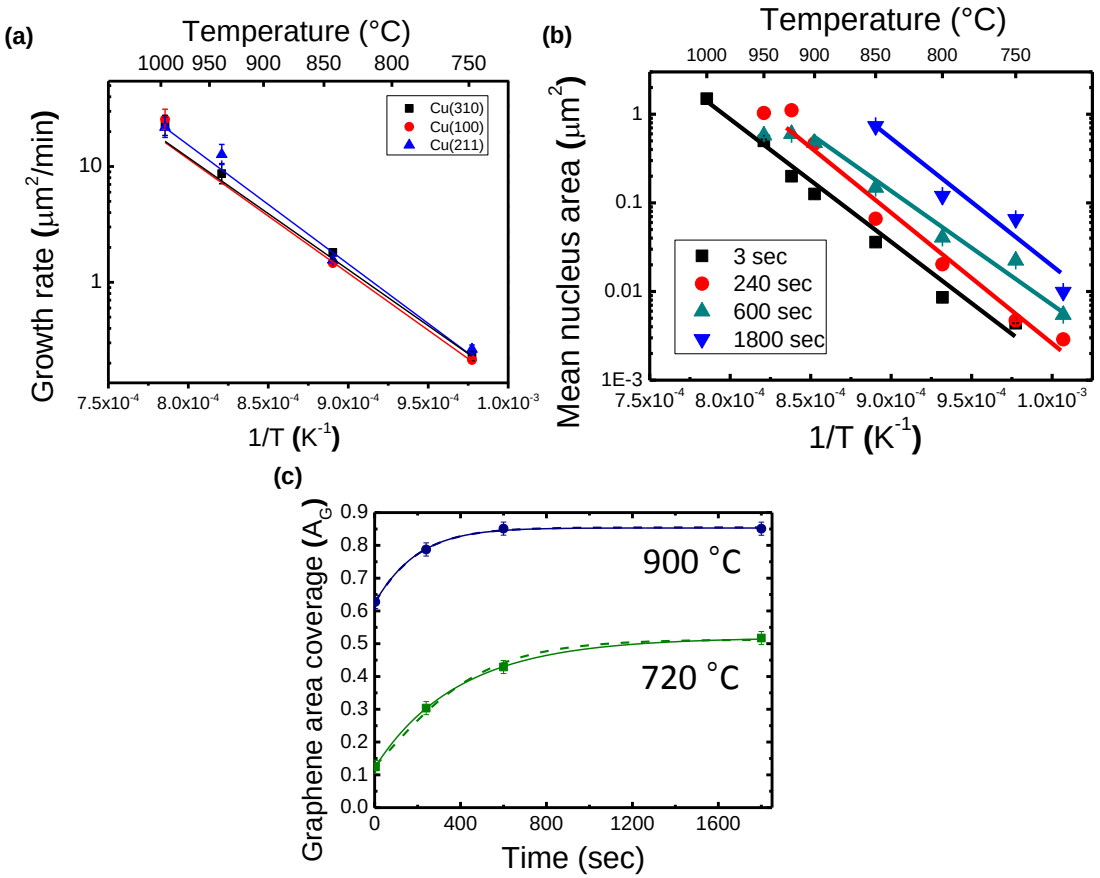


**Figure 60** Analysis of graphene growth behaviour. a) Semi-logarithmic plot of graphene nucleus growth rate *vs.* 1/T for the three main crystal orientations of the substrate [Cu(310), Cu(100), and Cu(211)]. The growth rate for each data point was obtained by calculating the mean nucleus area per growth time, assuming that the growth is linear for a short growth time. The activation energy for the growth of a nucleus is extracted from the slope of the linear fit. b) Natural logarithm of mean graphene nucleus area *vs.* 1/T for different growth time. The linear behaviour demonstrates a single mechanism for the entire range of growth temperature and time. c) Graphene area coverage *vs.* time behaviour comparing the curve fits from eq. 29 (dashed line) and eq. 31 (solid line).

### 7.3.5 Growth: Activation Energy of Growth

The graphene growth is a thermally activated process with an energy barrier of 2.6 ± 0.5 eV, as extracted from the Arrhenius plot given in Figure 60a, b. This calculated activation energy is the same for all growth times and temperature ranges where significant coalescence does not occur, indicating that the energy is not nucleus size dependent and that the whole growth can be described by a single mechanism. To define the activation energy path, we need to consider the fundamental processes that can lead to the growth of a nucleus: (1)

dissociative adsorption of $CH_4$ on the catalyst surface, (2) surface diffusion of the carbon species, and (3) enlargement of the graphene nuclei through attachment of carbon species. As the processes are sequential, the activation energy corresponds to the rate-limiting step with the largest energy barrier. We can firstly rule out step (1) as the possible rate-limiting step since the dissociative adsorption of $CH_4$ to carbon adatom on Cu(111) has an estimated barrier of 1.7 – 1.9 eV.[446,450,451] These values are significantly lower than the observed activation energy for the graphene growth. Also the low energy barrier for (2) has been estimated to be as low as 0.07 eV for a monomer and 0.6 eV for a dimer.[439,447] Therefore, on the bases of our analysis, the growth limiting factor appears to be the attachment of carbon at the growing front of a nucleus. This finding is consistent with previous work on graphene growth on Cu(100) under UHV conditions.[200]

The activation energy of carbon attachment in the graphene epitaxial growth on Ru(0001)[150,204] has been experimentally calculated to be 2 eV which is slightly lower than the energy that we found for graphene on Cu (2.6 eV). This suggests that metals with high carbon affinity may catalyse the formation of C $sp^2$ carbon more efficiently than Cu or other noble metals (Au and Ag).[459]

In order to determine whether the Cu grain orientation may affect the growth activation energy, we have specifically measured growth rates of graphene nuclei on three main crystalline orientations [Cu(211), Cu(100), and Cu(310)] of the polycrystalline Cu. No significant differences in the activation energies (Figure 60a) have been found which leads us to confirm that filled symmetric 3d-electron shell of Cu are very stable inducing Cu to form only soft bonds with carbon *via* charge transfer from the p electrons in the $sp^2$ hybridized carbon to the empty 4s states of Cu.[459] The energy involved in these bonds must be much lower than the activation energy for the graphene growth.

### 7.3.6 Growth: Evolution of Graphene Area Coverage

A simple model of edge controlled kinetics can be used to describe the growth of graphene islands on the Cu surface. Considering that graphene arises from the crystallization of supersaturated fraction of carbon adatom concentration ($c_{nuc} - c_{eq}$) according to our description, we could write the rate of graphene growth as the difference between carbon atoms attaching to the graphene edges and those leaving per unit time:

$$\frac{dA_G}{dt} = k_{att} c_{cu} \sqrt{A_G} - k_{det} \sqrt{A_G} \qquad (26)$$

where $k_{att} c_{cu} \sqrt{A_G}$ are the area increase due to the C adatoms arriving, that are proportional to the concentration of adsorbed atoms on the graphene-free Cu surface and to the perimeter of the graphene island ($\sqrt{A_G}$) and $k_{det} \sqrt{A_G}$ are the rate of area decrease due to the C adatoms leaving. All the magnitudes are per unit of area of substrate. Because in our model, the adsorption and desorption rate are balanced once supersaturation is reached, the total number of carbon atoms adsorbed per unit area during graphene nucleation and growth remains constant ($c_{nuc}$) such that we can write:

$$c_{cu} = c_{nuc} - c_G \qquad (27)$$

where $c_G$ are equal to the number of atoms in graphene. If $\rho_G$ is the atomic are density of graphene, 0.382 atoms·Å$^{-2}$:

$$c_G = A_G \rho_G \quad (28)$$

Solving equation ((26) we can write the evolution of the graphene area coverage as:

$$A_G = A_{sat} \left( \frac{e^{F(t-t_0)} + 1}{e^{F(t-t_0)} - 1} \right)^2 \qquad (29)$$

Where $F = k_1 \rho_G \sqrt{A_{sat}}$

$$A_{sat} = \frac{c_{nuc} - c_{eq}}{\rho_G} \qquad (30)$$

$A_{sat}$ is the saturation area of graphene for which $\frac{dA_G}{dt} = 0$ as $t \Rightarrow \infty$, $c_{cu} \Rightarrow c_{eq} = \frac{k_2}{k_1}$; $t_0$ is the nucleation time (time required for observable nuclei to form before significant growth). Eq. 29 fits well the experimental data (Figure 60c and Figure A4). This simple model assumes instantaneous nucleation (which seems to be consistent with the observations) and although it does not account for the coalescence of the graphene islands the fitting supports two of the key observations of our analysis: carbon attachment is the rate limiting step and the amount of supersaturation determines the final extent of coverage.

This analysis suggests that we can describe the formation of graphene as the two dimensional "crystallization" of the carbon layer adsorbed on the Cu surface. In this case, the overall behaviour from the early stage of nucleation to the later stage of graphene growth with coalescence and area saturation could also be described in a single step using the theoretical framework of the JMAK model. We can fit our data to an exponential curve using a modified JMAK equation to account for the saturation area ( $A_{sat}$ )[460] (Figure 60b):

$$A_G = A_{sat}\left(1 - e^{k(t-t_0)^n}\right) \quad (31)$$

where k is the rate constant and n is called the Avrami exponent which reflects dimensionality of the system and time-dependent rates of nucleation and growth. Under the JMAK model, n is expected to be defined by the following equation:[459]

$$n = b + pm \quad (32)$$

where the exact values of b, p, and m depend on the dimensionality of the growth and nucleation and growth rates with respect to time (Table 5). An average of n = 1.1 ± 0.5 is obtained for our experimental data. Although the large error for n possibly arises from inhomogeneous nucleation and anisotropic growth rates on the rough, facetted Cu foil surface that can affect the value of the Avrami exponent, this value appears to be consistent with our experimental observations that imply instant nucleation (b ~ 0) and non-linear 2D, attachment-controlled growth (p < 1, m = 2).

| Parameter | Value | Significance |
|---|---|---|
| **m** | 1 | 1D Growth |
| | 2 | 2D Growth |
| | 3 | 3D Growth |
| **p** | 1 | Linear growth |
| | 0.5 | Parabolic growth |
| **b** | >1 | Increasing nucleation rate |
| | 0 | Instant nucleation |
| | <1 | Decreasing nucleation rate |

**Table 5** Predicted parameters of Avrami exponent according to the eq. 31 and their dependence on the dimensionality of the system and time-dependence of the nucleation and growth behaviour.

### 7.3.7 Model for Coverage Saturation

Having established that the graphene area asymptotically saturates without reaching complete coverage, the question remains on how the final coverage of graphene can be precisely controlled by the growth conditions (temperature, $P_{CH4}$, $P_{H2}$, etc.). Figure 61 shows that $A_{sat}$ increases with growth temperature below 1000 °C with a some kind of exponential/power behaviour. This saturation behaviour has been observed often in the conditions (e.g. low $P_{CH4}$ and high $P_{H2}$) that lead to maximization of the graphene nuclei size which in turn hinder the possibility to obtain a complete layer of CVD graphene.[191,219,427] This often overlooked aspect of large grain graphene growth results in the lack of interdomain connectivity at the nm-scale,[219] which infers presence of pinholes or gaps in the polycrystalline graphene layers produced by CVD.

The saturation behaviour can be explained as following. A slow growth rate, dictated by a low supply of methane in a diluted environment, tends to minimize the nucleation density[191,219,427] but at the same time a balance of reactions on the Cu surface results in the saturation of graphene coverage before all the graphene grains are connected.[176,190] The result is that the grain boundaries contain gaps with a dimension spanning from a few nm up to hundreds of nm that fragmentize the graphene layer, degrading the electrical transport,[219] the mechanical properties,[461] and the chemical reactivity.[462]

Starting from this experimental observation, we can now try to model graphene growth as a function of temperature and gas partial pressures ($P_{CH4}$ and $P_{H2}$) over an extended range. We use the framework of the modified Langmuir adsorption theory to model the self-limited graphene growth and obtain the saturation coverage. In this context, we first need to consider the balance of chemical surface reactions that lead to the formation of graphene. The overall reaction consists in the conversion of $CH_{4(g)}$ to graphene on Cu surface and $H_{2(g)}$.

The overall reaction can be split into the three individual reversible reactions which lead to graphene formation: (1) the dissociative adsorption of $CH_4$ once it reaches the proximity of the Cu surface and bind to Cu surface sites ($S_{(Cu)}$); (2) desorption of adsorbed hydrogen ($H_{(a)}$); (3) graphene formation from carbon adsorbed ($C_{(a)}$) onto the Cu surface.

$$CH_{4(g)} + 5S_{(Cu)} \underset{k_{-1}}{\overset{k_{+1}}{\rightleftharpoons}} C_{(a)} + 4H_{(a)} \quad (33)$$

$$4H_{(a)} \underset{k_{-2}}{\overset{k_{+2}}{\rightleftarrows}} 2H_{2(g)} + 4S_{(Cu)} \quad (34)$$

$$C_{(a)} \underset{k_{-3}}{\overset{k_{+3}}{\rightleftarrows}} Graphene_{(a)} \quad (35)$$

On the basis of the observation that the direct interactions of $CH_{4(g)}$ and $H_{2(g)}$ with graphene surface are not likely to occur, as both the decomposition of $CH_{4(g)}$ onto graphene and the etching of graphene by $H_{2(g)}$ without metal catalysts are found to be negligible in the typical range of deposition temperatures (700 – 1050 °C)[219,463]; we consider only the adsorption and desorption of these species at the Cu surface.

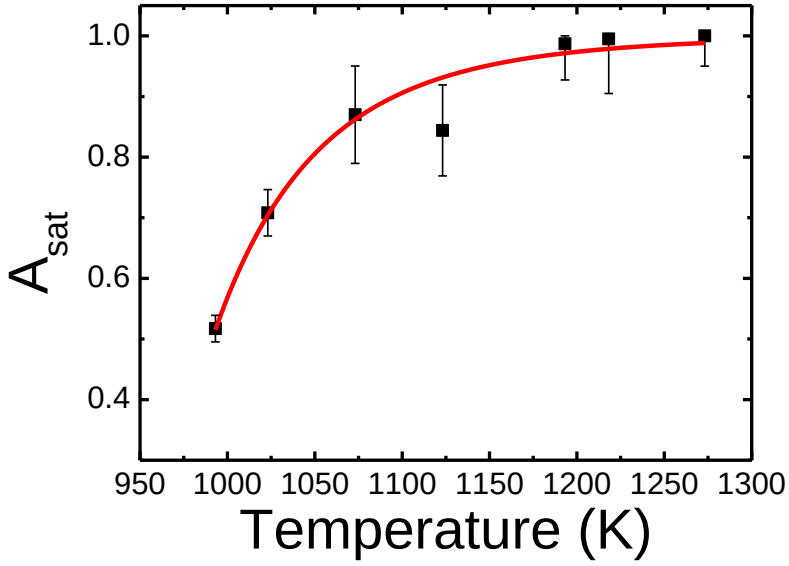


**Figure 61** Saturation graphene coverage versus growth temperature. The curve fitting was performed by using eq. 46.

We note that the reaction in eq. 33 can be broken down further into several steps involving the intermediate species that may form on Cu. However, the kinetic parameters of the intermediate steps can be combined to give an effective equilibrium constant for the overall reaction [details are given in the Appendix, *Model for Graphene Area Saturation: Full Details*], considering that the three reactions are sufficiently independent.

In addition, the intermediates (hydrogenated carbon species, $CH_x$) are not expected to be strongly bound to the surface[195,464] and at the high temperature used for the growth, they are expected to be ephemeral with lifetime much less than $C_{(a)}$,[465,466] which is often reported to

be the main active species for the formation of graphene on Cu.[194,200,208] As of now, there is no conclusive answer whether carbon adsorbed onto the Cu surface is in the form of adatoms or clusters of a few atoms. Indeed, no experimental evidence to address this issue has been reported while extended density functional theory (DFT) calculations support possible existence of these species and their active role in forming graphene, including coexistences of different species.[207,209,447]

In this context, we are however inclined to consider for our model that carbon adatoms (monomers) populate the Cu surface at high temperature and in the pressure conditions used for the graphene growth, as up until now a larger volume of publications has supported this case.[194,200,208,464-466] In addition, this represents the simplest case to be considered for the fundamental demonstration of our model, and given its flexibility; it can readily be refined in the light of future experimental evidence.

On the basis of the existing experimental data and DFT calculations available in the literature, we can estimate that the enthalpy of adsorption of methane on Cu is about 3.2 eV,[195,464,467] the hydrogen adsorption enthalpy is about -0.3 eV,[468-470] and the enthalpy of graphene formation from adsorbed carbon is about -2.4 eV.[207]

We then express the rate of adsorption of methane or hydrogen according to the gas kinetic theory as:

$$r_{ad} = \frac{P}{\sqrt{2\pi mkT}} s_0 \exp\left(\frac{-E_{ad}}{kT}\right) f\left(\theta_s\right) \qquad (36)$$

where $P$ is the partial pressure of a reactant, $m$ is the mass of a gas molecule, $k$, Boltzmann's constant, $T$, temperature, $s_0$ is the initial sticking coefficient pre-exponential factor, and $f(\theta_s)$ is free surface coverage ($\theta_s$) dependent sticking coefficient term, $E_{ad}$ activation energy of the adsorption.

Similarly, the rate of desorption of any adsorbed species on substrate sites can be expressed as:

$$r_{des} = v_n \exp\left(\frac{-E_{des}}{kT}\right)[A]^n \qquad (37)$$

where n, is the order of the reaction, $v_n$ is n-th order vibrational frequency and we assume $v_n = 10^{13}$ $s^{-1}$ for most of the cases, which is a generally used value of a vibrational frequency

when the experimental value is not known, [A] concentration of the adsorbed species, $E_{des}$, activation energy of desorption.

Therefore, the rates of adsorption ($r_{+1}$) and desorption ($r_{-1}$) for the methane decomposition reaction (eq 33) are respectively:

$$r_{+1} = k_{+1} P_{CH_4} \left[ S_{Cu} \right]^5 \quad (38)$$

and $$r_{-1} = k_{-1} \left[ C \right] \left[ H \right]^4 \quad (39)$$

Now, balancing the rates of $CH_4$ adsorption and desorption for the reaction (33) at equilibrium, we can define the constant of equilibrium, $K_1$ for the reaction (eq. 33) as:

$$K_1 = \frac{1}{\rho_s v_1 \sqrt{2\pi m_{CH_4} kT}} \exp\left( \frac{-\Delta H_{ad\_CH_4}}{kT} \right) = \frac{(\theta_C)(\theta_H)^4}{P_{CH_4} (\theta_S)^5 (1-\theta_G)^5} \quad (40)$$

Here, we assume that C and H adatoms competitively bind to the available surface sites that are not covered by graphene such that [C] = $\theta_C \rho_s / (1 - \theta_G)$ and [H] = $\theta_H \rho_s / (1 - \theta_G)$ where $\rho_s$ is the density of the surface sites on Cu (~1.5 × $10^{19}$ $m^{-2}$) and the sticking coefficient according to the Langmuir theory of monolayer adsorption is[171] :

$$s_0 f(\theta_s) = \theta_s = 1 - \theta_H - \theta_C - \theta_G \quad (41)$$

We note that the coverage by $CH_x$ species resulting from the decomposition of methane are not considered since they are considered to be short-lived.[465]

Similarly for the hydrogen adsorption/desorption reaction (eq.34):

$$K_2 = \rho_s^2 v_2^2 \left( 2\pi m_{H_2} kT \right) \exp\left( \frac{2\Delta H_{ad\_H_2}}{kT} \right) = \frac{\left( P_{H_2} \right)^2 (\theta_S)^4 (1-\theta_G)^4}{(\theta_H)^4} \quad (42)$$

Finally, for graphene formation reaction (eq. 35), we consider the balance of attachment and detachment rates of carbon atoms per unit length of graphene phase boundary based on two-dimensional crystallization kinetics.[171]

$$r_{+3} = k_{+3} \left[ C \right] = a_{cu} v_{+3\_Cu} \exp\left( \frac{-E_{att}}{kT} \right) \left[ C \right] \quad (43),$$

and $r_{-3} = k_{-3} = \frac{v_{-3\_G}}{a_G} \exp\left(\frac{-E_{\det}}{kT}\right)$ (44)

where $v_{+3\_Cu}$ and $v_{+3\_G}$ are the vibrational frequency factors for Cu and graphene, respectively, and $a_{Cu}$ = 2.3 $\times 10^{-10}$ m and $a_G$ = 1.42 $\times$ $10^{-10}$ m are the lattice spacing for Cu and graphene, respectively.

The equilibrium constant for reaction (35) is then:

$$K_3 = \frac{a_{cu} a_G v_{+3\_Cu}}{v_{-3\_G}} \exp\left(\frac{-\Delta H_{form\_G}}{kT}\right) = \frac{1-\theta_G}{\theta_C \rho_s} \quad (45)$$

Solving for the coverage of graphene from above equations, we obtain:

$$\theta_G = 1 - \frac{K_2^{\frac{1}{4}} \left(P_{H_2}\right)^2}{K_1 K_2^{\frac{5}{4}} K_3 P_{CH_4} \rho_s - K_1 K_2^{\frac{5}{4}} P_{CH_4} - \left(P_{H_2}\right)^{\frac{5}{2}}} \quad (46)$$

Thus, we now have an expression for the area coverage of graphene as a function of the temperature (eq. 46) and we can fit this to the experimentally obtained graphene coverage values. Fixing the enthalpy values and using the pre-exponential factor of $K_3$ as the only fitting parameter, we obtained the value of the pre-exponential coefficient from the curve fitting to be 6.3 x $10^{-18}$ $m^{-2}$ (Figure 61). This is a reasonable value as the vibrational frequency factors can vary over a few orders of magnitude.[471]

Based on the calculated values of equilibrium constants, we can identify the set of growth conditions for a continuous coverage of graphene, incomplete coverage of graphene, and no-possible formation of graphene. In Figure 62a, the contours plot for graphene area coverage is shown for extended range of experimental conditions of temperature and the ratio, $P_{CH4}/P_{H2}^2$, where we can assume that the enthalpy values and pre-exponential factors remain constant. Moreover, various experimental data points have been added in order to test our model in the light of the experimental results already published in the literature.

In the region with zero graphene coverage, $\theta_G < 0$, the adsorbed carbon remains as two dimensional gas without forming an extended $sp^2$ network as the surface concentration of carbon adatoms is low.[171] Between $\theta_G$ = 0.997 and $\theta_G$ = 0, the ensemble of growth parameters leads to the coexistence of graphene islands and adsorbed carbon in the copper

surface without actually enabling the formation of continuous coverage. Note that $P_{CH4}/P_{H2}^2$ was chosen as the main parameter for the gas phase because $\theta_G$ was found to be virtually independent of individual gas partial pressures if the ratio remained fixed (detail is given in the Appendix, *Details on graphene coverage in terms of degree of supersaturation*).

We can see that both the data points related to continuous graphene layer[18,20,70,143,341,350,472] and discontinuous graphene layer[196,473-477] fall within the range of $P_{CH4}/P_{H2}^2$ values and temperature predicted to provide the same behaviour. Further, we have also plotted our experimental data (red squares) referring[427] to graphene grown at different temperatures where the graphene coverage can be either complete or incomplete depending on the temperature.

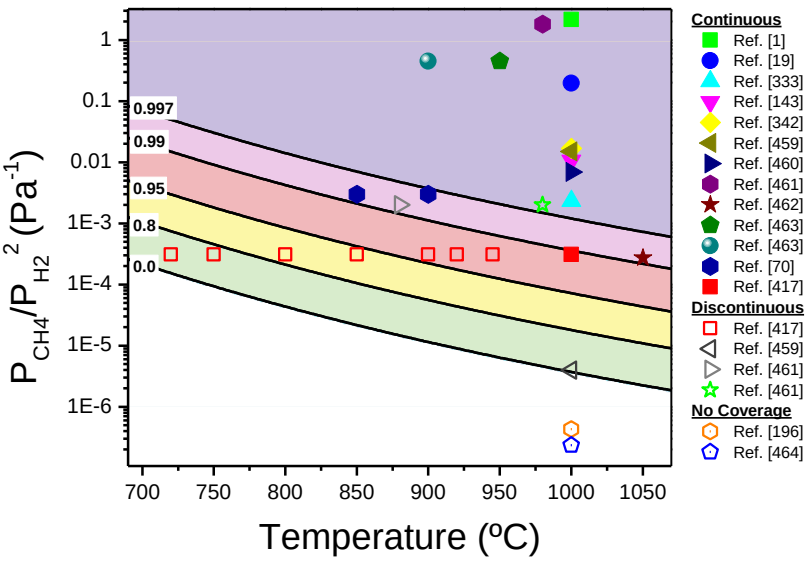


**Figure 62** Contour plot for saturation graphene coverage, $\theta_G$ ($\theta_G$ values are indicated by the labels near the left axis). Values calculated from experimental conditions reported in the literature for various growth conditions have been plotted for comparison.

Our theory can be further applied to provide a useful insight regarding the degree of supersaturation during graphene nucleation as the saturation area coverage can also be determined by the supersaturation concentration of adsorbed carbon, $[C]_{sup}$ at the onset of nucleation.[171] On the basis of Langmuir theory, the supersaturation concentration of carbon adatoms can be estimated to be $[C]_{sup} = \theta_c^{'}\rho_s$ where $\theta_c^{'}$ is the coverage of carbon atoms considering only the balance of reactions (33) and (34) on Cu surface before the onset of

graphene nucleation and growth. This sets upper limit on the physical supersaturation level of carbon adatoms. Within the limit of attachment/capture controlled nucleation and growth, this gives a reasonable upper limit for actual $[C]_{sup}$ since adsorption and desorption equilibrium (eq 33 and 34) is reached more quickly than the attachment/detachment equilibrium (eq 35). For a finite graphene coverage, $[C]_{sup}$ must be greater than the equilibrium carbon concentration, $[C]_{eq} = 1/K_3$. Figure 63a shows the variation of $[C]_{sup}$ and $[C]_{eq}$ as a function of temperature. The intersection (indicated by an arrow) determines the minimum growth temperature required to form graphene.

Thus, the equation for saturation area coverage can be rewritten as (details are provided in the Appendix, *Details on graphene coverage in terms of degree of supersaturation*):

$$\theta_G \approx 1 - \frac{[C]_{eq}}{[C]_{sup}} \qquad (47)$$

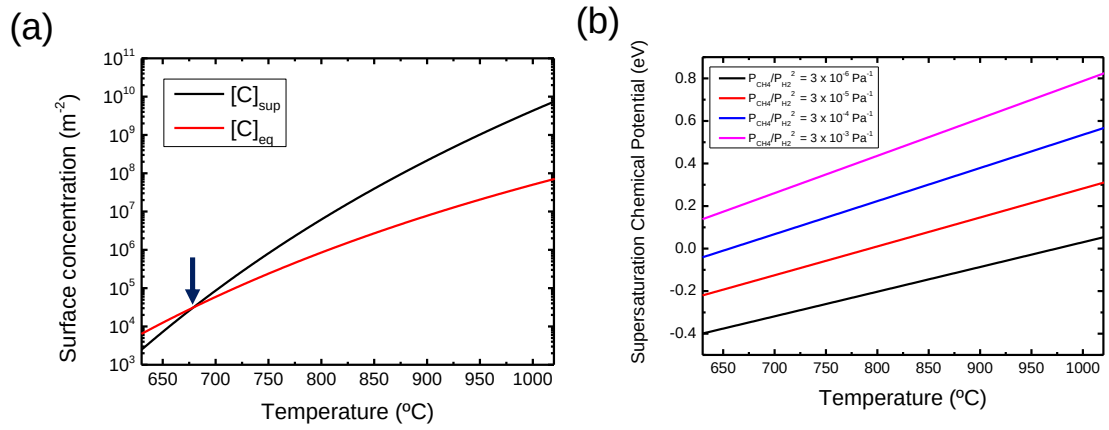


**Figure 63** a) Variation of supersaturation carbon concentration and equilibrium carbon concentration with temperature. The arrow indicates the temperature (~954 K) below which graphene formation does not occur as $c_{sup} > c_{eq}$. The $CH_4$ and $H_2$ partial pressures used for the calculation are $P_{CH4} = 40$ Pa and $P_{H2} = 360$ Pa. b) Variation of supersaturation chemical potential with partial pressure ratios and temperature.

The supersaturation chemical potential represents the driving force to form graphene at the onset of nucleation and it can be conveniently used as criteria for nucleation and growth of graphene for a set of various growth conditions. We have calculated the supersaturation chemical potential values for the data points based on the reported values of partial pressures

of $CH_4$, $H_2$ and growth temperatures. $\mu_{sup}$ as a function of partial pressures and temperature are illustrated in Figure 63b.

There are possible sources of error in the computed plots, such as inaccuracy of enthalpy values extrapolated by the DFT calculations, the equilibrium pre-exponential factors due to variability of the surface morphology and crystallinity of the Cu surface, and the systematic errors associated to accuracy in the partial pressure measurements. We have associated uncertainties to these values and computed the error bounds for the contours in Figure A3. It is worth noting that the errors are not significant (well below one order of magnitude) and the data from the literature fit well with our model within the range of the error bounds. Another challenge to our model is that in the limit of high $\theta_G$ close to 1, there may be an additional energy required to properly "stitch" the graphene grains of different orientations to for a continuous polycrytalline graphene. This may be especially true for Cu(100) and other high index planes where rotated domains of various misorientation angles are frequently observed. Since the formation energies for the grain boundaries are so far unknown, we assume the case of a single rotational domain as in the case of Cu(111). In the limit of low supersaturation, $\mu_{sup} \sim 0$, we have not considered the additional energy barrier to form the critical nuclei whose size has not been reliably predicted so far. $\theta_G$ value estimated by our model in this limit represents the upper limit where there is no barrier for nucleation. Further systematic experiments will help to refine the predictions.

Overall, on the basis of our model, it is generally advisable to perform graphene growth at high partial pressure of the carbon source and temperature in order to obtain a continuous layer. High temperature is also beneficial to decrease the density of nuclei, which is also in agreement with experimental observations[191,427] and the theoretical predictions of the rate equation model.[427,429] However, graphene grains of significantly larger size are formed under the extremely low pressure conditions in which continuous graphene coverage cannot be achieved.[191,219] To overcome this hurdle, one possible solution is employing two-step growth where large grains of graphene nucleate at low density and grow to saturation under low $P_{CH4}$ and high $P_{H2}$ in the first step, and then $P_{CH4}$ is increased in order reach a continuous graphene in the 2nd stage. Indeed this has been experimentally shown by X. Li et al.[190,191] after empirical observation that the density of nuclei increases at lower temperatures. Now to do so, appropriate gas pressures can be chosen by directly referring to the plot.

Another useful implication of our model is that fast cooling and termination of $H_2$ flow into the chamber during the cooling stage are preferred for defect free graphene coverage, because at lower temperature the chemical potential toward complete coverage of graphene decreases for fixed $P_{CH4}/P_{H2}$ which then leads to the catalytic etching of graphene by $H_2$ during cooling. This effect of $H_2$ etching has also been observed by Zhang et al.[195] where etching becomes more significant at lower temperature than 1000 ℃ as the equilibrium shifts toward the left side of the $CH_4$ decomposition reaction (eq. 33).

We can also estimate the concentration of C adatoms based on the experimental results of area coverage evolution over time. Previously, the expression for time-dependent graphene area coverage, $A_G$(t) could be obtained by solving the following differential equation of a simple, edge-controlled kinetics eq. 26:

where $k_{att}c_{cu}\sqrt{A_G}$ are the rate of graphene area coverage increase due to atoms arriving, that are proportional to the concentration of adsorbed atoms on the graphene-free Cu surface and to the perimeter of the graphene island ($\sqrt{A_G}$) and $k_{det}\sqrt{A_G}$ are the rate of decrease in the area coverage due to atoms leaving.

Eq. 26 and the solution to the equation (eq. 29) can be modified according to our model that: $c_{cu}(t=0)=c_{nuc}=[C]_{\text{sup}}$, assuming that adsorption and desorption equilibrium is reached much faster than the nucleation of and growth of graphene, $c_{\text{nuc}} = [C]_{\text{sup}}$ at the onset of the nucleation.

And $c_{cu}(t\to\infty)=c_{eq}=[C]_{eq}$ (48)

Using the relationship for the predicted saturation area, $\theta_G$, $[C]_{\text{sup}}$ and $[C]_{\text{eq}}$:

$$A_G(t\to\infty)=A_{sat}=\theta_G\approx 1-\frac{[C]_{eq}}{[C]_{\text{sup}}} \quad (49)$$

Also, $\frac{dA_G(t\to\infty)}{dt}=0\Rightarrow k_{att}c_{nuc}\left(1-\theta_G\right)=k_{det}$ (50)

Substituting the above relationships to eq. 26, and solving the equation, we can write the evolution of the graphene area coverage as:

$$A_G = \theta_G \left( \frac{e^{F(t-t_0)}+1}{e^{F(t-t_0)}-1} \right)^2 \quad (51)$$

where $F = k_{att}\sqrt{\theta_G} = \frac{k_{+3}c_{nuc}\sqrt{N_s\theta_G}}{\rho_G} = \frac{a_{cu}v_{+3\_Cu}}{\rho_G}\exp\left(\frac{-E_{att}}{kT}\right)c_{nuc}\sqrt{N_s\theta_G}$ (52)

Here, $k_{att}$ which gives the rate of the overall fractional area increase per unit time, can be linked to $k_{+3}$ which gives the number atoms arriving per unit length of a nucleus edge per unit time, as $\frac{da_G}{dt} = \frac{k_{+3}[C]}{\rho_S}\sqrt{a_G}$ and $A_G = N_s a_G$, where $a_G$ is a mean area of graphene nucleus, and $N_s$ is the density of nuclei independent of time assuming instantaneous nucleation.

Therefore, $k_{att} = \frac{k_{+3}\sqrt{N_s}}{\rho_G}$ (53)

Then the exponential factor, F, related to the rate constant of carbon attachment now becomes:

$$F = \frac{k_{+3}c_{nuc}\sqrt{N_s\theta_G}}{\rho_G} = \frac{a_{cu}v_{+3\_Cu}}{\rho_G}\exp\left(\frac{-E_{att}}{kT}\right)c_{nuc}\sqrt{N_s\theta_G} \quad (54)$$

Then, using the experimentally obtained $F$, and $N_s$, and $\theta_G$, and estimated value of $k_{+3}$, $c_{nuc}$ can be calculated by the following equation:

$$c_{nuc} = \frac{\rho_G F}{k_{+3}\sqrt{N_s\theta_G}} \quad (55)$$

The calculation for $c_{nuc}$ based on the analysis of the experimental values of F, $N_s$, and $\theta_G$ (Figure 64) yields the supersaturation surface carbon concentration values on the order of ~1 × $10^9$ $m^{-2}$ in the range of 720 – 1000 ℃, which are remarkably similar to the range of $[C]_{sup}$ values predicted by our model, although the large uncertainty in $v_{+3\_Cu}$ and F makes further analysis difficult. This $[C]_{sup}$ value is much lower than surface carbon adatom concentration of > $10^{16}$ $m^{-2}$ on Ru(0001)[204] (consequence of high adsorption energy of C on Ru) that has been measured by in-*situ* LEEM. The extremely low surface concentration is possibly the reason that the recent attempt to directly measure the surface carbon concentration on Cu by LEEM or XPEEM techniques[203] has been fruitless so far.

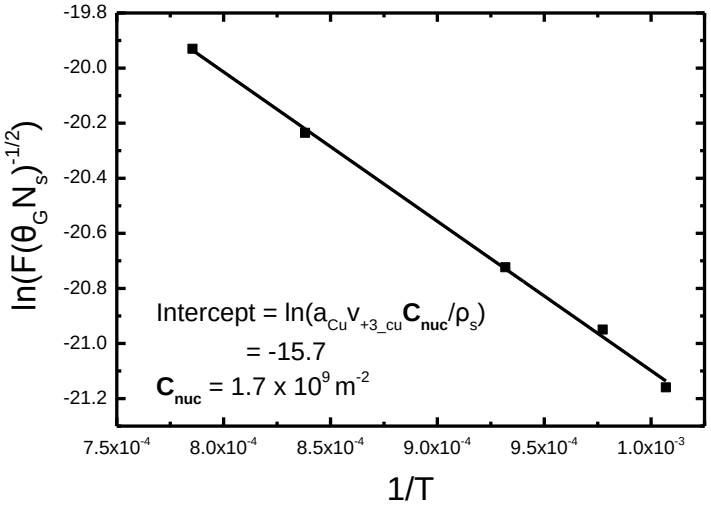


**Figure 64** The $\ln(F(\theta_G N_s)^{-1/2})$ vs. 1/T curve based on the temperature dependent experimental results. The temperature dependent F values were calculated from the fitted values of time-dependent graphene area coverage in Figure A2. The linear fitting was performed to estimate the value of critical supersaturation concentration, $c_{nuc}$.

It is worth noting that our basic approach based on the balance of adsorption/desorption and surface reactions could be extended to include the effect of other transient species (e.g. the $CH_x$). However this will not detract from the main conclusion (the existence of three regions defined by the balance of the reactions) and furthermore, the fact that we can obtain a good predictive fitting by considering only the C adatom species may indicate that this is the most important active carbon species.

### *7.4 Conclusions*

In summary, our analysis shows that graphene arises from the crystallization of a supersaturated fraction of carbon-adatom species and that its nucleation density is the result of competition between the rates of nucleus growth by adatom capture, surface diffusion of carbon species, and desorption of carbon adatoms. As the energetics of these phenomena varies with temperature, the nucleation activation energies can change significantly with temperature, thus defining two nucleation density regimes: one controlled by carbon adatom species capture at low temperatures (<870 ℃) and the other, controlled by desorption at high temperatures (>870 ℃). On the other hand, the graphene growth can be uniquely described by the carbon attachment to the graphene edges as the rate-limiting step with activation energy of 2.6 eV. In all cases, an important role is played by the substrate roughness.

Interestingly, on the basis of our model and experimental observation, the graphene nucleus density can be lower in the flat regions of an alternating rough/flat surface than the average density found on a uniformly flat substrate due to the effect of the nucleation exclusion zone.

Control over the supersaturation carbon concentration, which is needed to nucleate graphene, and the equilibrium concentration of adsorbed carbon species on the Cu surface enables production of a continuous, pinhole-free graphene film. To this end, we have modelled the graphene growth by CVD on Cu surfaces to formulate the criteria for specific graphene coverage. The latter provides the range of growth parameters (temperature and gas pressures) in which two phases (graphene and adsorbed carbon) uniquely define the conditions for a continuous polycrystalline graphene layer, an uncompleted polycrystalline graphene layer coexisting with adsorbed carbon and adsorbed carbon species without graphene coverage. The phase diagram provides strategies to address the fundamental problems of continuity, and crystalline grain dimensions. Thus, our analysis provides the physical model that can guide the synthesis of single crystal graphene films by carefully engineering the substrate surface and selecting growth conditions.

# 8 Effect of Cu Crystal Orientation on Shape, Orientation, and Alignment of Graphene Nuclei

## *8.1 Introduction*

In this chapter, the epitaxial relationship between the graphene overlayer and Cu substrate of various crystal orientations will be examined to provide a guideline for controlling the density, shape, and alignments of the polycrystalline CVD graphene at the mesoscale. The epitaxial relationship between graphene and Cu is not a very well explored subject in current literature because graphene's epitaxial registry on Cu has been perceived to be completely incommensurate without any preference for rotational alignments due to the large structural mismatch and weak C-Cu interaction. However, recent growth experiments performed on low index Cu surfaces, Cu(100) and Cu(111) have shown strong evidence for preferred alignments with respect to the Cu crystal orientations.[178,180,202,428,478-480] Moreover, the growth behavior (growth rates, density of nuclei, and shapes) appears to be affected by Cu crystal orientations.[175,481] In order to determine the detailed epitaxial relationships and select the best Cu surface for tailoring graphene mesoscale structures with desired properties, more comprehensive set of experiments is required.

In this work, CVD growth of graphene on Cu is performed on low index Cu surfaces, Cu(100), Cu(111), and Cu(110), as well as high index surfaces such as Cu(310), Cu(211), and Cu(221) at low $P_{CH4}$ conditions. This has been enabled by using polycrystalline Cu foil of random texture. Extrinsic surface defects of the foil such as rolling features and scratches have been eliminated by annealing and electro-polishing which has produced smooth surfaces to clearly distinguish the intrinsic dependence of graphene growth features on Cu crystal orientations. Using the general model of epitaxial deposition and group theory, the crystal orientation dependence of graphene nucleus symmetry, anisotropy, and alignments of the graphene nuclei is explained.

## *8.2 Results and Discussion*

The experimental setup, growth methods, and characterization techniques for the following results are described in Experimental Setup Chapter. Here we have used much lower $P_{CH4}$ (using a leak valve to control the flow rate of $CH_4$ instead of mass flow controller) than the experiments performed in the previous chapter reduce the growth rate in order to observe isolated graphene nuclei at low nucleus density and coverage.

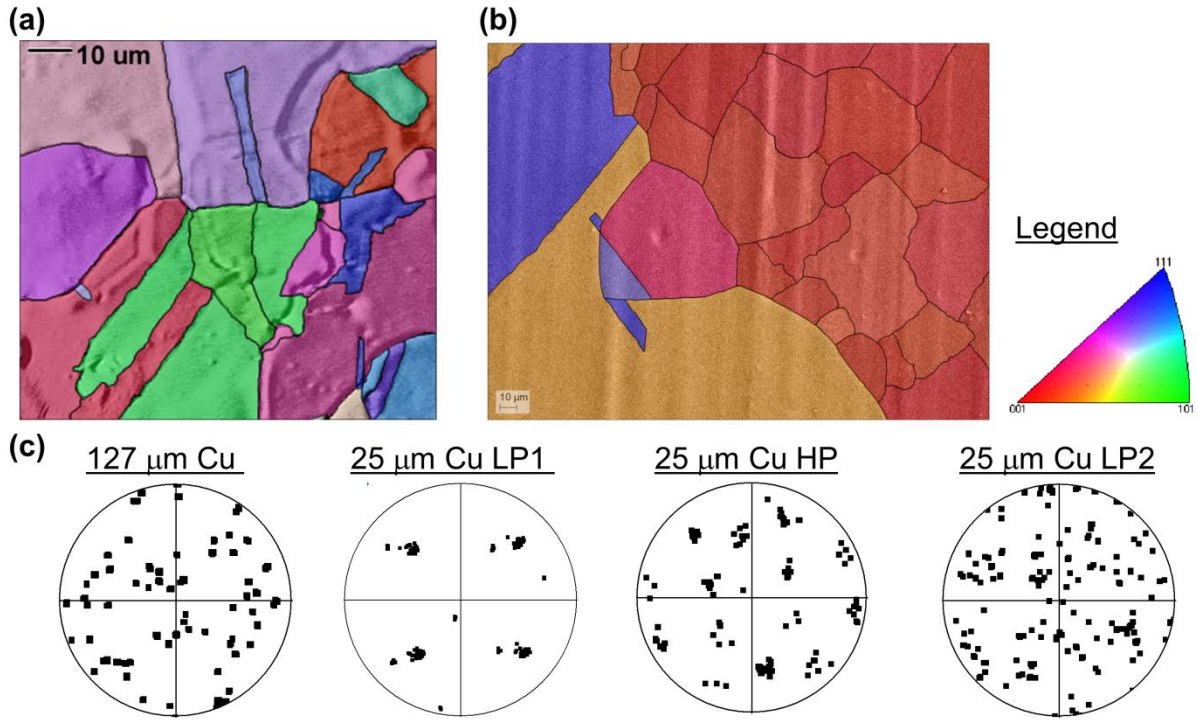


**Figure 65** Texture Analysis of Cu foils by EBSD. a) Cu crystal orientation colour map of 127 μm Cu. b) Crystal orientation colour map of 25 μm CuLP1. d) (111) pole figures for four types Cu foils.

### 8.2.1 Texture Analysis of Cu Foils

In order to determine the crystal orientation of Cu, extensive crystallographic characterization on various Cu foils after graphene growth was performed. It was found that the crystal orientations of Cu grain even after graphene growth at high temperatures over 1035 °C, heavily depends on the initial foil texture that likely originates during the manufacturing. The most commonly used Cu substrate in the literature and in this work is 25 μm thick, 99.8 at. % purity Alfa Aesar Cu foil #13302 lot H18W024 (25μm Cu-LP1). This foil is initially cubic textured (100) without significant misorientation as can be seen from the EBSD mapping in Figure A5 in Appendix and it undergoes abnormal grain growth at

temperatures greater than 900 ℃ (Figure 65 and Figure 66). Under abnormal growth, Cu(100) grains were consumed by the enlarged grains that mostly have either (310) or (221) type orientations. The reason for the abnormal grain growth of high index Cu crystals over low index surfaces in Cu #13302 is not clear, however, this may be due to the impurities or inherent strain within the Cu foil and accelerated grain boundary movements at the surface of the foil for certain grain orientations as the size of the grains become larger than the thickness of the foil.[482]

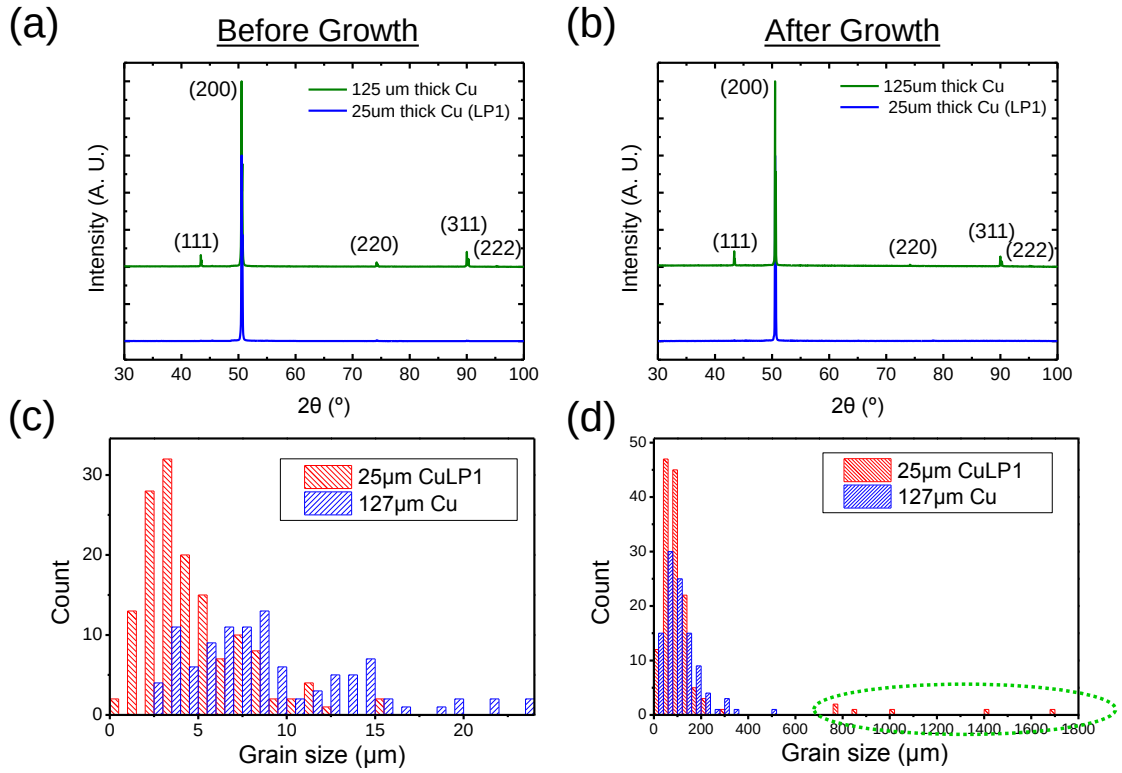


**Figure 66** a,b) XRD intensity of Cu foils (127 μm Cu and 25 μm Cu-LP1) before (a) and after (b) the growth. c,d) Cu grain size distribution for Cu foils (127 μm Cu and 25 μm Cu-LP1) before (c) and after growth (d).

Other types of Cu foil examined were #13380 127μm thick, 99.9 % purity Cu foil (127μm Cu), #10950 25 μm thick, Puratronic® 99.999 % purity Cu foil (25 μm Cu-HP), and #46986 25 μm thick, 99.9% purity Cu foil (25 μm Cu-LP2) which were all supplied by Alfa Aesar. In most cases, these Cu foils exhibit richer variety of Cu crystal orientations (Figure 65), and have less tendency to undergo abnormal grain growth. The XRD results in Figure 66a and Figure 66b suggest that the texture after growth was largely unchanged from the

initial textures. This highlights the importance of the manufacturing technique to prepare the Cu substrates of desired orientations.

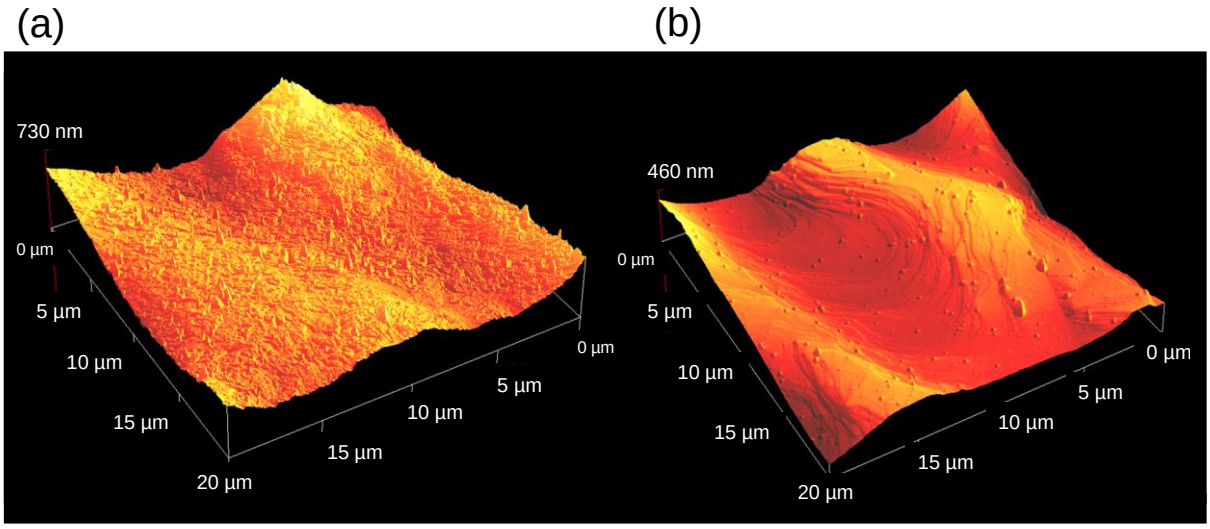


**Figure 67** AFM 3D topography of 127 µm thick Cu, and 25 µm thick Cu-LP1 after growth.

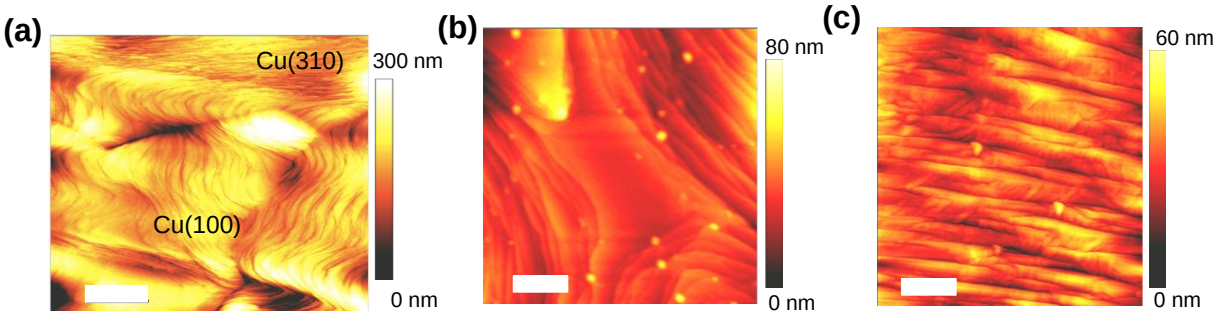


**Figure 68** AFM height profiles of 25 µm Cu-LP1 after growth. (a) Polycrystalline region with Cu(100) and Cu(310) grains. Scale bar, 10 µm. (b) High magnification AFM image of region of flat atomic terraces. Scale bar, 1 µm. (c) High magnification AFM image of Cu(210) region illustrating the presence of aligned, periodic facets. Scale bar, 1 µm.

### 8.2.2 Surface morphology of Cu foils

Before examining the influence of Cu crystal surfaces on the graphene growth, the effect of the extrinsic defects such as surface roughness and rolling features on Cu must be addressed. Figure 67 shows the AFM 3D topology profiles for 25 µm Cu-LP1 and 127 µm Cu foils after graphene growth. The large scale, parallel undulations in heights with periodicity of micrometres can be ascribed to the rolling features of Cu foil. Between the peak and trough of the undulations, 25 µm Cu-LP1 appears to have atomically flat terraces of

Cu(100) surface with vicinal step edges. On the other hand, 127 μm Cu has rougher and disordered surface facets that do not exhibit atomically flat surfaces as in the case of 25 μm Cu. In addition, on 25 μm Cu-LP1, crystal orientation dependence on the Cu surface topology can be clearly seen. The AFM image in Figure 68 clearly illustrates that appearance of the step edges depend on Cu crystalline orientations, with Cu(100) exhibiting larger patches of flat atomic terraces with curved step edges with irregular shapes, while Cu(211) surface exhibits aligned facets in one direction with regular periodicity. This formation on parallel ridges on high index surfaces has been attributed to minimization of surface energy by breaking up of the flat surface to low surface energy surface facets [usually Cu(100) and Cu(111)]. [483,484] This feature has been known to develop more prominently at low pressure and high temperature through the effect of thermal etching.

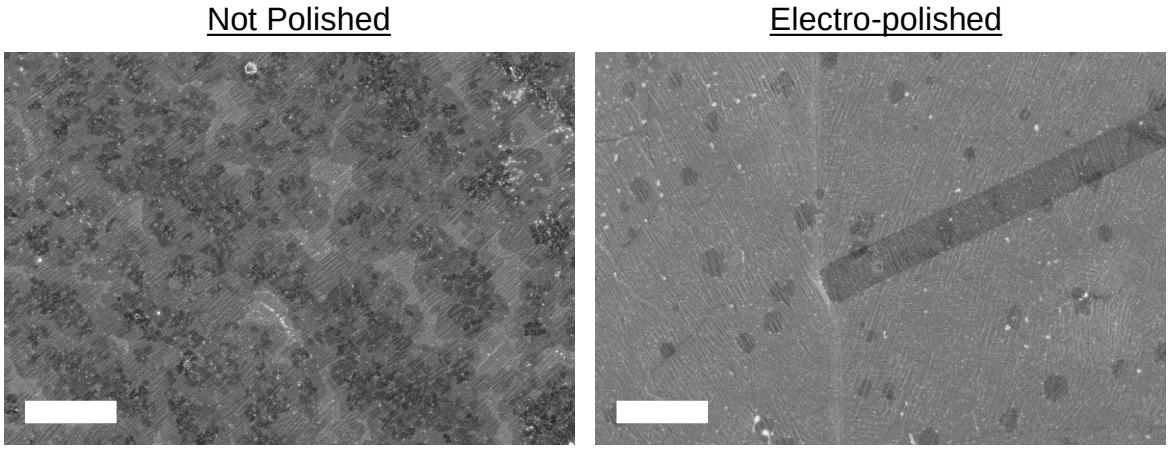


**Figure 69** SEM image of as grown graphene on 127 μm Cu without polishing (left) and with electro-polishing (right) for growth conditions of $P_{CH4}$ = 0.4 mbar, $P_{H2}$ = 3.6 mbar, $T_{growth}$ = 1030 ℃, $t_{growth}$ = 30 min. Scale bars, 10 μm.

### 8.2.3 Effect of Electropolishing on Graphene Growth: Removal of Extrinsic Surface Defects

As the extrinsic features of Cu morphology hinder detailed examination of graphene growth on flat Cu crystal surfaces, electropolishing has been employed to eliminate most of the extrinsic surface defects. The rougher nanoscopic surface features have lead 127 μm Cu to yield much higher coverage and number of graphene multilayer nuclei that what was obtained on 25 μm Cu-LP1 at the usual growth conditions. As can be seen in Figure 69, the multilayer coverage (darker contrast in the SEM images) is much smaller on the

electropolished sample with 127 μm Cu foil of the same crystal texture. This appears to be a general observation for all the Cu foils investigated where multilayer nucleation is initiated at the surface defects. The high thickness and non-uniformity in regions of high surface roughness have been explained by variation in flux of $CH_4$ arriving at the copper surface in the mass transport regime of the CVD.[143]

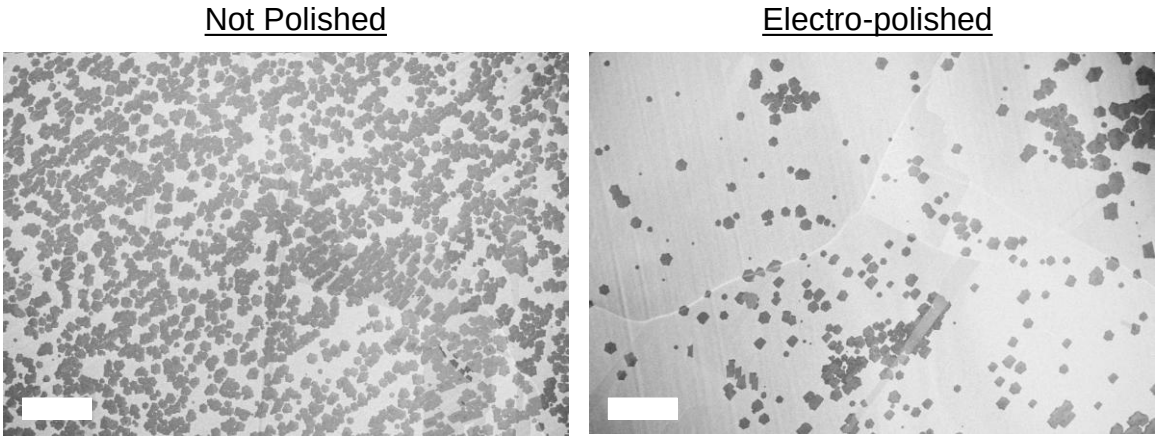


**Figure 70** Effect of electropolishing at low supersaturation on 25 μm Cu-LP1. The SEM images show that much larger density of nuclei is seen on as-received foil (left) than on the electropolished 25 μm Cu-LP1 (right). $P_{CH4}$ = 0.001 mbar, $P_{H2}$ = 1.4 mbar, $T_{growth}$= 1030 ℃, $t_{growth}$ = 50 min. Scale bars, 200 μm.

Moreover, the electropolished surface gives significantly lower density of nuclei at low methane pressure. Contrary to the high $P_{CH4}$ growth where instantaneous nucleation occurs uniformly over large area even on a flat surface,[427] the low $P_{CH4}$ results in low supersaturation of carbon adsorbates that results in non-instantaneous nucleation only on defect sites that can be eliminated by electropolishing. Figure 70 shows much less density of nuclei after the growth time of 50 minutes at low $P_{CH4}$ on an electropolished surface. This will be beneficial toward increasing the grain size of graphene when the continuous film is obtained.

It must be recognized that electropolishing cannot entirely eliminate the surface roughness (thereby surface defect induced nucleation) which are produced by grain boundary grooving and phantom grain boundaries[455] that occur during the annealing stage just before the growth (Figure 71a). In addition, a caution must be exercised as the pitting of the surface formed during non-ideal electropolishing conditions (voltage overshoot, oxygen bubble formation, etc.) can also induce extra seeding of graphene nuclei (Figure 71b).

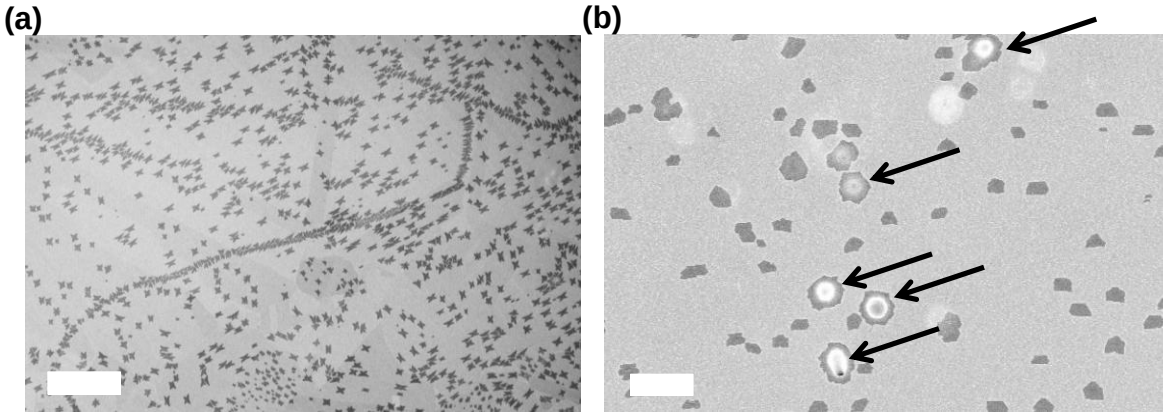


**Figure 71** Effect of surface imperfections present after electropolishing. a) SEM image of electropolished 127 μm Cu after growth. High density of nucleation along the grain boundary grooves is apparent. $P_{CH4}$ = 0.0015 mbar, $P_{H2}$ = 0.23 mbar, $T_{growth}$= 1030 ℃, $t_{growth}$ = 2 min. Scale bar, 200 μm. b) SEM image of graphene nuclei on 25 μm Cu-LP1. Preferred nucleation is evident at the pits indicated by arrows which were produced during the electropolishing process. $P_{CH4}$ = 0.0015 mbar, $P_{H2}$ = 2.2 mbar, $T_{growth}$= 850 ℃, $t_{growth}$ = 40 min. Scale bar, 20 μm.

One way to visualize the microstructure in continuous graphene is to employ LEED and dark-field LEEM analysis. Figure 72 shows the colour map of relative orientations of graphene grains superimposed on LEEM image within the continuous film on different substrates: as-grown on a unpolished Cu foil (25μm Cu-LP1), transferred on an Au/mica substrate, and transferred on a $SiO_2$/Si following the growth on electropolished substrate (25μm Cu-LP1). Below the dark-field images are the LEED patterns from the same areas used to construct the orientation dependent maps of the grains. The Cu substrate exhibited facets which did not allow the entire area within the field of view to be completely imaged by dark field analysis as the graphene grown on the surface facets does not lie normal to the rest of the imaged surface. This is also evident from the extra spots (indicated by the circles in Figure 72a) in the LEED patterns away from the main, first-order diffraction patterns that are likely coming from the tilted facets.

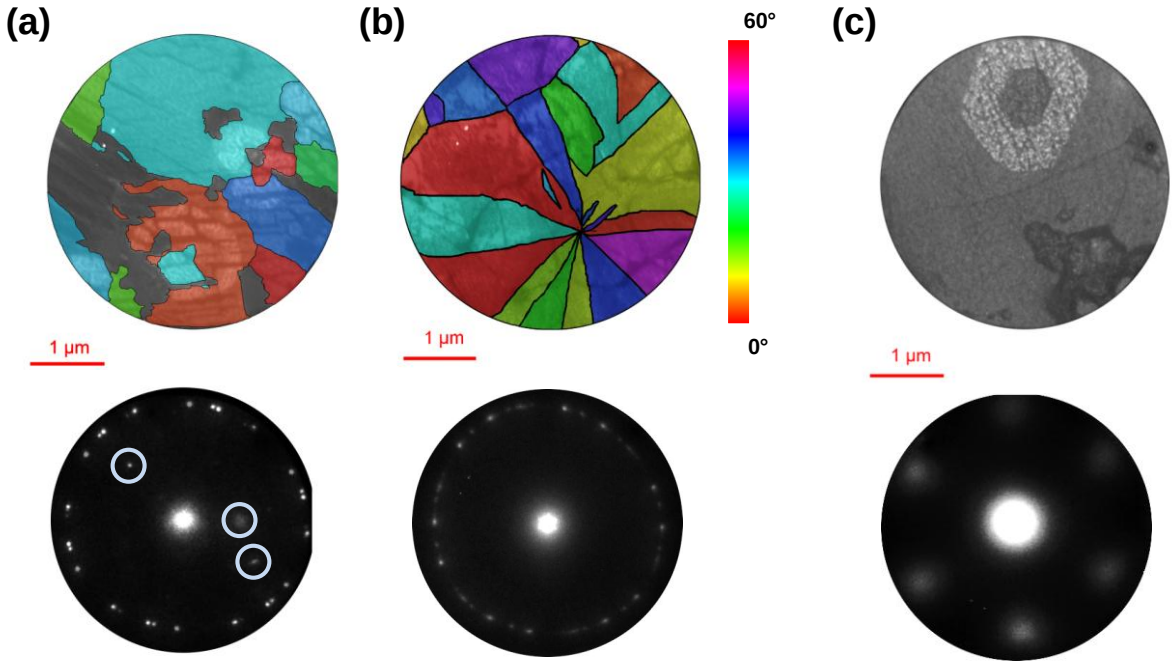


**Figure 72** Average dark field LEEM (top) and LEED (bottom) images of texture of continuous graphene films. a) as-grown on 25 µm Cu-LP1 without electropolishing. b) Grown on as-received 25 µm Cu-LP1 transferred on Au/mica substrate. c) Grown on electropolished 25 µm Cu LP1 transferred on $SiO_2$/Si substrate. The orientation colour map is overlaid on the LEEM images for non-electropolished, polycrystalline samples according to the relative orientations. The dark areas in LEEM image in (a) without colour mapping are facetted areas that could not be imaged by the angle dependent dark field imaging as the diffraction spots (indicated by the circles) lie away from the main 1$^{st}$ order diffraction patterns.

As can be seen from Figure 72c, the electropolished surface exhibited a larger domain size compared to graphene grown on unpolished Cu such that the grain size is bigger than the field of view of 4 µm diameter. Z. Luo et al.[176] and G. H. Han et al.[177] have demonstrated that surface roughness of Cu greatly increases the density of nuclei by comparing the growth experiments on scratched and electropolished Cu surfaces. S. Nie et al.[203] has also reported the breakup of a single graphene nucleus into multiple rotational domains as a nucleus enlarges across the step bunches on Cu(111). The role of the surface defects in producing misaligned, polycrystalline domains reported in the literature appears to be consistent with the current observations reported here.

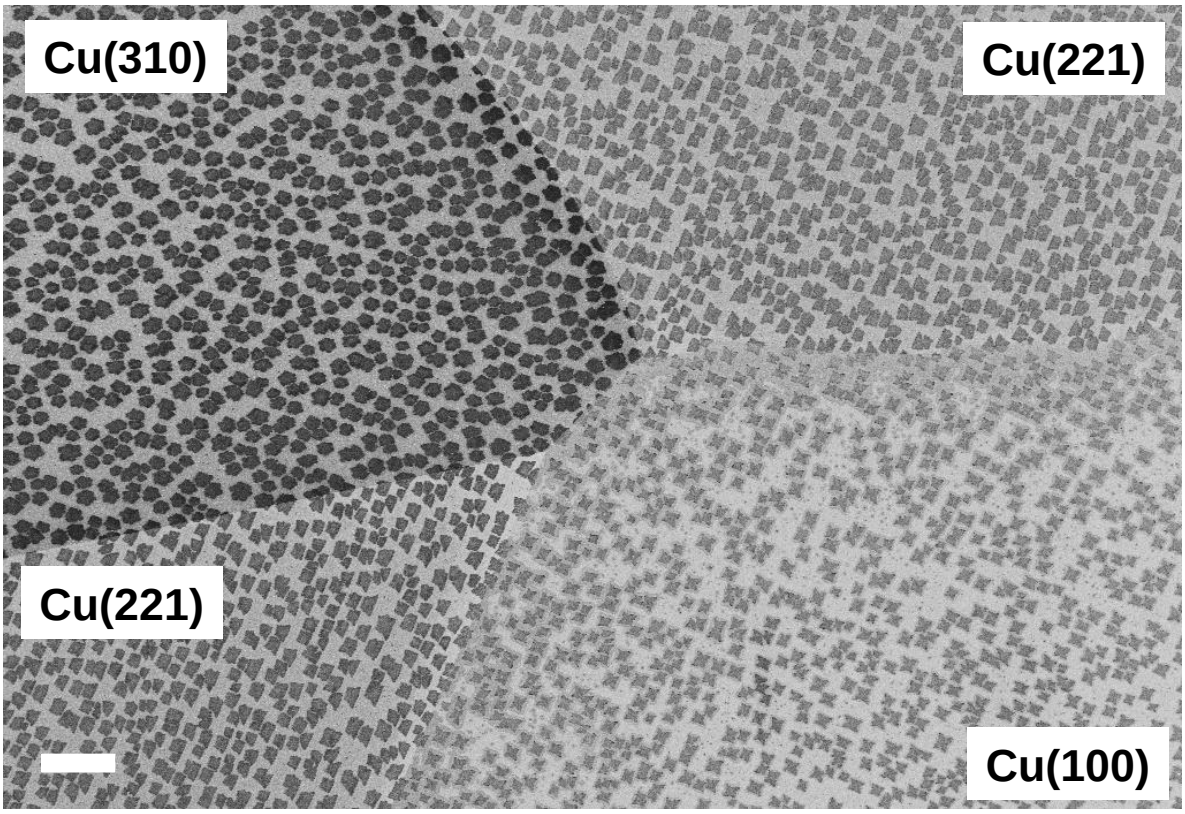


**Figure 73** SEM image of graphene grown on polycrystalline Cu of different crystal orientations. $P_{CH4}$ = 0.0001 mbar, $P_{H2}$ = 2.5 mbar, $T_{growth}$= 1030 ℃, $t_{growth}$ = 5 min. Scale bar, 20 μm.

### 8.2.4 Cu Crystal Orientation Dependence on Graphene Morphology

Now, we focus our attention to growth of graphene on electropolished surfaces of different Cu crystal orientations. In Figure 73, for instance, the graphene nuclei grown on different Cu crystal surfaces of a polycrystalline substrate were found to have different shapes, alignments, anisotropy, density, and coverage. After analysing the graphene nucleus morphology on Cu grains of known crystal orientations using 25μm Cu-LP1, 25μm Cu-LP2, and Cu single crystals for a wide range of growth conditions, three families of distinct symmetry were observed in the nucleus shape: (1) 6-fold on Cu(111) (Figure 74) and Cu(310) (Figure 75), (2) 4-fold on Cu(100) (Figure 76), and (3) 2-fold on Cu(110) (Figure 78), Cu(221) (Figure 77), and Cu(211) (Figure 79). This appears to be a general observation regardless of the substrate purity (99.8% to 99.9999 %). In addition, depending on the degree of supersaturation ($P_{CH4}/P_{H2}$ ratio) and density of nuclei, the shapes exhibit different anisotropy. For example, the four-lobed flower like structure on Cu(100) becomes more compact and square-like at high $P_{H2}$ especially when the nucleus is isolated and grown at high

temperature and long growth time as shown in Figure 76. This observation of more compact morphology has been previously observed by Vlassiouk et al.[196] Furthermore, the alignment of the graphene nuclei appears to be highly correlated with the orientation of underlying Cu grain indicating a preferential orientation of graphene crystal with respect to the substrate crystal lattice.

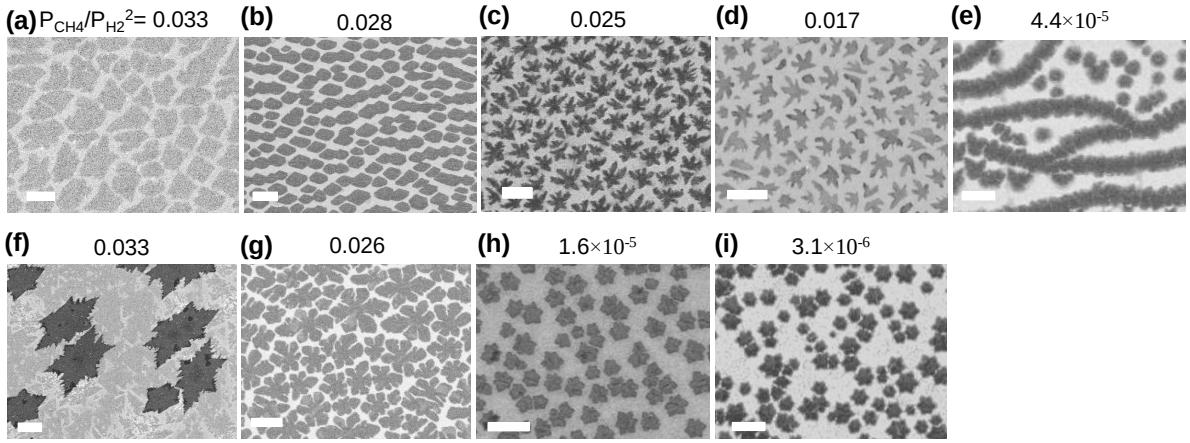


**Figure 74** SEM images of graphene nuclei grown on Cu(111) at various conditions. a) $P_{CH4}$ = 0.004 mbar, $P_{H2}$ = 0.35 mbar, $T_{growth}$= 1000 ℃, $t_{growth}$ = 0.5 min. Scale bar, 1 μm. b) $P_{CH4}$ = 0.0015 mbar, $P_{H2}$ = 0.23 mbar, $T_{growth}$= 1000 ℃, $t_{growth}$ = 2 min. Scale bar, 2 μm. c) $P_{CH4}$ = 0.0025 mbar, $P_{H2}$ = 1 mbar, $T_{growth}$= 1000 ℃, $t_{growth}$ = 0.5 min. Scale bar, 2 μm. d) $P_{CH4}$ = 0.002 mbar, $P_{H2}$ = 0.34 mbar, $T_{growth}$= 1000 ℃, $t_{growth}$ = 0.5 min. Scale bar, 2 μm. e) $P_{CH4}$ = 0.0003 mbar, $P_{H2}$ = 8.25 mbar, $T_{growth}$= 1000 ℃, $t_{growth}$ = 0.5 min. Scale bar, 2 μm. f) $P_{CH4}$ = 0.004 mbar, $P_{H2}$ = 0.35 mbar, $T_{growth}$= 1030 ℃, $t_{growth}$ = 4 min. Scale bar, 10 μm. g) $P_{CH4}$ = 0.004 mbar, $P_{H2}$ = 0.39 mbar, $T_{growth}$= 1030 ℃, $t_{growth}$ = 0.5 min. Scale bar, 2 μm. h) $P_{CH4}$ = 0.0001 mbar, $P_{H2}$ = 2.5 mbar, $T_{growth}$= 1030 ℃, $t_{growth}$ = 5 min. Scale bar, 4 μm. i) $P_{CH4}$ = 0.0002 mbar, $P_{H2}$ = 8 mbar, $T_{growth}$= 1030 ℃, $t_{growth}$ = 1 min. Scale bar, 4 μm.

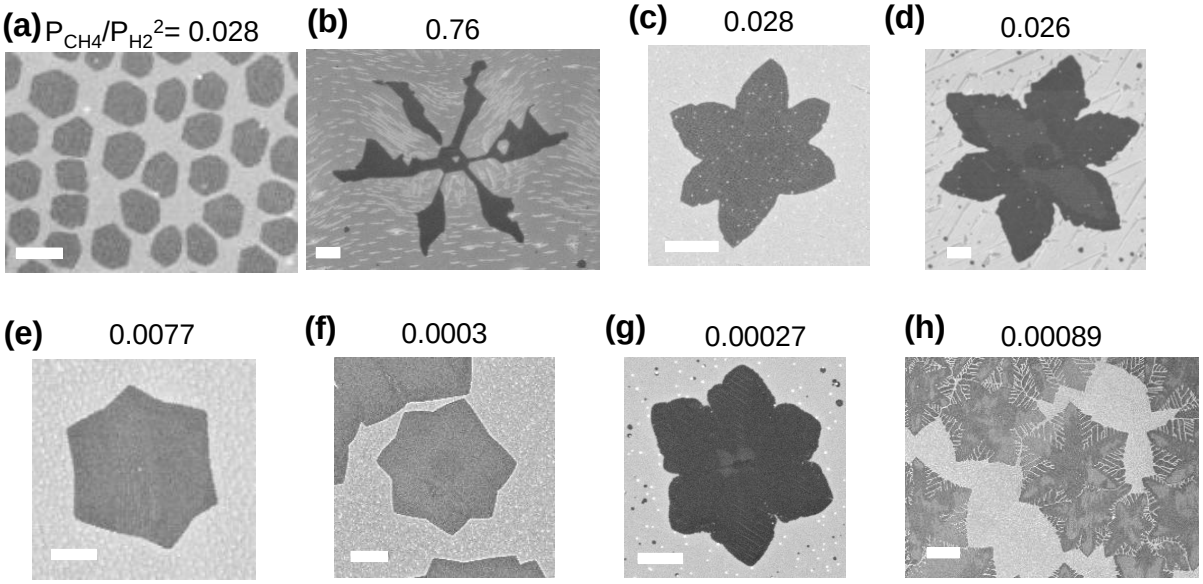


**Figure 75** SEM images of graphene nuclei grown on Cu(310) at various conditions. a) $P_{CH4}$ = 0.0015 mbar, $P_{H2}$ = 0.23 mbar, $T_{growth}$= 1000 ℃, $t_{growth}$ = 2 min. Scale bar, 2 μm. b) $P_{CH4}$ = 0.017 mbar, $P_{H2}$ = 0.15 mbar, $T_{growth}$= 1030 ℃, $t_{growth}$ = 4 min. Scale bar, 4 μm. c) $P_{CH4}$ = 0.0015 mbar, $P_{H2}$ = 0.23 mbar, $T_{growth}$= 1030 ℃, $t_{growth}$ = 2 min. Scale bar, 4 μm. d) $P_{CH4}$ = 0.004 mbar, $P_{H2}$ = 0.34 mbar, $T_{growth}$= 1030 ℃, $t_{growth}$ = 4 min. Scale bar, 4 μm. e) $P_{CH4}$ = 0.001 mbar, $P_{H2}$ = 0.36 mbar, $T_{growth}$= 1030 ℃, $t_{growth}$ = 50 min. Scale bar, 10 μm. f) $P_{CH4}$ = 0.0015 mbar, $P_{H2}$ = 2.2 mbar, $T_{growth}$= 1030 ℃, $t_{growth}$ = 40 min. Scale bar, 10 μm. g) $P_{CH4}$ = < 0.0001 mbar, $P_{H2}$ = 0.6 mbar, $T_{growth}$= 1070 ℃, $t_{growth}$ = 350 min. Scale bar, 4 μm. h) $P_{CH4}$ = 0.0015 mbar, $P_{H2}$ = 1.3 mbar, $T_{growth}$= 1070 ℃, $t_{growth}$ = 50 min. Scale bar, 50 μm.

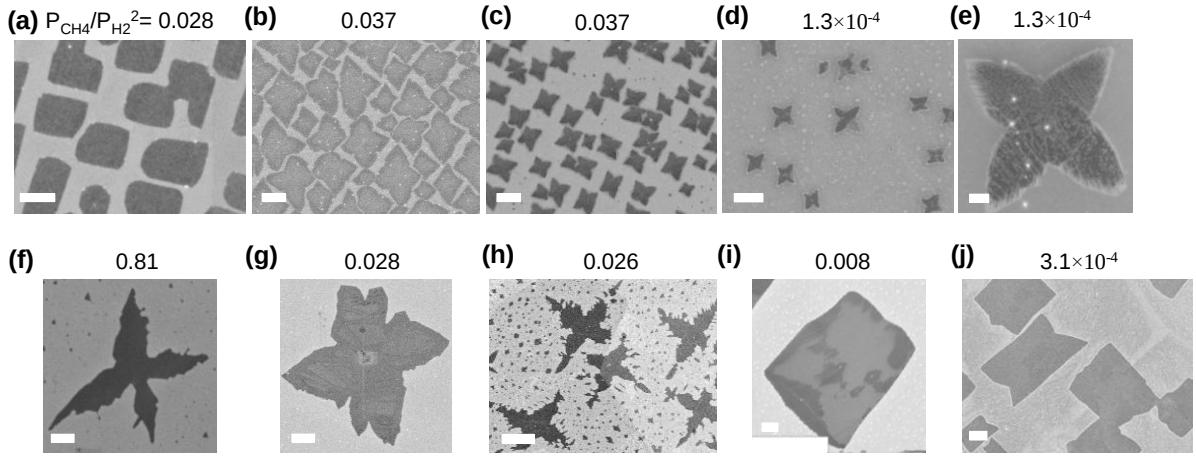


**Figure 76** SEM images of graphene nuclei grown on Cu(100) at various conditions. a) $P_{CH4}$ = 0.0015 mbar, $P_{H2}$ = 0.23 mbar, $T_{growth}$= 1000 ℃, $t_{growth}$ = 2 min. Scale bar, 1 μm. b) $P_{CH4}$ = 0.004 mbar, $P_{H2}$ = 0.33 mbar, $T_{growth}$= 1030 ℃, $t_{growth}$ = 0.5 min. Scale bar, 2 μm. c) $P_{CH4}$ = 0.0001 mbar, $P_{H2}$ = 2.5 mbar, $T_{growth}$= 1030 ℃, $t_{growth}$ = 5 min. Scale bar, 4 μm. d) $P_{CH4}$ = 0.0001 mbar, $P_{H2}$ = 0.87 mbar, $T_{growth}$= 1030 ℃, $t_{growth}$ = 7 min. Scale bar, 4 μm. e) $P_{CH4}$ = 0.0001 mbar, $P_{H2}$ = 0.87 mbar, $T_{growth}$= 1030 ℃, $t_{growth}$ = 7 min. Scale bar, 400 nm. f) $P_{CH4}$ = 0.017 mbar, $P_{H2}$ = 0.145 mbar, $T_{growth}$= 1030 ℃, $t_{growth}$ = 4 min. Scale bar, 4 μm. g) $P_{CH4}$ = 0.0015 mbar, $P_{H2}$ = 0.23 mbar, $T_{growth}$= 1030 ℃, $t_{growth}$ = 2 min. Scale bar, 2 μm. h) $P_{CH4}$ = 0.004 mbar, $P_{H2}$ = 0.389 mbar, $T_{growth}$= 1030 ℃, $t_{growth}$ = 4 min. Scale bar, 10 μm. (i) $P_{CH4}$ = 0.001 mbar, $P_{H2}$ = 0.36 mbar, $T_{growth}$= 1030 ℃, $t_{growth}$ = 50 min. Scale bar, 4 μm. (j) $P_{CH4}$ = 0.0015 mbar, $P_{H2}$ = 2.2 mbar, $T_{growth}$= 1030 ℃, $t_{growth}$ = 40 min. Scale bar, 10 μm.

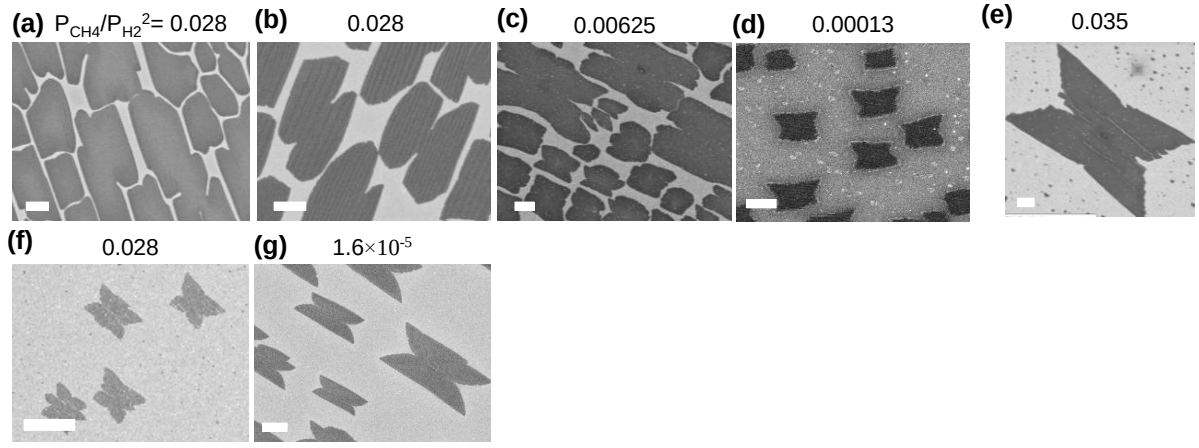


**Figure 77** SEM images of graphene nuclei grown on Cu(221) at various conditions. a) $P_{CH4}$ = 0.0015 mbar, $P_{H2}$ = 0.23 mbar, $T_{growth}$= 1030 ℃, $t_{growth}$ = 40 min. Scale bar, 4 μm. b) $P_{CH4}$ = 0.0015 mbar, $P_{H2}$ = 0.23 mbar, $T_{growth}$= 1000 ℃, $t_{growth}$ = 2 min. Scale bar, 4 μm. c) $P_{CH4}$ = 0.004 mbar, $P_{H2}$ = 0.8 mbar, $T_{growth}$= 1000 ℃, $t_{growth}$ = 0.5 min. Scale bar, 2 μm. d) $P_{CH4}$ = 0.0001 mbar, $P_{H2}$ = 0.87 mbar, $T_{growth}$= 1030 ℃, $t_{growth}$ = 7 min. Scale bar, 2 μm. e) $P_{CH4}$ = 0.004 mbar, $P_{H2}$ = 0.34 mbar, $T_{growth}$= 1030 ℃,

$t_{growth}$ = 4 min. Scale bar, 4 μm. f) $P_{CH4}$ = 0.0015 mbar, $P_{H2}$ = 0.23 mbar, $T_{growth}$= 1030 ℃, $t_{growth}$ = 2 min. Scale bar, 20 μm. g) $P_{CH4}$ = 0.0001 mbar, $P_{H2}$ = 2.5 mbar, $T_{growth}$= 1030 ℃, $t_{growth}$ = 5 min. Scale bar, 2 μm.

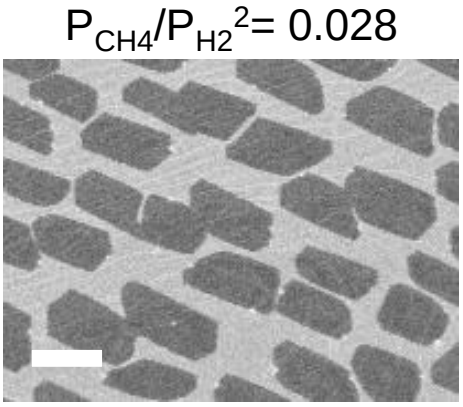


**Figure 78** SEM image of graphene nuclei grown on Cu(110). $P_{CH4}$ = 0.0015 mbar, $P_{H2}$ = 0.23 mbar, $T_{growth}$= 1000 ℃, $t_{growth}$ = 2 min. Scale bar, 2 μm.

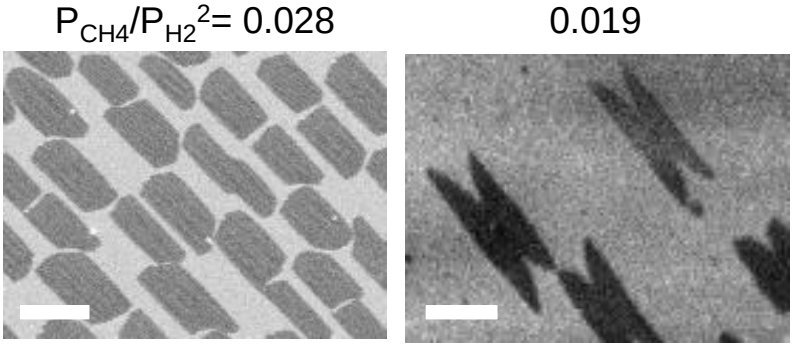


**Figure 79** SEM images of graphene nuclei grown on Cu(211) at two different conditions. a) $P_{CH4}$ = 0.0015 mbar, $P_{H2}$ = 0.23 mbar, $T_{growth}$= 1000 ℃, $t_{growth}$ = 2 min. Scale bar, 2 μm. b) $P_{CH4}$ = 0.001 mbar, $P_{H2}$ = 0.23 mbar, $T_{growth}$= 1000 ℃, $t_{growth}$ = 2 min. Scale bar, 10 μm.

The plot in Figure 80 shows the measured average domain size and density of nuclei graphene grown on various Cu surface crystal orientations at a fixed set of growth conditions. It is apparent that on Cu(111), the density of nuclei is significantly higher and average nuclei size is much lower in comparison with other Cu orientations. Cu(111) appears to be also unique in terms of dendritic growth features compared to others and nucleation and growth rates are much slower especially for low $P_{CH4}$ (Figure 82). The morphology and alignments are also significantly influenced by the step edges such that when grown on the area with a high density of step edges, nucleation tends to occur along the step edges and the 6-fold symmetry of the nucleus shape becomes either skewed or lost.

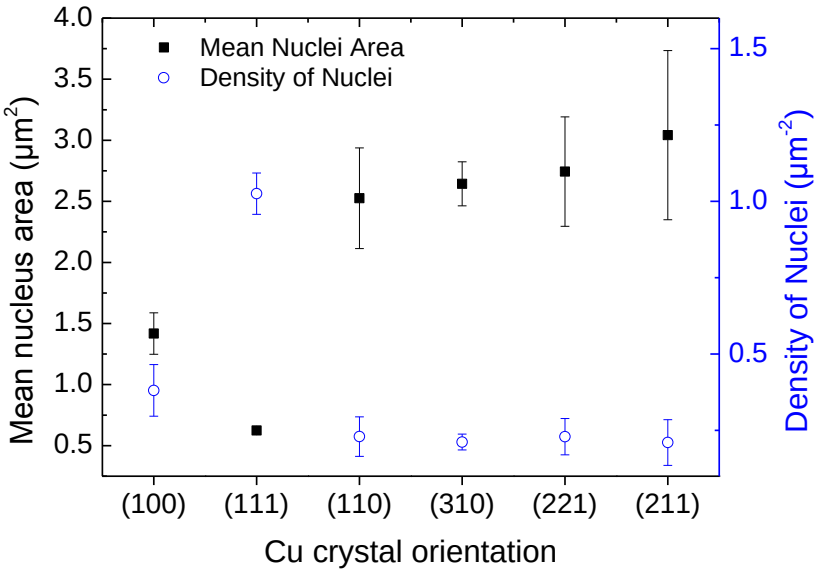


**Figure 80** Plot of Cu crystal orientation dependent mean nucleus area and density of nuclei. $P_{CH4}$ = 0.0015 mbar, $P_{H2}$ = 0.23 mbar, $T_{growth}$= 1000 ℃, $t_{growth}$ = 2 min. Scale bar, 1 μm.

This effect of the step edges was also seen in other Cu orientations especially at low growth temperatures (< 900 ℃). As seen in Figure 81, elongated graphene ribbons appear along the step edges together with more isotropic islands at flat terraces as in the case of high temperatures. The step driven nucleation leads to alignment of graphene nuclei strictly dictated by the step edges and the direction of alignment can be different from the alignment at high temperature (Figure 83). The anisotropic growth along the step edges direction is especially prominent in Cu(211) surface where the rectangular shaped graphene nuclei can reach length to width ratio of > ~10 at temperature below < 800 ℃ from the length to width ratio of ~2.5 at growth temperature of 1000 ℃ (Figure 81c).

On Cu(310), graphene can induce various surface facets that are aligned in multiple directions which are distinct from an exposed Cu surface (Figure 84). This surface reconstruction of graphene on Cu lattice due to the graphene-Cu interactions has been observed previously for graphene/Cu(100) indicating a significant overlayer-substrate interactions.[485] These surface facets on Cu(310), however, appear to have less influence on the aspect ratio of nucleus dimensions and alignments of nuclei than other high index facets such as Cu(211) in the investigated temperature range.

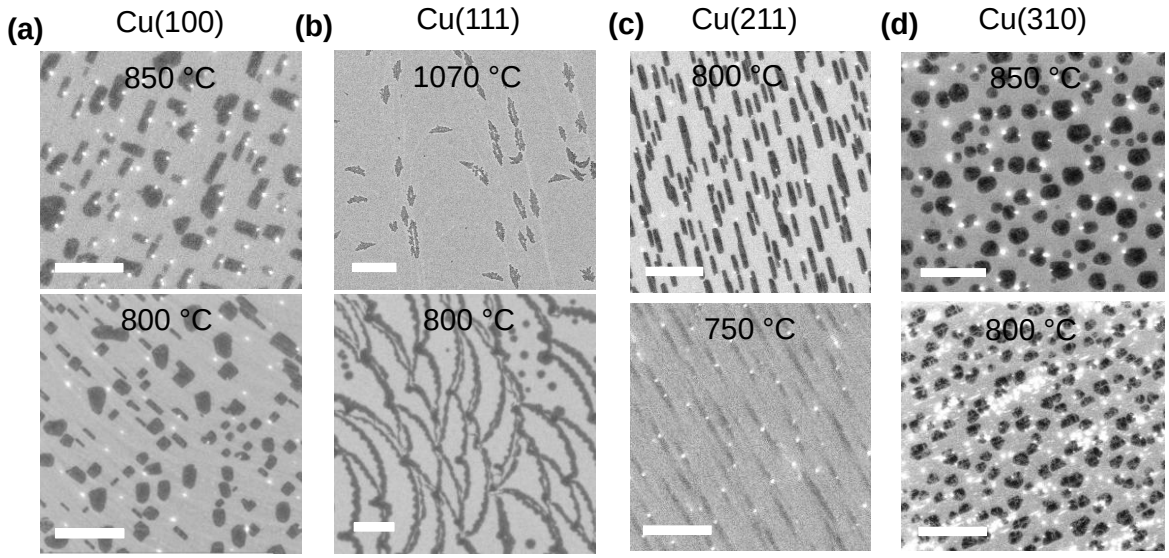


**Figure 81** SEM images of graphene nuclei grown on (a) Cu(100), (b) Cu(111), (c) Cu(211), and (d) Cu (310) illustrating the effect of lowering growth temperatures. a) (top) $P_{CH4}$ = 0.0003 mbar, $P_{H2}$ = 0.23 mbar, $t_{growth}$ = 0.5 min. Scale bar, 1 μm. (bottom) $P_{CH4}$ = 0.01 mbar, $P_{H2}$ = 0.2 mbar, $t_{growth}$ = 40 min. Scale bar, 1 μm. b) (top) $P_{CH4}$ = < 0.0001 mbar, $P_{H2}$ = 0.6 mbar, $T_{growth}$= 1070 ℃, $t_{growth}$ = 350 min. Scale bar, 20 μm. (bottom) $P_{CH4}$ = 0.0015 mbar $P_{H2}$ = 0.14 mbar, $T_{growth}$= 800 ℃, $t_{growth}$ = 1 min. Scale bar, 1 μm. c) (top) $P_{CH4}$ = 0.01 mbar $P_{H2}$ = 0.2 mbar, $T_{growth}$= 800 ℃, $t_{growth}$ = 40 min. Scale bar, 1 μm. (bottom) $P_{CH4}$ = 0.0004 mbar $P_{H2}$ = 0.24 mbar, $T_{growth}$= 750 ℃, $t_{growth}$ = 0.08 min. Scale bar, 1 μm. d) (top) $P_{CH4}$ = 0.01 mbar $P_{H2}$ = 0.2 mbar, $T_{growth}$= 850 ℃, $t_{growth}$ = 2 min. Scale bar, 1 μm. (bottom) $P_{CH4}$ = 0.01 mbar $P_{H2}$ = 0.2 mbar, $T_{growth}$= 800 ℃, $t_{growth}$ = 40 min. Scale bar, 1 μm.

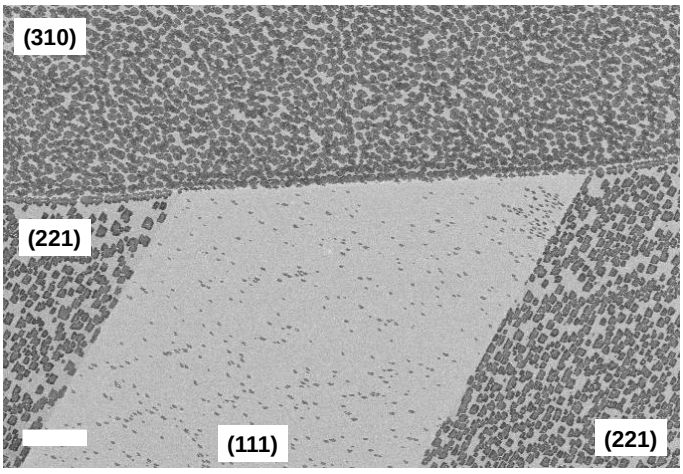


**Figure 82** SEM image of graphene grown on polycrystalline Cu showing low density of graphene nuclei and coverage on Cu at low supersaturation conditions with short growth time. This reflects low adsorption rate of CH4 on Cu(111) compared to other less densely packed surface orientations. $P_{CH4}$ = 0.0004 mbar, $P_{H2}$ = 8.25 mbar, $T_{growth}$= 1000 ℃, $t_{growth}$ = 0.5 min. Scale bar, 20 μm.

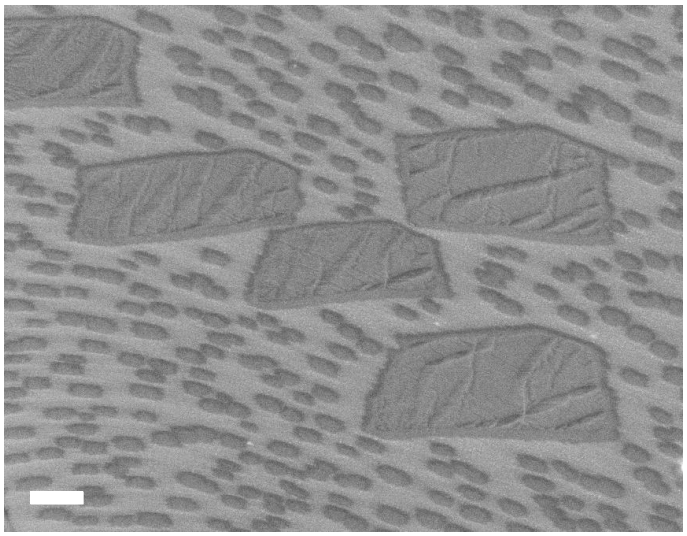

**Figure 83** SEM image of graphene nuclei grown at two different temperatures (first at 1035 °C and then 800 °C) on the same area with visible step edges. The larger nuclei were grown first on Cu at 1035 °C and then the furnace was cooled down to 800 °C to grow the smaller nuclei. The approximate orientation of the surface is Cu(110). $P_{CH4}$ = 0.0015 mbar, $P_{H2}$ = 0.14 mbar, $t_{growth}$ = 1 min (at each temperature). Scale bar, 400 nm.

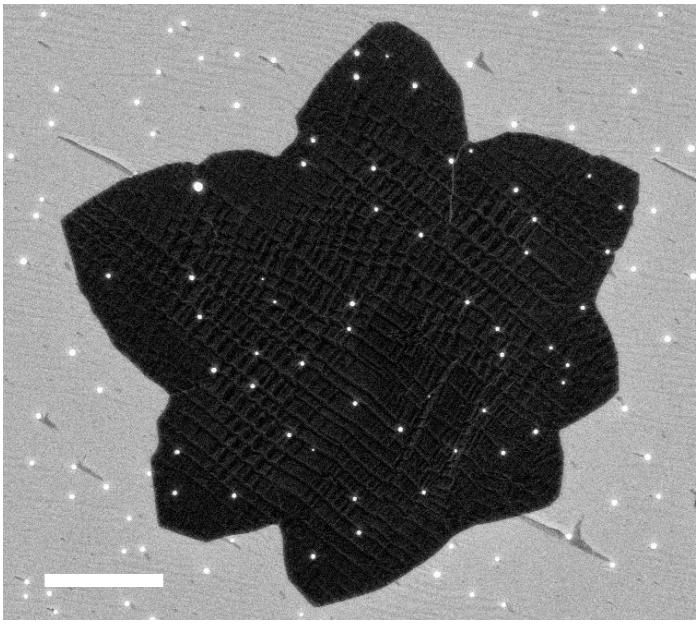

**Figure 84** Contrast enhanced, high magnification SEM image of a graphene nucleus on Cu(310). Note that the alignments of facets within the graphene nucleus are different from the alignment direction of the surface steps in the exposed Cu area outside the nucleus. Scale bar, 2 μm. $P_{CH4}$ = 0.0015 mbar $P_{H2}$ = 0.23 mbar, $T_{growth}$= 1030 °C, $t_{growth}$ = 2 min.

### 8.2.5 Epitaxial Basis for Poly-domain Formation of Graphene on Cu

From the density of nuclei dependence on Cu crystal orientations alone in Figure 80, it may seem that Cu(111) is the least ideal substrate for the production of CVD graphene of large single crystal grains. However, it is necessary to consider the relative crystal orientations of graphene nuclei as the property of the misorientation angles of the grain boundaries can significantly affect the properties of the polycrystalline graphene. The alignment of the graphene crystal on Cu can be predicted by application of group theory in 2 dimensions. Following the Curie's dissymmetry principle,[486] the highest possible symmetry of the composite structure between two lattices is the greatest common subgroup of the symmetry groups of the two lattices. Using this relationship, the number of crystallographically equivalent rotational variants for the epilayer, $N_{RD}$ is predicted as follows[487]:

$$N_{RD} = \frac{n(G_S)}{n(G_S \cap G_E)} \qquad (56)$$

where $n(G_s)$ and $n(G_E)$ are the group orders of the substrate and epilayer, respectively.

For epitaxial deposition on Cu(111) surface, which has a point group of 3m (when considering the first and 2$^{nd}$ layers), with graphene belonging to the point group of 6mm, the predicted number of rotational variant is 1 according to eq. 56. This is consistent with our observation that on the smooth surface of Cu(111), the 6-fold shaped nuclei have more or less the same rotational orientation. If one of either zigzag or armchair edge has the lowest energy, the equilibrium shape of a single crystal domain would be hexagonal. Vasilii et al.[442] has recently shown that zigzag orientation on Cu(111) is strongly preferred over armchair edge by constructing the Wulff plot through DFT calculations. This prediction appears to be true for high $P_{H2}$ case (Figure 74h, i) where the compact islands take a hexagonal form. Otherwise, the nuclei would take more isotropic shape (i.e. circular) if armchair and zigzag edges have comparable energies.[442,488] At lower $P_{H2}$, dendritic morphologies develops, but it still follows the symmetry relationship such that six lobed star shaped nuclei appear with the same rotational orientation. The single rotational domain on Cu(111) has also been reported for various growth conditions in existing publications[178,180,202] where [10] direction of graphene is oriented parallel to the $[0\text{-}11]_{Cu}$ direction as shown in Figure 85a.

On Cu(100), the number of rotational domains of graphene epilayer is expected to be 2 suggesting that two hexagonal domains that are rotated 90° (or equivalently 30 °) from each other. However, the observed 4-fold symmetry in each nucleus without misorientation suggests a potential symmetry breaking process where each nucleus consists of 4 rotational domains oriented 30° from the each other. The emergence of 4 rotational domains from a single nucleation point has already been reported in literature,[200] and suggests a strong graphene/Cu(100) interaction at the nucleation stage. This is reasonable as the stable geometrical configuration of a small carbon cluster on Cu can be far different from that of the bulk, honeycomb structure when the stabilization of the dangling bonds at the edges by Cu atoms can dominate[207] at the expense of forming grain boundaries. One of the postulated supercritical nucleus structures is presented in Figure 85b. Note that the edges of the square shape nucleus consist of mostly armchair edges and exhibit 4-fold rotational symmetry which is made possible by introducing four of energetically stable, Σ = 13 grain boundary made of alternating heptagonal and pentagonal rings giving grain boundary angle of ~30°.[489] This type of boundary has been observed frequently in CVD graphene grown on the Cu foils likely exhibiting Cu(100) texture.[218,490]

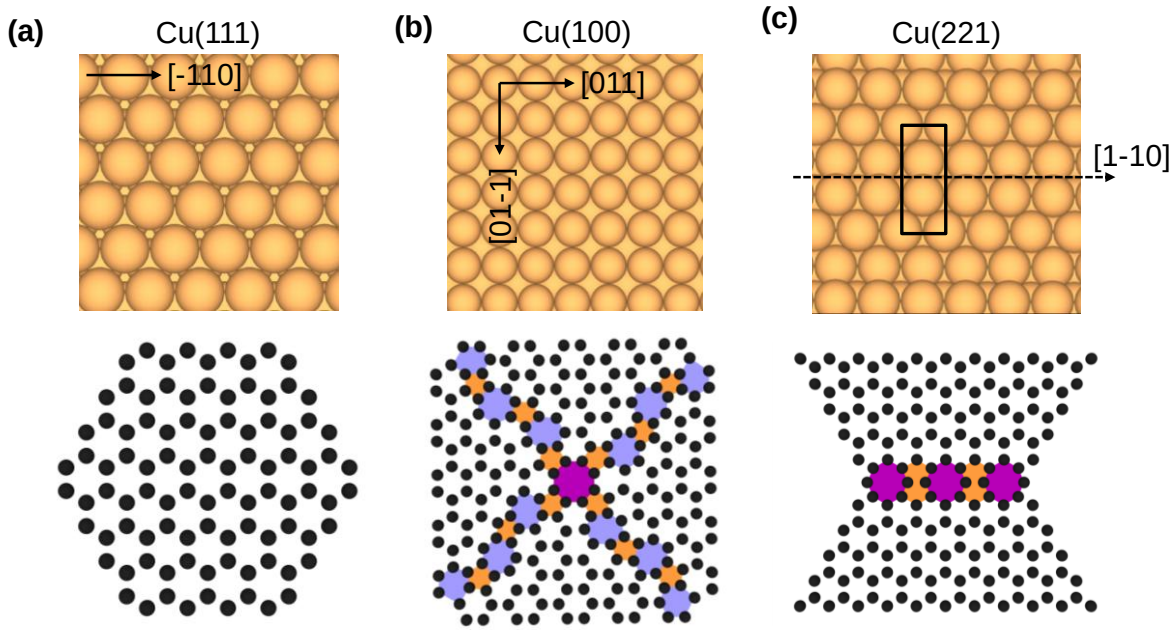


**Figure 85** Hard sphere representation of Cu surfaces (top) and proposed graphene nuclei structure (bottom) on Cu(111) (a), Cu(100) (b), and Cu(211) (c). The non-hexagonal rings along the grain boundaries were coloured purple (octagon), blue (heptagon), and orange (pentagon).

Similar symmetry breaking effect appears to be present on Cu(110), Cu(221), and Cu(211) surfaces with 2mm symmetry. The directional alignment of the rectangular nuclei may be due to preferential nucleation and growth along the step edge directions. However, the butterfly shape (e.g. Figure 77d) of the nuclei cannot be fully explained by anisotropy of the edge energies and growth rates alone. Similar to growth on Cu(100), a twin-like mirror grain boundary may be present along the step edge direction passing through the centre of a nucleus dividing it into two mirror domains with misorientation of 180 °C. One possible structure is depicted in Figure 85c where the repeating arrangement of paired octagonal and pentagonal rings (Stone-Thrower-Wales defects[491]) form an energetically stable twin boundary[489] which has also been observed in graphene grown on Ni(111) along a line defect.[224] The growth rate of the grain boundary should be much slower as the formation of such structure is likely more energetically costly[442] favouring faster growth of the hexagonal edges away from the mirror axis ([1-10] in this case). The presence of the twin grain boundary indicates that there are no rotational misalignments as only translational symmetry is broken at the grain boundary. However, this proposition must be verified by further characterizations at atomic scale.

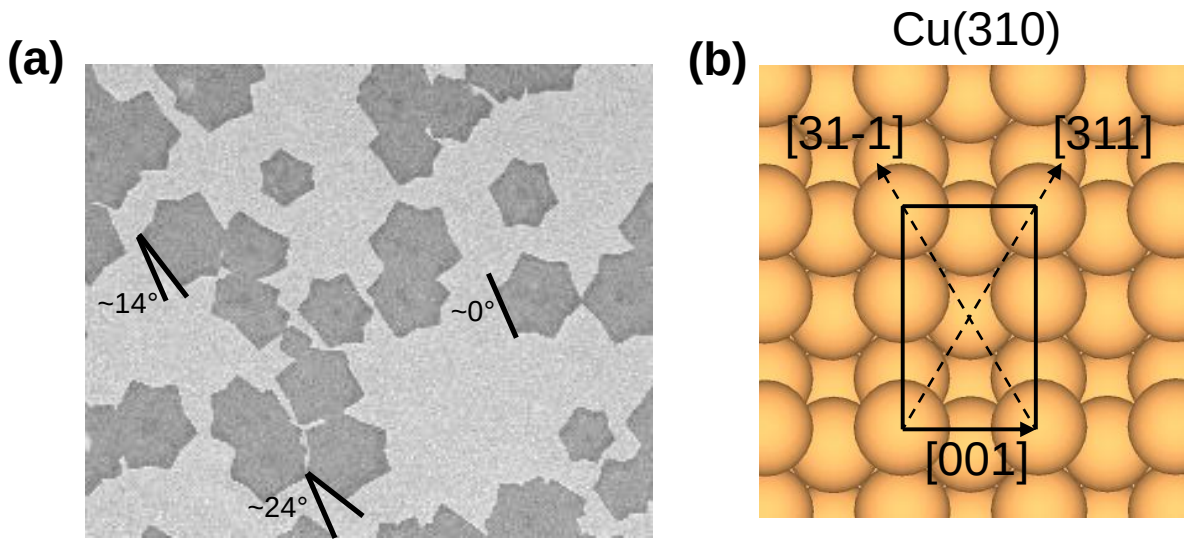


**Figure 86** Preferred alignments of graphene nuclei on Cu(310). a) SEM images of graphene nuclei graphene on Cu(310). Three main orientations (0°, 14°, 24°) appear to be dominant. Scale bar, 50 μm. b) Schematic of Cu(310) surface with depiction of the primitive unit mesh and preferred alignment directions.

On Cu(310), where only a mirror symmetry is present, there seems to be a nucleation of hexagonal, single crystal domains indicating weaker influence of the substrate, however, unlike Cu(111), the three dominant rotational domains are apparent with approximate misorientation angles of 0 °, 14°, and 24° measured by comparing the alignments of edges of each nucleus from the SEM imaging analysis (Figure 86a). Similar distribution of the multiple domain orientations was also reported by others[218,490,492] using 25um Cu-LP1 foil which is likely to exhibit Cu(310) type surfaces. This rotational variants can possibly be attributed to the accidentally degenerate alignments of graphene lattice along the step edge direction, $[001]_{Cu}$ and the two crystallographically equivalent diagonals of the 2D rectangular primitive mesh of Cu(310) ($[31\text{-}1]_{Cu}$ and $[311]_{Cu}$) which result in misorientation of 72.5° and 35.1° (equivalent to 12.5°, and 24.9°, respectively) as depicted in Figure 86b. These alignments may result in the matching of the in-plane directions of densely packed atomic line similar to the case of coincidental lattice site registry leading to minimization of the strain and interfacial energies.[493] Furthermore, the interplay between multiply degenerate alignments of surface facets (e.g. Figure 84) and graphene nuclei may also be responsible for inducing the preferred rotational domains during the nucleation stages.

Let's now consider why the graphene morphology on Cu(111) appears more dendritic and has the highest saturation nucleation density. The anisotropic crystal growth kinetics involves interplay of competing forces such as surface diffusion, adatom de/attachment, edge mobility, and reconstruction at the non-equilibrium conditions of CVD. For slow growth and low supersaturation, there's a time for the edge reconstruction to take place making the shape close to the compact, equilibrium shape that minimizes the edge energy. When the supersaturation is high or when the growth rate is higher than the edge mobility, the corners of an isolated nucleus undergo faster growth as the flux of carbon adatoms are higher for the exposed corners and other protrusions leading to dendritic growth.[494] This is more prominent for the case of low nucleation density since the presence of other nuclei in the vicinity within the nucleation exclusion zone can facilitate inter-nucleus migration of carbon atoms at the periphery and hinder preferential attachment at the corners. Furthermore, lowering of the energy of specific edges (e.g. zigzag) and etching of the protruding edges by the increased concentration of H adatoms may also contribute to more compact nucleus shape at high $P_{H2}$.[194-196,225] On the (111) plane of FCC lattice, particularly, an additional effect has been observed that due to the high coordination of adatoms on the densely packed (111)

surface, edge atoms are more stable, whilst there's an anisotropic corner diffusion which facilitates the dendritic growth.[495,496] Furthermore, it has been predicted by DFT calculations that carbon adatoms have higher potential energy on Cu(111) than on Cu(100) leading to effectively higher supersaturation chemical potential.[207] For instance, the adsorption energy difference between an C adatom and a C atom within graphene lattice on Cu(111) has been calculated to be 3.01 eV, while it is 1.78 eV on Cu(100). This in turn effectively results in higher supersaturation chemical potential on Cu(111) for the same adatom concentration. These effects can therefore also explain the higher nucleation density as nucleation is more preferred on Cu(111) against the capture by nuclei because of the lower edge energies and higher degree of supersaturation.

Step edges also can serve as high coordination sites that lower the barrier for nucleation. In addition, the step edges also tend to have larger barrier for diffusion and edge attachment. This barrier is akin to the Ehrlich-Schwoebel barrier in thin film epitaxy where an atom from the upper terrace experience higher attachment barrier as it descends down a step edge compared to the attachment from the lower terrace.[497] Thus, the hindered growth across the step edge without thermal activation in contrast to the easy growth and stabilization of edge structure along the step edge leads to the elongation of the graphene nucleus morphology at low growth temperatures.

It must be distinguished that as shown in low index surfaces of low surface energies [i.e. Cu(100), Cu(111), and Cu(110)], the step edges arise from the extrinsic factors on the surface (rolling features, small miss-cut angle variations, scratches, etc.). This results in more or less random, irregular arrangements of curved step edges, whereas in high index surfaces such as Cu(211), Cu(221), and Cu(310), the surface naturally break down into low index Cu facets of regular periodicity with aligned, straight step edges due to the tendency to minimize the total surface energy. For example, the periodic array of step edges along $[01\text{-}1]_{Cu}$ direction on Cu(211) as illustrated in Figure 87 provides a suitable template for directed growth of graphene nanoribbons. Moreover, controlling the thermal etching and faceting[483,484] of high-index Cu surfaces by tuning growth conditions provides an additional window of opportunity to dictate the periodicity and height of the surface steps. Therefore, one can envision an efficient, large scale production of highly aligned nanoribbon graphene along well defined

crystallographic directions with controlled density, edge structures, and dimensions as small as < 10 nm on high index single crystal Cu surfaces such as Cu(211) and (221).

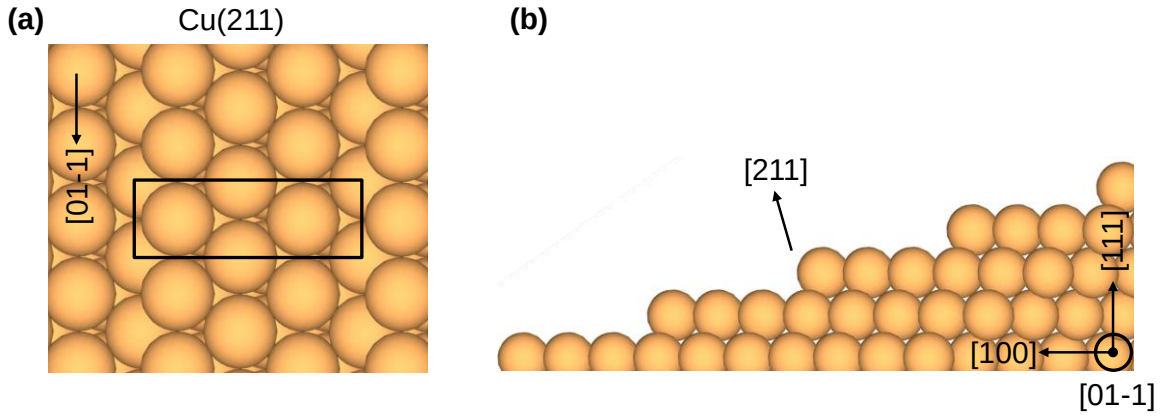


**Figure 87** Hard sphere representations of Cu(211). a) Top-view. b) Cross-sectional view.

### *8.3 Conclusion*

In summary, non-equilibrium graphene mesoscale structures of various shapes and alignments can be efficiently produced by exploiting the epitaxial relationship between the substrate and graphene overlayer. Based on the symmetry argument, shapes, numbers, and orientations of rotational domains on Cu substrate of a known crystal orientation can be predicted. The anisotropy of the nucleus shape results from high supersaturation and the symmetry breaking process especially at high temperatures (> 900 ℃) when the density of nuclei is low. At low temperature (< 900 ℃), effect of the surface facets and step edges may play more significant role in the alignment and shape of nuclei.

The growth on Cu(111) appears to be special. It tends to be less reactive toward decomposition of methane, but nuclei of graphene can form more easily especially at the step edges. The lack of rotational domains on a smooth surface Cu(111) makes it the most suitable substrate for high quality single crystal graphene growth, although merging of the nuclei without formation significant defects at the boundaries needs further confirmation. The rotational variants on other Cu crystal surfaces allow the fundamental study of effect of grain boundaries of known rotational angles on the properties of polycrystalline graphene. The anisotropy of the growth morphology on high index Cu surfaces such as Cu(211) can be exploited for self-template growth of aligned semiconducting graphene nanoribbons with controllable dimensions, edge structure, and density. Overall, the fascinating bottom-up control of the polycrystalline graphene structures offers abundance of opportunities for

development of various technological applications and fundamental studies of low dimensional materials.

# 9 Characterization of Bilayer and Few-layer graphene on Cu

## *9.1 Introduction*

So far this dissertation has focused on the CVD of an ideal monolayer graphene which is expected from the model of self-limited growth on Cu. However, it has been often observed that a stack of FLG simultaneously nucleates from a single point in a concentric fashion (the "wedding cake" structure).[170,196,477,498] The exact mechanism for the multilayer growth, which departs from the simple model of 2 dimensional, surface-limited monolayer growth, is currently under debate in the literature. A few studies have suggested that vapour phase, catalytic decomposition of the hydrocarbons by the copper vapour sublimated from the exposed areas of copper can lead to the deposition of thicker layers at elevated temperature.[160,499] Several works have proposed mechanism of inverted "wedding cake" multilayer formation underneath a monolayer nucleus via segregation of carbon from the bulk to the graphene/Cu interface.[205,500] Catalyst free decomposition of hydrocarbons in the vapour phase is also a possibility especially for high $P_{CH4}$ and high temperature.[501-504] Recently, homogenous large-area bilayer growth of AB stacked graphene on Cu has been realized offering a promising route for a thickness controlled growth of graphene on Cu.[160,205]

In addition to the most stable AB stacking, FLG on Cu can exhibit variety of different stacking orientations which can give rise to novel electronic properties in CVD grown FLG.[505-508] Various electron diffraction studies have suggested a mixed distribution of turbostratic, rhombohedral (ABC), and Bernal stacking orientations in multilayer CVD graphene on Cu.[212,214,509] However, challenge still remains in finding the exact distribution of the stacking orientations, and whether the stacking order can be controlled by tuning the conditions of the experiments. In order to address this issue, this chapter will focus on determining the stacking orientation and distribution of the FLG. The chapter will discuss the

following: (1) growth morphology of FLG of large domain size observed by SEM, (2) Raman spectra of bilayer graphene correlated to the growth morphology, (3) quantized energy dependent low electron energy reflectance from the graphene multilayer, (4) cross-sectional TEM of FLG on Cu, (5) LEED electron reflectance analysis of the multilayers, (6) electronic band structure of multilayer and single layer graphene on Cu probed by ARPES, and (7) brief discussion on the formation of multilayers and their stacking orientations.

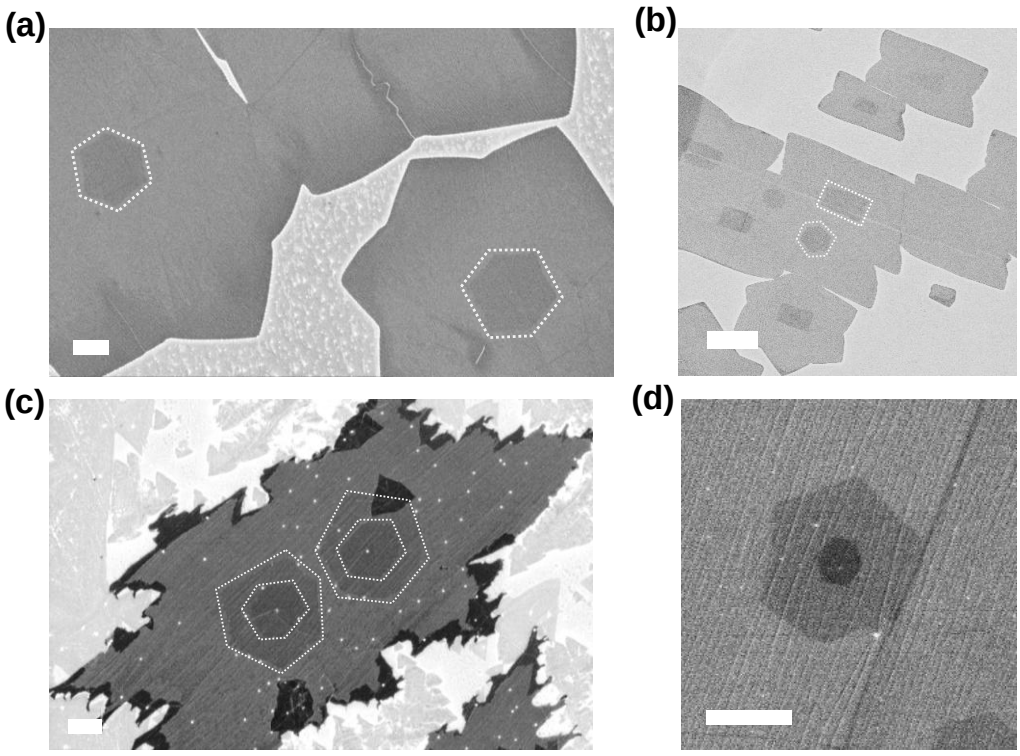


**Figure 88** SEM images of micro-scale FLG "wedding-cake" structures. a) Bilayer graphene nuclei grown on Cu(310). Note the two different orientations of the bilayers with respect to the underlying monolayer. The two bilayer regions of different orientational rotations are outlined by dashed lines. Scale bar, 4 μm. b) Bilayer graphene nuclei of various geometrical configurations. Rectangular bilayer within rectangular monolayer, rectangular bilayer within hexagonal monolayer, and hexagonal bilayer within rectangular monolayer nuclei are visible. Scale bar, 20 μm. c) Trilayer graphene nuclei grown on Cu(111). The $2^{nd}$ and $3^{rd}$ layers are outlined by dashed lines. Scale bar, 2 μm. d) Trilayer graphene island within a continuous monolayer graphene. Note the ~30° relative orientation between the $2^{nd}$ and $3^{rd}$ layers. Scale bar, 2 μm.

### *9.2 Growth of FLG of Large Domain Size*

Even at low $CH_4$ pressure conditions, where the density of nuclei is low, a large domain of FLG with lateral size bigger than 10 μm can be grown at the centre of the nuclei on various Cu crystal orientations at the growth temperature of > 1000 ℃ (Figure 88). The shapes and orientation of the multilayers come in various configurations which reflect the multiplicity in the overlayer interaction with the underlying polycrystalline substrate as discussed in the last chapter. The 2$^{nd}$ and 3$^{rd}$ layers usually tend to follow the shape and orientation of the first layer. However, shape and orientational mismatch is also observed frequently between the layers (Figure 88b). For instance, rectangular 2$^{nd}$ layer can be grown on 6-fold shaped (hexagonal) nuclei or vice versa. Even the stack of FLGs that individually exhibits hexagonal shape can have a staggered configuration where the angle of misorientations of the hexagons is approximately 30° in most of the cases (Figure 88a,c,d) as have been observed previously.[196,477]

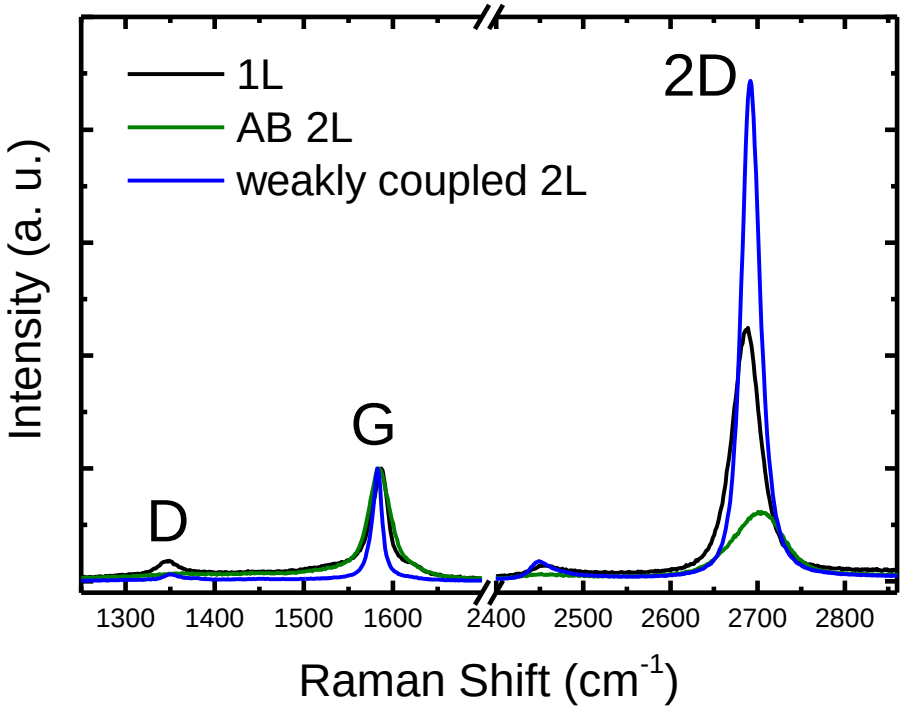


**Figure 89** Normalized Raman spectra of monolayer (1L) and two main types of CVD grown bilayer (AB 2L and weakly coupled 2L) transferred onto SiO2/Si substrate in the region of D, G and 2D peaks. $\lambda_L$ = 514 nm.

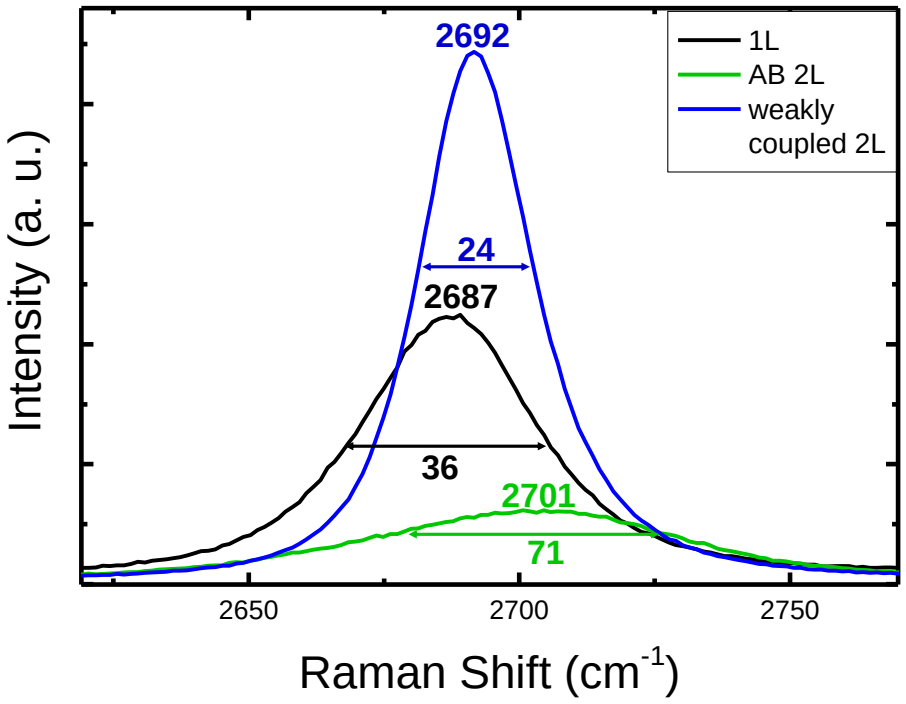


**Figure 90** Close-up of 2D band spectra of monolayer (1L), and the two main types of CVD grown bilayer (AB 2L and weakly coupled 2L) with the intensities normalized to the G peak intensity. The FWHM value and the peak position for each spectrum are shown.

### *9.3 Raman Spectra of Graphene Bilayer*

The Raman spectra of typical monolayer and bilayer stacks of two different types in the range of D, G and 2D bands are shown in Figure 89. The two different types of bilayer graphene exhibit dramatically different spectra which suggest a large difference in the stacking orientation and interlayer interactions. The first bilayer type appears to be of a typical AB-stacked structure where it has a broad 2D FWHM of ~71 $cm^{-1}$, and 2D peak at ~ 2701 $cm^{-1}$ (with single Lorentzian peak fitting) with I(2D)/I(G) < 1 whereas the monolayer with the same processing conditions have the 2D peak position at ~2687 $cm^{-1}$ with FWHM of ~35 $cm^{-1}$ and with I(2D)/I(G) ~ 2 (Figure 90) with the laser wavelength ($\lambda_L$) of 514 nm. This broad, blue-shifted 2D peak with low intensity is consistent with general features of the AB stacked bilayer in comparison with that of a monolayer. The G peak of the bilayer also appears to be broader than that of monolayer as expected from the AB stacked bilayer. The $2^{nd}$ type of bilayer exhibits much unique structure where it has a narrower 2D band (~24 $cm^{-1}$) than that of monolayer and even higher I(2D)/I(G) (~4-5) than I(2D)/I(G) of monolayer. The

blue-shift of the 2D peak is also very small with value of < 10 $cm^{-1}$ relative to the 2D peak position of monolayer graphene ($\lambda_L$ = 514 nm). The 2D band is quite sensitive to the interlayer interactions and the similarity to the monolayer spectra suggests that the layers are strongly "decoupled" from each other. Figure 91 shows distributions of 2D peak FWHM and normalized A(2D) obtained from different bilayers of graphene from the same sample. These bilayers have almost equal chance of exhibiting the AB like or decoupled structure on the polycrystalline Cu foils as shown in Figure 91. Figure 92 shows I(2D)/I(G) and 2D FWHM mapping of a decoupled bilayer graphene. The Raman spectra of the bilayer appear to be relatively homogenous except for the right hand side close to the edge where the spectra appear to be split which may be attributed to further decoupling or inhomogeneous doping or strain.

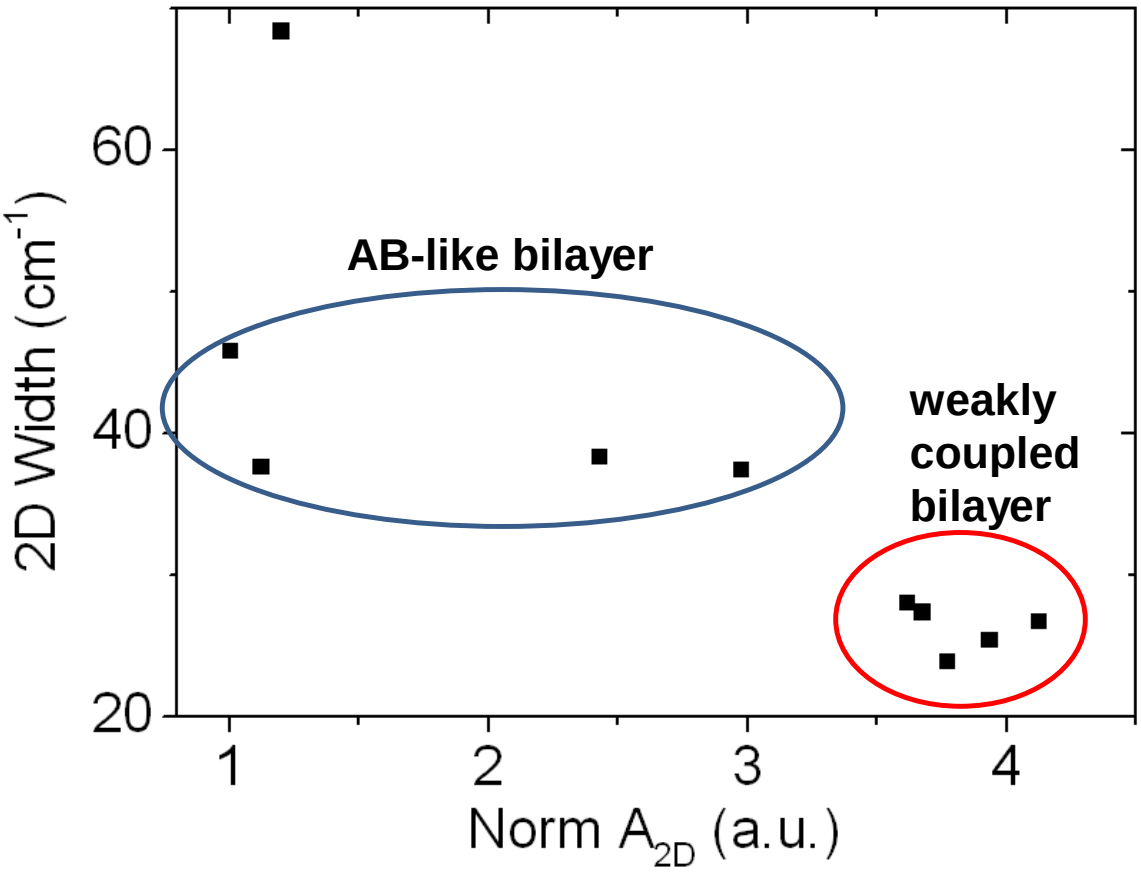


**Figure 91** Distribution of 2D FWHM versus normalized A(2D) values obtained from single Lorentzian peak fitting of the 2D Raman peaks of CVD bilayers of largely two different types; AB-like (blue circle) and weakly coupled (red circle). $\lambda_L$ = 514 nm.

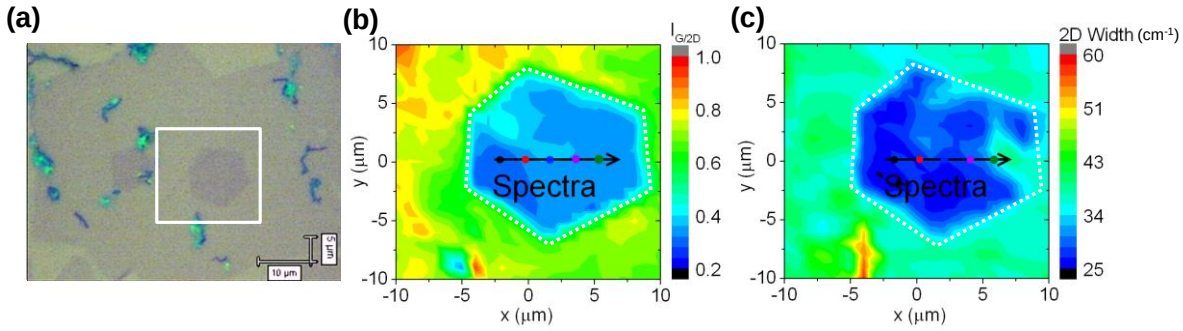


**Figure 92** Raman maps of I(G)/I(2D) (0.2 – 1) (b) and 2D FWHM (25 – 60 $cm^{-1}$) (c) on a weakly coupled bilayer/monolayer region shown in the optical microscope image (a). $\lambda_L$ = 514 nm.

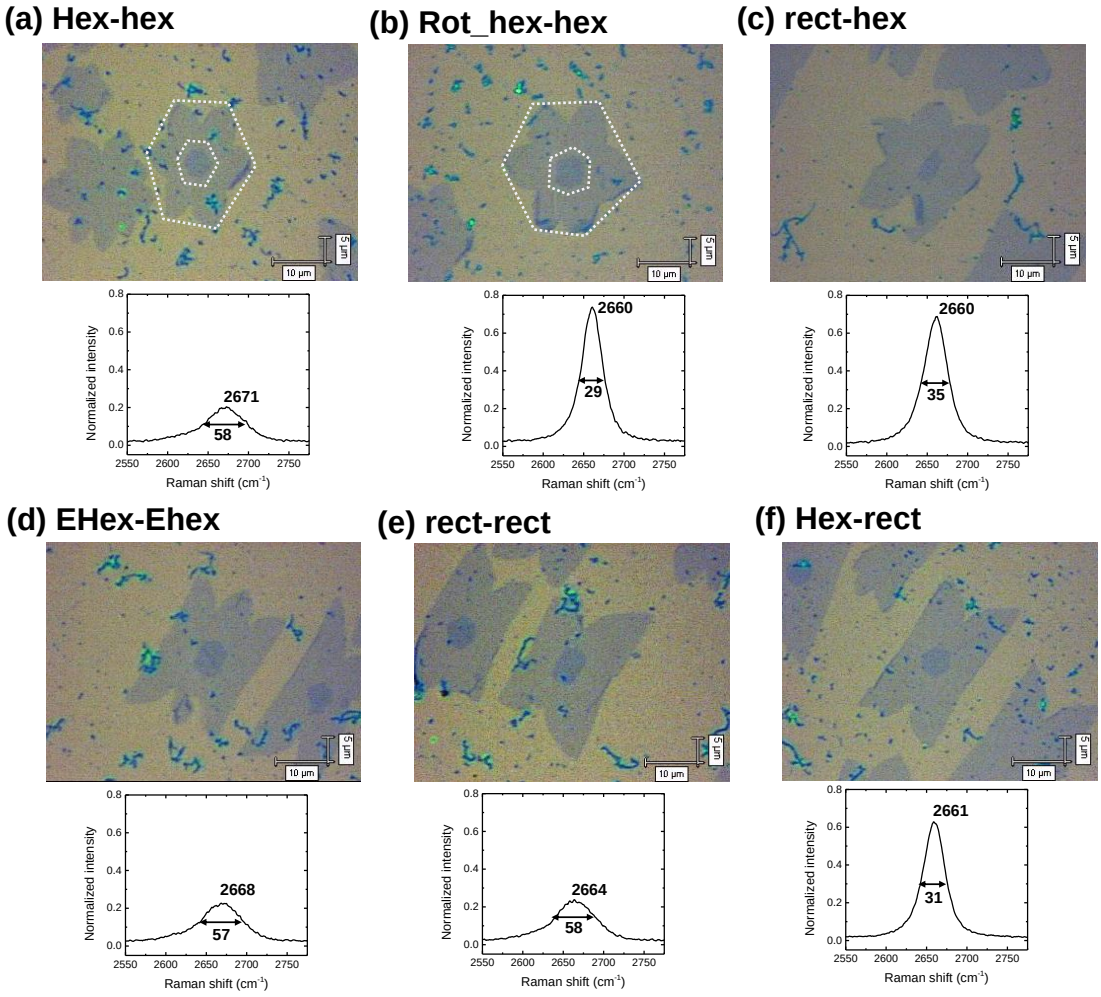


**Figure 93** Optical microscope images of bilayers (top) and corresponding Raman 2D band peaks (bottom) of various geometrical morphologies. The numbers within the plots of the 2D band spectra indicate the FWHM and peak position. $\lambda_L$ = 633 nm. The bright blue spots in the images are likely debris of graphene from the back side of Cu foil substrate remain with the sample during etching process.

By studying bilayer stacks of overlapped graphene monolayers with various misorientation angles made by consecutively transferring two monolayers of CVD graphene onto a TEM grid, the overlapped stack of the bilayer with 30° misorientation angle has been shown to exhibit a spectrum similar to our "decoupled" bilayer structure.[510] However, the predicted blue-shifts in 2D peak positions are much higher (~12 $cm^{-1}$) for the bilayer of 30° misorientation. Thus, a further analysis is required to identify the exact stacking order of the bilayers.

In addition, the narrower and more symmetric G peak in the decoupled bilayer compared to the monolayer has been attributed to the half of a bilayer (the interlayer space) being protected from the unintentional doping from air or moisture from the ambient environment and substrate.[511]

Remarkably, the two types of bilayer can be identified from the relative orientation and shape differences between the two layers imaged by SEM or optical microscopes. The unroated hexagon-hexagon (hex-hex; Figure 93a), elongated hexagon-hexagon (ehex-ehex; Figure 93d), and rectangle-rectangle (rect-rect; Figure 93e) structures all exhibit AB-like characteristics in Raman spectra whereas rotated hexagon-hexagon (rot_hex-hex; Figure 93b), hexagon-rectangle (hex-rect; Figure 93c), and rectangle-hexagon (rect-hex; Figure 93f) structures all exhibit the spectra of the decoupled bilayer.

### *9.4 Quantized Energy Dependent Reflectance in LEEM*

The multilayer structures within a continuous film of CVD graphene as grown on Cu, and transferred onto other substrates have been analysed by LEEM. One of the characteristic features of FLG in LEEM is the quantized reflectance of low energy electrons resulting from the wave nature of the electrons and the stack of the graphene layers acting as a quantum well. [384] Due to the constructive (destructive) interference of the incident electrons reflected at the graphene-substrate interface and at the graphene surface, a number of maxima (minima) in the intensity of the reflected electrons as function of layer thickness can result when a specific resonance condition is met.

Eq. 57 describes the resonance conditions for the electrons reflected from a quantum well structure[384]:

$$2K(E)Na + \Phi_S + \Phi_I = 2n\pi \qquad (57)$$

Here, $K(E)$ is the energy dependent wave number of electrons in the thin film, N, number of layers, $a$, interlayer distance between the graphene sheets, $\Phi_S$ and $\Phi_I$ are phase change at the surface and interface, respectively, and n is a quantization number (n<N).

We assume that the thin film of transferred graphene to be quasi-free standing, such that $\Phi_I = \Phi_S = 0$. [384] And using the free electron estimation for the dispersion relationship, the maxima and minima of the reflectance curve as integer multiples of $\pi$ can be fitted by rewriting the eq. 57 as[385]:

$$\Phi = l\pi = \frac{2aN}{\hbar}\sqrt{2m\left(E + V_0\right)} \qquad (58)$$

where $\Phi$ is phase change, $l$, a quantum number ($l$ = 1, 2, 3, etc.), ħ, reduced Planck's constant, $m$, electron mass (assumed to be rest mass of a free electron), $V_0$, the quantum well potential.

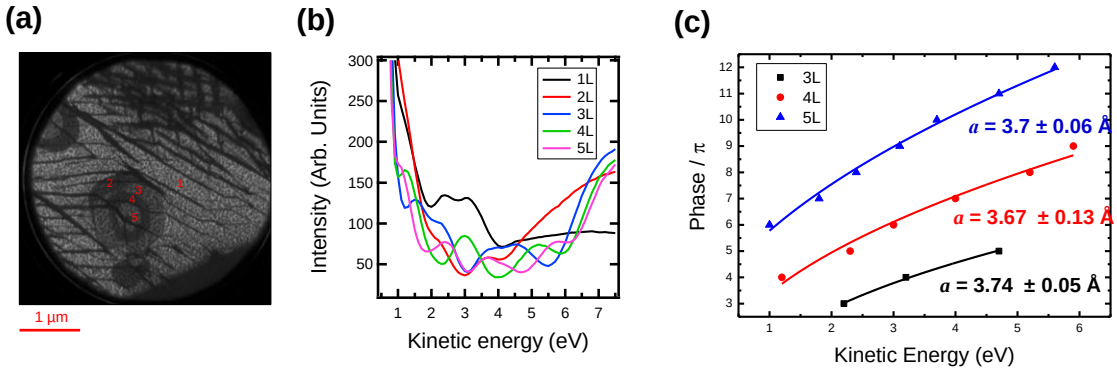


**Figure 94** LEEM reflectance analysis of as-grown FLG film on Cu. a) LEEM image of a FLG on Cu. $E_k$ = 2.5 eV. b) Reflected electron intensity versus the incident electron energy curves for 1-5 L in the region of quantum well resonance. c) Plot of minima and maxima of the curves for 3-5L in (b) and fitted curves using the free electron energy model; *a* indicates the lattice spacing obtained from the fitting for each thickness.

This simple model corresponds well with the observed position of minima and maxima for all cases of as-grown and transferred graphene (Figure 94). Furthermore, using, $n$, $a$, and $V_0$ as fitting parameters, we found that in all cases $a \sim 3.7 \pm 0.1$ Å, much bigger than the interlayer spacing of ideal AB stacked structure (~3.35 Å).

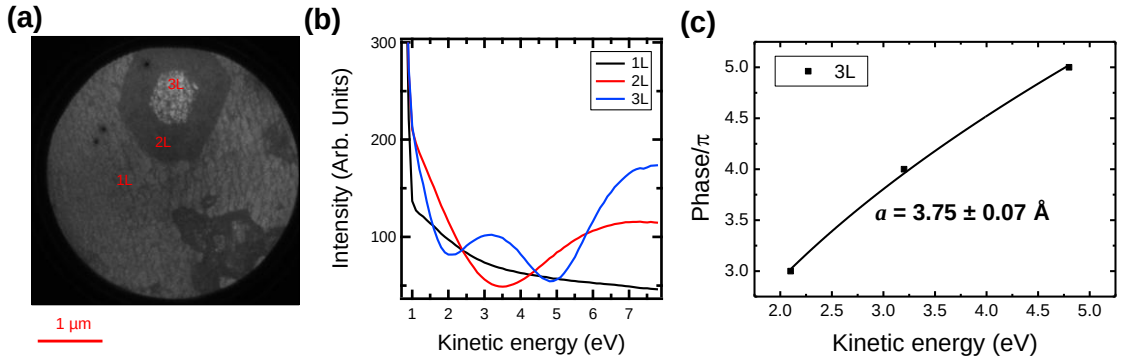


**Figure 95** LEEM reflectance analysis of FLG film transferred onto SiO2/Si substrate. a) LEEM image of a FLG. $E_k$ = 2.5 eV. b) Reflected electron intensity versus the incident electron energy curves for 1-3 L in the region of quantum well resonance. c) Plot of minima and maxima of the curves for 3L in (b) and fitted curves using the free electron energy model.

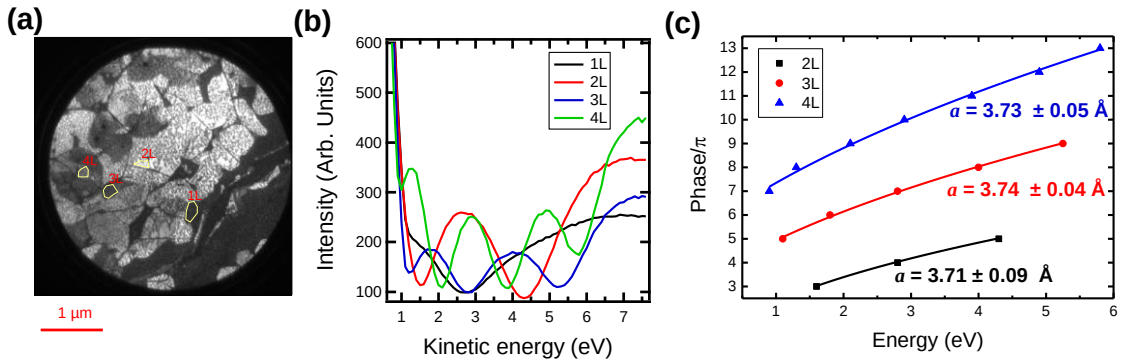


**Figure 96** LEEM reflectance analysis of FLG film transferred onto Au/mica substrate. a) LEEM image of a FLG. $E_k$ = 2.5 eV. The areas analysed for the reflectance curves are marked by the yellow boundaries. b) Reflected electron intensity versus the incident electron energy curves for 1-4 L in the region of quantum well resonance. c) Plot of minima and maxima of the curves for 2-4L in (b) and fitted curves using the free electron energy model.

Some of the differences between the effects of different substrates and the reflectance curves from literature must be noted here. On Cu, extra features are observed possibly coming from the graphene-Cu interface for a monolayer graphene (Figure 94b). This effect decreases as the graphene layer becomes thicker. This is similar to what has been observed previously for as-grown CVD graphene on Cu.[500] In addition, the 1st layer of graphene on $SiO_2$/Si appears to be more strongly coupled to the substrate than the 1st layered is coupled to the 2nd layer such that no minima is observed and the resonance condition starts to appear from the 2nd layer such that n layers have n-1 minima (Figure 95b). This behaviour is different from AB stacked, mechanically exfoliated graphene on $SiO_2$/Si as the n number of

layers (n>1) has a n minima in the reflectance curve.[512] Graphene on Au/mica substrate exhibits more ideal reflectance curve that a minimum is observed from the very first layer (Figure 96b).

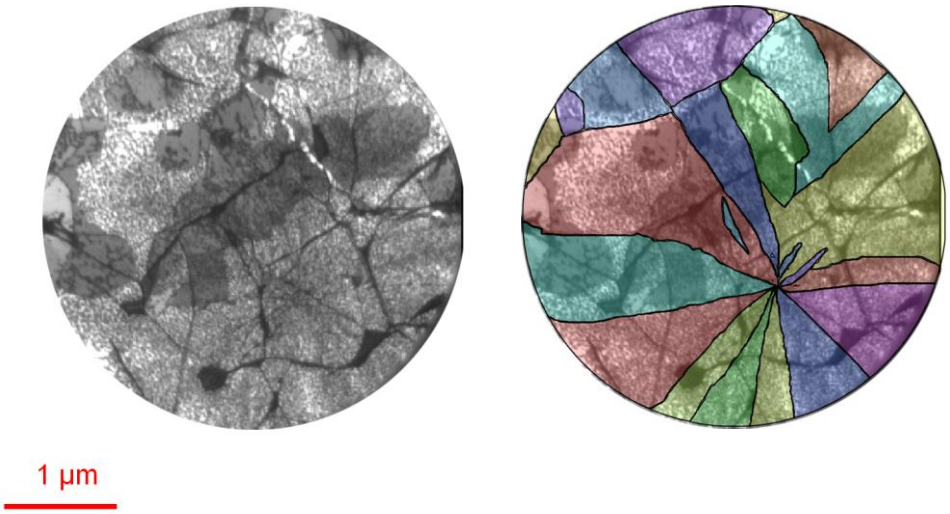


**Figure 97** LEEM image of FLG/monolayer regions on Au/mica (left) and the colour map overlay (right) of rotational domains obtained by angle dependent LEED dark-field imaging analysis on the same area. Note that the FLGs do not appear to have its own rotational domains.

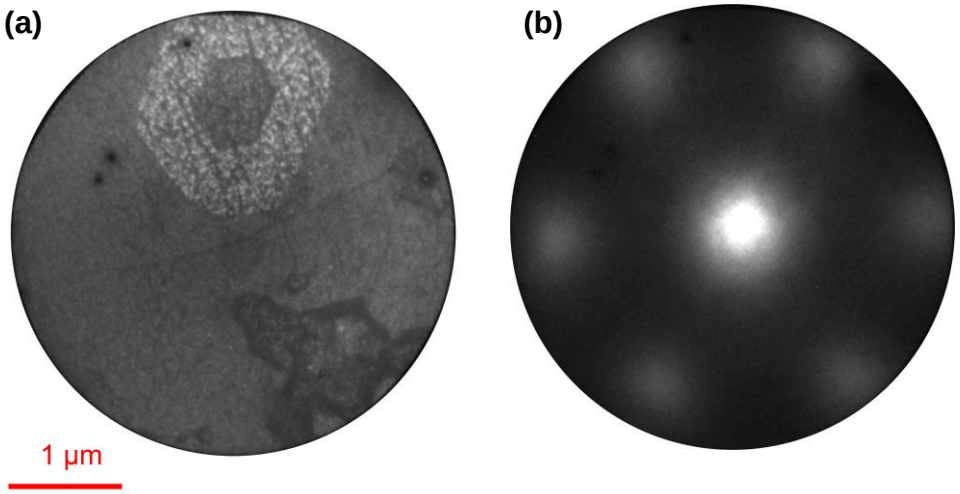


**Figure 98** a) LEEM image of a single crystal graphene containing a trilayer region on $SiO_2$/Si. $E_k$ = 13 eV. b) The LEED diffraction pattern from the trilayer region. $E_k$ = 42 eV. Note that presence of a single hexagonal spot indicates that the entire region is made of a single crystal domain even for the FLG. The orientation of LEED pattern suggests that the edges of hexagonal islands of the FLG are dominantly zigzag.

### *9.5 LEED Reflectance Analysis*

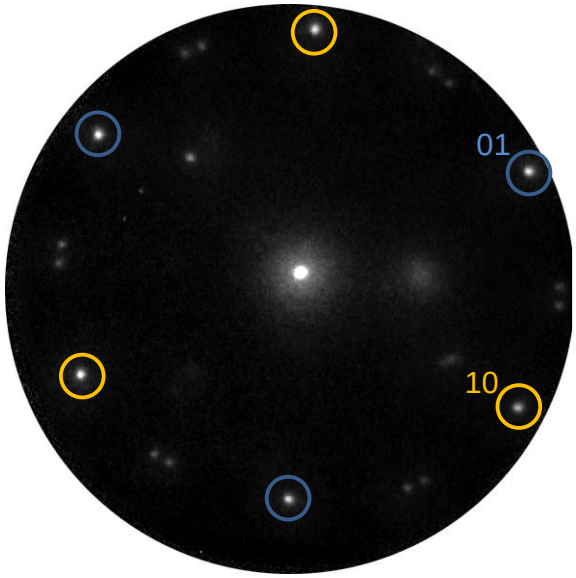


**Figure 99** 1st order LEED pattern of a FLG structure. For the main diffraction pattern, the two different families of inequivalent diffraction spots expected for 3-fold AB staking are indicated by light blue (01) and orange (10) circles.

In order to determine the angle of misorientations between the layers, we have employed the LEED techniques on the multilayers. However, our extensive dark-field imaging and diffraction pattern analysis has shown that in most of the cases the FLG rather follows the orientation of the underlying monolayer. One of the examples is shown in Figure 97, where rotational domains of graphene do not match well with the regions of multilayers. Another example is given in Figure 98, where the entire region within the field of view is made of a single crystal. In addition, correlating the orientation of the LEED pattern with the orientation of hexagonal FLG islands suggests that each side of the 2nd and 3rd layers consists of a zigzag edges.[513]

This observation suggests that either AB, or AA like stacking is frequently present in the multilayers. These two structures can be distinguished by the differences in the intensities between (10) and (01) diffraction spots (Figure 99).[514] In the AB stacked structure, which has a 3-fold symmetry, the (10) and (01) spots are expected to have different incident electron energy dependence whereas, the 6-fold AA stacked structure exhibits the diffraction pattern in which (10) and (01) spots are equivalent. The energy dependent (10) and (01) diffraction spot intensity curves from the three different samples in Figure 100 demonstrate that the multilayers are stacked in AA fashion since the two curves are not significantly different

compared to those expected for AB stacked graphene. The difference from sample to sample in Figure 100 can be attributed to differences in substrate-graphene interactions for Cu, Au, and $SiO_2$ substrates. The Cu substrates may also contain layers of copper oxides as the sample was exposed to air before the LEEM measurement.

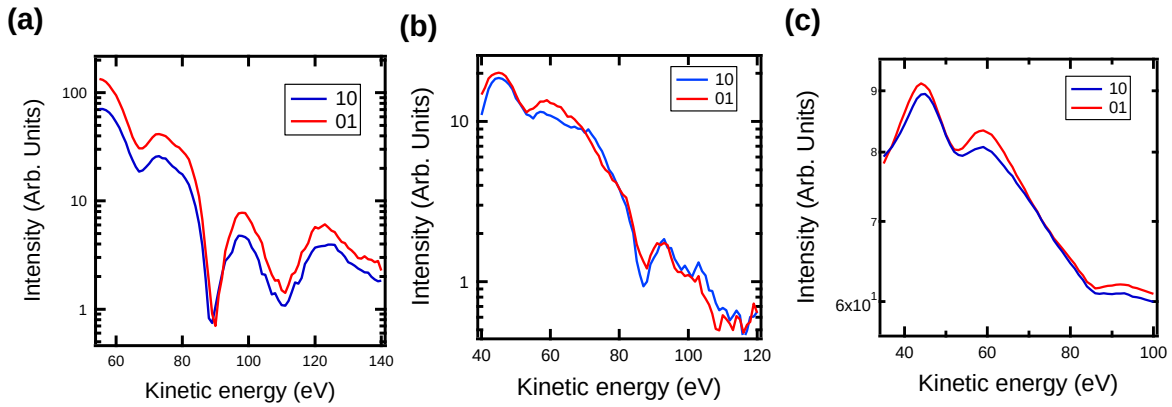


**Figure 100** Comparison of LEED diffraction intensity curves from the (10) and (01) spots from the FLGs on a) as-grown graphene film on Cu, b) transferred onto Au/mica, and c) transferred onto $SiO_2$/Si.

### *9.6 Cross-sectional TEM*

In order to directly image the cross-section of the multilayer stacks of graphene, we have performed cross-sectional TEM on as-grown FLG on Cu. For this, a thin layer of PMMA was spin-coated on the as-grown graphene followed by the focused ion beam milling to cut out the cross-section which was transferred to a TEM grid. From the high resolution images, we observed a bilayer graphene with an interlayer spacing of 3.6 ± 0.1 Å (Figure 101) which is close to the interlayer spacing calculated from the LEEM reflectance analysis. A few theoretical publications have suggested that the interlayer spacing in AA stacked graphene is about ~3.64 Å.[515-518] Experimentally, interlayer spacing between 3.5 and 3.7 Å has been reported in AA stacked FLG that were produced by the vertical growth on a the (111) surface of diamond[519] or annealing of exfoliated graphite.[520] The direct observation of the larger lattice spacing and agreement with literature data give a strong support for the existence of AA stacked graphene in our samples.

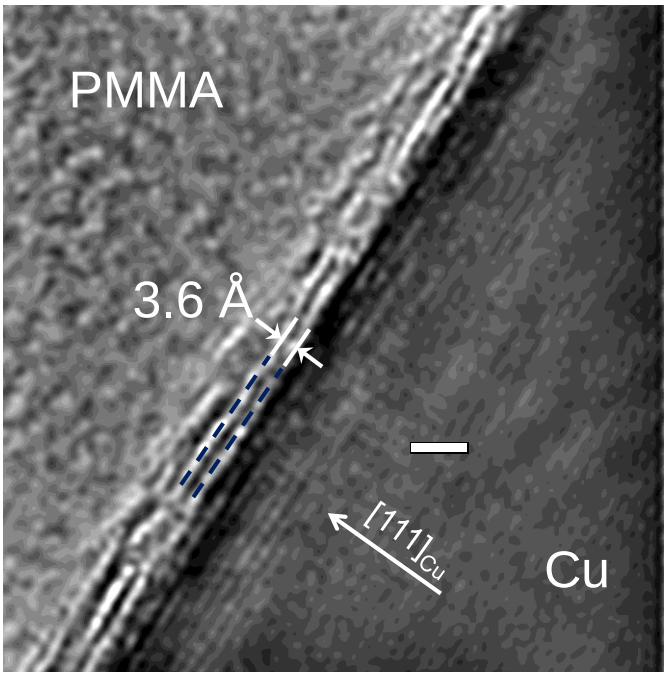


**Figure 101** Cross-sectional, high resolution TEM of as-grown bilayer graphene on Cu with interlayer spacing of 3.6 Å . $E_{acl.}$ = 300 kV.

### *9.7 Electronic Band Structure of FLG*

As a final experimental evidence for AA stacking in the FLG, ARPES has been performed on the both single and FLG on Cu as shown in Figure 102. For the monolayer graphene, Dirac-cone like linear dispersion relationship is observed with the Dirac point very close to the Fermi level as evident by the linear extrapolation of the two branches of the valence band. This is expected as copper does not strongly interact with graphene with negligible charge transfer at the interface and similar to what has been reported before.[211] In FLG, a linear dispersion is observed which is clearly different from the hyperbolic dispersion relationship of AB stacked graphene. Moreover, the Dirac point is shifted by about 0.2 eV below the Fermi level. This is likely a result of interlayer interaction that leads to a small shift in the energy levels of each layer in opposite directions (due to Pauli's exclusion principle). This effect has also been predicted theoretically by others using tight binding and DFT calculations.[521]

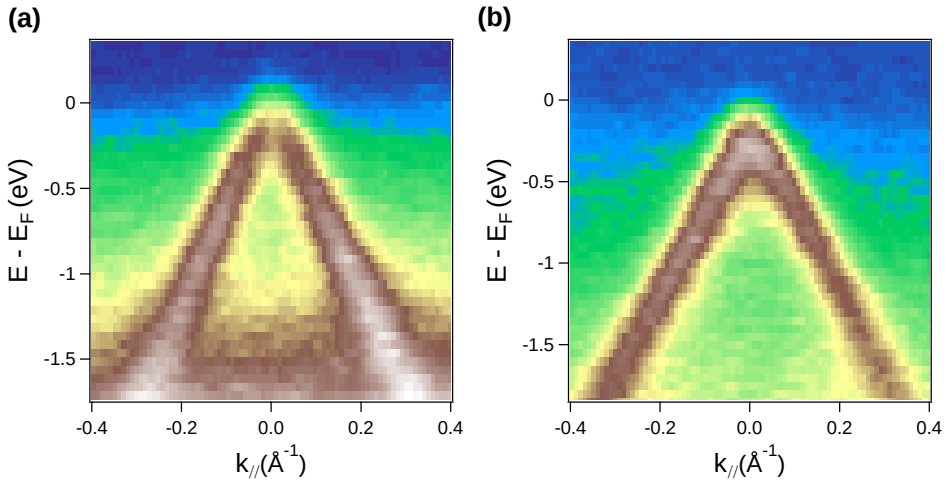


**Figure 102** ARPES of as-grown monolayer graphene and FLG on Cu. a) Electronic structure of monolayer about the K point with the Dirac point located at the Fermi level. $E_{hv}$ = 50 eV. b) Electronic structure of FLG about the K point with the Dirac point down shifted by ~ 0.2 eV from the Fermi level. $E_{hv}$ = 40 eV.

### *9.8 Discussion on the Preferred Stacking Order*

The deviation from the most stable AB stacking configuration in the FLG is possible considering that though the AB stacking order is thermodynamically favoured via a small energy difference from other orientations, misoriented graphene sheets form due to kinetic reasons as a large energy barrier may exist for them to rotate and to transform into the AB stacked structure.[515,522] Indeed, pryolytic graphite which initially exhibits random stacking order, would only transform to the AB stacking structure when annealed at a temperature greater than 2300 ℃.[523,524] Moreover, FLG flakes exfoliated from natural graphite annealed at 2000 ℃ can exhibit both AB and AA stacking orders[520] indicating that there is not much difference between the energies of the two configurations. Theoretically, the energy difference between the two stacking orders of the free-standing bilayer has been estimated to be only 20 meV/atom.[525]

The influence of the substrate crystal lattice extended to the growth of FLG is expected to impart a certain set of preferred orientations distinct from a free standing FLG. AA stacking is naturally expected if the underlying Cu lattice imposes the same kind of epitaxial relationship that is identical to the orientation and position of the 1$^{st}$ layer whereas the AB stacking involves translation (or rotation) of lattice away from the lowest energy Cu sites and symmetry breaking transition from the 6-fold symmetry to 3-fold. This is especially

reasonable for the growth underneath the 1st layer (inverted wedding cake type growth). The prevalence of the AA like orientation was also observed previously in TEM diffraction studies where a large fraction of rotational angles was found to be close to 0° in CVD bilayer graphene[214] although the direct evidence for AA stacking was not given until now.

Orientations other than AA or AB stacking can exist if the Cu lattice supports multiple rotational domains depending on the lattice and symmetry mismatch between the substrate and overlayers as discussed in the previous chapter. The thickness dependent differences in the substrate-overlayer interactions may also give rise to additional rotational relationships such as the frequently observed 30° rotation angles. This kind of substrate induced rotational domains has been also observed for the multilayer growth on other transition metals such as Ir,[526] Pd.[513]

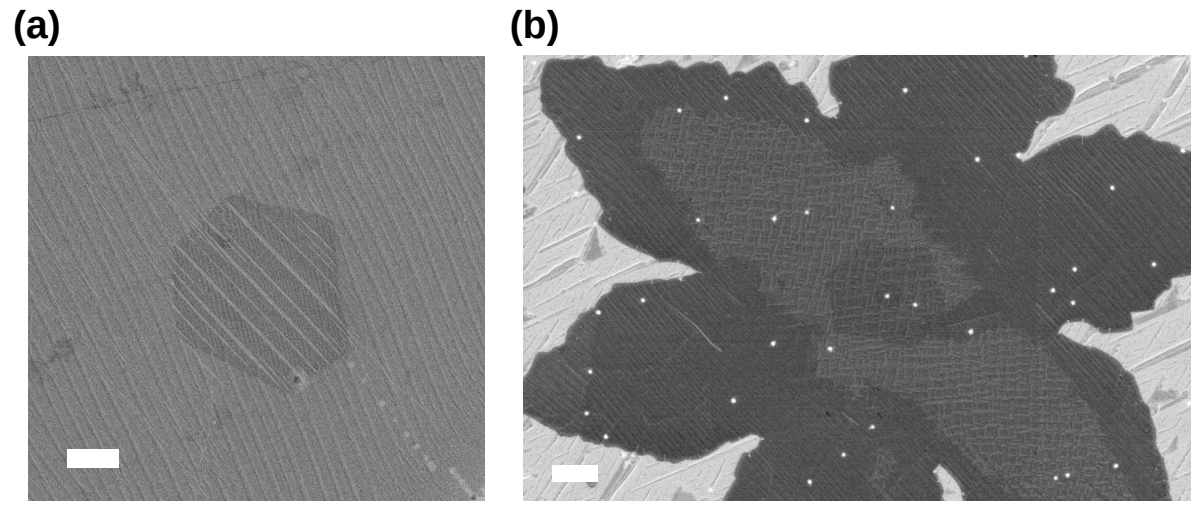


**Figure 103** SEM images of as grown monolayer/FLGs on Cu and their thickness dependence of graphene-Cu morphologies. a) The bilayer graphene island (at the centre) clearly exhibits different alignments of surface facets from the continuous monolayer graphene film surrounding the bilayer. Scale bar, 2 m. b) FLG nuclei on Cu(310) with a different set of surface facets appearing through the centre.

Indirect evidence for thickness dependent FLG-substrate interaction is shown in Figure 103, where the FLG's induce a set of surface facets that are very different from the monolayer-Cu surfaces in terms of alignments and periodicity of the alternating ridges arising from the surface faceting. These unusual graphene induced surface morphologies are often observed for FLG on high index Cu surfaces [e.g. Cu(310)] where the Cu surface has tendency to breakdown into low index facets [e.g. Cu(111) and Cu(100)] in order to minimize

the total surface energy. The origin of the multiplicity in the way that the surface can reconstruct and decompose depending on the thickness of graphene is not well understood as of now and requires further analysis.

## *9.9 Conclusion*

In this chapter, various structural characterizations on FLG produced by CVD on Cu have shown that the FLGs can exhibit various stacking orders that are different from the most common AB stacking order. The LEED analysis has shown that AA stacking is often present although further statistical analysis is required to determine the exact distribution of different stacking orders and how the crystal orientations of Cu affect the preferred stacking order in order to selectively grow CVD FLGs of desired orientations. The analysis using Raman spectroscopy suggests that approximately half of the bilayers are either AB stacked or "decoupled", but further confirmation is required to determine whether all the "decoupled" bilayers correspond to AA stacked layers or twisted bilayers of 30° misorientations. It is not also clear that up to which extent the Cu substrate influences the preferred orientations of the graphene sheets. Nevertheless, this study has shown that the CVD method provides an accessible way to produce bilayers of unique electronic properties (e.g. weak interlayer interaction and preserved linear dispersion relationship) of large domain sizes up to ~10 μm.

# 10 Conclusions

## *10.1 Summary*

This dissertation has investigated the ways that the two promising routes toward large area graphene, solution-based non-covalent exfoliation and chemical vapour deposition, can be improved for optoelectronic applications through the fundamental understanding and optimization of the processing conditions. In the first part of the work, an efficient solution based exfoliation method to produce high-quality graphene dispersion of high concentration in NMP and large-scale thin film deposition method via Langmuir-Blodgett assembly has been demonstrated. By simultaneously stirring and sonicating graphite in NMP during the exfoliation process, a large concentration of monolayer and FLG, greater than 1 mg/mL has been achieved. The analysis of the relationship between the morphology and thickness dependent conductivity has revealed the percolative behaviour in the charge carrier conduction. The temperature dependent conductivity of the film suggests the band-like transport in polycrystalline graphite unlike that of the covalently functionalized graphene which typically exhibits hopping-like conduction. However, the large-area electronic properties of exfoliated graphene are limited by a small flake size of less than 1 μm and loose packing of the flakes that result in much smaller value of charge carrier mobility (< 0.9 $cm^2/Vs$) and relatively high sheet resistance values (5 kΩ/□ at transmittance of 73%) in the Langmuir-Blodgett films compared to those of pristine graphene.

This limitation of the solution based graphene has motivated us to investigate the CVD of graphene on Cu via catalytic decomposition of $CH_4$ in the latter part of dissertation where continuous sheet of high-quality graphene can be produced with the scale of the film limited only by the size of the substrate and the reaction chamber. The analysis of the growth kinetics using the model of two-dimensional surface nucleation has shown that an intricate relationship among surface adsorption, surface diffusion, carbon adatom attachment, and desorption is present. This relationship has been used to explain the growth process and reveal the critical atomic processes that govern the nucleation and growth kinetics depending

on growth conditions. For example, the low growth temperature (<870 ℃) imparts capture controlled nucleation regime where the nucleation is controlled by the competition between adatom capture by the supercritical nuclei and creation of a new nucleus. On the other hand, the high growth temperature (> 870 C) leads to desorption controlled regime where desorption of carbon adatoms also competes with the capture and nucleation processes. Moreover, our study provides the guidelines for tailoring the 2D structure of graphene for various applications. For instance, a large single crystalline graphene can be produced by the growth at high temperature (> 1000 ℃), low hydrocarbon concentration ($P_{CH4}/P_{H2} < 0.01$), on a smooth Cu(111) surface. However, high $P_{CH4}/P_{H2}$ is preferred for the production of continuous graphene film. The general model for graphene coverage has been developed based on Langmuir adsorption theory in order to address this issue and to provide quantitative predictions for the appropriate values of $P_{CH4}/P_{H2}$ and temperature in order to achieve the desired graphene coverage at the final stage of CVD.

The close examination of graphene growth on various Cu crystal orientations has demonstrated that geometry of graphene domains of selective rotational orientations can be realized to offer the opportunity for large scale production of tailor-made novel graphene nanostructures of desired alignments, density, dimensions, and edge structures. Cu(111) facet is expected to be an ideal crystal orientation for graphene growth as it has only a single rotational domain leading to the absence of high-angle grain boundaries, which is detrimental to graphene's electrical properties, when the final continuous film is obtained.

Lastly, the structure of FLG produced by CVD has been characterized by Raman spectroscopy, low energy electron microscopy, and low energy electron diffraction. This has shown that apart from the most stable AB stacking, AA stacked graphene multilayers can be frequently observed in CVD grown graphene on Cu paving the way to produce high mobility FLG with linear dispersion relationship.

### *10.2 Future Works*

Although non-covalently exfoliated graphene exhibits lower electronic quality compared to CVD graphene, it may still be applied to low-end areas such as multi-functional composites, antistatic coating and electro-magnetic shielding. To this end, the average size of the flakes must be much greater than the typical size obtained in this work. Various solvents and surfactants and gentler exfoliation conditions (e.g low sonication power) should be

investigated, in order to increase the lateral size and the overall quality of the solution based graphene.

Regarding the future work on the CVD of graphene on Cu, further characterization is needed to probe the micro/nano structures of graphene produced on various Cu crystal orientations to confirm the presence of rotational domains and grain boundaries predicted by the dissertation. Moreover, electronic characterizations should be performed on such structures to test and exploit the unique properties such as weak localization for the specific line defects and semiconducting behaviours in nanoribbons predicted by the theory. For large scale applications, an accessible way to produce Cu crystal substrates with the desired crystal orientations should be sought by employing different approaches; e.g. electrochemical deposition, physical vapour deposition, etc. In addition, strains and wrinkles produced by thermal lattice expansion coefficient mismatch, and effect of surface facets in high index Cu surfaces have not been well studied here and should be explored in the future as they can impart interesting features to the properties of CVD graphene.

The implication of this work is not only limited to the growth of graphene on Cu using $CH_4$. This work is expected to initiate the future studies on the growth mechanism of other two dimensional materials (e.g. metal chalcogenides, boron nitride, and silicene) with a different set of precursors and catalysts. If the energetics of the reaction pathways are known (e.g. decomposition energy and attachment barrier), this study will aid the selection of appropriate precursors and catalysts to optimize the growth time, temperature, and required amount of materials for commercial manufacturing process.

Moreover, this work has considered the growth kinetics of the monolayer graphene predicted by the ideal, self-limited growth mechanism. The growth kinetics of FLG should be probed further to unveil the growth mechanism and high-yield method to create homogenous FLG of controlled thickness of controlled stacking order should be realized in order to bring the CVD graphene closer to its implementation in a wide range of transparent conductor and interconnect applications.

# Appendix

**Saturation nucleus density solution**

Under the theoretical framework of Robinson and Robins,[429,433] we can obtain the solution for the nucleation rate equations based on the assumption that critical size of nucleus is a monomer, and coalescence of supercritical nucleus does not occur significantly during the nucleation stage, the governing processes are adsorption, surface diffusion, capture by supercritical nucleus, and desorption (at high temperature).

For the case of desorption controlled regime (high temperature), the nucleation rate ($\dot{n}_s$) is:

$$\dot{n}_s = R\tau_a w_1 - R\tau_a g_s w_s n_s^2$$

$R$ is the rate of $CH_4$ impinging and decomposing at the Cu surface:

$$R = \frac{P_{CH_4}}{\sqrt{2m_{CH_4}kT}} s_0 \exp\left(\frac{-E_{ad}}{kT}\right)$$

where $P_{CH_4}$ is partial pressure of methane, $m_{CH_4}$ molecular weight of methane, k, Boltzmann constant, $s_0$, initial sticking coefficient of methane on Cu and $E_{ad}$, adsorption activation energy.

$\tau_a$ is the adsorption lifetime of a carbon adatom at the surface which can be described by:

$$\tau_a = \nu_0 \exp\left(\frac{E_{des}}{kT}\right)$$

Where $\nu_0$ is the vibrational frequency and $E_{des}$ is desorption activation energy of carbon adatom.

$w_1$ is the rate for adatoms to form a larger immobile cluster of graphene nucleus:

$$w_1 = \sigma_1 \nu_0 \exp\left(\frac{-E_d}{kT}\right)$$

Where $\sigma_1$ is a dimensionless geometric factor between 1 and 10 for the formation rate of a stable cluster, and $E_d$ is surface diffusion barrier.

$w_s$ is the rate of attachment of adatoms at the edge of graphene nucleus:

$$w_s = \sigma_s \nu_0 \exp\left(\frac{-E_{att}}{kT}\right)$$

Where $\sigma_s \approx 2\sigma_1$ is a dimensionless geometric factor for the capture term, $E_{att}$ is attachment activation energy.

And $g_s$ is a dimensionless geometric factor concerning coalescence of supercritical nuclei and is often treated as constant close to 1.

Then the saturation nucleus density ( $N_s$ ) for desorption controlled regime when $\dot{n}_s = 0$ is[433]:

$$N_s^2 = R\tau_a w_1 / g_s w_s$$
$$= \frac{P_{CH_4}}{g_s \sqrt{2m_{CH_4} kT}} s_0 \exp\left(\frac{E_{des} + E_{att} - E_d - E_{ad}}{kT}\right)$$

For the case of capture controlled regime, the nucleation rate ( $\dot{n}_s$ ) is:

$$\dot{n}_s = Rw_1 / \left(w_s n_s\right)^2 - Rg_s n_s$$

Then the saturation nucleus density is:

$$N_s^3 = Rw_1 / g_s w_s^2$$
$$= \frac{\sigma_1 P_{CH_4}}{g_s \sigma_s^2 \sqrt{2m_{CH_4} kT}} s_0 \exp\left(\frac{2E_{att} - E_d - E_{ad}}{kT}\right)$$

**Measurement of Mean Nucleus Density and Graphene Area Coverage**

The mean nucleus density for each sample was computed by image analysis of high magnification SEM images. The mean nucleus density ( $\bar{n}$ ), mean nucleus area ( $a_G$ ), and area coverage ( $A_G$ ) follows the equation:

$$\bar{n}a_G = A_G$$
$$\therefore \bar{n} = \frac{A_G}{a_G}$$

The mean nucleus area was obtained by measuring the individual area of more four hundred individual nuclei by using "ImageJ" software for each sample and finding the average. The fractional area coverage ( $A_G$ ) was obtained by using "ImageJ" software through the threshold method.

## Model for Graphene Area Saturation: Full Details

Consider three main reversible reactions that result in conversion of $CH_{4(g)}$ to graphene formed on Cu and $H_{2(g)}$:

$$CH_{4(g)} + 5S_{(Cu)} \rightleftharpoons Graphene_{(a)} + 2H_{2(g)}$$

Dissociative adsorption of methane:

$$CH_{4(g)} + 5S_{(Cu)} \underset{k_{-1}}{\overset{k_{+1}}{\rightleftharpoons}} C_{(a)} + 4H_{(a)} \quad \Delta H_{ad\_CH4} \cong 3.2 \text{ eV}^{[207,464]}$$

Hydrogen Desorption:

$$4H_{(a)} \underset{k_{-2}}{\overset{k_{+2}}{\rightleftharpoons}} 2H_{2(g)} + 4S_{(Cu)} \quad \Delta H_{ad\_H2} \cong - 0.3 \text{ eV}^{[468\text{-}470]} \text{ per } H_2$$

Graphene Formation from adsorbed carbon:

$$C_{(a)} \underset{k_{-3}}{\overset{k_{+3}}{\rightleftharpoons}} Graphene_{(a)} \quad \Delta H_{form\_G} \cong -2.4 \text{ eV}^{[207]}$$

Generally, the rate of adsorption:

$$r_{ad} = \frac{P}{\sqrt{2\pi mkT}} s_0 \exp\left(\frac{-E_{ad}}{kT}\right) f(\theta_s)$$

Where P is the partial pressure of the reactant gas, m is the mass of the reactant molecule, $k$, Boltzmann's constant, $T$, temperature, $s_0$ is the initial sticking coefficient pre-expoential factor, and $f(\theta_s)$ is free surface coverage ($\theta_s$), dependent sticking coefficient term, $E_{ad}$, activation energy of the adsorption.

The rate of desorption is:

$$r_{des} = v_n \exp\left(\frac{-E_{des}}{kT}\right)[A]^n$$

Where n, is the order of the reaction, $v_n$ is n-th order vibrational frequency, $[A]$, the surface concentration of the adsorbate, and $E_{des}$, activation energy of desorption.

We note that the $CH_4$ decomposition reaction can be broken down into many intermediate steps, but it can be combined to give effective kinetic constants for (1). Several contributions[465,466] consider the intermediate steps of the $CH_4$ decomposition on transition metal surfaces in the usual growth conditions to be the following:

$$(1\_1)\ CH_{4(g)} + S_{(Cu)} \underset{k_{-1\_1}}{\overset{k_{+1\_1}}{\rightleftharpoons}} CH_{4(a)}$$

$$(1\_2)\ CH_{4(a)} + S_{(Cu)} \underset{k_{-1\_2}}{\overset{k_{+1\_2}}{\rightleftharpoons}} CH_{3(a)} + H_{(a)}$$

$$(1\_3)\ CH_{3(a)} + S_{(Cu)} \underset{k_{-1\_3}}{\overset{k_{+1\_3}}{\rightleftharpoons}} CH_{2(a)} + H_{(a)}$$

$$(1\_4)\ CH_{2(a)} + S_{(Cu)} \underset{k_{-1\_4}}{\overset{k_{+1\_4}}{\rightleftharpoons}} CH_{(a)} + H_{(a)}$$

$$(1\_5)\ CH_{(a)} + S_{(Cu)} \underset{k_{-1\_5}}{\overset{k_{+1\_5}}{\rightleftharpoons}} C_{(a)} + H_{(a)}$$

Here, we do not consider any side reactions that leads to direct formation of dimers and its derivatives ($C_2$, $C_2H_x$, etc.) from $CH_x$'s and we consider the above reactions to be the general reaction pathway for the dissociative adsorption of $CH_4$[465,466].

For the reaction (1_1), the rates and the equilibrium constants are:

$$r_{+1\_1} = k_{+1\_1} P_{CH_4} (\theta_S \rho_s)$$

$$r_{-1\_1} = k_{-1\_1} (\theta_{CH_4} \rho_s)$$

$$k_{+1\_1} P_{CH_4} (\theta_S \rho_s) = k_{-1\_1} [CH_4]_{eq}$$

$$\frac{k_{+1\_1}}{k_{-1\_1}} = \frac{[CH_4]_{eq}}{P_{CH_4} (\theta_S \rho_s)} = K_{1\_1}$$

$$K_{1\_1} = \frac{1}{\rho_s v_{-1\_1} \sqrt{2\pi m_{CH_4} kT}} \exp\left(\frac{-\Delta H_{1\_1}}{kT}\right)$$

And for the reaction (1_2),

$$r_{+1\_2} = k_{+1\_2}\left(\theta_{CH_4}\rho_s\right)\left(\theta_S\rho_s\right)$$

$$r_{-1\_2} = k_{-1\_2}\left(\theta_{CH_3}\rho_s\right)\left(\theta_H\rho_s\right)$$

$$k_{+1\_2}\left[CH_4\right]_{eq}\left(\theta_S\rho_s\right) = k_{-1\_2}\left[CH_3\right]_{eq}\left[H\right]_{eq}$$

$$\frac{k_{+1\_2}}{k_{-1\_2}} = K_{1\_2} = \frac{\left[CH_3\right]_{eq}\left[H\right]_{eq}}{\left[CH_4\right]_{eq}\left(\theta_S\rho_s\right)}$$

$$K_{1\_2} = \frac{\nu_{+1\_2}}{\nu_{-1\_2}}\exp\left(\frac{-\Delta H_{1\_2}}{kT}\right)$$

Combining the reactions (1_1 and 1_2), the effective equilibrium constant, $K_{1\_1+2}$ is:

$$K_{1\_1+2} = \frac{\left[CH_3\right]_{eq}\left[H\right]_{eq}}{P_{CH4}\left(\theta_S\rho_s\right)^2} = \frac{K_{1\_2}\left[CH_4\right]_{eq}\left(\theta_S\rho_s\right)}{\frac{\left[CH_4\right]_{eq}}{K_{1\_1}}\left(\theta_S\rho_s\right)} = K_{1\_1}K_{1\_2}$$

$$K_{1\_1}K_{1\_2} = \frac{\nu_{+1\_2}}{\rho_s\nu_{-1\_1}\nu_{-1\_2}\sqrt{2\pi m_{CH_4}kT}}\exp\left(\frac{-\left(\Delta H_{1\_2}+\Delta H_{1\_1}\right)}{kT}\right)$$

$$= \frac{1}{\rho_s\nu_{1\_1+2}\sqrt{2\pi m_{CH_4}kT}}\exp\left(\frac{-\Delta H_{1\_1+2}}{kT}\right)$$

with the effective vibrational frequency factor, $\nu_{1\_1+2} = \frac{\nu_{-1\_1}\nu_{-1\_1+2}}{\nu_{+1\_2}}$,

and overall enthalpy, $\Delta H_{1\_1+2} = \Delta H_{1\_2} + \Delta H_{1\_1}$.

In this manner, the kinetic parameters of intermediate steps can be reduced to a single set of effective constants.

Therefore, balancing rates of adsorption and desorption for the overall decomposition reaction:

$$r_{+1} = k_{+1}P_{CH_4}\left(\theta_S\rho_s\right)^5$$

$$r_{-1} = k_{-1}\left(\theta_C\rho_s\right)\left(\theta_H\rho_s\right)^4$$

$$k_{+1}P_{CH_4}\left(\theta_S\rho_s\right)^5 = k_{-1}\left[C\right]_{eq}\left[H\right]_{eq}^{\ 4}$$

$$\frac{k_{+1}}{k_{-1}} = \frac{[C]_{eq}[H]_{eq}^{4}}{P_{CH_4}(\theta_S\rho_s)^5} = \frac{(\theta_C\rho_s)(\theta_H\rho_s)^4}{P_{CH_4}(\theta_S\rho_s)^5(1-\theta_G)^5} = \frac{(\theta_C)(\theta_H)^4}{P_{CH_4}(\theta_S)^5(1-\theta_G)^5} = K_1$$

$$K_1 = \frac{1}{\rho_s v_1\sqrt{2\pi m_{CH_4}kT}}\exp\left(\frac{-\Delta H_{ad\_CH_4}}{kT}\right)$$

where $v_1 = 10^{13}$ $s^{-1}$, which is a generally used value of a vibrational frequency when the experimental value is not known,[171] $m_{CH_4} = 2.67 \times 10^{-23}$ kg, and $\rho_{s\_Cu} \sim 1.53 \times 10^{19}$ sites/$m^2$.

Here, we use the assumption of the Langmuir adsorption mechanism for the sticking coefficient:

$$s_0 f(\theta_s) = \theta_s = 1-\theta_H-\theta_C-\theta_G$$

Generally, $[A] = \theta_A\rho_s$, where $\theta_A$ is the overall coverage of the adsorbed species A, and $\rho_s$ is the concentration of surface sites. However, due to the presence of graphene the effective overall free area is decreased by the area coverage of graphene which effectively increases the surface concentration of the adsorbed species. Thus, we assume that C and H adatoms competitively bind only to the available surface that is not covered by graphene so that the surface concentrations of carbon and hydrogen can be expressed in terms of carbon, hydrogen, graphene coverage as:

$$[C] = \frac{\theta_C\rho_s}{1-\theta_G}, \text{ and } [H] = \frac{\theta_H\rho_s}{1-\theta_G}$$

Similarly, for the adsorption and desorption of $H_2$:

$$r_{+2} = k_{+2}[H]^4$$

$$r_{-2} = k_{-2}\left(P_{H_2}\right)^2(\theta_S\rho_s)^4$$

$$k_{+2}[H]_{eq}^{4} = \frac{k_{+2}(\theta_S\rho_s)^4}{(1-\theta_G)^4} = k_{-2}\left(P_{H_2}\right)^2(\theta_S\rho_s)^4$$

$$\frac{k_{+2}}{k_{-2}} = \frac{\left(P_{H_2}\right)^2(\theta_S)^4(1-\theta_G)^4}{(\theta_H)^4} = K_2$$

$$K_2 = \rho_s^{\,2}v_2^{\,2}\left(2\pi m_{H_2}kT\right)\exp\left(\frac{2\Delta H_{ad\_H_2}}{kT}\right)$$

Where $v_2$=$10^{-13}$ s, and $m_{H_2}$ = 3.347 x $10^{-24}$ kg.

For the graphene formation from adsorbed carbon, the rates of attachment ($r_{+3}$) and detachment ($r_{-3}$) of the carbon adatoms per unit length of graphene phase boundary are to be balanced for the steady state. According to the 2D crystallization kinetics[471]:

$$r_{+3} = k_{+3}[C] = a_{cu} v_{+3\_Cu} \exp\left(\frac{-E_{att}}{kT}\right)[C]$$

$$r_{-3} = k_{-3} = \frac{v_{-3\_G}}{a_G} \exp\left(\frac{-E_{\det}}{kT}\right)$$

$$k_{+3}[C]_{eq} = k_{-3}$$

$$\frac{k_{+3}}{k_{-3}} = \frac{1}{[C]_{eq}} = \frac{1-\theta_G}{\theta_C \rho_s} = K_3$$

$$K_3 = \frac{a_{cu} a_G v_{+3\_Cu}}{v_{-3\_G}} \exp\left(\frac{-\Delta H_{form\_G}}{kT}\right)$$

Here, graphene interatomic spacing, $a_G$= 1.42 x $10^{-10}$ m and $a_{Cu}$ =2.3 x $10^{-10}$ m. $v_{+3\_Cu}$ is related to the vibrational frequency of Cu, $v_{-3\_G}$ is related to the vibrational frequency of graphene. If $v_{+3\_Cu} \approx v_{-3\_G}$, the approximate value of the pre-exponential factor is in the order of $10^{-20}$ $m^2$.

Then,

$$\theta_C = \frac{K_1 K_2 P_{CH_4} \theta_S (1-\theta_G)}{\left(P_{H_2}\right)^2} = \frac{(1-\theta_G)}{K_3 \rho_s}, \quad \theta_S = \frac{\left(P_{H_2}\right)^2}{K_1 K_2 K_3 \rho_s P_{CH_4}}, \quad \theta_H = \frac{\left(P_{H_2}\right)^{\frac{1}{2}} \theta_S (1-\theta_G)}{\left(K_2\right)^{\frac{1}{4}}}$$

Using the relationship, $\theta_H + \theta_C + \theta_S + \theta_G = 1$ and solving the system of equations:

$$\theta_G = 1 - \frac{K_2^{\frac{1}{4}} \left(P_{H_2}\right)^2}{K_1 K_2^{\frac{5}{4}} K_3 P_{CH_4} \rho_s - K_1 K_2^{\frac{5}{4}} P_{CH_4} - \left(P_{H_2}\right)^{\frac{5}{2}}}$$

In the typical experimental conditions ($P_{CH4}$, $P_{H2}$ < 1 MPa, T = 300 K – 1080 K), $\theta_S \gg \theta_C, \theta_H$. Thus, $\frac{\left(P_{H_2}\right)^2}{K_1 K_2 K_3 \rho_s P_{CH_4}} = \theta_S$ is the dominant term giving rise to exponential behaviour with apparent activation energy of $\Delta H_{ad\_CH4} - 2\Delta H_{ad\_H2} + \Delta H_{form\_G}$.

Fixing the activation energies as given by the literature values and $\nu_1, \nu_2$ = $10^{-13}$ s and using the pre-exponential factor of $K_3$ as the only fitting parameter, the following curve fitting was performed on our experimental data with $\frac{a_{cu} a_G \nu_{+3\_Cu}}{\nu_{-3\_G}} = 6.3\times10^{-18}$ $m^{-2}$. This is a reasonable value as the vibrational factors can vary over a few orders of magnitude.[171]

**Details on graphene coverage in terms of degree of supersaturation**

$\theta_G \approx 1 - \frac{[C]_{eq}}{[C]_{sup}}$ because:

$$\frac{[C]_{eq}}{[C]_{sup}} = \frac{1/K_3}{\theta_C' \rho_s}$$

$$\theta_C' = \frac{K_1 K_2 P_{CH4} \theta_s'}{\left(P_{H_2}\right)^2}$$

$\theta_s' = 1 - \theta_C' - \theta_H' \approx 1$ as $\theta_s' \gg \theta_C', \theta_H'$

$$\frac{[C]_{eq}}{[C]_{sup}} = \frac{1/K_3}{\theta_c' \rho_s} \approx \frac{\left(P_{H_2}\right)^2}{K_1 K_2 K_3 P_{CH_4} \rho_s} = \theta_s$$

Rearranging this this, we obtain the overall equilibrium constant, $K_G$, for the conversion of methane ($CH4_{(g)}$) to graphene ($C_{(s)}$) on Cu ((1)+(2)+(3)):

$$K_G = K_1 K_2 K_3 = \frac{\left(P_{H_2}\right)^2}{P_{CH_4} \theta_s \rho_s} = \frac{\left(P_{H_2}\right)^2}{P_{CH_4} [S_{Cu}]}$$

Then, the graphene coverage can also be written as:

$$\theta_G \approx 1 - \frac{\left(P_{H_2}\right)^2}{K_G \rho_s P_{CH_4}}$$

Thus, $\theta_G$ is a strong function of $P_{CH4}/P_{H2}^2$, i.e. independent of any change in individual values of $P_{CH4}$, $P_{H2}$ if $P_{CH4}/P_{H2}^2$ remains fixed.

## Details on estimating $c_{nuc}$ from the Experimental Data

Starting from eq. (26, $\frac{dA_G}{dt} = k_{att} c_{cu} \sqrt{A_G} - k_{det} \sqrt{A_G}$

where $k_{att} c_{cu} \sqrt{A_G}$ are the rate of graphene area coverage increase due to atoms arriving, that are proportional to the concentration of adsorbed atoms on the graphene-free Cu surface and to the perimeter of the graphene island ($\sqrt{A_G}$) and $k_{det} \sqrt{A_G}$ are the rate of decrease in the area coverage due to atoms leaving. According to our modified Langmuir model,

$c_{cu}(t=0) = c_{nuc} = [C]_{\text{sup}}$, at the onset of the nucleation (t = 0)

An $c_{cu}(t \to \infty) = c_{eq} = [C]_{eq}$

Using the relationship for the predicted saturation area, $\theta_G$, $[C]_{\text{sup}}$ and $[C]_{\text{eq}}$:

$$A_G(t \to \infty) = A_{sat} = \theta_G \approx 1 - \frac{[C]_{eq}}{[C]_{\text{sup}}}$$

Also $\frac{dA_G(t \to \infty)}{dt} = 0 \Rightarrow k_{att} c_{nuc} \left(1 - \theta_G\right) = k_{det}$

Substituting the above relationships to eq. (26, and solving the equation, we can write the evolution of the graphene area coverage as:

$$A_G = A_{sat} \left( \frac{e^{F(t-t_0)} + 1}{e^{F(t-t_0)} - 1} \right)^2$$

Here, $F = \frac{k_{+3} c_{nuc} \sqrt{N_s A_{sat}}}{\rho_G} = \frac{a_{cu} v_{+3\_Cu}}{\rho_G} \exp\left( \frac{-E_{att}}{kT} \right) c_{nuc} \sqrt{N_s A_{sat}}$

as $k_{att} = \frac{k_{+3}\sqrt{N_s}}{\rho_G}$ [remember that $k_{att}$ is the rate of ***overall*** fractional area increase per unit time (/s) whereas $k_{+3}$ is the number atoms arriving per unit length of an edge per unit time (atoms/m/s)]

Then, using experimentally obtained $F$, and $N_s$, and Asat, and estimated value of $k_{+3}$, c can be calculated by the following equation:

$$c_{nuc} = \frac{\rho_G F}{k_{+3}\sqrt{N_s A_{sat}}}$$

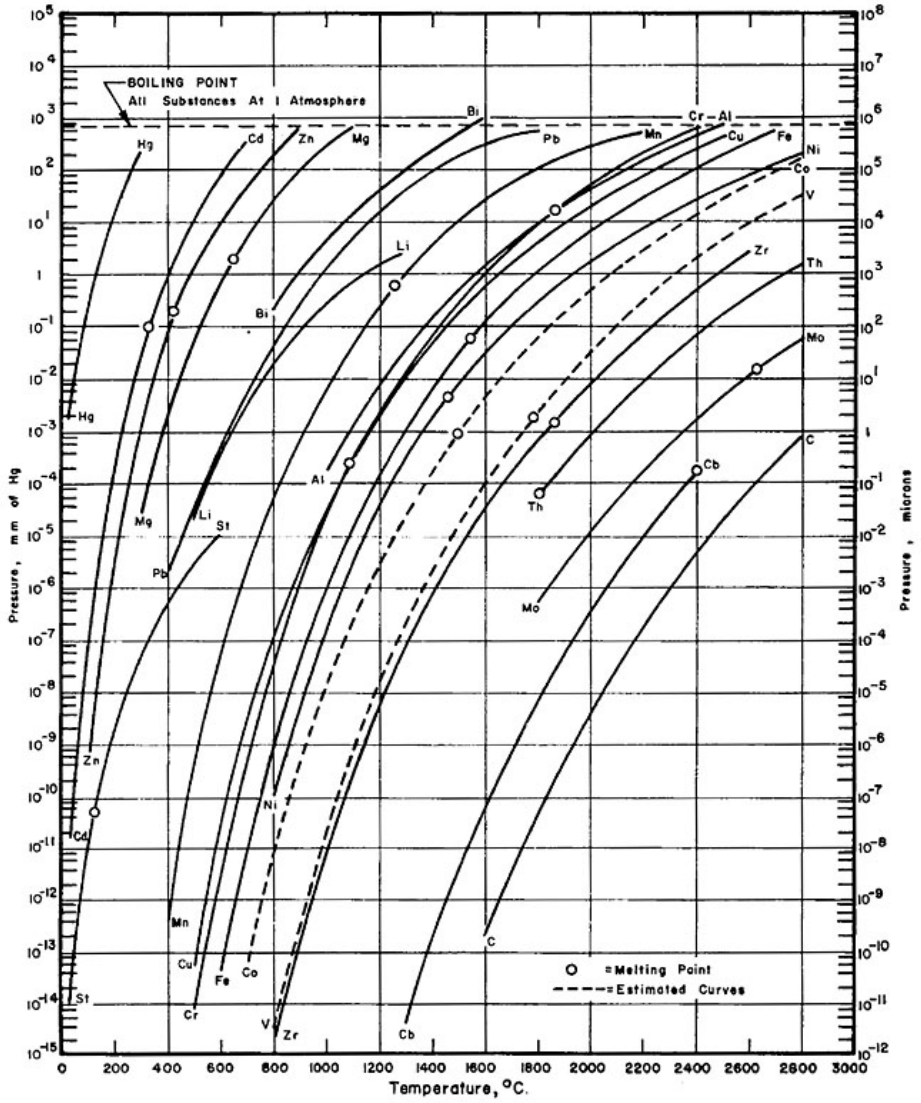


**Figure A1** Temperature dependent vapour pressures of selected metals[349]

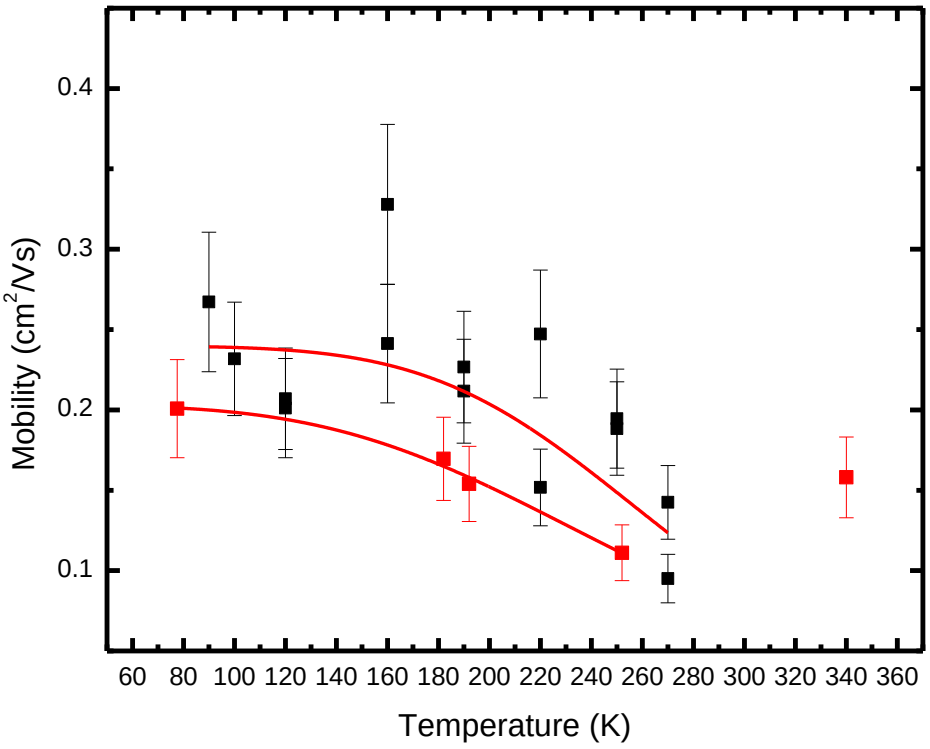


**Figure A2** Temperature dependent mobility from two different devices fabricated from GNMP2. The solid curves are fitted based on eq. 20.

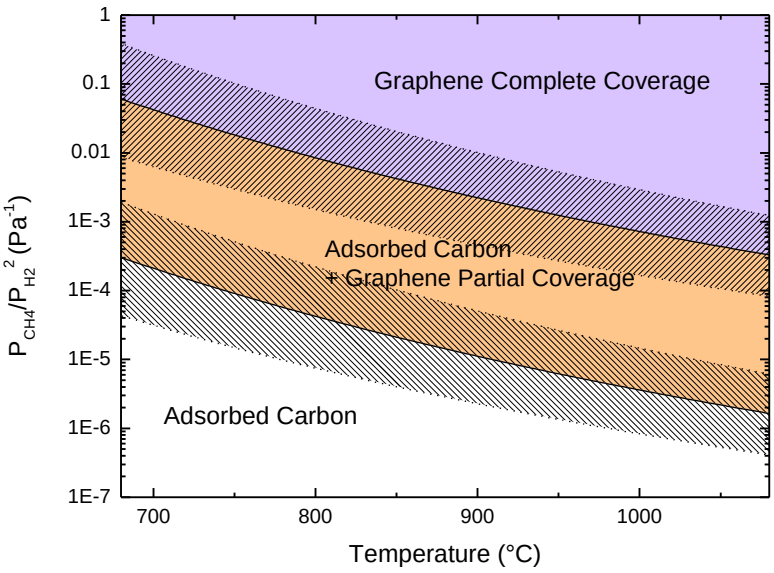


**Figure A3** Contour diagram for complete graphene coverage ($\theta_G > 0.995$ ), adsorbed carbon ($\theta_G = 0$), and partial graphene coverage ($0 < \theta_G < 0.995$) with error bounds (shaded areas) considering 5 % error in the pre-exponential factors, 10% error in pressure values, and 14% error in the energy values (estimated based on the curve fitting).

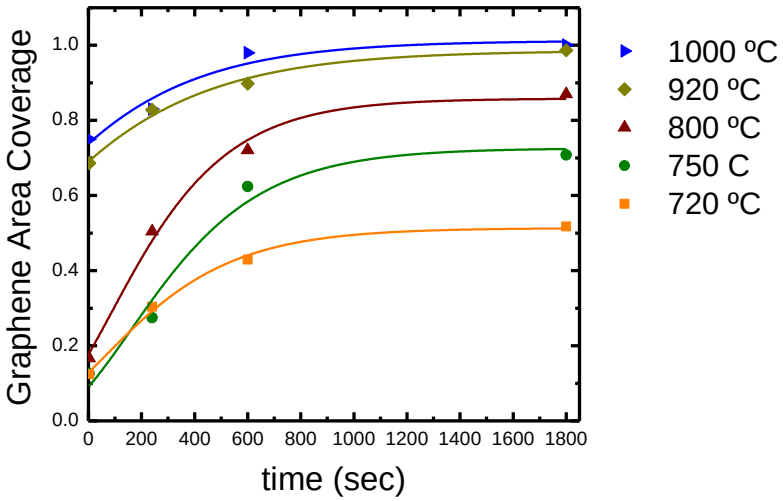


**Figure A4** Time-dependent graphene area coverage for different temperatures with the curve fitting using the edge-controlled kinetics of graphene formation.

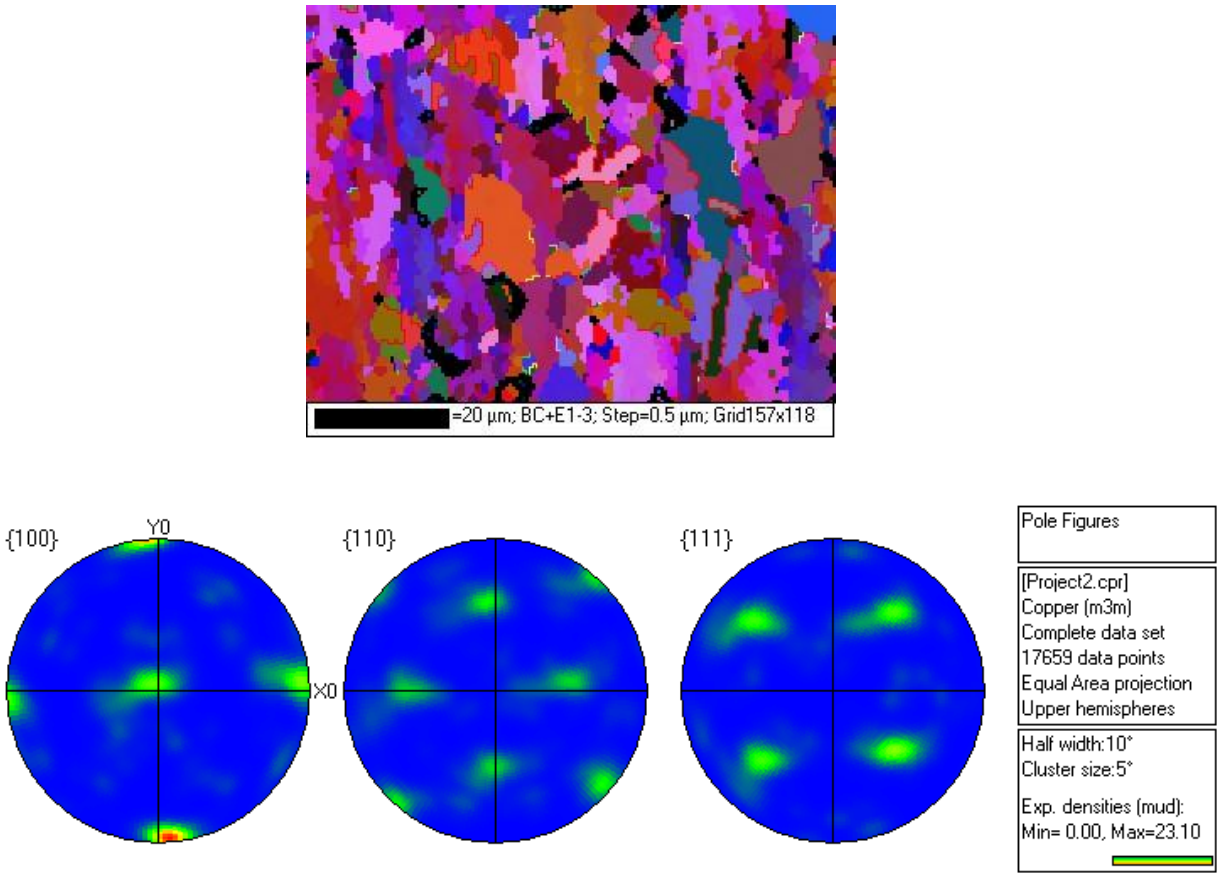


**Figure A5** EBSD texture map and pole figures of as-received 25µm Cu-LP1. Strong (100) texture is evident in the pole figure.

**Table A1** Conditions of the CVD growth experiments.

| Exp. # | Total Pressure (mbar) | Heating Rate | Annealing time (min) | Annealing Temp. ( ˚C) | Growth Time (min) | Growth Temp. (˚C) | $H_2$ Flow Rate (sccm) | $CH_4$ Flow Rate (sccm) | Partial pressure of $CH_4$ (mbar) | Ar Flow Rate (sccm) | Cooling Rate |
|---|---|---|---|---|---|---|---|---|---|---|---|
| 1 | 1013 | normal | 30 | 1000 | 20 | 1000 | 5 | 35 | ~800 | | normal |
| 2 | 100 | normal | 30 | 1000 | 10 | 1000 | 5 | 35 | 87.5 | | normal |
| 3 | 100 | normal | 30 | 1000 | 30 | 1000 | 5 | 35 | 87.5 | | normal |
| 4 | 4 | normal | 30 | 1000 | 10 | 1000 | 5 | 35 | 3.5 | | normal |
| 5 | 4 | normal | 30 | 1000 | 2.5 | 1000 | 5 | 35 | 3.5 | | normal |
| 6 | 4 | normal | 30 | 1000 | 0 | - | 25 | 0 | 0.0 | | normal |
| 7 | 4 | normal | 30 | 1000 | 10 | 1000 | 5 | 35 | 3.5 | | normal |
| 8 | 4 | normal | 30 | 1000 | 2.5 | 1000 | 5 | 35 | 3.5 | | normal |

| | | | | | | | | | | | |
|---|---|---|---|---|---|---|---|---|---|---|---|
| 9 | 4 | normal | 30 | 1000 | 30 | 1000 | 5 | 35 | 3.5 | | normal |
| 10 | 4 | normal | 30 | 1000 | 10 | 1000 | 5 | 35 | 3.5 | | rapid |
| 11 | 4 | normal | 30 | 1000 | 2 | 1000 | 5 | 35 | 3.5 | | rapid |
| 12 | 4 | normal | 30 | 1000 | 30 | 1000 | 5 | 35 | 3.5 | | rapid |
| 13 | 4 | normal | 30 | 1000 | 10 | 1000 | 8 | 32 | 3.2 | | normal |
| 14 | 4 | normal | 30 | 1000 | 2 | 1000 | 8 | 32 | 3.2 | | normal |
| 15 | 4 | normal | 30 | 1000 | 30 | 1000 | 8 | 32 | 3.2 | | normal |
| 16 | 4 | normal | 30 | 1000 | 10 | 1000 | 13.33 | 26.66 | 2.7 | | normal |
| 17 | 4 | normal | 30 | 1000 | 2.5 | 1000 | 13.33 | 26.66 | 2.7 | | normal |
| 18 | 4 | normal | 30 | 1000 | 30 | 1000 | 25 | 13.33 | 1.4 | | normal |
| 19 | 4 | normal | 30 | 1000 | 30 | 1000 | 13.33 | 26.66 | 2.7 | | normal |
| 20 | 4 | normal | 30 | 1000 | 30 | 1000 | 5 | 35 | 3.5 | | normal |
| 21 | 4 | normal | 30 | 1000 | 10 | 1000 | 2 | 8 | 3.2 | | normal |
| 22 | 4 | normal | 30 | 1000 | 30 | 1000 | 2 | 8 | 3.2 | | normal |
| 23 | 4 | normal | 30 | 1000 | 2 | 1000 | 2 | 8 | 3.2 | | normal |
| 24 | 4 | normal | 30 | 1000 | 0.5 | 1000 | 2 | 8 | 3.2 | | normal |
| 25 | 4 | normal | 240 | 1000 | 2 | 1000 | 13.33 | 26.66 | 2.7 | | normal |
| 26 | 4 | normal | 30 | 1000 | 2 | 1000 | 2 | 8 | 3.2 | | normal |
| 27 | 4 | normal | 30 | 1000 | 0.5 | 1000 | 13.33 | 26.66 | 2.7 | | normal |
| 28 | 8 | normal | 30 | 1000 | 30 | 1000 | 13.33 | 26.66 | 5.3 | | normal |
| 29 | 8 | normal | 30 | 1000 | 30 | 1000 | 13.33 | 26.66 | 5.3 | | normal |
| 30 | 6 | normal | 30 | 1000 | 10 | 1000 | 13.33 | 26.66 | 4.0 | | normal |
| 31 | 6 | normal | 60 | 1000 | 10 | 1000 | 13.33 | 26.66 | 4.0 | | normal |
| 32 | 8 | normal | 30 | 1000 | 30 | 1000 | 13.33 | 26.66 | 5.3 | | normal |
| 33 | 8 | normal | 30 | 1000 | 30 | 1000 | 13.33 | 26.66 | 5.3 | | normal |
| 34 | 8 | normal | 30 | 1000 | 30 | 1000 | 13.33 | 26.66 | 5.3 | | normal |
| 35 | 8 | normal | 30 | 1000 | 10 | 1000 | 13.33 | 26.66 | 5.3 | | normal |
| 36 | 8 | normal | 30 | 1000 | 2 | 1000 | 13.33 | 26.66 | 5.3 | | normal |
| 37 | 8 | normal | 30 | 1000 | 0.5 | 1000 | 13.33 | 26.66 | 5.3 | | normal |
| 38 | 8 | normal | 30 | 1000 | 0 | 1000 | 13.33 | 26.66 | 5.3 | | normal |
| 39 | 8 | normal | 30 | 1000 | 30 | 1000 | 13.33 | 26.66 | 5.3 | | normal |

| | | | | | | | | | | | |
|---|---|---|---|---|---|---|---|---|---|---|---|
| 40 | 8 | normal | 30 | 1000 | 30 | 1000 | 13.33 | 26.66 | 5.3 | | normal |
| 41 | 8 | normal | 30 | 1000 | 10 | 1000 | 13.33 | 26.66 | 5.3 | | normal |
| 42 | 8 | normal | 30 | 1000 | 30 | 1000 | 13.33 | 26.66 | 5.3 | | normal |
| 43 | 8 | normal | 30 | 1000 | 4 | 1000 | 13.33 | 26.66 | 5.3 | | normal |
| 44 | 8 | normal | 30 | 1000 | 3 | 1000 | 13.33 | 26.66 | 5.3 | | normal |
| 45 | 8 | normal | 30 | 1000 | 5 | 1000 | 13.33 | 26.66 | 5.3 | | normal |
| 46 | 8 | normal | 30 | 1000 | 0.05 | 1000 | 13.33 | 26.66 | 5.3 | | normal |
| 47 | 8 | normal | 30 | 1000 | 0.05 | 1000 | 13.33 | 26.66 | 5.3 | | normal |
| 48 | 8 | normal | 30 | 1000 | 30 | 1000 | 13.33 | 26.66 | 5.3 | | normal |
| 49 | 4.4 | normal | 30 | 1000 | 4 | 1000 | 5 | 1 | 0.7 | | normal |
| 50 | 4 | normal | 30 | 1000 | 10 | 1000 | 5 | 1 | 0.7 | | normal |
| 51 | 4 | normal | 30 | 1000 | 4 | 1000 | 5 | 0.5 | 0.4 | | normal |
| 52 | 4 | normal | 30 | 1000 | 0.05 | 1000 | 5 | 0.5 | 0.4 | | normal |
| 53 | 4 | normal | 30 | 1000 | 4 | 1000 | 20 | 1 | 0.2 | | normal |
| 54 | 4 | normal | 30 | 1050 | 0.05 | 1050 | 5 | 0.5 | 0.4 | | normal |
| 55 | 4 | normal | 30 | 1050 | 4 | 1050 | 5 | 0.5 | 0.4 | | normal |
| 56 | 4 | normal | 30 | 1000 | 10 | 1000 | 5 | 0.5 | 0.4 | | normal |
| 57 | 4 | normal | 30 | 1000 | 30 | 1000 | 5 | 0.5 | 0.4 | | normal |
| 58 | 4 | normal | 30 | 1000 | 150 | 1000 | 5 | 0.5 | 0.4 | | normal |
| 59 | 4 | normal | 30 | 1000 | 30 | 1000 | 5 | 0.5 | 0.4 | | normal |
| 60 | 4 | normal | 30 | 1050 | 30 | 1050 | 5 | 0.5 | 0.4 | | normal |
| 61 | 8 | normal | 30 | 1000 | 10 | 1000 | 13.33 | 26.66 | 5.3 | | normal |
| 62 | 4 | normal | 30 | 1000 | 60 | 1000 | 5 | 0.5 | 0.4 | | normal |
| 63 | 8 | normal | 30 | 1000 | 10 | 1000 | 13.33 | 26.66 | 5.3 | | normal |
| 64 | 4 | normal | 30 | 1000 | 30 | 1000 | 5 | 0.5 | 0.4 | | normal |
| 65 | 4 | normal | 30 | 1000 | 30 | 1000 | 5 | 0.5 | 0.4 | | normal |
| 66 | 4 | normal | 30 | 1000 | 30 | 1000 | 5 | 0.5 | 0.4 | | normal |
| 67 | 4 | normal | 30 | 1000 | 30 | 1000 | 5 | 0.5 | 0.4 | | normal |
| 68 | 4 | normal | 30 | 1000 | 30 | 1000 | 5 | 0.5 | 0.4 | | normal |
| 69 | 8 | normal | 30 | 1000 | 30 | 1000 | 13.33 | 26.66 | 5.3 | | normal |
| 70 | 4 | normal | 30 | 1000 | 0 | 1000 | 5 | 0 | 0.0 | | normal |

| | | | | | | | | | | | |
|---|---|---|---|---|---|---|---|---|---|---|---|
| 71 | 4 | normal | 30 | 1000 | 30 | 1000 | 5 | 0.5 | 0.4 | | normal |
| 72 | 4 | normal | 30 | 1000 | 30 | 1000 | 5 | 0.5 | 0.4 | | normal |
| 73 | 4 | normal | 30 | 1000 | 40 | 1000 | 5 | 0.5 | 0.4 | | normal |
| 74 | 4 | normal | 30 | 1000 | 30 | 1000 | 5 | 0.5 | 0.4 | | normal |
| 75 | 8 | normal | 30 | 1000 | 30 | 1000 | 13.33 | 26.66 | 5.3 | | normal |
| 76 | 4 | normal | 30 | 1000 | 0.05 | 1000 | 5 | 0.5 | 0.4 | | normal |
| 77 | 4 | normal | 30 | 1000 | 4 | 1000 | 5 | 0.5 | 0.4 | | normal |
| 78 | 4 | normal | 30 | 1000 | 0.05 | 1000 | 5 | 0.5 | 0.4 | | normal |
| 79 | 4 | normal | 30 | 1000 | 30 | 1000 | 1 | 4 | 3.2 | | normal |
| 80 | 4 | normal | 30 | 1000 | 30 | 1000 | 13.33 | 26.66 | 2.7 | | normal |
| 81 | 4 | normal | 30 | 1000 | 10 | 1000 | 5 | 0.5 | 0.4 | | normal |
| 82 | 4 | normal | 30 | 1000 | 30 | 1000 | 1 | 4 | 3.2 | | normal |
| 83 | 4 | normal | 30 | 1000 | 0.05 | 1000 | 5 | 0.5 | 0.4 | | normal |
| 84 | 4 | normal | 30 | 1000 | 30 | 1000 | 5 | 0.5 | 0.4 | | normal |
| 85 | 4 | normal | 30 | 1000 | 2 | 1000 | 5 | 0.5 | 0.4 | | normal |
| 86 | 4 | normal | 30 | 1000 | 30 | 1000 | 5 | 0.5 | 0.4 | | normal |
| 87 | 4 | normal | 30 | 1000 | 2 | 880 | 5 | 0.5 | 0.4 | | normal |
| 88 | 8 | normal | 30 | 1000 | 2 | 880 | 13.33 | 26.66 | 5.3 | | normal |
| 89 | 8 | normal | 30 | 1000 | 2 | 900 | 13.33 | 26.66 | 5.3 | | normal |
| 90 | 4 | normal | 30 | 1000 | 30 | 1000 | 1 | 4 | 3.2 | | normal |
| 91 | 4 | normal | 30 | 1000 | 30 | 1000 | 1 | 4 | 3.2 | | normal |
| 92 | 4 | normal | 30 | 1000 | 2 | 1000 | 5 | 0.5 | 0.4 | | normal |
| 93 | 4 | normal | 30 | 1000 | 30 | 1000 | 5 | 0.5 | 0.4 | | normal |
| 94 | 4 | normal | 30 | 1000 | 0 | 0 | 5 | 0 | 0.0 | | normal |
| 95 | 4 | normal | 30 | 1000 | 30 | 1000 | 5 | 0.5 | 0.4 | | normal |
| 96 | 1.64 | normal | 30 | 1000 | 2 | 1050 | 0.8 | 3.2 | 1.3 | | normal |
| 97 | 0.66 | normal | 30 | 1000 | 2 | 1000 | 2 | 0.5 | 0.1 | | normal |
| 98 | 4 | normal | 30 | 1000 | 30 | 1000 | 1 | 0.5 | 1.3 | 4 | normal |
| 99 | 4 | normal | 30 | 1000 | 30 | 1000 | 5 | 0.5 | 0.4 | | normal |
| 100 | 4 | normal | 30 | 1000 | 0.05 | 880 | 5 | 0.5 | 0.4 | | normal |
| 101 | 4 | normal | 30 | 1000 | 4 | 880 | 5 | 0.5 | 0.4 | | normal |

| | | | | | | | | | | | |
|---|---|---|---|---|---|---|---|---|---|---|---|
| 102 | 4 | normal | 30 | 1000 | 10 | 880 | 5 | 0.5 | 0.4 | | normal |
| 103 | 4 | normal | 30 | 1000 | 30 | 880 | 5 | 0.5 | 0.4 | | normal |
| 104 | 4 | normal | 30 | 1000 | 30 | 1000 | 1 | 0.5 | 1.3 | 4 | normal |
| 105 | 4 | normal | 30 | 1000 | 30 | 1000 | 5 | 0.5 | 0.4 | | normal |
| 106 | 4 | normal | 30 | 1000 | 30 | 1000 | 1 | 1 | 2.0 | 3.6 | normal |
| 107 | 6 | normal | 30 | 1000 | 30 | 1000 | 5 | 0.5 | 0.5 | | normal |
| 108 | 4 | normal | 30 | 1000 | 30 | 1000 | 5 | 0.5 | 0.4 | | normal |
| 109 | 4 | normal | 30 | 1000 | 30 | 1000 | 5 | 0.5 | 0.4 | | normal |
| 110 | 4 | normal | 30 | 1000 | 30 | 1000 | 5 | 0.5 | 0.4 | | normal |
| 111 | 4 | normal | 30 | 1000 | 30 | 1000 | 5 | 0.5 | 0.4 | | normal |
| 112 | 4 | normal | 30 | 1000 | 30 | 1000 | 3.5 | 1.5 | 1.2 | | normal |
| 113 | 4 | normal | 30 | 1000 | 30 | 1000 | 1 | 5 | 3.3 | 4 | normal |
| 114 | 4 | normal | 30 | 1000 | 30 | 1000 | 5 | 5 | 2.0 | 0 | normal |
| 115 | 4 | normal | 30 | 1035 | 30 | 1035 | 5 | 0.5 | 0.4 | | normal |
| 116 | 4 | normal | 30 | 1000 | 30 | 1000 | 1 | 0.5 | 1.3 | 3.5 | normal |
| 117 | 4 | normal | 30 | 1035 | 30 | 1035 | 5 | 0.5 | 0.4 | | normal |
| 118 | 4 | normal | 30 | 1035 | 30 | 1035 | 5 | 0.5 | 0.4 | | normal |
| 119 | 4 | normal | 30 | 1035 | 30 | 1035 | 1 | 0.5 | 1.3 | | normal |
| 120 | 4 | normal | 30 | 1035 | 30 | 1035 | 5 | 0.5 | 0.4 | 20 | normal |
| 121 | 4 | normal | 30 | 1035 | 30 | 1035 | 5 | 0.5 | 0.4 | 50 | normal |
| 122 | 0.72 | normal | 30 | 1035 | 50 | 1035 | | | | | normal |
| 123 | | normal | 30 | 1035 | 30 | 1035 | 25 | 0.5 | 0.0 | 0 | normal |
| 124 | | normal | 30 | 1035 | 30 | 1035 | 5 | 0.5 | 0.0 | 20 | normal |
| 125 | 0.48 | normal | 30 | 1035 | 90 | | | | 0.002 | | normal |
| 126 | 4 | normal | 30 | 1035 | 40 | 1035 | 5 | 0.5 | 0.4 | 20 | normal |
| 127 | 4 | normal | 30 | 1035 | 30 | 1035 | 5 | 0.5 | 0.4 | 20 | normal |
| 128 | 4 | normal | 30 | 1035 | 40 | 1035 | 5 | 0.5 | 0.4 | 20 | normal |
| 129 | 4 | normal | 30 | 1035 | 30 | 1035 | 5 | 0.5 | 0.4 | 20 | normal |
| 130 | 4 | normal | 30 | 1035 | 30 | 1035 | 5 | 0.5 | 0.4 | 20 | normal |
| 131 | 4 | normal | 30 | 1035 | 30 | 1035 | 5 | 0.5 | 0.4 | 20 | normal |
| 132 | 4 | normal | 30 | 1035 | 30 | 1035 | 5 | 0.5 | | 20 | normal |

| | | | | | | | | | | | |
|---|---|---|---|---|---|---|---|---|---|---|---|
| 133 | | normal | 30 | 1035 | 30 | 1035 | 5 | 0.2 | 0.04 | 20 | normal |
| 134 | 4 | normal | 30 | 1035 | 30 | 1035 | 5 | | 0.03 | 20 | normal |
| 135 | 4 | normal | 30 | 1035 | 30 | 1035 | 5 | | 0.01 | 20 | normal |
| 136 | 4 | normal | 30 | 1035 | 30 | 1035 | 5 | | 0.009 | 20 | normal |
| 137 | 4 | normal | 30 | 1035 | 30 | 1035 | 5 | | 0.0057 | 20 | normal |
| 138 | 4 | normal | 30 | 1000 | 30 | 1000 | 7 | 15 | 0.0057 | 0 | normal |
| 139 | 4 | normal | 30 | 1000 | 30 | 1000 | 5 | 15 | 0.01 | 0 | normal |
| 140 | 4 | normal | 30 | 1000 | 30 | 1000 | 2 | | 0.6 | 0 | normal |
| 141 | 0.75 | normal | 30 | 1000 | 30 | 1000 | 2.3 | | 0.59 | 0 | normal |
| 142 | 0.75 | normal | 30 | 1000 | 30 | 1000 | 2.4 | | 0.59 | 0 | normal |
| 143 | 0.75 | normal | 30 | 1000 | 30 | 1000 | 2.4 | | 0.59 | 0 | normal |
| 144 | 0.75 | normal | 30 | 1000 | 15 | 1000 | 2.4 | | 0.59 | 0 | normal |
| 145 | 0.75 | normal | 30 | 1000 | 15 | 1000 | 2.4 | | 0.59 | 0 | rapid |
| 146 | 0.75 | normal | 30 | 1000 | 15 | 1000 | 2.4 | | 0.59 | 0 | normal |
| 147 | 0.75 | normal | 30 | 1000 | 15 | 1000 | 2.4 | | 0.594 | | normal |
| 148 | 0.2 | normal | 30 | 1000 | 15 | 1000 | 60 | 10 | | 150 | normal |
| 149 | 0.2 | normal | 30 | 1000 | 30 | 1000 | 17 | 23 | | | normal |
| 150 | 0.2 | normal | 30 | 1000 | 15 | 1000 | 15 | 10 | | 95 | normal |
| 151 | 0.2 | normal | 30 | 1000 | 15 | 1000 | 16 | 33 | | 6 | normal |
| 152 | 0.2 | normal | 30 | 1000 | 15 | 1000 | 3 | 19 | | | normal |
| 153 | 0.2 | normal | 30 | 1000 | 15 | 1000 | 5 | 17 | | | normal |
| 154 | 0.2 | normal | 30 | 1000 | 30 | 1000 | 16 | 33 | | | normal |
| 155 | 0.2 | normal | 30 | 1000 | 30 | 1000 | 16 | 33 | | | normal |
| 156 | 0.2 | normal | 30 | 1000 | 30 | 1000 | 16 | 33 | | | normal |
| 157 | 0.2 | normal | 30 | 1000 | 30 | 1000 | 16 | 33 | | | normal |
| 158 | 0.75 | normal | 30 | 1000 | 15 | 1000 | 2.5 | | 0.589 | | normal |
| 159 | 0.75 | normal | 30 | 1000 | 30 | 1000 | 2.5 | | 0.589 | | normal |
| 160 | 0.75 | normal | 30 | 1000 | 15 | 1000 | 2.6 | | 0.589 | | normal |
| 161 | 0.2 | normal | 30 | 1000 | 30 | 1000 | 2.5 | | 0.6 | 22.5 | noraml |
| 162 | 0.75 | normal | 30 | 1000 | 30 | 1000 | 2.5 | | 0.59 | | normal |
| 163 | 0.2 | normal | 30 | 1000 | 30 | 1000 | 2.5 | | 0.6 | 22.5 | normal |

| | | | | | | | | | | | |
|---|---|---|---|---|---|---|---|---|---|---|---|
| 164 | 0.75 | normal | 30 | 1000 | 30 | 1000 | | | 0.59 | | normal |
| 165 | 0.75 | normal | 30 | 1000 | 30 | 1000 | 2.5 | 35 | 0.755 | 22.5 | normal |
| 166 | 0.2 | normal | 30 | 1000 | 15 | 1000 | | | 0.595 | | normal |
| 167 | 0.2 | normal | 30 | 1000 | 15 | 1000 | | | 0.595 | | normal |
| 168 | 0.2 | normal | 30 | 1000 | 15 | 1000 | | | 0.595 | | normal |
| 169 | 0.75 | normal | 30 | 1000 | 30 | 1000 | 16 | | 0.4 | | normal |
| 170 | 0.2 | normal | 30 | 750 | 30 | 750 | 5 | | 0.4 | | normal |
| 171 | 0.75 | normal | 30 | 1000 | 15 | 1000 | 2.7 | | 0.595 | | normal |
| 172 | 0.2 | normal | 10 | 1000 | 30 | 750 | 5 | | 0.4 | | normal |
| 173 | 0.2 | normal | 30 | 750 | 0.5 | 750 | 5 | | 0.115 | | normal |
| 174 | 0.2 | normal | 10 | 1000 | 0.5 | 750 | 5 | | 0.11 | | normal |
| 175 | 0.2 | normal | 10 | 1000 | 0.5 | 750 | 5 | | 0.11 | | normal |
| 176 | 0.2 | normal | 10 | 1000 | 0.5 | 850 | 5 | | 0.11 | | normal |
| 177 | 0.75 | normal | 30 | 1000 | 15 | | | | 0.6 | | normal |
| 178 | 0.2 | normal | 30 | 1030 | 40 | 1030 | 5 | | 0.017 | 0 | normal |
| 179 | 0.113 | normal | 30 | 1030 | 40 | 1030 | 25 | | 0.01 | 0 | normal |
| 180 | 2.7 | normal | 30 | 1030 | 40 | 1030 | 1.2 | | 0.01 | 10 | normal |
| 181 | 4.97 | normal | 30 | 1030 | 40 | 1030 | 0.4 | | 0.01 | 30.2 | normal |
| 182 | 5 | normal | 30 | 1030 | 40 | 1030 | 39.3 | | 0.0015 | 8.6 | normal |
| 183 | 2.6 | normal | 30 | 1030 | 40 | 1030 | 12.5 | | 0.001 | 8.6 | normal |
| 184 | 2.6 | normal | 30 | 1030 | 40 | 1030 | 1.2 | | 0.0015 | 10 | normal |
| 185 | 2.6 | normal | 30 | 1030 | 2 | 1030 | 1.2 | | 0.0015 | 10 | normal |
| 186 | 2.6 | normal | 30 | 1030 | 2 | 1030 | 1.2 | | 0.0015 | 10 | normal |
| 187 | 2.6 | normal | 30 | 1030 | 2 | 1030 | 1.2 | | 0.0015 | 10 | normal |
| 188 | 2.7 | normal | 30 | 1030 | 40 | 1030 | 1.2 | | 0.0015 | 10 | normal |
| 189 | 2.6 | normal | 30 | 1030 | 0.5 | 1030 | 1.2 | | 0.0015 | 10 | normal |
| 190 | 2.7 | normal | 30 | 1030 | 4 | 1030 | 1.2 | | 0.0015 | 10 | normal |
| 191 | 2.6 | normal | 30 | 1030 | 0.5 | 1030 | 0 | | 0.0015 | 10 | normal |
| 192 | 2.6 | normal | 30 | 1030 | 10 | 1030 | 1.2 | | 0.0015 | 10 | normal |
| 193 | 2.7 | normal | 30 | 1030 | 10 | 1030 | 1.2 | | 0.0015 | 10 | normal |
| 194 | 2.6 | normal | 30 | 1030 | 0.5 | 1030 | 1.2 | | 0.0015 | 10 | normal |

| | | | | | | | | | | | |
|---|---|---|---|---|---|---|---|---|---|---|---|
| 195 | 2.7 | normal | 30 | 1030 | 50 | 1030 | 24 | | 0.0011 | 10 | normal |
| 196 | 9.2 | normal | 30 | 1060 | 46 | 1060 | 52 | | 0.0011 | 2.8 | normal |
| 197 | 7.6 | normal | 30 | 1030 | 50 | 1030 | 87.2 | | 0.002 | 10 | normal |
| 198 | 7.6 | normal | 30 | 1030 | 61 | 1030 | 87.2 | | 0.0015 | 10 | normal |
| 199 | 7.7 | normal | 30 | 1030 | 42 | 1030 | 87.2 | | 0.0015 | 10 | normal |
| 200 | 4.5 | normal | 30 | 1030 | 50 | 1030 | 1.2 | | 0.004 | 10 | normal |
| 201 | 3.9 | normal | 30 | 1030 | 4 | 1030 | 1.2 | | 0.004 | 10 | normal |
| 202 | 4.3 | normal | 30 | 1030 | 4 | 1030 | 1.2 | | 0.003 | 10 | normal |
| 203 | 3.73 | normal | 30 | 1030 | 0.5 | 1030 | 1.2 | | 0.004 | 10 | rapid |
| 204 | 4.22 | normal | 30 | 1030 | 0.5 | 1000 | 1.2 | | 0.004 | 10 | rapid |
| 205 | 4.1 | normal | 30 | 1030 | 0.5 | 1000 | 8.9 | | 0.004 | 6.2 | rapid |
| 206 | 4 | normal | 30 | 1030 | 0.5 | 1000 | 12.8 | | 0.004 | 3.2 | rapid |
| 207 | 4 | normal | 30 | 1030 | 0.5 | 1000 | 27 | | 0.004 | 0.4 | rapid |
| 208 | 4.3 | normal | 30 | 1030 | 0.5 | 1000 | 90 | | 0.004 | 0 | rapid |
| 209 | 4.2 | normal | 20 | 1030 | 0.5 | 1000 | 12.8 | | 0.0025 | 5.4 | rapid |
| 210 | 4.2 | normal | 20 | 1030 | 0.5 | 1000 | 90 | | 0.003 | 0 | rapid |
| 211 | 3.9 | normal | 20 | 1030 | 0.5 | 1000 | 1.2 | | 0.002 | 10 | rapid |
| 212 | 4.2 | normal | 20 | 1030 | 0.5 | 1000 | 90 | | 0.0025 | 0 | rapid |
| 213 | 4.3 | normal | 20 | 1030 | 0.5 | 1000 | 90 | | 0.0025 | 0 | rapid |
| 214 | 4.2 | normal | 20 | 1030 | 0.5 | 1000 | 90 | | 0.0025 | 0 | rapid |
| 215 | 8.3 | normal | 20 | 1030 | 0.5 | 1000 | 90 | | 0.0003 | 0 | rapid |
| 216 | 8 | normal | 20 | 1030 | 1 | 1000 | 90 | | 0.001 | 0 | rapid |
| 217 | 8.3 | normal | 30 | 1030 | 30 | 1030 | 90 | | 0.001 | 0 | rapid |
| 218 | 2.5 | normal | 30 | 1030 | 5 | 1030 | 90 | | 0.0001 | 0 | rapid |
| 219 | 2.5 | normal | 30 | 1030 | 5 | 1030 | 90 | | 0.0001 | 75 | rapid |
| 220 | 3.7 | normal | 30 | 1030 | 5 | 1030 | 95 | | 0.0001 | 0 | rapid |
| 221 | 3.9 | normal | 30 | 1040 | 10 | 1040 | 95 | | 0.0001 | 0 | rapid |
| 222 | 3 | normal | 30 | 1030 | 10 | 1030 | 90 | | 0.0001 | 0 | rapid |
| 223 | 3 | normal | 30 | 1030 | 15 | 1030 | 95 | | 0.0001 | 180 | rapid |
| 224 | 2.6 | normal | 30 | 1030 | 20 | 1030 | 90 | | 0.0001 | 0 | rapid |
| 225 | 3.3 | normal | 30 | 1040 | 55 | 1040 | 90 | | 0.0001 | 0 | rapid |

| | | | | | | | | | | | |
|---|---|---|---|---|---|---|---|---|---|---|---|
| 226 | 6 | normal | 20 | 1060 | 40 | 1060 | 1.2 | | 0.0001 | 10 | rapid |
| 227 | 3 | normal | 45 | 1070 | 230 | 1070 | 1.2 | | 0.0001 | 10 | rapid |
| 228 | 7 | normal | 30 | 1080 | 350 | 1080 | 1.2 | | <0.0001 | 10 | rapid |
| 229 | 7.6 | normal | 30 | 1080 | 350 | 1080 | 10 | | 0.0015 | 10 | rapid |
| 230 | 2.2 | normal | 30 | 1035 | 1 | 800 | 1.2 | | 0.0015 | 30 | rapid |
| 231 | 2.5 | normal | 5 | 1040 | 2 | 775 | 2.4 | | 0.0017 | 50 | rapid |
| 232 | 2.2 | normal | 60 | 950 | 1 | 775 | 2.4 | | 0.001 | 50 | rapid |
| 233 | 2.2 | normal | 50 | 1080 | 1 | 775 | 1.2 | | 0.001 | 30 | rapid |
| 234 | 2.7 | normal | 50 | 800 | 0.5 | 800 | 1.2 | | 0.0015 | 10 | rapid |
| 235 | 2.3 | normal | 20 | 880 | 0.083 | 775 | 2.4 | | 0.001 | 30 | rapid |
| 236 | 2 | normal | 30 | 880 | 0.17 | 775 | 20 | | 0.001 | 30 | rapid |
| 237 | 2.1 | normal | 120 | 870 | 0.033 | 750 | 20 | | 0.001 | 30 | rapid |
| 238 | 0.8 | normal | 180 | 880 | 0.083 | 750 | 20 | | 0.0004 | 30 | rapid |

Note 1: after Exp #134, the leak valve was used instead of MFC and accurate measurements of mass flow were not available.

Note 2: For Exp. #230, two growth steps with two different growth temperatures were used (800 and 1030 ℃).

# Bibliography


[1] Novoselov, K. S.; Geim, A. K.; Morozov, S. V.; Jiang, D.; Zhang, Y.; Dubonos, S. V.; Grigorieva, I. V.; Firsov, A. A., *Science* **2004,** 306, (5696), 666-669.
[2] Geim, A. K.; Novoselov, K. S., *Nat. Mater.* **2007,** 6, (3), 183-191.
[3] Novoselov, K. S.; Geim, A. K.; Morozov, S. V.; Jiang, D.; Katsnelson, M. I.; Grigorieva, I. V.; Dubonos, S. V.; Firsov, A. A., *Nature* **2005,** 438, (7065), 197-200.
[4] Geim, A. K., *Rev. Mod. Phys.* **2011,** 83, (3), 851-862.
[5] Akturk, A.; Goldsman, N., *J. Appl. Phys.* **2008,** 103, (5), 053702.
[6] Chen, J. H.; Jang, C.; Xiao, S.; Ishigami, M.; Fuhrer, M. S., *Nat. Nanotechnol.* **2008,** 3, (4), 206-209.
[7] Bonaccorso, F.; Sun, Z.; Hasan, T.; Ferrari, A. C., *Nat. Photonics* **2010,** 4, (9), 611-622.
[8] Gunho, J.; Minhyeok, C.; Sangchul, L.; Woojin, P.; Yung Ho, K.; Takhee, L., *Nanotechnology* **2012,** 23, (11), 112001.
[9] Lee, C.; Wei, X.; Kysar, J. W.; Hone, J., *Science* **2008,** 321, (5887), 385-388.
[10] Green, A. A.; Hersam, M. C., *Nano Lett.* **2009,** 9, (12), 4031-4036.
[11] Tung, V. C.; Allen, M. J.; Yang, Y.; Kaner, R. B., *Nat. Nanotechnol.* **2009,** 4, (1), 25-29.
[12] Umar, K.; Arlene, O. N.; Mustafa, L.; Sukanta, D.; Jonathan, N. C., *Small* **2010,** 6, (7), 864-871.
[13] Hernandez, Y.; Nicolosi, V.; Lotya, M.; Blighe, F. M.; Sun, Z.; De, S.; McGovern, I. T.; Holland, B.; Byrne, M.; Gun'Ko, Y. K.; Boland, J. J.; Niraj, P.; Duesberg, G.; Krishnamurthy, S.; Goodhue, R.; Hutchison, J.; Scardaci, V.; Ferrari, A. C.; Coleman, J. N., *Nat. Nanotechnol.* **2008,** 3, (9), 563-568.
[14] Hass, J.; Heer, W. A. d.; Conrad, E. H., *J. Phys.: Condens. Matter* **2008,** 20, (32), 323202.
[15] Mallet P, V. F. N. C. M. L. B. C.; Veuillen, J. Y., *Phys. Rev. B* **2007,** 76, (4), 041403.
[16] Hass, J.; Feng, R.; Millán-Otoya, J. E.; Li, X.; Sprinkle, M.; First, P. N.; de Heer, W. A.; Conrad, E. H.; Berger, C., *Phys. Rev. B* **2007,** 75, (21), 214109.
[17] Reina, A.; Jia, X.; Ho, J.; Nezich, D.; Son, H.; Bulovic, V.; Dresselhaus, M. S.; Kong, J., *Nano Lett.* **2008,** 9, (1), 30-35.
[18] Bae, S.; Kim, H.; Lee, Y.; Xu, X.; Park, J.-S.; Zheng, Y.; Balakrishnan, J.; Lei, T.; Ri Kim, H.; Song, Y. I.; Kim, Y.-J.; Kim, K. S.; Ozyilmaz, B.; Ahn, J.-H.; Hong, B. H.; Iijima, S., *Nat. Nanotechnol.* **2010,** 5, (8), 574-578.
[19] Kim, K. S.; Zhao, Y.; Jang, H.; Lee, S. Y.; Kim, J. M.; Kim, K. S.; Ahn, J.-H.; Kim, P.; Choi, J.-Y.; Hong, B. H., *Nature* **2009,** 457, (7230), 706-710.
[20] Li, X.; Cai, W.; An, J.; Kim, S.; Nah, J.; Yang, D.; Piner, R.; Velamakanni, A.; Jung, I.; Tutuc, E.; Banerjee, S. K.; Colombo, L.; Ruoff, R. S., *Science* **2009,** 324, (5932), 1312-1314.
[21] Yu, Q.; Lian, J.; Siriponglert, S.; Li, H.; Chen, Y. P.; Pei, S.-S., *Appl. Phys. Lett.* **2008,** 93, (11), 113103-3.
[22] Wallace, P. R., *Phys. Rev.* **1947,** 71, 622-634.
[23] Peierls, R. E., *Ann.I.H.Poincare* **1935,** 5, 177-222.
[24] Landau, L. D., *Phys.Z.Sowjetunion* **1937,** 11, 26-35.
[25] Banerjee, B. C.; Hirt, T. J.; Walker, P. L., *Nature* **1961,** 192, (4801), 450-451.

[26] Hagstrom, S.; Lyon, H. B.; Somorjai, G. A., *Phys. Rev. Lett.* **1965,** 15, (11), 491.
[27] Rhead, G. E., *C. R. Acad. Sc. Paris. Series C* **1969,** 268, 1817-1820.
[28] Schlögl, R., *Handbook of Heterogeneous Catalysis*. Wiley-VCH: Weinheim, 2008; p 357.
[29] Karu, A. E.; Beer, M., *J. Appl. Phys.* **1966,** 37, (5), 2179-2181.
[30] Robertson, S. D., *Nature* **1969,** 221, (5185), 1044-1046.
[31] Lu, X.; Minfeng, Y.; Hui, H.; Rodney, S. R., *Nanotechnology* **1999,** 10, (3), 269.
[32] Castro Neto, A. H.; Guinea, F.; Peres, N. M. R.; Novoselov, K. S.; Geim, A. K., *Rev. Mod. Phys.* **2009,** 81, (1), 109-162.
[33] Nilsson, J.; Castro Neto, A. H.; Guinea, F.; Peres, N. M. R., *Phys. Rev. B* **2008,** 78, (4), 045405.
[34] Baskin, Y.; Meyer, L., *Phys. Rev.* **1955,** 100, (2), 544.
[35] Haering, R. R., *Canadian Journal of Physics* **1958,** 36, 352.
[36] Shenderova, O. A.; Zhirnov, V. V.; Brenner, D. W., *Crit. Rev. Solid State Mater. Sci.* **2002,** 27, (3-4), 227-356.
[37] Zhi, L.; Müllen, K., *J. Mater. Chem.* **2008,** 18, (13), 1472-1484.
[38] Andrei, E. Y.; Li, G.; Du, X., *Rep. Prog. Phys.* **2012,** 75, (5), 056501.
[39] Stone, A. J.; Wales, D. J., *Chem. Phys. Lett.* **1986,** 128, (5–6), 501-503.
[40] Hashimoto, A.; Suenaga, K.; Gloter, A.; Urita, K.; Iijima, S., *Nature* **2004,** 430, (7002), 870-873.
[41] Meyer, J. C.; Kisielowski, C.; Erni, R.; Rossell, M. D.; Crommie, M. F.; Zettl, A., *Nano Lett.* **2008,** 8, (11), 3582-3586.
[42] Zan, R.; Ramasse, Q. M.; Bangert, U.; Novoselov, K. S., *Nano Lett.* **2012,** 12, (8), 3936-3940.
[43] Eva, Y. A.; Guohong, L.; Xu, D., *Rep. Prog. Phys.* **2012,** 75, (5), 056501.
[44] Elias, D. C.; Gorbachev, R. V.; Mayorov, A. S.; Morozov, S. V.; Zhukov, A. A.; Blake, P.; Ponomarenko, L. A.; Grigorieva, I. V.; Novoselov, K. S.; Guinea, F.; Geim, A. K., *Nat. Phys.* **2011,** 7, (9), 701-704.
[45] Morozov, S. V.; Novoselov, K. S.; Katsnelson, M. I.; Schedin, F.; Elias, D. C.; Jaszczak, J. A.; Geim, A. K., *Phys. Rev. Lett.* **2008,** 100, (1), 016602.
[46] Bolotin, K. I.; Sikes, K. J.; Hone, J.; Stormer, H. L.; Kim, P., *Phys. Rev. Lett.* **2008,** 101, (9), 096802.
[47] Chen, J. H.; Jang, C.; Ishigami, M.; Xiao, S.; Cullen, W. G.; Williams, E. D.; Fuhrer, M. S., *Solid State Commun.* **2009,** 149, (27-28), 1080-1086.
[48] Xue, J.; Sanchez-Yamagishi, J.; Bulmash, D.; Jacquod, P.; Deshpande, A.; Watanabe, K.; Taniguchi, T.; Jarillo-Herrero, P.; LeRoy, B. J., *Nat. Mater.* **2011,** 10, (4), 282-285.
[49] Dean, C. R.; Young, A. F.; Meric, I.; Lee, C.; Wang, L.; Sorgenfrei, S.; Watanabe, K.; Taniguchi, T.; Kim, P.; Shepard, K. L.; Hone, J., *Nat. Nanotechnol.* **2010,** 5, (10), 722-726.
[50] Zhang, Y.; Brar, V. W.; Girit, C.; Zettl, A.; Crommie, M. F., *Nat. Phys.* **2009,** 5, (10), 722-726.
[51] Balandin, A. A.; Ghosh, S.; Bao, W.; Calizo, I.; Teweldebrhan, D.; Miao, F.; Lau, C. N., *Nano Lett.* **2008,** 8, (3), 902-907.
[52] Faugeras, C.; Faugeras, B.; Orlita, M.; Potemski, M.; Nair, R. R.; Geim, A. K., *ACS Nano* **2010**.
[53] Seol, J. H.; Jo, I.; Moore, A. L.; Lindsay, L.; Aitken, Z. H.; Pettes, M. T.; Li, X.; Yao, Z.; Huang, R.; Broido, D.; Mingo, N.; Ruoff, R. S.; Shi, L., *Science* **2010,** 328, (5975), 213-216.

[54] Chen, S.; Wu, Q.; Mishra, C.; Kang, J.; Zhang, H.; Cho, K.; Cai, W.; Balandin, A. A.; Ruoff, R. S., *Nat. Mater.* **2012,** 11, (3), 203-207.
[55] Cai, W.; Moore, A. L.; Zhu, Y.; Li, X.; Chen, S.; Shi, L.; Ruoff, R. S., *Nano Lett.* **2010,** 10, (5), 1645-1651.
[56] Ghosh, S.; Calizo, I.; Teweldebrhan, D.; Pokatilov, E. P.; Nika, D. L.; Balandin, A. A.; Bao, W.; Miao, F.; Lau, C. N., *Appl. Phys. Lett.* **2008,** 92, (15), 151911-151913.
[57] Grosse, K. L.; Bae, M.-H.; Lian, F.; Pop, E.; King, W. P., *Nat. Nanotechnol.* **2011,** 6, (5), 287-290.
[58] Nair, R. R.; Blake, P.; Grigorenko, A. N.; Novoselov, K. S.; Booth, T. J.; Stauber, T.; Peres, N. M. R.; Geim, A. K., *Science* **2008,** 320, (5881), 1308.
[59] Kuzmenko, A. B.; van Heumen, E.; Carbone, F.; van der Marel, D., *Phys. Rev. Lett.* **2008,** 100, (11), 117401.
[60] Tatar, R. C.; Rabii, S., *Phys. Rev. B* **1982,** 25, (6), 4126-4141.
[61] Pagliara, S.; Galimberti, G.; Mor, S.; Montagnese, M.; Ferrini, G.; Grandi, M. S.; Galinetto, P.; Parmigiani, F., *J. Am. Chem. Soc.* **2011,** 133, (16), 6318-6322.
[62] Wang, F.; Zhang, Y.; Tian, C.; Girit, C.; Zettl, A.; Crommie, M.; Shen, Y. R., *Science* **2008,** 320, (5873), 206-209.
[63] Mak, K. F.; Ju, L.; Wang, F.; Heinz, T. F., *Solid State Commun.* **2012,** 152, (15), 1341-1349.
[64] Lee, C.; Kim, J. Y.; Bae, S.; Kim, K. S.; Hong, B. H.; Choi, E. J., *Appl. Phys. Lett.* **2011,** 98, (7), 071905-3.
[65] Sensale-Rodriguez, B.; Yan, R.; Kelly, M. M.; Fang, T.; Tahy, K.; Hwang, W. S.; Jena, D.; Liu, L.; Xing, H. G., *Nat. Commun.* **2012,** 3, 780.
[66] Thongrattanasiri, S.; Silveiro, I.; de Abajo, F. J. G., *Appl. Phys. Lett.* **2012,** 100, (20), 201105-4.
[67] Chen, J.; Badioli, M.; Alonso-Gonzalez, P.; Thongrattanasiri, S.; Huth, F.; Osmond, J.; Spasenovic, M.; Centeno, A.; Pesquera, A.; Godignon, P.; Zurutuza Elorza, A.; Camara, N.; de Abajo, F. J. G.; Hillenbrand, R.; Koppens, F. H. L., *Nature* **2012,** advance online publication.
[68] Li, T.; Luo, L.; Hupalo, M.; Zhang, J.; Tringides, M. C.; Schmalian, J.; Wang, J., *Phys. Rev. Lett.* **2012,** 108, (16), 167401.
[69] Hong, L.; Chuan, X.; Srivastava, N.; Banerjee, K., *IEEE Trans. Electron Devices* **2009,** 56, (9), 1799-1821.
[70] Cai, W.; Zhu, Y.; Li, X.; Piner, R. D.; Ruoff, R. S., *Appl. Phys. Lett.* **2009,** 95, (12), 123115.
[71] Terrones, M.; Botello-Méndez, A. R.; Campos-Delgado, J.; López-Urías, F.; Vega-Cantú, Y. I.; Rodríguez-Macías, F. J.; Elías, A. L.; Muñoz-Sandoval, E.; Cano-Márquez, A. G.; Charlier, J.-C.; Terrones, H., *Nano Today* **2010,** 5, (4), 351-372.
[72] Woldman, N. E.; Frick, J. P., *Woldman's Engineering Alloys*. Asm International: 2000.
[73] Geim, A. K., *Science* **2009,** 324, (5934), 1530-1534.
[74] Pereira, V. M.; Castro Neto, A. H.; Peres, N. M. R., *Phys. Rev. B* **2009,** 80, (4), 045401.
[75] Stankovich, S.; Dikin, D. A.; Dommett, G. H. B.; Kohlhaas, K. M.; Zimney, E. J.; Stach, E. A.; Piner, R. D.; Nguyen, S. T.; Ruoff, R. S., *Nature* **2006,** 442, (7100), 282-286.
[76] Bunch, J. S.; van der Zande, A. M.; Verbridge, S. S.; Frank, I. W.; Tanenbaum, D. M.; Parpia, J. M.; Craighead, H. G.; McEuen, P. L., *Science* **2007,** 315, (5811), 490-493.
[77] Wu, Z.-S.; Ren, W.; Gao, L.; Zhao, J.; Chen, Z.; Liu, B.; Tang, D.; Yu, B.; Jiang, C.; Cheng, H.-M., *ACS Nano* **2009,** 3, (2), 411-417.

[78] Boehm, H. P.; Clauss, A.; Fischer, G.; Hofmann, U. In *Surface properties of extremely thin graphite lamellae*, London, 1962, 1962; Pergamon Press: London, 1962; p 73.
[79] Peigney, A.; Laurent, C.; Flahaut, E.; Bacsa, R. R.; Rousset, A., *Carbon* **2001,** 39, (4), 507-514.
[80] Schedin, F.; Geim, A. K.; Morozov, S. V.; Hill, E. W.; Blake, P.; Katsnelson, M. I.; Novoselov, K. S., *Nat. Mater.* **2007,** 6, (9), 652-655.
[81] Muszynski, R.; Seger, B.; Kamat, P. V., *J. Phys. Chem. C* **2008,** 112, (14), 5263-5266.
[82] Loh, K. P.; Bao, Q.; Ang, P. K.; Yang, J., *J. Mater. Chem.* **2010,** 20, (12), 2277-2289.
[83] Dreyer, D. R.; Park, S.; Bielawski, C. W.; Ruoff, R. S., *Chem. Soc. Rev.* **2010,** 39, (1), 228-240.
[84] Elias, D. C.; Nair, R. R.; Mohiuddin, T. M. G.; Morozov, S. V.; Blake, P.; Halsall, M. P.; Ferrari, A. C.; Boukhvalov, D. W.; Katsnelson, M. I.; Geim, A. K.; Novoselov, K. S., *Science* **2009,** 323, (5914), 610-613.
[85] Zhou, J.; Wu, M. M.; Zhou, X.; Sun, Q., *Appl. Phys. Lett.* **2009,** 95, (10), 103108-3.
[86] Nair, R. R.; Ren, W.; Jalil, R.; Riaz, I.; Kravets, V. G.; Britnell, L.; Blake, P.; Schedin, F.; Mayorov, A. S.; Yuan, S.; Katsnelson, M. I.; Cheng, H.-M.; Strupinski, W.; Bulusheva, L. G.; Okotrub, A. V.; Grigorieva, I. V.; Grigorenko, A. N.; Novoselov, K. S.; Geim, A. K., *Small* **2010,** 6, (24), 2877-2884.
[87] Ebbesen, T. W.; Hiura, H., *Adv. Mater.* **1995,** 7, (6), 582-586.
[88] Zhang, Y.; Small, J. P.; Pontius, W. V.; Kim, P., *Appl. Phys. Lett.* **2005,** 86, (7), 073104-3.
[89] Minkel, J. R. D.I.Y. Graphene: How to Make One-Atom-Thick Carbon Layers With Sticky Tape. http://www.scientificamerican.com/slideshow.cfm?id=diy-graphene-how-to-make-carbon-layers-with-sticky-tape (4/5/2010),
[90] Liang, X.; Fu, Z.; Chou, S. Y., *Nano Lett.* **2007,** 7, (12), 3840-3844.
[91] Dongsheng, L.; Wolfgang, W.; Nitin, P. P., *Adv. Mater.* **2009,** 21, (12), 1243-1246.
[92] Chen, C.-H.; Reddy, K. M.; Padture, N. P., *Nanotechnology* **2012,** 23, (23), 235603.
[93] Stankovich, S.; Dikin, D. A.; Piner, R. D.; Kohlhaas, K. A.; Kleinhammes, A.; Jia, Y.; Wu, Y.; Nguyen, S. T.; Ruoff, R. S., *Carbon* **2007,** 45, (7), 1558-1565.
[94] Park, S.; Ruoff, R. S., *Nat. Nanotechnol.* **2009,** 4, (4), 217-224.
[95] Staudenmaier, L., *Berichte der deutschen chemischen Gesellschaft* **1898,** 31, (2), 1481-1487.
[96] Hummers, W. S.; Offeman, R. E., *J. Am. Chem. Soc.* **1958,** 80, (6), 1339-1339.
[97] Eda, G.; Fanchini, G.; Chhowalla, M., *Nat. Nanotechnol.* **2008,** 3, (5), 270-274.
[98] Zhou, M.; Wang, Y. L.; Zhai, Y. M.; Zhai, J. F.; Ren, W.; Wang, F. A.; Dong, S. J., *Chem. Eur. J.* **2009,** 15, (25), 6116-6120.
[99] Cote, L. J.; Cruz-Silva, R.; Huang, J., *J. Am. Chem. Soc.* **2009,** 131, (31), 11027-11032.
[100] Williams, G.; Seger, B.; Kamat, P. V., *ACS Nano* **2008,** 2, (7), 1487-1491.
[101] He, H.; Klinowski, J.; Forster, M.; Lerf, A., *Chem. Phys. Lett.* **1998,** 287, (1-2), 53-56.
[102] Kaiser, A. B.; Gómez-Navarro, C.; Sundaram, R. S.; Burghard, M.; Kern, K., *Nano Lett.* **2009,** 9, (5), 1787-1792.
[103] Eda, G.; Mattevi, C.; Yamaguchi, H.; Kim, H.; Chhowalla, M., *J. Phys. Chem. C* **2009,** 113, (35), 15768-15771.
[104] Mkhoyan, K. A.; Contryman, A. W.; Silcox, J.; Stewart, D. A.; Eda, G.; Mattevi, C.; Miller, S.; Chhowalla, M., *Nano Lett.* **2009,** 9, (3), 1058-1063.
[105] Gomez-Navarro, C.; Meyer, J. C.; Sundaram, R. S.; Chuvilin, A.; Kurasch, S.; Burghard, M.; Kern, K.; Kaiser, U., *Nano Lett.* **2010,** 10, (4), 1144-1148.

[106] Vadukumpully, S.; Paul, J.; Valiyaveettil, S., *Carbon* **2009,** 47, (14), 3288-3294.
[107] Lotya, M.; Hernandez, Y.; King, P. J.; Smith, R. J.; Nicolosi, V.; Karlsson, L. S.; Blighe, F. M.; De, S.; Wang, Z.; McGovern, I. T.; Duesberg, G. S.; Coleman, J. N., *J. Am. Chem. Soc.* **2009,** 131, (10), 3611-3620.
[108] Blake, P.; Brimicombe, P. D.; Nair, R. R.; Booth, T. J.; Jiang, D.; Schedin, F.; Ponomarenko, L. A.; Morozov, S. V.; Gleeson, H. F.; Hill, E. W.; Geim, A. K.; Novoselov, K. S., *Nano Lett.* **2008,** 8, (6), 1704-1708.
[109] Hamilton, C. E.; Lomeda, J. R.; Sun, Z.; Tour, J. M.; Barron, A. R., *Nano Lett.* **2009,** 9, (10), 3460-3462.
[110] Hernandez, Y.; Lotya, M.; Rickard, D.; Bergin, S. D.; Coleman, J. N., *Langmuir* **2009,** 26, (5), 3208-3213.
[111] Biswas, S.; Drzal, L. T., *Nano Lett.* **2008,** 9, (1), 167-172.
[112] Ausman, K. D.; Piner, R.; Lourie, O.; Ruoff, R. S.; Korobov, M., *J. Phys. Chem. B* **2000,** 104, (38), 8911-8915.
[113] An, X.; Simmons, T.; Shah, R.; Wolfe, C.; Lewis, K. M.; Washington, M.; Nayak, S. K.; Talapatra, S.; Kar, S., *Nano Lett.* **2010,** 10, (11), 4295-4301.
[114] Behabtu, N.; Lomeda, J. R.; Green, M. J.; Higginbotham, A. L.; Sinitskii, A.; Kosynkin, D. V.; Tsentalovich, D.; Parra-Vasquez, A. N. G.; Schmidt, J.; Kesselman, E.; Cohen, Y.; Talmon, Y.; Tour, J. M.; Pasquali, M., *Nat. Nanotechnol.* **2010,** 5, (6), 406-411.
[115] Liu, W. W.; Wang, J. N.; Wang, X. X., *Nanoscale* **2012,** 4, (2), 425-428.
[116] Coleman, J. N., *Acc. Chem. Res.* **2012**.
[117] Li, X.; Zhang, G.; Bai, X.; Sun, X.; Wang, X.; Wang, E.; Dai, H., *Nat. Nanotechnol.* **2008,** 3, (9), 538-542.
[118] Robinson, J. T.; Perkins, F. K.; Snow, E. S.; Wei, Z.; Sheehan, P. E., *Nano Lett.* **2008,** 8, (10), 3137-3140.
[119] Eda, G.; Chhowalla, M., *Nano Lett.* **2009,** 9, (2), 814-818.
[120] Eda, G.; Unalan, H. E.; Rupesinghe, N.; Amaratunga, G. A. J.; Chhowalla, M., *Appl. Phys. Lett.* **2008,** 93, (23), 233502-3.
[121] Yamaguchi, H.; Eda, G.; Mattevi, C.; Kim, H.; Chhowalla, M., *ACS Nano* **2010,** 4, (1), 524-528.
[122] Dikin, D. A.; Stankovich, S.; Zimney, E. J.; Piner, R. D.; Dommett, G. H. B.; Evmenenko, G.; Nguyen, S. T.; Ruoff, R. S., *Nature* **2007,** 448, (7152), 457-460.
[123] Robinson, J. T.; Zalalutdinov, M.; Baldwin, J. W.; Snow, E. S.; Wei, Z.; Sheehan, P.; Houston, B. H., *Nano Lett.* **2008,** 8, (10), 3441-3445.
[124] Cote, L. J.; Kim, F.; Huang, J., *J. Am. Chem. Soc.* **2008,** 131, (3), 1043-1049.
[125] Torrisi, F.; Hasan, T.; Wu, W.; Sun, Z.; Lombardo, A.; Kulmala, T. S.; Hsieh, G.-W.; Jung, S.; Bonaccorso, F.; Paul, P. J.; Chu, D.; Ferrari, A. C., *ACS Nano* **2012,** 6, (4), 2992-3006.
[126] Kong, D.; Le, L. T.; Li, Y.; Zunino, J. L.; Lee, W., *Langmuir* **2012**.
[127] The Lemelson, M. I. T. P. Edward Acheson – Carborundum. http://web.mit.edu/invent/iow/acheson.html
[128] Acheson, F. E. G., Production of artificial crystalline carbonaceous materials. In Google Patents: 1893.
[129] van Bommel, A. J.; Crombeen, J. E.; van Tooren, A., *Surf. Sci.* **1975,** 48, (2), 463-472.
[130] First, P. N.; de Heer, W. A.; Seyller, T.; Berger, C.; Stroscio, J. A.; Moon, J. S., *MRS Bulletin* **2010,** 35, (4), 296-305.

[131] Sprinkle, M.; Soukiassian, P.; Heer, W. A.; Berger, C.; Conrad, E. H., *Phys. Status Solidi RRL* **2009,** 3, (6), A91-A94.
[132] Emtsev, K. V.; Bostwick, A.; Horn, K.; Jobst, J.; Kellogg, G. L.; Ley, L.; McChesney, J. L.; Ohta, T.; Reshanov, S. A.; Rohrl, J.; Rotenberg, E.; Schmid, A. K.; Waldmann, D.; Weber, H. B.; Seyller, T., *Nat. Mater.* **2009,** 8, (3), 203-207.
[133] Hass, J.; Varchon, F.; Millán-Otoya, J. E.; Sprinkle, M.; Sharma, N.; de Heer, W. A.; Berger, C.; First, P. N.; Magaud, L.; Conrad, E. H., *Phys. Rev. Lett.* **2008,** 100, (12), 125504.
[134] Ni, Z. H.; Chen, W.; Fan, X. F.; Kuo, J. L.; Yu, T.; Wee, A. T. S.; Shen, Z. X., *Phys. Rev. B* **2008,** 77, (11), 115416.
[135] Bostwick, A.; McChesney, J.; Ohta, T.; Rotenberg, E.; Seyller, T.; Horn, K., *Prog. Surf. Sci.* **2011,** 84, (11-12), 380-413.
[136] Sprinkle, M.; Siegel, D.; Hu, Y.; Hicks, J.; Tejeda, A.; Taleb-Ibrahimi, A.; Le Fèvre, P.; Bertran, F.; Vizzini, S.; Enriquez, H.; Chiang, S.; Soukiassian, P.; Berger, C.; de Heer, W. A.; Lanzara, A.; Conrad, E. H., *Phys. Rev. Lett.* **2009,** 103, (22), 226803.
[137] Berger, C.; Song, Z.; Li, X.; Wu, X.; Brown, N.; Naud, C.; Mayou, D.; Li, T.; Hass, J.; Marchenkov, A. N.; Conrad, E. H.; First, P. N.; de Heer, W. A., *Science* **2006,** 312, (5777), 1191-1196.
[138] de Heer, W. A.; Berger, C.; Wu, X.; First, P. N.; Conrad, E. H.; Li, X.; Li, T.; Sprinkle, M.; Hass, J.; Sadowski, M. L.; Potemski, M.; Martinez, G., *Solid State Commun.* **2007,** 143, (1–2), 92-100.
[139] Wu, X.; Hu, Y.; Ruan, M.; Madiomanana, N. K.; Hankinson, J.; Sprinkle, M.; Berger, C.; de Heer, W. A., *Appl. Phys. Lett.* **2009,** 95, (22), 223108-3.
[140] Wu, Y.; Jenkins, K. A.; Valdes-Garcia, A.; Farmer, D. B.; Zhu, Y.; Bol, A. A.; Dimitrakopoulos, C.; Zhu, W.; Xia, F.; Avouris, P.; Lin, Y.-M., *Nano Lett.* **2012,** 12, (6), 3062-3067.
[141] Gomez De Arco, L.; Zhang, Y.; Schlenker, C. W.; Ryu, K.; Thompson, M. E.; Zhou, C., *ACS Nano* **2010,** 4, (5), 2865-2873.
[142] Van Noorden, R., *Nature* **2012,** 483, (7389), S32-S33.
[143] Bhaviripudi, S.; Jia, X.; Dresselhaus, M. S.; Kong, J., *Nano Lett.* **2010,** 10, (10), 4128-4133.
[144] Kondo, D.; Sato, S.; Yagi, K.; Harada, N.; Sato, M.; Nihei, M.; Yokoyama, N., *Appl. Phys. Express* **2010,** 3, (2), 025102.
[145] Chong-an, D.; Dacheng, W.; Gui, Y.; Yunqi, L.; Yunlong, G.; Daoben, Z., *Adv. Mater.* **2008,** 20, (17), 3289-3293.
[146] Oznuluer, T.; Pince, E.; Polat, E. O.; Balci, O.; Salihoglu, O.; Kocabas, C., *Appl. Phys. Lett.* **2011,** 98, (18), 183101-3.
[147] M. Wofford, J.; Starodub, E.; Walter, A., L.; Nie, S.; Bostwick, A.; C. Bartelt, N.; Thürmer, K.; Rotenberg, E.; McCarty, K. F.; Dubon, O. D., *New J. Phys.* **2012,** 14, (5), 053008.
[148] Di, C.-a.; Wei, D.; Yu, G.; Liu, Y.; Guo, Y.; Zhu, D., *Adv. Mater.* **2008,** 20, (17), 3289-3293.
[149] Eom, D.; Prezzi, D.; Rim, K. T.; Zhou, H.; Lefenfeld, M.; Xiao, S.; Nuckolls, C.; Hybertsen, M. S.; Heinz, T. F.; Flynn, G. W., *Nano Lett.* **2009,** 9, (8), 2844-2848.
[150] Loginova, E.; Bartelt, N. C.; Feibelman, P. J.; McCarty, K. F., *New J. Phys.* **2009,** 11, (6), 063046.
[151] Ueta, H.; Saida, M.; Nakai, C.; Yamada, Y.; Sasaki, M.; Yamamoto, S., *Surf. Sci.* **2004,** 560, (1-3), 183-190.

[152] Gao, L.; Ren, W.; Xu, H.; Jin, L.; Wang, Z.; Ma, T.; Ma, L.-P.; Zhang, Z.; Fu, Q.; Peng, L.-M.; Bao, X.; Cheng, H.-M., *Nat. Commun.* **2012,** 3, 699.
[153] Coraux, J.; N'Diaye, A. T.; Engler, M.; Busse, C.; Wall, D.; Buckanie, N.; Heringdorf, F. J. M. z.; Gastel, R. v.; Poelsema, B.; Michely, T., *New J. Phys.* **2009,** 11, (2), 023006.
[154] Kwon, S. Y.; Ciobanu, C. V.; Petrova, V.; Shenoy, V. B.; Baren¦âo, J.; Gambin, V.; Petrov, I.; Kodambaka, S., *Nano Lett.* **2009,** 9, (12), 3985-3990.
[155] Preobrajenski, A. B.; Ng, M. L.; Vinogradov, A. S.; Mårtensson, N., *Phys. Rev. B* **2008,** 78, (7), 073401.
[156] Robin, J.; Ashokreddy, A.; Vijayan, C.; Pradeep, T., *Nanotechnology* **2011,** 22, (16), 165701.
[157] Gullapalli, H.; Mohana Reddy, A. L.; Kilpatrick, S.; Dubey, M.; Ajayan, P. M., *Small* **2011,** 7, (12), 1697-1700.
[158] Chen, S.; Brown, L.; Levendorf, M.; Cai, W.; Ju, S.-Y.; Edgeworth, J.; Li, X.; Magnuson, C. W.; Velamakanni, A.; Piner, R. D.; Kang, J.; Park, J.; Ruoff, R. S., *ACS Nano* **2011,** 5, (2), 1321-1327.
[159] Liu, N.; Fu, L.; Dai, B.; Yan, K.; Liu, X.; Zhao, R.; Zhang, Y.; Liu, Z., *Nano Lett.* **2010,** 11, (1), 297-303.
[160] Wu, Y.; Chou, H.; Ji, H.; Wu, Q.; Chen, S.; Jiang, W.; Hao, Y.; Kang, J.; Ren, Y.; Piner, R. D.; Ruoff, R. S., *ACS Nano* **2012,** 6, (9), 7731-7738.
[161] Weatherup, R. S.; Bayer, B. C.; Blume, R.; Ducati, C.; Baehtz, C.; Schlögl, R.; Hofmann, S., *Nano Lett.* **2011,** 11, (10), 4154-4160.
[162] Dai, B.; Fu, L.; Zou, Z.; Wang, M.; Xu, H.; Wang, S.; Liu, Z., *Nat. Commun.* **2011,** 2, 522.
[163] Papagno, L.; Caputi, L. S., *Phys. Rev. B* **1984,** 29, (3), 1483.
[164] Geng, D.; Wu, B.; Guo, Y.; Huang, L.; Xue, Y.; Chen, J.; Yu, G.; Jiang, L.; Hu, W.; Liu, Y., *Proc. Natl. Acad. Sci.* **2012,** 109, (21), 7992-7996.
[165] Wang, Y.; Zheng, Y.; Xu, X.; Dubuisson, E.; Bao, Q.; Lu, J.; Loh, K. P., *ACS Nano* **2011,** 5, (12), 9927-9933.
[166] Lock, E. H.; Baraket, M.; Laskoski, M.; Mulvaney, S. P.; Lee, W. K.; Sheehan, P. E.; Hines, D. R.; Robinson, J. T.; Tosado, J.; Fuhrer, M. S.; Hernández, S. C.; Walton, S. G., *Nano Lett.* **2011,** 12, (1), 102-107.
[167] Yoon, T.; Shin, W. C.; Kim, T. Y.; Mun, J. H.; Kim, T.-S.; Cho, B. J., *Nano Lett.* **2012,** 12, (3), 1448-1452.
[168] Kwak, J.; Chu, J. H.; Choi, J.-K.; Park, S.-D.; Go, H.; Kim, S. Y.; Park, K.; Kim, S.-D.; Kim, Y.-W.; Yoon, E.; Kodambaka, S.; Kwon, S.-Y., *Nat. Commun.* **2012,** 3, 645.
[169] Lizzit, S.; Larciprete, R.; Lacovig, P.; Dalmiglio, M.; Orlando, F.; Baraldi, A.; Gammelgaard, L.; Barreto, L.; Bianchi, M.; Perkins, E.; Hofmann, P., *Nano Lett.* **2012**.
[170] Li, X.; Cai, W.; Colombo, L.; Ruoff, R. S., *Nano Lett.* **2009,** 9, (12), 4268-4272.
[171] Masel, R. I., *Principles of Adsorption and Reaction on Solid Surfaces*. John Wiley & Sons, Inc.: New York, USA, 1996.
[172] Cai, W.; Piner, R.; Zhu, Y.; Li, X.; Tan, Z.; Floresca, H.; Yang, C.; Lu, L.; Kim, M.; Ruoff, R., *Nano Research* **2009,** 2, (11), 851-856.
[173] Singleton, M.; Nash, P., *J. Phase Equilib.* **1989,** 10, (2), 121-126.
[174] Lopez, G. A.; Mittemeijer, E. J., *Scr. Metall* **2004,** 51, 1.
[175] Wood, J. D.; Schmucker, S. W.; Lyons, A. S.; Pop, E.; Lyding, J. W., *Nano Lett.* **2011,** 11, (11), 4547-4554.

[176] Luo, Z.; Lu, Y.; Singer, D. W.; Berck, M. E.; Somers, L. A.; Goldsmith, B. R.; Johnson, A. T. C., *Chem. Mat.* **2011,** 23, (6), 1441-1447.
[177] Han, G. H.; Güneş, F.; Bae, J. J.; Kim, E. S.; Chae, S. J.; Shin, H.-J.; Choi, J.-Y.; Pribat, D.; Lee, Y. H., *Nano Lett.* **2011,** 11, (10), 4144-4148.
[178] Ogawa, Y.; Hu, B.; Orofeo, C. M.; Tsuji, M.; Ikeda, K.-i.; Mizuno, S.; Hibino, H.; Ago, H., *J. Phys. Chem. Lett.* **2011,** 3, (2), 219-226.
[179] Saadi, S.; Abild-Pedersen, F.; Helveg, S.; Sehested, J.; Hinnemann, B.; Appel, C. C.; Nørskov, J. K., *J. Phys. Chem. C* **2010,** 114, (25), 11221-11227.
[180] Hu, B.; Ago, H.; Ito, Y.; Kawahara, K.; Tsuji, M.; Magome, E.; Sumitani, K.; Mizuta, N.; Ikeda, K.-i.; Mizuno, S., *Carbon* **2012,** 50, (1), 57-65.
[181] Wu, Y. A.; Fan, Y.; Speller, S.; Creeth, G. L.; Sadowski, J. T.; He, K.; Robertson, A. W.; Allen, C. S.; Warner, J. H., *ACS Nano* **2012,** 6, (6), 5010-5017.
[182] Somani, P. R.; Somani, S. P.; Umeno, M., *Chem. Phys. Lett.* **2006,** 430, (1-3), 56-59.
[183] Li, Z.; Wu, P.; Wang, C.; Fan, X.; Zhang, W.; Zhai, X.; Zeng, C.; Li, Z.; Yang, J.; Hou, J., *ACS Nano* **2011,** 5, (4), 3385-3390.
[184] Zhang, B.; Lee, W. H.; Piner, R.; Kholmanov, I.; Wu, Y.; Li, H.; Ji, H.; Ruoff, R. S., *ACS Nano* **2012,** 6, (3), 2471-2476.
[185] Dong, X.; Wang, P.; Fang, W.; Su, C.-Y.; Chen, Y.-H.; Li, L.-J.; Huang, W.; Chen, P., *Carbon* **2011,** 49, (11), 3672-3678.
[186] Sun, Z.; Yan, Z.; Yao, J.; Beitler, E.; Zhu, Y.; Tour, J. M., *Nature* **2010,** 468, (7323), 549-552.
[187] Huigao, D.; Erqing, X.; Li, H.; Zhi, X., *Adv. Mater.* **2008,** 20, (17), 3284-3288.
[188] Byun, S.-J.; Lim, H.; Shin, G.-Y.; Han, T.-H.; Oh, S. H.; Ahn, J.-H.; Choi, H. C.; Lee, T.-W., *J. Phys. Chem. Lett.* **2011,** 2, (5), 493-497.
[189] Ruan, G.; Sun, Z.; Peng, Z.; Tour, J. M., *ACS Nano* **2011,** 5, (9), 7601-7607.
[190] Li, X.; Magnuson, C. W.; Venugopal, A.; Tromp, R. M.; Hannon, J. B.; Vogel, E. M.; Colombo, L.; Ruoff, R. S., *J. Am. Chem. Soc.* **2011,** 133, 2816.
[191] Li, X.; Magnuson, C. W.; Venugopal, A.; An, J.; Suk, J. W.; Han, B.; Borysiak, M.; Cai, W.; Velamakanni, A.; Zhu, Y.; Fu, L.; Vogel, E. M.; Voelkl, E.; Colombo, L.; Ruoff, R. S., *Nano Lett.* **2010,** 10, (11), 4328-4334.
[192] Teo, K. B. K.; Singh, C.; Chhowalla, M.; Milne, W. I., Catalytic growth of carbon nanotubes and nanofibers. In *Encyclopedia of Nanoscience and Nanotechnology*, Nalwa, H., Ed. 2005.
[193] Nolan, P. E.; Lynch, D. C.; Cutler, A. H., *J. Phys. Chem. B* **1998,** 102, (21), 4165-4175.
[194] Luo, Z.; Kim, S.; Kawamoto, N.; Rappe, A. M.; Johnson, A. T. C., *ACS Nano* **2011,** 5, (11), 9154-9160.
[195] Zhang, Y.; Li, Z.; Kim, P.; Zhang, L.; Zhou, C., *ACS Nano* **2011,** 6, (1), 126-132.
[196] Vlassiouk, I.; Regmi, M.; Fulvio, P.; Dai, S.; Datskos, P.; Eres, G.; Smirnov, S., *ACS Nano* **2011,** 5, (7), 6069-6076.
[197] Kalbac, M.; Frank, O.; Kavan, L., *Carbon* **2012,** 50, (10), 3682-3687.
[198] Butt, M. Z., *J. Mater. Sci. Lett.* **1983,** 2, (1), 1-2.
[199] Thiele, S.; Reina, A.; Healey, P.; Kedzierski, J.; Wyatt, P.; Hsu, P.-L.; Keast, C.; Schaefer, J.; Kong, J., *Nanotechnology* **2010,** 21, (1), 015601.
[200] Wofford, J. M.; Nie, S.; McCarty, K. F.; Bartelt, N. C.; Dubon, O. D., *Nano Lett.* **2010,** 10, (12), 4890-4896.

[201] van Gastel, R.; N'Diaye, A. T.; Wall, D.; Coraux, J.; Busse, C.; Buckanie, N. M.; Heringdorf, F. J. M. z.; von Hoegen, M. H.; Michely, T.; Poelsema, B., *Appl. Phys. Lett.* **2009,** 95, (12), 121901-121903.
[202] Gao, L.; Guest, J. R.; Guisinger, N. P., *Nano Lett.* **2010,** 10, (9), 3512-3516.
[203] Nie, S.; Wofford, J. M.; Bartelt, N. C.; Dubon, O. D.; McCarty, K. F., *Phys. Rev. B* **2011,** 84, (15), 155425.
[204] Loginova, E.; Bartelt, N. C.; Feibelman, P. J.; McCarty, K. F., *New J. Phys.* **2008,** 10, (9), 093026.
[205] Lee, S.; Lee, K.; Zhong, Z., *Nano Lett.* **2010,** 10, (11), 4702-4707.
[206] Liu, L.; Zhou, H.; Cheng, R.; Yu, W. J.; Liu, Y.; Chen, Y.; Shaw, J.; Zhong, X.; Huang, Y.; Duan, X., *ACS Nano* **2012**.
[207] Zhang, W.; Wu, P.; Li, Z.; Yang, J., *J. Phys. Chem. C* **2011,** 115, (36), 17782-17787.
[208] Shu, H.; Chen, X.; Tao, X.; Ding, F., *ACS Nano* **2012,** 6, (4), 3243-3250.
[209] Yuan, Q.; Gao, J.; Shu, H.; Zhao, J.; Chen, X.; Ding, F., *J. Am. Chem. Soc.* **2011,** 134, (6), 2970-2975.
[210] Riikonen, S.; Krasheninnikov, A. V.; Halonen, L.; Nieminen, R. M., *J. Phys. Chem. C* **2012,** 116, (9), 5802-5809.
[211] Walter, A. L.; Nie, S.; Bostwick, A.; Kim, K. S.; Moreschini, L.; Chang, Y. J.; Innocenti, D.; Horn, K.; McCarty, K. F.; Rotenberg, E., *Phys. Rev. B* **2011,** 84, (19), 195443.
[212] Ping, J.; Fuhrer, M. S., *Nano Lett.* **2012,** 12, (9), 4635-4641.
[213] Luo, Z.; Yu, T.; Shang, J.; Wang, Y.; Lim, S.; Liu, L.; Gurzadyan, G. G.; Shen, Z.; Lin, J., *Adv. Funct. Mater.* **2011,** 21, (5), 911-917.
[214] Brown, L.; Hovden, R.; Huang, P.; Wojcik, M.; Muller, D. A.; Park, J., *Nano Lett.* **2012,** 12, (3), 1609-1615.
[215] Ni, G.-X.; Zheng, Y.; Bae, S.; Kim, H. R.; Pachoud, A.; Kim, Y. S.; Tan, C.-L.; Im, D.; Ahn, J.-H.; Hong, B. H.; Özyilmaz, B., *ACS Nano* **2012,** 6, (2), 1158-1164.
[216] Cao, H.; Yu, Q.; Jauregui, L. A.; Tian, J.; Wu, W.; Liu, Z.; Jalilian, R.; Benjamin, D. K.; Jiang, Z.; Bao, J.; Pei, S. S.; Chen, Y. P., *Appl. Phys. Lett.* **2010,** 96, (12), 122106-3.
[217] Fallahazad, B.; Hao, Y.; Lee, K.; Kim, S.; Ruoff, R. S.; Tutuc, E., *Phys. Rev. B* **2012,** 85, (20), 201408.
[218] Huang, P. Y.; Ruiz-Vargas, C. S.; van der Zande, A. M.; Whitney, W. S.; Levendorf, M. P.; Kevek, J. W.; Garg, S.; Alden, J. S.; Hustedt, C. J.; Zhu, Y.; Park, J.; McEuen, P. L.; Muller, D. A., *Nature* **2011,** 469, (7330), 389-392.
[219] Tsen, A. W.; Brown, L.; Levendorf, M. P.; Ghahari, F.; Huang, P. Y.; Havener, R. W.; Ruiz-Vargas, C. S.; Muller, D. A.; Kim, P.; Park, J., *Science* **2012,** 336, (6085), 1143-1146.
[220] Song, H. S.; Li, S. L.; Miyazaki, H.; Sato, S.; Hayashi, K.; Yamada, A.; Yokoyama, N.; Tsukagoshi, K., *Sci. Rep.* **2012,** 2.
[221] Petrone, N.; Dean, C. R.; Meric, I.; van der Zande, A. M.; Huang, P. Y.; Wang, L.; Muller, D.; Shepard, K. L.; Hone, J., *Nano Lett.* **2012,** 12, (6), 2751-2756.
[222] Areshkin, D. A.; Gunlycke, D.; White, C. T., *Nano Lett.* **2006,** 7, (1), 204-210.
[223] Yazyev, O. V.; Louie, S. G., *Nat. Mater.* **2010,** 9, (10), 806-809.
[224] Lahiri, J.; Lin, Y.; Bozkurt, P.; Oleynik, I. I.; Batzill, M., *Nat. Nanotechnol.* **2010,** 5, (5), 326-329.
[225] Yu, Q.; Jauregui, L. A.; Wu, W.; Colby, R.; Tian, J.; Su, Z.; Cao, H.; Liu, Z.; Pandey, D.; Wei, D.; Chung, T. F.; Peng, P.; Guisinger, N. P.; Stach, E. A.; Bao, J.; Pei, S.-S.; Chen, Y. P., *Nat. Mater.* **2011,** 10, (6), 443-449.

[226] Venugopal, A.; Chan, J.; Li, X.; Magnuson, C. W.; Kirk, W. P.; Colombo, L.; Ruoff, R. S.; Vogel, E. M., *J. Appl. Phys.* **2011,** 109, (10), 104511-5.
[227] Chan, J.; Venugopal, A.; Pirkle, A.; McDonnell, S.; Hinojos, D.; Magnuson, C. W.; Ruoff, R. S.; Colombo, L.; Wallace, R. M.; Vogel, E. M., *ACS Nano* **2012,** 6, (4), 3224-3229.
[228] Wu, J.; Pisula, W.; Müllen, K., *Chem. Rev.* **2007,** 107, (3), 718-747.
[229] Yang, X.; Dou, X.; Rouhanipour, A.; Zhi, L.; Rader, H. J.; Müllen, K., *J. Am. Chem. Soc.* **2008,** 130, (13), 4216-4217.
[230] Simpson, C. D.; Brand, J. D.; Berresheim, A. J.; Przybilla, L.; Räder, H. J.; Müllen, K., *Chem. Eur. J.* **2002,** 8, (6), 1424-1429.
[231] Allen, M. J.; Tung, V. C.; Kaner, R. B., *Chem. Rev.* **2009,** 110, (1), 132-145.
[232] Chen, L.; Hernandez, Y.; Feng, X.; Müllen, K., *Angew. Chem. Int. Ed.* **2012,** 51, (31), 7640-7654.
[233] Choucair, M.; Thordarson, P.; Stride, J. A., *Nat. Nanotechnol.* **2009,** 4, (1), 30-33.
[234] Xianbao, W.; Haijun, Y.; Fangming, L.; Mingjian, L.; Li, W.; Shaoqing, L.; Qin, L.; Yang, X.; Rong, T.; Ziyong, Y.; Dong, X.; Jing, C., *Chem. Vap. Deposition* **2009,** 15, (1-3), 53-56.
[235] Dato, A.; Radmilovic, V.; Lee, Z.; Phillips, J.; Frenklach, M., *Nano Lett.* **2008,** 8, (7), 2012-2016.
[236] Dato, A.; Lee, Z.; Jeon, K.-J.; Erni, R.; Radmilovic, V.; Richardson, T. J.; Frenklach, M., *Chem. Commun.* **2009**, (40), 6095-6097.
[237] Wang, X.; Zhi, L.; Müllen, K., *Nano Lett.* **2007,** 8, (1), 323-327.
[238] Tung, V. C.; Chen, L.-M.; Allen, M. J.; Wassei, J. K.; Nelson, K.; Kaner, R. B.; Yang, Y., *Nano Lett.* **2009,** 9, (5), 1949-1955.
[239] Wang, Y.; Tong, S. W.; Xu, X. F.; Özyilmaz, B.; Loh, K. P., *Adv. Mater.* **2011,** 23, (13), 1514-1518.
[240] Park, H.; Brown, P. R.; Bulović, V.; Kong, J., *Nano Lett.* **2011,** 12, (1), 133-140.
[241] Wu, J.; Agrawal, M.; Becerril, H. ü. A.; Bao, Z.; Liu, Z.; Chen, Y.; Peumans, P., *ACS Nano* **2009,** 4, (1), 43-48.
[242] Lee, C.-H.; Kim, Y.-J.; Hong, Y. J.; Jeon, S.-R.; Bae, S.; Hong, B. H.; Yi, G.-C., *Adv. Mater.* **2011,** 23, (40), 4614-4619.
[243] Kim, R.-H.; Bae, M.-H.; Kim, D. G.; Cheng, H.; Kim, B. H.; Kim, D.-H.; Li, M.; Wu, J.; Du, F.; Kim, H.-S.; Kim, S.; Estrada, D.; Hong, S. W.; Huang, Y.; Pop, E.; Rogers, J. A., *Nano Lett.* **2011,** 11, (9), 3881-3886.
[244] Han, T.-H.; Lee, Y.; Choi, M.-R.; Woo, S.-H.; Bae, S.-H.; Hong, B. H.; Ahn, J.-H.; Lee, T.-W., *Nat. Photonics* **2012,** 6, (2), 105-110.
[245] Matyba, P.; Yamaguchi, H.; Eda, G.; Chhowalla, M.; Edman, L.; Robinson, N. D., *ACS Nano* **2010,** 4, (2), 637-642.
[246] Zhu, Y.; Sun, Z.; Yan, Z.; Jin, Z.; Tour, J. M., *ACS Nano* **2011,** 5, (8), 6472-6479.
[247] David, S. G.; Clark, B., *MRS Bulletin* **2008,** 25, (8), 15-18.
[248] Granqvist, C. G.; Hultaker, A., *Thin Solid Films* **2002,** 411, (1), 1-5.
[249] Kumar, A.; Zhou, C., *ACS Nano* **2010,** 4, (1), 11-14.
[250] Dressel, M.; Grunner, G., *Electrodynamics of Solids: Optical Properties of Electrons in Matter*. Cambridge University Press: Cambridge, 2002.
[251] Kim, J. Y.; Sohn, D.; Kim, E. R., *Appl. Phys. A* **2001,** 72, (6), 699-704.
[252] Kim, J. Y.; Kim, T. W.; Lee, J. H.; Kwon, S. J.; Jung, W. G.; Ju, S. H., *Jpn. J. Appl. Phys.* **2009,** 48, (9), 091501.
[253] De, S.; Coleman, J. N., *ACS Nano* **2010,** 4, (5), 2713-2720.

[254] Wang, S.; Ang, P. K.; Wang, Z.; Tang, A. L. L.; Thong, J. T. L.; Loh, K. P., *Nano Lett.* **2009,** 10, (1), 92-98.
[255] Li, X.; Zhu, Y.; Cai, W.; Borysiak, M.; Han, B.; Chen, D.; Piner, R. D.; Colombo, L.; Ruoff, R. S., *Nano Lett.* **2009,** 9, (12), 4359-4363.
[256] Yoo, E.; Kim, J.; Hosono, E.; Zhou, H. s.; Kudo, T.; Honma, I., *Nano Lett.* **2008,** 8, (8), 2277-2282.
[257] Chang, K.; Chen, W., *J. Mater. Chem.* **2011,** 21, (43), 17175-17184.
[258] Latorre-Sanchez, M.; Atienzar, P.; Abellán, G.; Puche, M.; Fornés, V.; Ribera, A.; García, H., *Carbon* **2012,** 50, (2), 518-525.
[259] Liang, M.; Luo, B.; Zhi, L., *Int. J. Energy Res.* **2009,** 33, (13), 1161-1170.
[260] Liu, H.; Gao, P.; Fang, J.; Yang, G., *Chem. Commun.* **2011,** 47, (32), 9110-9112.
[261] Wang, H.; Yang, Y.; Liang, Y.; Cui, L.-F.; Sanchez Casalongue, H.; Li, Y.; Hong, G.; Cui, Y.; Dai, H., *Angew. Chem. Int. Ed.* **2011,** 50, (32), 7364-7368.
[262] Zhou, X.; Wang, F.; Zhu, Y.; Liu, Z., *J. Mater. Chem.* **2011,** 21, (10), 3353-3358.
[263] Seger, B.; Kamat, P. V., *J. Phys. Chem. C* **2009,** 113, (19), 7990-7995.
[264] Lee, S. H.; Kakati, N.; Jee, S. H.; Maiti, J.; Yoon, Y.-S., *Mater. Lett.* **2011,** 65, (21–22), 3281-3284.
[265] Hur, S. H.; Park, J.-N., *Asia Pac. J. Chem. Eng.* **2012,** advance online publication.
[266] Jyothirmayee Aravind, S. S.; Imran Jafri, R.; Rajalakshmi, N.; Ramaprabhu, S., *J. Mater. Chem.* **2011,** 21, (45), 18199-18204.
[267] Zhang, L.; Xia, Z., *J. Phys. Chem. C* **2011,** 115, (22), 11170-11176.
[268] Yang, H.; Zhong, X.; Dong, Z.; Wang, J.; Jin, J.; Ma, J., *RSC Adv.* **2012,** 2, (12), 5038-5040.
[269] Stoller, M. D.; Park, S.; Zhu, Y.; An, J.; Ruoff, R. S., *Nano Lett.* **2008,** 8, (10), 3498-3502.
[270] El-Kady, M. F.; Strong, V.; Dubin, S.; Kaner, R. B., *Science* **2012,** 335, (6074), 1326-1330.
[271] Fan, Z.; Yan, J.; Wei, T.; Zhi, L.; Ning, G.; Li, T.; Wei, F., *Adv. Funct. Mater.* **2011,** 21, (12), 2366-2375.
[272] Gao, W.; Singh, N.; Song, L.; Liu, Z.; Reddy, A. L. M.; Ci, L.; Vajtai, R.; Zhang, Q.; Wei, B.; Ajayan, P. M., *Nat. Nanotechnol.* **2011,** 6, (8), 496-500.
[273] Shi, W.; Zhu, J.; Sim, D. H.; Tay, Y. Y.; Lu, Z.; Zhang, X.; Sharma, Y.; Srinivasan, M.; Zhang, H.; Hng, H. H.; Yan, Q., *J. Mater. Chem.* **2011,** 21, (10), 3422-3427.
[274] Si, P.; Ding, S.; Lou, X.-W.; Kim, D.-H., *RSC Adv.* **2011,** 1, (7), 1271-1278.
[275] Yu, G.; Hu, L.; Liu, N.; Wang, H.; Vosgueritchian, M.; Yang, Y.; Cui, Y.; Bao, Z., *Nano Lett.* **2011,** 11, (10), 4438-4442.
[276] Zhou, W.; Liu, J.; Chen, T.; Tan, K. S.; Jia, X.; Luo, Z.; Cong, C.; Yang, H.; Li, C. M.; Yu, T., *Phys. Chem. Chem. Phys.* **2011,** 13, (32), 14462-14465.
[277] Zhu, Y.; Murali, S.; Stoller, M. D.; Ganesh, K. J.; Cai, W.; Ferreira, P. J.; Pirkle, A.; Wallace, R. M.; Cychosz, K. A.; Thommes, M.; Su, D.; Stach, E. A.; Ruoff, R. S., *Science* **2011,** 332, (6037), 1537-1541.
[278] Murali, R.; Brenner, K.; Yinxiao, Y.; Beck, T.; Meindl, J. D., *IEEE Electron Device Lett.* **2009,** 30, (6), 611-613.
[279] Moser, J.; Barreiro, A.; Bachtold, A., *Appl. Phys. Lett.* **2007,** 91, (16), 163513-3.
[280] Ponomarenko, L. A.; Schedin, F.; Katsnelson, M. I.; Yang, R.; Hill, E. W.; Novoselov, K. S.; Geim, A. K., *Science* **2008,** 320, (5874), 356-358.

[281] Lee, S.-K.; Kim, B. J.; Jang, H.; Yoon, S. C.; Lee, C.; Hong, B. H.; Rogers, J. A.; Cho, J. H.; Ahn, J.-H., *Nano Lett.* **2011,** 11, (11), 4642-4646.
[282] Ahn, J.-H.; Je, J. H., *J. Phys. D: Appl. Phys.* **2012,** 45, (10), 103001.
[283] Hong, S. W.; Du, F.; Lan, W.; Kim, S.; Kim, H.-S.; Rogers, J. A., *Adv. Mater.* **2011,** 23, (33), 3821-3826.
[284] Marko, B.; Hagen, K.; Klaus, K., *Adv. Mater.* **2009,** 21, (25-26), 2586-2600.
[285] Han, M. Y.; Ozyilmaz, B.; Zhang, Y.; Kim, P., *Phys. Rev. Lett.* **2007,** 98, (20), 206805.
[286] Son, Y. W.; Cohen, M. L.; Louie, S. G., *Phys. Rev. Lett.* **2006,** 97, (21), 216803.
[287] Barone, V.; Hod, O.; Scuseria, G. E., *Nano Lett.* **2006,** 6, (12), 2748-2754.
[288] Bai, J.; Duan, X.; Huang, Y., *Nano Lett.* **2009,** 9, (5), 2083-2087.
[289] Jiao, L.; Zhang, L.; Wang, X.; Diankov, G.; Dai, H., *Nature* **2009,** 458, (7240), 877-880.
[290] Kosynkin, D. V.; Higginbotham, A. L.; Sinitskii, A.; Lomeda, J. R.; Dimiev, A.; Price, B. K.; Tour, J. M., *Nature* **2009,** 458, (7240), 872-876.
[291] Nakada, K.; Fujita, M.; Dresselhaus, G.; Dresselhaus, M. S., *Phys. Rev. B* **1996,** 54, (24), 17954.
[292] Wu, Y.; Perebeinos, V.; Lin, Y.-m.; Low, T.; Xia, F.; Avouris, P., *Nano Lett.* **2012,** 12, (3), 1417-1423.
[293] Kim, K.; Choi, J.-Y.; Kim, T.; Cho, S.-H.; Chung, H.-J., *Nature* **2011,** 479, (7373), 338-344.
[294] Lin, Y.-M.; Dimitrakopoulos, C.; Jenkins, K. A.; Farmer, D. B.; Chiu, H.-Y.; Grill, A.; Avouris, P., *Science* **2010,** 327, (5966), 662.
[295] Kim, H.; Abdala, A. A.; Macosko, C. W., *Macromolecules* **2010,** 43, (16), 6515-6530.
[296] Potts, J. R.; Dreyer, D. R.; Bielawski, C. W.; Ruoff, R. S., *Polymer* **2011,** 52, (1), 5-25.
[297] Bai, S.; Shen, X., *RSC Adv.* **2012,** 2, (1), 64-98.
[298] Xu, Y.; Shi, G., *J. Mater. Chem.* **2011,** 21, (10), 3311-3323.
[299] Bai, H.; Li, C.; Shi, G., *Adv. Mater.* **2011,** 23, (9), 1089-1115.
[300] Alzari, V.; Nuvoli, D.; Scognamillo, S.; Piccinini, M.; Gioffredi, E.; Malucelli, G.; Marceddu, S.; Sechi, M.; Sanna, V.; Mariani, A., *J. Mater. Chem.* **2011,** 21, (24), 8727-8733.
[301] Sanna, R.; Sanna, D.; Alzari, V.; Nuvoli, D.; Scognamillo, S.; Piccinini, M.; Lazzari, M.; Gioffredi, E.; Malucelli, G.; Mariani, A., *J. Polym. Sci., Part A: Polym. Chem.* **2012,** 50, (19), 4110-4118.
[302] Alwarappan, S.; Erdem, A.; Liu, C.; Li, C. Z., *J. Phys. Chem. C* **2009,** 113, (20), 8853-8857.
[303] Chun-Hua, L.; Huang-Hao, Y.; Chun-Ling, Z.; Xi, C.; Guo-Nan, C., *Angew. Chem. Int. Ed.* **2009,** 48, (26), 4785-4787.
[304] Dan, Y.; Lu, Y.; Kybert, N. J.; Luo, Z.; Johnson, A. T. C., *Nano Lett.* **2009,** 9, (4), 1472-1475.
[305] Fowler, J. D.; Allen, M. J.; Tung, V. C.; Yang, Y.; Kaner, R. B.; Weiller, B. H., *ACS Nano* **2009,** 3, (2), 301-306.
[306] Li, J.; Guo, S.; Zhai, Y.; Wang, E., *Electrochem. Commun.* **2009,** 11, (5), 1085-1088.
[307] Sakhaee-Pour, A.; Ahmadian, M. T.; Vafai, A., *Solid State Commun.* **2008,** 145, (4), 168-172.
[308] Avouris, P.; Dimitrakopoulos, C., *Materials Today* **2012,** 15, (3), 86-97.
[309] Liu, M.; Yin, X.; Ulin-Avila, E.; Geng, B.; Zentgraf, T.; Ju, L.; Wang, F.; Zhang, X., *Nature* **2011,** 474, (7349), 64-67.
[310] Mueller, T.; Xia, F.; Avouris, P., *Nat. Photonics* **2010,** 4, (5), 297-301.

[311] Konstantatos, G.; Badioli, M.; Gaudreau, L.; Osmond, J.; Bernechea, M.; de Arquer, F. P. G.; Gatti, F.; Koppens, F. H. L., *Nat. Nanotechnol.* **2012,** 7, (6), 363-368.
[312] Malesevic, A.; Kemps, R.; Vanhulsel, A.; Chowdhury, M. P.; Volodin, A.; Van Haesendonck, C., *J. Appl. Phys.* **2008,** 104, (8), 084301-084305.
[313] Zhong-Shuai, W.; Songfeng, P.; Wencai, R.; Daiming, T.; Libo, G.; Bilu, L.; Feng, L.; Chang, L.; Hui-Ming, C., *Adv. Mater.* **2009,** 21, (17), 1756-1760.
[314] Bunch, J. S.; Verbridge, S. S.; Alden, J. S.; van der Zande, A. M.; Parpia, J. M.; Craighead, H. G.; McEuen, P. L., *Nano Lett.* **2008,** 8, (8), 2458-2462.
[315] Nair, R. R.; Wu, H. A.; Jayaram, P. N.; Grigorieva, I. V.; Geim, A. K., *Science* **2012,** 335, (6067), 442-444.
[316] McBride, J. R.; Lupini, A. R.; Schreuder, M. A.; Smith, N. J.; Pennycook, S. J.; Rosenthal, S. J., *ACS Appl. Mater. Interfaces* **2009,** 1, (12), 2886-2892.
[317] Tan, W. D.; Su, C. Y.; Knize, R. J.; Xie, G. Q.; Li, L. J.; Tang, D. Y., *Appl. Phys. Lett.* **2010,** 96, (3), 031106-3.
[318] Qiaoliang, B.; Han, Z.; Yu, W.; Zhenhua, N.; Yongli, Y.; Ze Xiang, S.; Kian Ping, L.; Ding Yuan, T., *Adv. Funct. Mater.* **2009,** 19, (19), 3077-3083.
[319] Tylianakis, E.; Dimitrakakis, G. K.; Melchor, S.; Dobado, J. A.; Froudakis, G. E., *Chem. Commun.* **2011,** 47, (8), 2303-2305.
[320] Dimitrakakis, G. K.; Tylianakis, E.; Froudakis, G. E., *Nano Lett.* **2008,** 8, (10), 3166-3170.
[321] De, S.; King, P. J.; Lotya, M.; O'Neill, A.; Doherty, E. M.; Hernandez, Y.; Duesberg, G. S.; Coleman, J. N., *Small* **2010,** 6, (3), 458-464.
[322] Pan, S.; Aksay, I. A., *ACS Nano* **2011,** 5, (5), 4073-4083.
[323] Novoselov, K. S.; Falko, V. I.; Colombo, L.; Gellert, P. R.; Schwab, M. G.; Kim, K., *Nature* **2012,** 490, (7419), 192-200.
[324] Zhang, Y.; Li, D.; Tan, X.; Zhang, B.; Ruan, X.; Liu, H.; Pan, C.; Liao, L.; Zhai, T.; Bando, Y.; Chen, S.; Cai, W.; Ruoff, R. S., *Carbon* **2013,** 54, (0), 143-148.
[325] Srivastava, N.; Guowei, H.; Luxmi; Mende, P. C.; Feenstra, R. M.; Yugang, S., *J. Phys. D: Appl. Phys.* **2012,** 45, (15), 154001.
[326] Yike, H.; Ming, R.; Zelei, G.; Rui, D.; James, P.; John, H.; Claire, B.; Walt, A. d. H., *J. Phys. D: Appl. Phys.* **2012,** 45, (15), 154010.
[327] Chen, S.; Ji, H.; Chou, H.; Li, Q.; Li, H.; Suk, J. W.; Piner, R.; Liao, L.; Cai, W.; Ruoff, R. S., *Adv. Mater.* **2013**, n/a-n/a.
[328] Yan, Z.; Lin, J.; Peng, Z.; Sun, Z.; Zhu, Y.; Li, L.; Xiang, C.; Samuel, E. L.; Kittrell, C.; Tour, J. M., *ACS Nano* **2012,** 6, (10), 9110-9117.
[329] Hildebrand, J. H.; Prausnitz, J. M.; Scott, R. L., *Regular and related solutions: the solubility of gases, liquids, and solids*. Van Nostrand Reinhold Co.: 1970.
[330] Israelachvili, J., *Intermolecular and Surface Forces*. Academic Press Limited: London, 1991.
[331] Blodgett, K. B., *J. Am. Chem. Soc.* **1935,** 57, (6), 1007-1022.
[332] Peterson, I. R., *J. Phys. D: Appl. Phys.* **1990,** 23, (4), 379.
[333] Knobler, C. M.; Desai, R. C., *Annu. Rev. Phys. Chem.* **1992,** 43, 207-236.
[334] Fendler, J. H., *Curr. Opin. Colloid Interface Sci.* **1996,** 1, (2), 202-207.
[335] Kim, F.; Kwan, S.; Akana, J.; Yang, P. D., *J. Am. Chem. Soc.* **2001,** 123, (18), 4360-4361.
[336] Di Luccio, T.; Antolini, F.; Aversa, P.; Scalia, G.; Tapfer, L., *Carbon* **2004,** 42, (5–6), 1119-1122.

[337] Eda, G.; Ball, J.; Mattevi, C.; Acik, M.; Artiglia, L.; Granozzi, G.; Chabal, Y.; Anthopoulos, T. D.; Chhowalla, M., *J. Mater. Chem.* **2011,** 21, (30), 11217-11223.
[338] Langmuir, I., *J. Am. Chem. Soc.* **1917,** 39, (9), 1848-1906.
[339] Franklin, B.; Brownrigg, W.; Farish, M., *Philosophical Transactions* **1774,** 64, 445-460.
[340] Langmuir, I.; Schaefer, V. J., *J. Am. Chem. Soc.* **1938,** 60, (6), 1351-1360.
[341] Lee, Y.; Bae, S.; Jang, H.; Jang, S.; Zhu, S.-E.; Sim, S. H.; Song, Y. I.; Hong, B. H.; Ahn, J.-H., *Nano Lett.* **2010,** 10, (2), 490-493.
[342] Sivaram, S., *Chemical vapor deposition: thermal and plasma deposition of electronic materials*. Van Nostrand Reinhold: 1995.
[343] Dawe, R. A.; Smith, E. B., *Science* **1969,** 163, (3868), 675-676.
[344] Guevara, F. A.; McInteer, B. B.; Wageman, W. E., *Phys. Fluids* **1969,** 12, (12), 2493-2505.
[345] Younglove, B. A.; Ely, J. F., *J. Phys. Chem. Ref. Data* **1987,** 16, (4), 577-798.
[346] Streeter, V. L., *Fluid Mechanics, 8th Edition*. Mcgraw-Hill: 1985.
[347] Dobkin, D. M.; Zuraw, K., *Principles of Chemical Vapor Deposition*. Springer: 2003.
[348] Jousten, K., *Handbook of Vacuum Technology*. John Wiley & Sons: 2008.
[349] Fabian, R., *Vacuum Technology: Practical Heat Treating and Brazing*. Asm International: 1993.
[350] Levendorf, M. P.; Ruiz-Vargas, C. S.; Garg, S.; Park, J., *Nano Lett.* **2009,** 9, (12), 4479-4483.
[351] Ogura, T., *Biochem. Biophys. Res. Commun.* **2009,** 380, (2), 254-259.
[352] Donald, A. M., *Nat. Mater.* **2003,** 2, (8), 511-516.
[353] Kochat, V.; Pal, A. N.; Sneha, E. S.; Sampathkumar, A.; Gairola, A.; Shivashankar, S. A.; Raghavan, S.; Ghosh, A., *J. Appl. Phys.* **2011,** 110, (1), 014315-5.
[354] Scrivener, K. L., *Cem. Concr. Compos.* **2004,** 26, (8), 935-945.
[355] Pawley, J., *J. Microsc.* **1984,** 136, (1), 45-68.
[356] Zaefferer, S., *Cryst. Res. Technol.* **2011,** 46, (6), 607-628.
[357] Shao, W.; Zangari, G., *J. Phys. Chem. C* **2009,** 113, (23), 10097-10102.
[358] Humphreys, F. J., *Scr. Mater.* **2004,** 51, (8), 771-776.
[359] Cardona, M.; Güntherodt, G., *Light Scattering in Solids II: basic concepts and instrumentation*. Springer: New York, 1982; Vol. 50, p 19.
[360] Das, A.; Pisana, S.; Chakraborty, B.; Piscanec, S.; Saha, S. K.; Waghmare, U. V.; Novoselov, K. S.; Krishnamurthy, H. R.; Geim, A. K.; Ferrari, A. C.; Sood, A. K., *Nat. Nanotechnol.* **2008,** 3, (4), 210-215.
[361] Ni, Z.; Wang, Y.; Yu, T.; Shen, Z., *Nano Research* **2008,** 1, (4), 273-291.
[362] Costa, S. D.; Righi, A.; Fantini, C.; Hao, Y.; Magnuson, C.; Colombo, L.; Ruoff, R. S.; Pimenta, M. A., *Solid State Commun.* **2012,** 152, (15), 1317-1320.
[363] Cançado, L. G.; Jorio, A.; Ferreira, E. H. M.; Stavale, F.; Achete, C. A.; Capaz, R. B.; Moutinho, M. V. O.; Lombardo, A.; Kulmala, T. S.; Ferrari, A. C., *Nano Lett.* **2011,** 11, (8), 3190-3196.
[364] Ferrari, A. C.; Meyer, J. C.; Scardaci, V.; Casiraghi, C.; Lazzeri, M.; Mauri, F.; Piscanec, S.; Jiang, D.; Novoselov, K. S.; Roth, S.; Geim, A. K., *Phys. Rev. Lett.* **2006,** 97, (18), 187401.
[365] Ferrari, A. C.; Robertson, J., *Phys. Rev. B* **2000,** 61, (20), 14095-14107.
[366] Ferrari, A. C., *Solid State Commun.* **2007,** 143, (1–2), 47-57.

[367] Piscanec, S.; Lazzeri, M.; Mauri, F.; Ferrari, A. C.; Robertson, J., *Phys. Rev. Lett.* **2004,** 93, (18), 185503.
[368] Ferrari, A. C.; Robertson, J., *Phys. Rev. B* **2001,** 64, (7), 075414.
[369] Tuinstra, F.; Koenig, J. L., *J. Chem. Phys.* **1970,** 53, (3), 1126-1130.
[370] Eckmann, A.; Felten, A.; Mishchenko, A.; Britnell, L.; Krupke, R.; Novoselov, K. S.; Casiraghi, C., *Nano Lett.* **2012**.
[371] Pimenta, M. A.; Dresselhaus, G.; Dresselhaus, M. S.; Cancado, L. G.; Jorio, A.; Saito, R., *Phys. Chem. Chem. Phys.* **2007,** 9, (11), 1276-1290.
[372] Malard, L. M.; Pimenta, M. A.; Dresselhaus, G.; Dresselhaus, M. S., *Phys. Rep.* **2009,** 473, (5-6), 51-87.
[373] Yu, V.; Whiteway, E.; Maassen, J.; Hilke, M., *Phys. Rev. B* **2011,** 84, (20), 205407.
[374] Pisana, S.; Lazzeri, M.; Casiraghi, C.; Novoselov, K. S.; Geim, A. K.; Ferrari, A. C.; Mauri, F., *Nat. Mater.* **2007,** 6, (3), 198-201.
[375] Carozo, V.; Almeida, C. M.; Ferreira, E. H. M.; Cançado, L. G.; Achete, C. A.; Jorio, A., *Nano Lett.* **2011,** 11, (11), 4527-4534.
[376] Gupta, A. K.; Tang, Y.; Crespi, V. H.; Eklund, P. C., *Phys. Rev. B* **2010,** 82, (24), 241406.
[377] Rao, R.; Podila, R.; Tsuchikawa, R.; Katoch, J.; Tishler, D.; Rao, A. M.; Ishigami, M., *ACS Nano* **2011,** 5, (3), 1594-1599.
[378] Cong, C.; Yu, T.; Saito, R.; Dresselhaus, G. F.; Dresselhaus, M. S., *ACS Nano* **2011,** 5, (3), 1600-1605.
[379] Tan, P. H.; Han, W. P.; Zhao, W. J.; Wu, Z. H.; Chang, K.; Wang, H.; Wang, Y. F.; Bonini, N.; Marzari, N.; Pugno, N.; Savini, G.; Lombardo, A.; Ferrari, A. C., *Nat. Mater.* **2012,** advance online publication.
[380] Schmitz, I.; Schreiner, M.; Friedbacher, G.; Grasserbauer, M., *Anal. Chem.* **1997,** 69, (6), 1012-1018.
[381] Fernando, G. W., Chapter 5 Probing Layered Systems: A Brief Guide to Experimental Techniques. In *Handbook of Metal Physics*, Gayanath, W. F., Ed. Elsevier: 2008; Vol. Volume 4, pp 111-130.
[382] Locatelli, A.; Bianco, A.; Cocco, D.; Cherifi, S.; Heun, S.; Marsi, M.; Pasqualetto, M.; Bauer, E., *J. Phys. IV France* **2003,** 104, 99-102.
[383] Jin, L.; Fu, Q.; Mu, R.; Tan, D.; Bao, X., *Phys. Chem. Chem. Phys.* **2011,** 13, (37), 16655-16660.
[384] Altman, M. S., *J. Phys.: Condens. Matter* **2005,** 17, (16), S1305.
[385] Sutter, P.; Sadowski, J. T.; Sutter, E., *Phys. Rev. B* **2009,** 80, (24), 245411.
[386] Einstein, A., *Annalen der Physik* **1905,** 322, (6), 132-148.
[387] Mentes, T. O.; Ni; ntilde; o, M. A.; Locatelli, A., *e-J. Surf. Sci. Nanotech.* **2011,** 9, 72-79.
[388] Locatelli, A.; Aballe, L.; Mentes, T. O.; Kiskinova, M.; Bauer, E., *Surf. Interface Anal.* **2006,** 38, (12-13), 1554-1557.
[389] Johansson, L. I.; Watcharinyanon, S.; Zakharov, A. A.; Iakimov, T.; Yakimova, R.; Virojanadara, C., *Phys. Rev. B* **2011,** 84, (12), 125405.
[390] Dan, B.; Irvin, G. C.; Pasquali, M., *ACS Nano* **2009,** 3, (4), 835-843.
[391] Skulason, H. S.; Gaskell, P. E.; Szkopek, T., *Nanotechnology* **2010,** 21, (29), 295709.
[392] Thurber, W. R. Hall Effect Measurements. http://www.nist.gov/pml/div683/hall.cfm (August 9),
[393] Cross, M. M., *Rheologica Acta* **1979,** 18, (5), 609-614.

[394] Marrucci, G.; Maffettone, P. L., *Macromolecules* **1989,** 22, (10), 4076-4082.
[395] Werner, P.; Verdejo, R.; Wöllecke, F.; Altstädt, V.; Sandler, J. K. W.; Shaffer, M. S. P., *Adv. Mater.* **2005,** 17, (23), 2864-2869.
[396] Kuijpers, M. W. A.; Iedema, P. D.; Kemmere, M. F.; Keurentjes, J. T. F., *Polymer* **2004,** 45, (19), 6461-6467.
[397] Hennrich, F.; Krupke, R.; Arnold, K.; Rojas Stütz, J. A.; Lebedkin, S.; Koch, T.; Schimmel, T.; Kappes, M. M., *J. Phys. Chem. B* **2007,** 111, (8), 1932-1937.
[398] Fowkes, F. M., *J. Phys. Chem.* **1962,** 66, (2), 382-382.
[399] Wang, S.; Zhang, Y.; Abidi, N.; Cabrales, L., *Langmuir* **2009,** 25, (18), 11078-11081.
[400] De, S.; King, P. J.; Lyons, P. E.; Khan, U.; Coleman, J. N., *ACS Nano* **2010,** 4, (12), 7064-7072.
[401] McLachlan, D. S.; Blaszkiewicz, M.; Newnham, R. E., *J. Am. Ceram. Soc.* **1990,** 73, (8), 2187-2203.
[402] McLachlan, D. S., *J. Phys. C* **1985,** 18, (9), 1891.
[403] Gingold, D. B.; Lobb, C. J., *Phys. Rev. B* **1990,** 42, (13), 8220-8224.
[404] Frank, D. J.; Lobb, C. J., *Phys. Rev. B* **1988,** 37, (1), 302-307.
[405] De, S. C., Jonathan N. , *MRS Bulletin* **2011,** 36, 774-781.
[406] Celzard, A.; Marêché, J. F.; Furdin, G., *Prog. Mater Sci.* **2005,** 50, (1), 93-179.
[407] Klein, C. A., *Rev. Mod. Phys.* **1962,** 34, (1), 56-79.
[408] Meric, I.; Han, M. Y.; Young, A. F.; Ozyilmaz, B.; Kim, P.; Shepard, K. L., *Nat. Nanotechnol.* **2008,** 3, (11), 654-659.
[409] Durkop, T.; Getty, S. A.; Cobas, E.; Fuhrer, M. S., *Nano Lett.* **2003,** 4, (1), 35-39.
[410] Mott, N. F., *Conduction in Noncrystalline Materials*. Clarendon Press: 1987.
[411] Sheng, P.; Sichel, E. K.; Gittleman, J. I., *Phys. Rev. Lett.* **1978,** 40, (18), 1197-1200.
[412] Ishiguro, T.; Kaneko, H.; Nogami, Y.; Ishimoto, H.; Nishiyama, H.; Tsukamoto, J.; Takahashi, A.; Yamaura, M.; Hagiwara, T.; Sato, K., *Phys. Rev. Lett.* **1992,** 69, (4), 660-663.
[413] Reghu, M.; Cao, Y.; Moses, D.; Heeger, A. J., *Phys. Rev. B* **1993,** 47, (4), 1758-1764.
[414] Nardes, A. M.; Kemerink, M.; Janssen, R. A. J.; Bastiaansen, J. A. M.; Kiggen, N. M. M.; Langeveld, B. M. W.; van Breemen, A. J. J. M.; de Kok, M. M., *Adv. Mater.* **2007,** 19, (9), 1196-1200.
[415] Ravi, S.; Kaiser, A. B.; Bumby, C. W., *Chem. Phys. Lett.* **2010,** 496, (1–3), 80-85.
[416] Behnam, A.; Biswas, A.; Bosman, G.; Ural, A., *Phys. Rev. B* **2010,** 81, (12), 125407.
[417] Yanagi, K.; Udoguchi, H.; Sagitani, S.; Oshima, Y.; Takenobu, T.; Kataura, H.; Ishida, T.; Matsuda, K.; Maniwa, Y., *ACS Nano* **2010,** 4, (7), 4027-4032.
[418] Barnes, T. M.; Blackburn, J. L.; van de Lagemaat, J.; Coutts, T. J.; Heben, M. J., *ACS Nano* **2008,** 2, (9), 1968-1976.
[419] Li, Z.; Kandel, H. R.; Dervishi, E.; Saini, V.; Xu, Y.; Biris, A. R.; Lupu, D.; Salamo, G. J.; Biris, A. S., *Langmuir* **2008,** 24, (6), 2655-2662.
[420] Pantin, V.; Avila, J.; Valbuena, M. A.; Esquinazi, P.; Dávila, M. E.; Asensio, M. C., *J. Phys. Chem. Solids* **2006,** 67, (1–3), 546-551.
[421] McKee, D. W., *Annual Review of Materials Science* **1973,** 3, (1), 195-231.
[422] Klein, C. A., *J. Appl. Phys.* **1964,** 35, (10), 2947-2957.
[423] Craciun, M. F.; Russo, S.; Yamamoto, M.; Oostinga, J. B.; Morpurgo, A. F.; Tarucha, S., *Nat. Nanotechnol.* **2009,** 4, (6), 383-388.
[424] Woolf, L. D.; Chin, J.; Lin-Liu, Y. R.; Ikezi, H., *Phys. Rev. B* **1984,** 30, (2), 861-869.
[425] Issi, J. P.; Langer, L.; Heremans, J.; Olk, C. H., *Carbon* **1995,** 33, (7), 941-948.
[426] Charlier, J. C.; Issi, J. P., *Applied Physics A* **1998,** 67, (1), 79-87.

[427] Kim, H.; Mattevi, C.; Calvo, M. R.; Oberg, J. C.; Artiglia, L.; Agnoli, S.; Hirjibehedin, C. F.; Chhowalla, M.; Saiz, E., *ACS Nano* **2012,** 6, (4), 3614-3623.
[428] Zhao, L.; Rim, K. T.; Zhou, H.; He, R.; Heinz, T. F.; Pinczuk, A.; Flynn, G. W.; Pasupathy, A. N., *Solid State Commun.* **2011,** 151, (7), 509-513.
[429] Robinson, V. N. E.; Robins, J. L., *Thin Solid Films* **1974,** 20, (1), 155-175.
[430] Zinsmeister, G., *Thin Solid Films* **1968,** 2, (5–6), 497-507.
[431] Venables, J. A., *Philos. Mag.* **1973,** 27, (3), 697-738.
[432] Lewis, B.; Campbell, D. S., *J. Vac. Sci. Technol.* **1967,** 4, (5), 209-218.
[433] Lewis, B.; Anderson, J. C., *Nucleation and Growth of Thin Films*. Academic Press Inc.: New York, 1978.
[434] Avrami, M., *J. Chem. Phys.* **1939,** 7, (12), 1103-1112.
[435] Kolmogorov, A. N., *Izv. Akad. Nauk SSSR, Ser. Fiz. Mat. Nauk.* **1937,** 3, 355-360.
[436] Johnson, W. A.; Mehl, R. F., *Trans. Am. Inst. Min., Metall. Pet. Eng.* **1939,** 135, 416.
[437] Langmuir, I., *J. Am. Chem. Soc.* **1918,** 40, (9), 1361-1403.
[438] Van Wesep, R. G.; Chen, H.; Zhu, W.; Zhang, Z., *J. Chem. Phys.* **2011,** 134, (17), 171105-4.
[439] Wu, P.; Zhang, W.; Li, Z.; Yang, J.; Hou, J. G., *J. Chem. Phys.* **2010,** 133, (7), 071101-4.
[440] Krug, J., *Physica A* **2002,** 313, (1–2), 47-82.
[441] Kashchiev, D., *Nucleation*. Elsevier Science: 2000.
[442] Artyukhov, V. I.; Liu, Y.; Yakobson, B. I., *Proc. Natl. Acad. Sci.* **2012**.
[443] Vanin, M.; Mortensen, J. J.; Kelkkanen, A. K.; Garcia-Lastra, J. M.; Thygesen, K. S.; Jacobsen, K. W., *Phys. Rev. B* **2010,** 81, (8), 081408.
[444] Khomyakov, P. A.; Giovannetti, G.; Rusu, P. C.; Brocks, G.; van den Brink, J.; Kelly, P. J., *Phys. Rev. B* **2009,** 79, (19), 195425.
[445] Evans, J. W.; Thiel, P. A.; Bartelt, M. C., *Surf. Sci. Rep.* **2006,** 61, (1–2), 1-128.
[446] Gajewski, G.; Pao, C.-W., *J. Chem. Phys.* **2011,** 135, (6), 064707.
[447] Yazyev, O. V.; Pasquarello, A., *Phys. Rev. Lett.* **2008,** 100, (15), 156102.
[448] Kuznetsov, V. L.; Usoltseva, A. N.; Chuvilin, A. L.; Obraztsova, E. D.; Bonard, J.-M., *Phys. Rev. B* **2001,** 64, (23), 235401.
[449] Hayashi, K.; Sato, S.; Ikeda, M.; Kaneta, C.; Yokoyama, N., *J. Am. Chem. Soc.* **2012,** 134, (30), 12492-12498.
[450] An, W.; Zeng, X. C.; Turner, C. H., *J. Chem. Phys.* **2009,** 131, (17), 174702-11.
[451] Au, C.-T.; Ng, C.-F.; Liao, M.-S., *J. Catal.* **1999,** 185, (1), 12-22.
[452] Venables, J. A., *Phys. Rev. B* **1987,** 36, (8), 4153-4162.
[453] Venables, J. A.; Spiller, G. D. T.; Hanbucken, M., *Rep. Prog. Phys.* **1984,** 47, (4), 399.
[454] Mullins, W. W., *J. Appl. Phys.* **1957,** 28, (3), 333-339.
[455] Mullins, W. W.; Shewmon, P. G., *Acta Metall.* **1959,** 7, (3), 163-170.
[456] Hoehne, K.; Sizmann, R., *Phys. Status Solidi A* **1971,** 5, (3), 577-589.
[457] Díaz, J.; Paolicelli, G.; Ferrer, S.; Comin, F., *Phys. Rev. B* **1996,** 54, (11), 8064-8069.
[458] Markov, I.; Kashchiev, D., *Thin Solid Films* **1973,** 15, (2), 181-189.
[459] Earnshaw, A.; Harrington, T. J., *The chemistry of the transition elements*. Clarendon Press: 1973.
[460] Sharples, A., Introduction to Polymer Crystallization. In *Overall Kinetics of Crystallization*, Sharples, A., Ed. Edward Arnold Ltd. : London, 1966; pp 44-59.
[461] Grantab, R.; Shenoy, V. B.; Ruoff, R. S., *Science* **2010,** 330, (6006), 946-948.
[462] Sharma, R.; Baik, J. H.; Perera, C. J.; Strano, M. S., *Nano Lett.* **2010,** 10, (2), 398-405.

[463] Datta, S. S.; Strachan, D. R.; Khamis, S. M.; Johnson, A. T. C., *Nano Lett.* **2008,** 8, (7), 1912-1915.
[464] Liu, H.; Zhang, R.; Yan, R.; Li, J.; Wang, B.; Xie, K., *Appl. Surf. Sci.* **2012,** 258, (20), 8177-8184.
[465] Edwards, J. H.; Maitra, A. M., *Fuel Process. Technol.* **1995,** 42, (2–3), 269-289.
[466] Alstrup, I.; Tavares, M. T., *J. Catal.* **1993,** 139, (2), 513-524.
[467] Lin, Y.-Z.; Sun, J.; Yi, J.; Lin, J.-D.; Chen, H.-B.; Liao, D.-W., *J. Mol. Struct. THEOCHEM* **2002,** 587, (1–3), 63-71.
[468] Wilmer, H.; Genger, T.; Hinrichsen, O., *J. Catal.* **2003,** 215, (2), 188-198.
[469] Tabatabaei, J.; Sakakini, B. H.; Watson, M. J.; Waugh, K. C., *Catal. Lett.* **1999,** 59, (2), 143-149.
[470] Genger, T.; Hinrichsen, O.; Muhler, M., *Catal. Lett.* **1999,** 59, (2), 137-141.
[471] Markov, I., *Crystal Growth for Beginners: fundamentals of Nucleation, crystal growth, and epitaxy*. 2nd ed.; World Scientific Publishing Co. Pte. Ltd.: Singapore, 2004.
[472] Gao, L.; Ren, W.; Zhao, J.; Ma, L.-P.; Chen, Z.; Cheng, H.-M., *Appl. Phys. Lett.* **2010,** 97, (18), 183109.
[473] Sun, J.; Lindvall, N.; Cole, M. T.; Angel, K. T. T.; Teng, W.; Teo, K. B. K.; Chua, D.; Liu, J.; Yurgens, A., *IEEE Trans. Nanotechnol.* **2012,** 11, (2), 255-260.
[474] Liu, W.; Li, H.; Xu, C.; Khatami, Y.; Banerjee, K., *Carbon* **2011,** 49, (13), 4122-4130.
[475] Liu, L.; Zhou, H.; Cheng, R.; Chen, Y.; Lin, Y.-C.; Qu, Y.; Bai, J.; Ivanov, I. A.; Liu, G.; Huang, Y.; Duan, X., *J. Mater. Chem.* **2012,** 22, (4), 1498-1503.
[476] Hwang, J.-Y.; Kuo, C.-C.; Chen, L.-C.; Chen, K.-H., *Nanotechnology* **2010,** 21, (46), 465705.
[477] Wu, B.; Geng, D.; Guo, Y.; Huang, L.; Xue, Y.; Zheng, J.; Chen, J.; Yu, G.; Liu, Y.; Jiang, L.; Hu, W., *Adv. Mater.* **2011,** 23, (31), 3522-3525.
[478] Rasool, H. I.; Song, E. B.; Mecklenburg, M.; Regan, B. C.; Wang, K. L.; Weiller, B. H.; Gimzewski, J. K., *J. Am. Chem. Soc.* **2011,** 133, (32), 12536-12543.
[479] Rasool, H. I.; Song, E. B.; Allen, M. J.; Wassei, J. K.; Kaner, R. B.; Wang, K. L.; Weiller, B. H.; Gimzewski, J. K., *Nano Lett.* **2011,** 11, (1), 251-256.
[480] Cho, J.; Gao, L.; Tian, J.; Cao, H.; Wu, W.; Yu, Q.; Yitamben, E. N.; Fisher, B.; Guest, J. R.; Chen, Y. P.; Guisinger, N. P., *ACS Nano* **2011,** 5, (5), 3607-3613.
[481] Lili, F.; Jie, Z.; Zhen, L.; Xiao, L.; Kunlin, W.; Jinquan, W.; Minlin, Z.; Dehai, W.; Zhiping, X.; Hongwei, Z., *Nanotechnology* **2012,** 23, (11), 115605.
[482] Frost, H. J., *Mater. Charact.* **1994,** 32, (4), 257-273.
[483] Mullins, W. W., *Philos. Mag.* **1961,** 6, (71), 1313-1341.
[484] Moore, A. J. W., *Acta Metall.* **1958,** 6, (4), 293-304.
[485] Tian, J.; Cao, H.; Wu, W.; Yu, Q.; Guisinger, N. P.; Chen, Y. P., *Nano Lett.* **2012,** 12, (8), 3893-3899.
[486] Curie, P., *Journal De Physique Théorique et Appliquee* **1894,** 3, 393.
[487] Portier, R.; Gratias, D., *J. Phys. Colloques* **1982,** 43, (C4), C4-17-C4-34.
[488] Gao, J.; Zhao, J.; Ding, F., *J. Am. Chem. Soc.* **2012,** 134, (14), 6204-6209.
[489] Carlsson, J. M.; Ghiringhelli, L. M.; Fasolino, A., *Phys. Rev. B* **2011,** 84, (16), 165423.
[490] An, J.; Voelkl, E.; Suk, J. W.; Li, X.; Magnuson, C. W.; Fu, L.; Tiemeijer, P.; Bischoff, M.; Freitag, B.; Popova, E.; Ruoff, R. S., *ACS Nano* **2011,** 5, (4), 2433-2439.
[491] Song, J.; Liu, H.; Jiang, H.; Sun, Q.-f.; Xie, X. C., *Phys. Rev. B* **2012,** 86, (8), 085437.
[492] Kim, K.; Lee, Z.; Regan, W.; Kisielowski, C.; Crommie, M. F.; Zettl, A., *ACS Nano* **2011,** 5, (3), 2142-2146.

[493] Hooks, D. E.; Fritz, T.; Ward, M. D., *Adv. Mater.* **2001,** 13, (4), 227-241.
[494] Lewis, B.; Stirland, D. J., *J. Cryst. Growth* **1968,** 3–4, (0), 200-205.
[495] Zhang, Z.; Lagally, M. G., *Science* **1997,** 276, (5311), 377-383.
[496] Brune, H.; Röder, H.; Bromann, K.; Kern, K.; Jacobsen, J.; Stoltze, P.; Jacobsen, K.; NØrskov, J., *Surf. Sci.* **1996,** 349, (1), L115-L122.
[497] Schwoebel, R. L.; Shipsey, E. J., *J. Appl. Phys.* **1966,** 37, (10), 3682-3686.
[498] Robertson, A. W.; Warner, J. H., *Nano Lett.* **2011,** 11, (3), 1182-1189.
[499] Yan, K.; Peng, H.; Zhou, Y.; Li, H.; Liu, Z., *Nano Lett.* **2011,** 11, (3), 1106-1110.
[500] Nie, S.; Wu, W.; Xing, S.; Yu, Q.; Bao, J.; Pei, S.-s.; McCarty, K. F., *New J. Phys.* **2012,** 14, (9), 093028.
[501] Kim, K.-B.; Lee, C.-M.; Choi, J., *J. Phys. Chem. C* **2011,** 115, (30), 14488-14493.
[502] Li, Z.; Zhang, W.; Fan, X.; Wu, P.; Zeng, C.; Li, Z.; Zhai, X.; Yang, J.; Hou, J., *J. Phys. Chem. C* **2012,** 116, (19), 10557-10562.
[503] La Cava, A. I.; Bernardo, C. A.; Trimm, D. L., *Carbon* **1982,** 20, (3), 219-223.
[504] Lobo, L. S.; Trimm, D. L., *Nature Physical Science* **1971,** 234, 15-16.
[505] Luican, A.; Li, G.; Reina, A.; Kong, J.; Nair, R. R.; Novoselov, K. S.; Geim, A. K.; Andrei, E. Y., *Phys. Rev. Lett.* **2011,** 106, (12), 126802.
[506] Wang, W.; Chen, L.; Wang, Z.; Wang, Y.; Li, T.; Wang, Y., *Carbon* **2012,** 50, (14), 5242-5246.
[507] Shallcross, S.; Sharma, S.; Kandelaki, E.; Pankratov, O. A., *Phys. Rev. B* **2010,** 81, (16), 165105.
[508] Trambly de Laissardière, G.; Mayou, D.; Magaud, L., *Nano Lett.* **2010,** 10, (3), 804-808.
[509] Robertson, A. W.; Bachmatiuk, A.; Wu, Y. A.; Schäffel, F.; Rellinghaus, B.; Büchner, B.; Rümmeli, M. H.; Warner, J. H., *ACS Nano* **2011,** 5, (8), 6610-6618.
[510] Kim, K.; Coh, S.; Tan, L. Z.; Regan, W.; Yuk, J. M.; Chatterjee, E.; Crommie, M. F.; Cohen, M. L.; Louie, S. G.; Zettl, A., *Phys. Rev. Lett.* **2012,** 108, (24), 246103.
[511] Awnish, K. G.; Cristiano, N.; Paul, E. L.; Vincent, H. C.; Peter, C. E., *J. Phys.: Condens. Matter* **2010,** 22, (33), 334205.
[512] Locatelli, A.; Knox, K. R.; Cvetko, D.; Menteş, T. O.; Niño, M. A.; Wang, S.; Yilmaz, M. B.; Kim, P.; Osgood, R. M.; Morgante, A., *ACS Nano* **2010,** 4, (8), 4879-4889.
[513] Murata, Y.; Nie, S.; Ebnonnasir, A.; Starodub, E.; Kappes, B. B.; McCarty, K. F.; Ciobanu, C. V.; Kodambaka, S., *Phys. Rev. B* **2012,** 85, (20), 205443.
[514] Hibino, H.; Mizuno, S.; Kageshima, H.; Nagase, M.; Yamaguchi, H., *Phys. Rev. B* **2009,** 80, (8), 085406.
[515] Aoki, M.; Amawashi, H., *Solid State Commun.* **2007,** 142, (3), 123-127.
[516] Charlier, J. C.; Gonze, X.; Michenaud, J. P., *Europhys. Lett.* **1994,** 28, (6), 403.
[517] Wang, L.-W., *Phys. Rev. B* **2002,** 65, (15), 153410.
[518] Zhang, Y.; Tsu, R., *Nanoscale Res. Lett.* **2010,** 5, (5), 805 - 808.
[519] Lee, J.-K.; Lee, S.-C.; Ahn, J.-P.; Kim, S.-C.; Wilson, J. I. B.; John, P., *J. Chem. Phys.* **2008,** 129, (23), 234709-4.
[520] Liu, Z.; Suenaga, K.; Harris, P. J. F.; Iijima, S., *Phys. Rev. Lett.* **2009,** 102, (1), 015501.
[521] Borysiuk, J.; Soltys, J.; Piechota, J., *J. Appl. Phys.* **2011,** 109, (9), 093523-6.
[522] Zhang, X.; Xu, Z.; Hui, L.; Xin, J.; Ding, F., *J. Phys. Chem. Lett.* **2012**, 2822-2827.
[523] Jia, X.; Hofmann, M.; Meunier, V.; Sumpter, B. G.; Campos-Delgado, J.; Romo-Herrera, J. M.; Son, H.; Hsieh, Y.-P.; Reina, A.; Kong, J.; Terrones, M.; Dresselhaus, M. S., *Science* **2009,** 323, (5922), 1701-1705.

[524] Cançado, L. G.; Takai, K.; Enoki, T.; Endo, M.; Kim, Y. A.; Mizusaki, H.; Speziali, N. L.; Jorio, A.; Pimenta, M. A., *Carbon* **2008,** 46, (2), 272-275.
[525] Charlier, J. C.; Gonze, X.; Michenaud, J. P., *Carbon* **1994,** 32, (2), 289-299.
[526] Nie, S.; Walter, A. L.; Bartelt, N. C.; Starodub, E.; Bostwick, A.; Rotenberg, E.; McCarty, K. F., *ACS Nano* **2011,** 5, (3), 2298-2306.